Application of *hp*-adaptive finite element method to two-scale computation

Ph.D. thesis presented by

Marta Serafin, M.Sc.

advisor: Witold Cecot, Ph.D., prof. of CUT

Cracow University of Technology
Faculty of Civil Engineering
Institute for Computational Civil Engineering

Kraków 2012

Contents

Acknowledgment

I would like to express my gratitude and great appreciation to **Professor Witold Cecot** for his supervision during my doctoral work, guidance, many discussions and supporting me in carrying out this research.

This work was supported by Polish Ministry for Science and Higher Education under the grant 3697/B/T02/2008/34 (2008–2010) *Multiscale modeling of inelastic heterogeneous materials with hp-adaptive finite element method* and European Social Fund under *DOCTUS* scholarship (2009–2011).

Notation

Latin symbols

$\boldsymbol{C}$	elasticity tensor
$\boldsymbol{C}_{eff}$	effective elasticity tensor
$\boldsymbol{C}^{ep}$	elastic–plastic tensor
$\boldsymbol{C}^{ep}_{eff}$	elastic–plastic effective tensor
E	Young modulus
E_{eff}	effective Young modulus
H	kinematic hardening parameter
k	shear yield limit
$\boldsymbol{s}$	deviator of stress tensor
$\boldsymbol{t}$	traction
t	time
$\boldsymbol{u}$	displacement vector
$\boldsymbol{u}_0$	homogenized or averaged displacement vector

Greek symbols

γ	plastic multiplier
λ	Lame's first parameter
μ	shear modulus
μ_{eff}	effective shear modulus
ν	Poisson ratio
ν_{eff}	effective Poisson ratio
$\boldsymbol{\sigma}$	stress tensor
$\boldsymbol{\sigma}_0$	homogenized or averaged stress tensor
σ^y	yield strength
$\boldsymbol{\varepsilon}$	strain tensor

$\boldsymbol{\varepsilon}_0$	homogenized or averaged strain tensor
$\boldsymbol{\varepsilon}^p$	plastic strain tensor
$\boldsymbol{\varepsilon}_0^p$	homogenized or averaged plastic strain tensor

Abbreviations

FE	finite element
FEM	finite element method
NDOF	number of degrees of freedom
RVE	representative volume element
1D, 2D, 3D	one, two or three–dimensional (problem), respectively

Miscellaneous

$\cdot$, :	inner products of vectors and tensors, respectively
$\langle \cdot \rangle$	volume average of property over domain

Chapter 1

Introduction

1.1 Motivation and objectives of the research

Innovative materials are one of the major factors influencing technology development observed in recent years. In this area metal matrix composites, made of two or more different constituents, are ones of the most popular materials used by engineers e.g. in automotive industry, aerospace, rail engineering, building industry, military, marine, electronics, sports equipment, etc. However, application of new materials has to be preceded by long and expensive experiments in laboratories. In order to reduce both costs and time of experiments it is necessary to supplement them by computer modeling that enables not only prediction of new material features, but also safety examination of structures, in which they will be used.

Computer modeling always introduces certain simplifications, therefore it is a challenging task, especially when inelastic deformations occur. Thus, the idea is to use a multiscale approach, where one can predict overall properties of a material by systematic reduction of huge, and in majority unneeded, amount of information from the micro-level. Such a process is called *homogenization*. In particular its computational version proved to be an efficient modeling tool.

Numerical techniques for multiscale modeling that allow obtaining reliable results in a reasonable time, are now intensively developed. In this work structural components made of heterogeneous material that globally possesses either elastic or inelastic properties are modeled. *hp*-adaptive finite element method that enables effective computation with reliable assessment of the solution quality is proposed for computation. Thus, the main objective of this work is to combine computational homogenization and adaptive FEM to obtain an effective method for efficient modeling of metal matrix composites.

1.2 Scope of the work

The thesis is organized as follows. Chapter 1 contains state of the art of multiscale modeling approaches and adaptation techniques in finite element analysis. Chapter 2 provides description of mathematical models, their formulations and general assumptions. Chapter 3 describes preliminary tests of computational homogenization, including verification of the algorithm and details of finite element discretization. Next,

two-scale computational homogenization for elastic-plastic composites is presented and validated by solution of several numerical examples. Chapter 5 deals with homogenization error estimation that is crucial for obtaining reliable results. Selected examples illustrate the proposed approaches. Chapter 6 contains tests of possible modifications of *hp*-adaptive algorithm for inelastic problems. In Chapter 7 possibilities of mixed formulation in finite element method to multiscale modeling are presented. Chapter 8 summarizes the thesis.

1.3 Basis of multiscale modeling

All materials used in engineering have a heterogeneous physical structure, which may be observed in the appropriate fine-scales. Various scales (levels) are defined by their characteristic dimensions, which are usually related to the geometrical dimensions of the basic elements of material structure, e.g. the nominal diameter of the aggregate in concrete mixture, but it can be also size of the wavelength for acoustics problems.

One may distinguish certain space and corresponding time scales modeled by different laws of physics. They are schematically illustrated in Fig. 1.1.

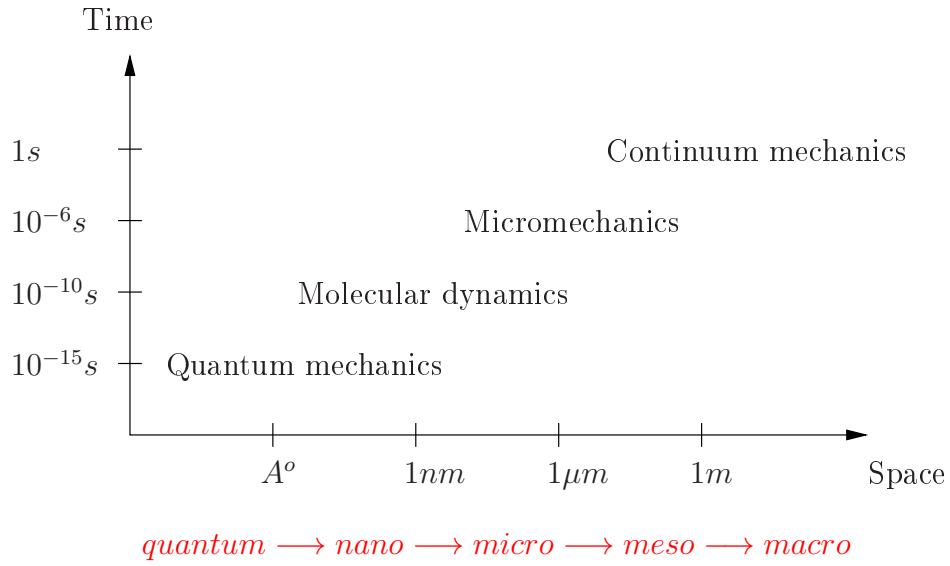

Figure 1.1: Scales of analysis.

In this work only principles of continuum mechanics are used, but at two different space scales (called *micro* and *macro*).

The so-called brute force computation, which is one of the possible methods to model heterogeneous materials with a periodic or random microstructure, takes into account all heterogeneities without any simplification. One may use high performance computers and advanced numerical techniques e.g. adaptive [6, 12, 29, 40] or extended [69, 96] finite element methods, multigrid approaches [63, 108], domain decomposition [1] and parallel computation. However, the computational cost and time will still be very huge, and usually such an elaborated modeling of structures is actually unnecessary.

In the case of composites with linear constitutive behavior the simplest approaches to modeling of heterogeneous materials are the direct and inverse *mixture rules*. These methods take into account only material characteristics and proportions of components. However, even if direction of e.g. fibers is also accounted for, their estimation is very rough and may be used only for the initial elastic calculation.

The most commonly used theoretical methods are *bound approaches*. The upper and lower bounds of effective moduli were first obtained by Voigt [107] and Reuss [88] approximation. These approximations, based on the rule of mixtures, are independent of the size and shape of inclusions. Voigt assumed that the average strain of each phase is equal to the applied strain, under uniform strain exterior loading. Later Reuss assumed that the average stress of each phase is uniform (constant), under uniform stress exterior loading. Both bounds provide a rough determination of aggregate responses for micro-heterogeneous materials. Those ideas are more precisely discussed in e.g. [72]. Another, more accurate bound estimation, was derived from the variational principle, known as the Hashin-Shtrikman bounds [42, 43]. However, all these bounds are sensitive to sample size and are valid only when the body is assumed to be infinite, the microstructure isotropic and the effective responses are isotropic [54].

Another possibility is the *Eshelby effective eigenstrain approach* for an isolated ellipsoidal inclusion embedded in an infinite medium [32]. An extension of the Eshelby method is the *self-consistent approach* [21, 47], in which a single particle of one phase is embedded in the effective material (equivalent medium) that represents influence of all other microstructural elements on this single inclusion. The influences of the other elements on this single particle are smeared over the equivalent medium.

Mori-Tanaka mean field theory [71] is based on concept of the average stress in the matrix. Material properties are evaluated as an analytical solution of a boundary value problem for a single inclusion in an infinite matrix made of another material.

Differential effective medium approximation (DEM) [14, 89, 98] is another approach. The process of DEM consists of iterative addition of inclusion volume to homogeneous matrix. Thus, the new effective properties of the background material are re-calculated until the final volume fraction is reached.

A different group of techniques is represented by *asymptotic homogenization* method [13, 60, 86, 90, 97, 98], where the displacement field (as well as the stress field) in a heterogeneous domain is expanded asymptotically about its values at a macroscopic point $x = X/L$, in terms of a microscopic coordinates $y = X/l$ as

$$u(x,y) = u^{(0)}(x,y) + \varepsilon u^{(1)}(x,y) + \varepsilon^2 u^{(2)}(x,y) + \ldots, \qquad \varepsilon = \frac{l}{L} \Rightarrow y = \frac{x}{\varepsilon}$$

where: l is the micro-size, L is the macro-size, x is a physical spatial variable at both scales. In the asymptotic analysis the normalized cell of periodicity is mapped onto a sequence of finer structures as ε tends to 0. Asymptotic homogenization theory explicitly uses periodic boundary conditions in modeling of linear and nonlinear composite materials, and gives overall properties for strain and stress values. Other popular possibilities of multiscale modeling are collected in [54].

One of the recently developed techniques is *local numerical homogenization* [49, 50]. This approach is based on two-scale analysis. In the macro-scale the coarse finite element mesh is selected. Then, in each coarse element fine mesh is generated in order to take into account heterogeneity (the micro-scale analysis). In this way, the coarse

mesh and the fine-scale structure become naturally compatible. The homogenization, consisting of calculation of the finite element stiffness matrix based on a fine-mesh solution, is performed individually for each element. This method is very efficient when the scale separation condition (characteristic inclusion size should be much smaller than the matrix) is not satisfied, e.g. in asphalt pavement modeling [55].

The structure of a material on the microscopic level is often of a discrete character. Thus, interactions between individual grains and inside grain interiors can be simulated e.g. using cellular automata (CA) method. For two-scale analysis a specific coupling of the CA with the finite element method is referred to as a CAFE approach that combines cellular automata model of microstructure development and finite element (FE) macroscopic simulation [22, 38, 64].

However, the most popular method in recent years for multiscale problems is **computational homogenization** (also called global - local analysis) [13, 18, 31, 35, 36, 52, 56, 68, 78, 104, 113] that enables determination of material parameters of heterogeneous material on the basis of multiscale approach. This technique does not require any constitutive assumption on the macro-level. The stress-strain relation is computed at each point of interest at the macro-scale by detailed analysis of the microstructure in so-called representative volume elements (RVE), attributed to those points. Since RVE are typically analyzed by FEM, the method is sometimes called FE^2.

In this work such an approach is used. Two scales of analysis are considered and they are referred to as *micro* and *macro*. In the macro-level material is considered as homogeneous and the heterogeneity is taken into account in the micro-scale by RVE analysis. RVE should be statistically representative for the microstructure and also small enough to satisfy the scale separation condition [39, 46, 79], which states fundamental assumption of the homogenization theory:

$$d < l << L \tag{1.1}$$

where d is the inclusion size, l and L are the characteristic scales of RVE and the macro-domain, respectively. In practice, the maximum value of the ratio of dimensions l/L, for which the homogenization theory can be used, is assumed as 0.1.

The classical algorithm of computational homogenization for nonlinear problems begins by discretization at the macro-level and association of the representative volume elements (RVE) to selected points (usually the Gauss integration points for finite element analysis). At first in the macro-scale preliminary material parameters are assumed (e.g. as the result of tension test performed over RVE) to compute the current strains increment $\Delta\boldsymbol{\varepsilon}_0$ (or averaged stresses $\langle\boldsymbol{\sigma}\rangle$) for the given load increment. Such a strain state (or stress state) at a macro-point determines boundary conditions for associated RVE. Afterward, in each time step the initial-boundary value problems defined over RVE are solved by FEM to evaluate average plastic strain increment $\langle\Delta\boldsymbol{\varepsilon}^p\rangle$ or average stress increment $\langle\Delta\boldsymbol{\sigma}\rangle$, both for elastic and elastic-plastic materials. The effective material parameters obtained this way are transfered to the Gauss integration points. Error estimation is conducted and either mesh is refined or computation is terminated at the current time step.

The general algorithm looks as follows:

1. Discretization

   – initial mesh generation at both macro and micro-scales

   – selection of points (RVE) at which the effective properties are evaluated by analysis at the micro-scale

2. Initial determination of homogenized material parameters (e.g. by tension test for RVE)

3. Macro-scale analysis

   – determine the strain/stress state in the macro-body to impose appropriate boundary conditions for RVE

4. Micro-scale analysis

   – solution of the RVE problem for current $\Delta\boldsymbol{\varepsilon}_0$ given from the macro-scale

   – error estimation, reduction of the RVE solution error by adaptive mesh refinement

   – $\langle\Delta\boldsymbol{\varepsilon}^p\rangle$ computation

5. Transfer of effective parameters to the Gauss points

6. Solution of the macro-scale problem with effective material parameters and effective plastic strains

7. Macro-scale error estimation and

   – mesh refinement or

   – load increment or

   – end of the analysis

8. GO TO 3

Computational homogenization algorithm presented above is schematically illustrated in Fig. 1.2. From numerical point of view such an algorithm is rather time-consuming. The main drawback is a large number of RVE since they are associated to each Gauss integration point. In this work various modifications are proposed to avoid this problem.

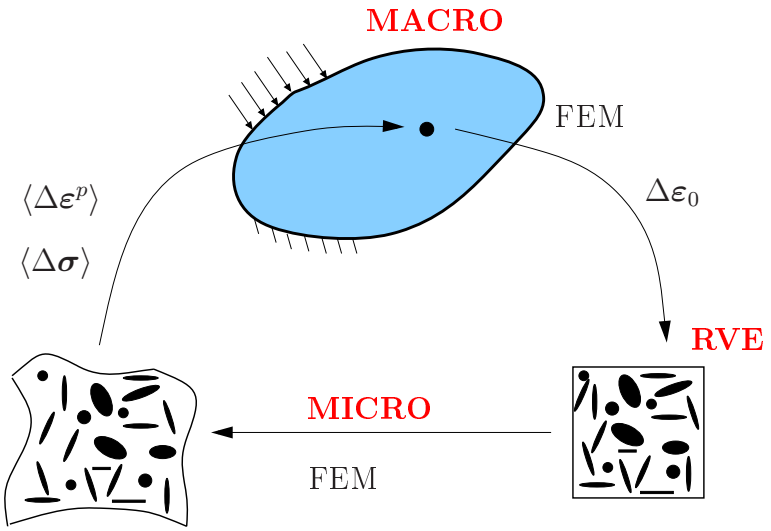

Figure 1.2: Computational homogenization algorithm.

1.4 Adaptive finite element methods

Adaptive mesh refinement strategies are very efficient techniques that enable users to solve problems with good accuracy in a relatively short time. An a-posteriori error estimate is its important component. Adaptive methods are very useful, especially when the considered problem has an irregular solution or singularities appear. In such cases regular finite element meshes are not optimal, because increase of the number of degrees of freedom is not related to proportional improvement of the solution.

Generally, one may distinguish two main types of adaptation: h-adaptation [6, 40], where the element size varies without changing the order of approximation; p-adaptation [9, 10, 12], where the element sizes are constant, but the orders of the shape functions vary. In order to clarify these methods both mesh refinement strategies for a cube domain that is initially discretized by 27 elements with second order shape functions (Fig. 1.3), are presented in Fig. 1.4.

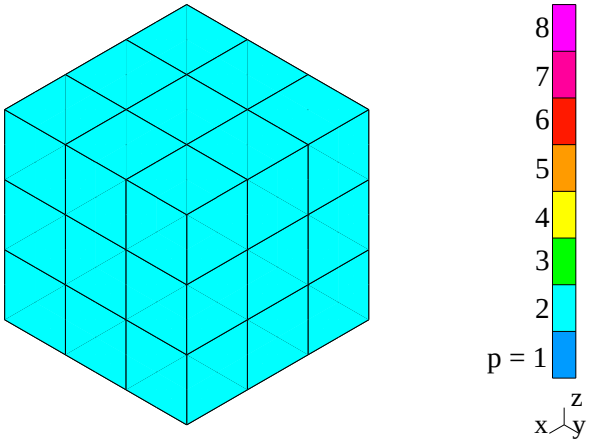

Figure 1.3: Initial mesh. The colors denote order of approximation p.

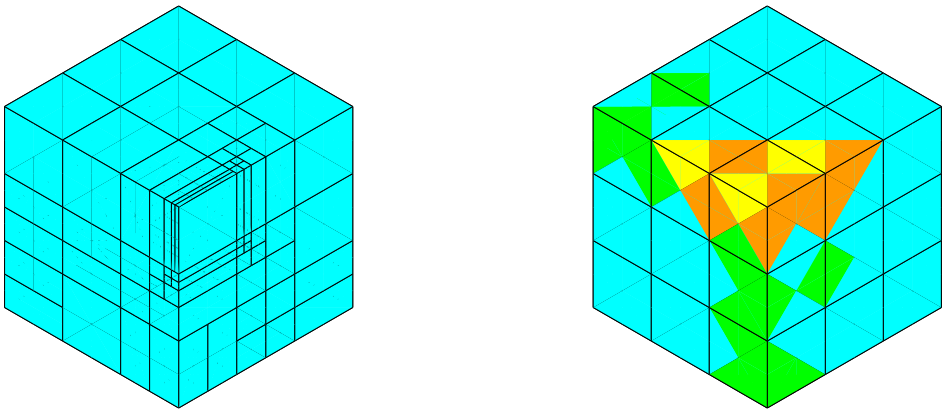

Figure 1.4: h and p mesh refinement strategies.

The next possibility is an adaptive relocation of the existing nodes (r-adaptation) [44, 103] in order to minimize a solution error. This method may be also combined with the p-method, where the shape functions may be increased locally with additional ability of nodes movement. Its application is presented e.g. in paper [73].

Another alternative of adaptation, known as the hp-method [28, 29, 40, 41], combines both h and p ones. Its main advantage is the exponential convergence, i.e.

$$||u - u_h||_{1,\Omega} \leq Ce^{-\alpha N^{\beta}} \tag{1.2}$$

superior to h and p adaptation techniques, where only algebraic convergence may be obtained, e.g. for 3D problems one may expect that

$$||u - u_h||_{1,\Omega} \leq CN^{-p/3} \tag{1.3}$$

where: u and u_h denote exact and FE solutions, respectively; C, $\alpha > 0$ are constants, $\beta \simeq \frac{1}{3}$, N denotes the number of degrees of freedom, p is the order of approximation. The qualitative comparison of the error convergence for various, above mentioned, adaptive mesh refinement strategies is illustrated in Fig. 1.5.

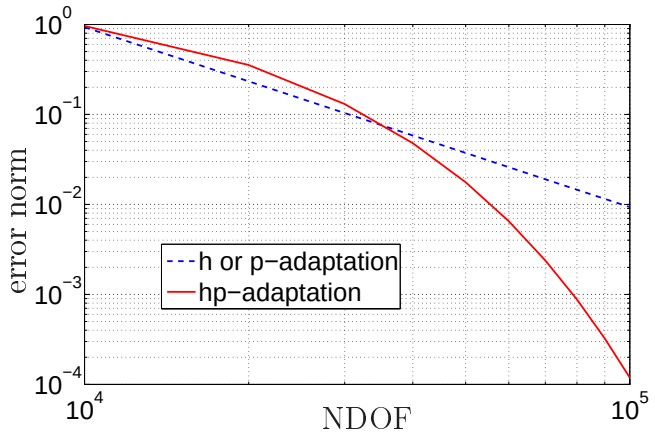

Figure 1.5: Error convergence for various adaptation strategies.

Goal-oriented algorithm [75, 84] is an efficient alternative of adaptation strategy for approximation a specific feature of the solution. Refinement strategies of this type are based on minimizing the error of a prescribed quantity of interest, e.g. displacement at selected point, rather than the global error norm.

In this work the computations were performed by the automatic *hp*-adaptative FEM proposed by Demkowicz et al. [26, 27, 29] that delivers error-controlled results with the smallest possible number of degrees of freedom. This automatic mesh adaptation was successfully used for various linear problems. Its key issue is an appropriate strategy of anisotropic h, p or hp mesh refinement. The strategy proposed in [29] is based on the interpolation error estimate, which is a good upper bound of the best approximation error that in turn, for coercive problems by the Cea's lemma, is the upper bound for the actual approximation error. The aforementioned interpolation error is estimated making use of a fine mesh solution ($\boldsymbol{u}_{h/2,p+1}$, denoted here for the sake of brevity by $\boldsymbol{u}$) that serves as a substitute for the exact solution. Such an "exact" solution is interpolated locally by the possible new *hp*-refined meshes. The difference between $\boldsymbol{u}$ and its interpolant approximates the interpolation error and the optimal anisotropic mesh refinement is determined in such a way that the reduction of the interpolation error per number of additional degrees of freedom is maximal. It means that for the coarse mesh the optimal (h, p or hp) refinement is determined by maximizing the following expression

$$\omega = \frac{|\boldsymbol{u} - \Pi_{hp}\boldsymbol{u}|^2_{H^1} - |\boldsymbol{u} - \Pi_{hp_{opt}}\boldsymbol{u}|^2_{H^1}}{N_0 - N_c} \rightarrow \max \tag{1.4}$$

with additional assumption that the mesh is one-irregular, where Π_{hp}, $\Pi_{hp_{opt}}$ denote H^1 projection-based interpolants [74] on the current and optimal meshes, respectively; N_0, N_c are the numbers of degrees of freedom in optimal and current meshes. The maximization is performed by search over a suitable subset of all possible *hp* refinements.

Thus, the algorithm of adaptation approach starts with the solution of the problem on the current (coarse) mesh ($\boldsymbol{u}_{hp}$). Then, the refinement in both h and p is performed and the optimal mesh is selected by maximization of the function ω defined by Eq. (1.4).

For large problems computation of the fine mesh solution may be time-consuming. However, only partially convergent solution obtained by e.g. a fast two-grid solver may be used to guide the optimal *hp*-refinement.

The single *hp*-adaptation step for finite element mesh is briefly presented below:

1. Solve the problem on the current (coarse) mesh $\longrightarrow \quad \boldsymbol{u}_{h,\,p}$
2. Solve the problem on the fine mesh $\longrightarrow \quad \boldsymbol{u}_{h/2,\,p+1}$
3. If $||\boldsymbol{u}_{h/2,\,p+1} - \boldsymbol{u}_{h,\,p}||$ is acceptable then STOP
4. For the coarse mesh elements determine the optimal (h, p or hp) refinement using objective function defined by Eq. (1.4) and assumption that the mesh is one-irregular as a constraint.

An example of finite element mesh generated during automatic *hp*-adaptation process is shown in Fig. 1.6. This automatic *hp* method is a technique, which enables application of significantly elongated or flattened elements without locking effect. This is ensured by appropriate raising of the order of approximation along the larger dimensions, typically to order 4 or higher, demonstrated in [100, 102] for thin-walled structures modeling.

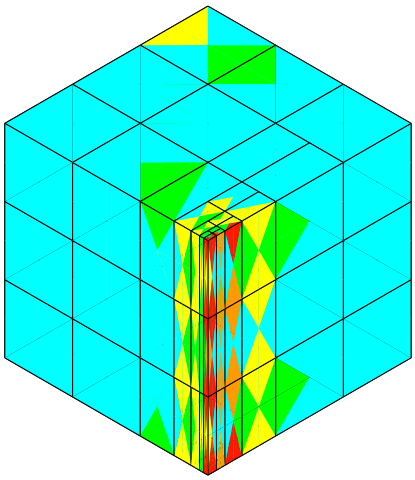

Figure 1.6: Adaptive *hp* mesh refinement strategy (colors indicate order of approximation).

It can be also noticed the existence of one-irregular meshes with hanging nodes, where the continuity of displacements is enforced by the constraint approximation. This way number of unknowns is reduced.

Chapter 2

Problem formulations

This section summarizes the mathematical formulations, which were the basis of numerical calculation.

2.1 Macro-scale problem for heterogeneous material

The macro-scale problem for heterogeneous domain Ω is formulated in the following way: *find fields of displacements* $\boldsymbol{u}(\boldsymbol{x},t)$*, stresses* $\boldsymbol{\sigma}(\boldsymbol{x},t)$*, total strains* $\boldsymbol{\varepsilon}(\boldsymbol{x},t)$ *and plastic strains* $\boldsymbol{\varepsilon}^p(\boldsymbol{x},t)$*, such that at every time instant* t *and for every subdomain* ω_i *with smooth enough tensor of elastic material parameters* $\boldsymbol{C}$ *the following standard system of equations is satisfied*

$$\begin{cases} \mathbf{div}\,\dot{\boldsymbol{\sigma}} + \dot{\boldsymbol{X}} = 0 & \forall\, t, \quad \boldsymbol{x} \in \omega_i \subset \Omega \\ \dot{\boldsymbol{\sigma}} = \boldsymbol{C}[\dot{\boldsymbol{\varepsilon}}(\dot{\boldsymbol{u}}) - \dot{\boldsymbol{\varepsilon}}^p] & \forall\, t, \quad \boldsymbol{x} \in \omega_i \subset \Omega \\ \dot{\boldsymbol{\varepsilon}} = \frac{1}{2}[\nabla\dot{\boldsymbol{u}} + (\nabla\dot{\boldsymbol{u}})^T] & \forall\, t, \quad \boldsymbol{x} \in \omega_i \subset \Omega \\ \dot{\boldsymbol{\varepsilon}}^p = f(\boldsymbol{\sigma}, \boldsymbol{\chi}, \dots) & \forall\, t, \quad \boldsymbol{x} \in \omega_i \subset \Omega \\ + \text{ initial and boundary conditions} \\ + \text{ continuity conditions} \end{cases} \tag{2.1}$$

where: $\boldsymbol{X}$ denotes body forces, f indicates the evaluation law of plastic strain rates. Solution of this problem is very time-consuming and requires enormous computer cost. Moreover, from engineering point of view, its solution is usually unnecessary. Determination of the critical state of material and the global behavior of the whole structure is relevant, therefore, two-scale analysis is proposed to minimize computation cost without losing reliability of the results.

2.2 Macro-scale homogenized problem

Instead of original problem (2.1) the following, simplified due to homogenization, model will be analyzed: *find fields of displacements* $\boldsymbol{u}_0(\boldsymbol{x},t)$*, stresses* $\boldsymbol{\sigma}_0(\boldsymbol{x},t)$*, total strains* $\boldsymbol{\varepsilon}_0(\boldsymbol{x},t)$ *and plastic strains* $\boldsymbol{\varepsilon}_0^p(\boldsymbol{x},t)$*, such that for every time instant* $t \in [0,T]$ *the following relations hold:*

$$\begin{cases} \mathbf{div}\,\dot{\boldsymbol{\sigma}}_0 + \dot{\boldsymbol{X}} = 0 & \forall t, \quad \boldsymbol{x} \in \Omega \\ \dot{\boldsymbol{\sigma}}_0 = \boldsymbol{C}_{eff}[\dot{\boldsymbol{\varepsilon}}_0(\dot{\boldsymbol{u}}_0) - \dot{\boldsymbol{\varepsilon}}_0^p] = \boldsymbol{C}_{eff}^{ep}(t)\dot{\boldsymbol{\varepsilon}}_0 & \forall t, \quad \boldsymbol{x} \in \Omega \\ \dot{\boldsymbol{\varepsilon}}_0 = \frac{1}{2}[\nabla\dot{\boldsymbol{u}}_0 + (\nabla\dot{\boldsymbol{u}}_0)^T] & \forall t, \quad \boldsymbol{x} \in \Omega \\ + \text{ initial \& boundary conditions} \end{cases} \tag{2.2}$$

where averaged values are denoted by subscript "0", rates of stresses may be computed using either tensor of elastic effective material parameters $\boldsymbol{C}_{eff}$ and inelastic strain rates $\dot{\boldsymbol{\varepsilon}}_0^p$ or elastic-plastic effective tensor $\boldsymbol{C}_{eff}^{ep}$ and total strain rates. These quantities are evaluated only at selected points of the body by local analysis performed at the micro-scale in RVE attributed to those points.

The weak formulation of the macro-scale problem may be stated in the form: *find field of displacements* $\boldsymbol{u}_0(\boldsymbol{x},t) \in \boldsymbol{V}_0 + \hat{\boldsymbol{u}}_0$*, such that for every* $t \in [0,T]$

$$\begin{aligned} \int_\Omega \boldsymbol{\varepsilon}_0(\boldsymbol{v}) : \boldsymbol{C}_{eff}\,\dot{\boldsymbol{\varepsilon}}_0(\dot{\boldsymbol{u}}_0)\,\mathrm{d}\Omega &= \int_{\partial\Omega_N} \dot{\hat{\boldsymbol{t}}}_0\,\boldsymbol{v}\,\mathrm{d}s + \int_\Omega \boldsymbol{\varepsilon}_0(\boldsymbol{v}) : \boldsymbol{C}_{eff}\,\dot{\boldsymbol{\varepsilon}}_0^p\,\mathrm{d}\Omega + \int_\Omega \dot{\boldsymbol{X}}\boldsymbol{v}\,\mathrm{d}\Omega \\ & \qquad\qquad \forall \boldsymbol{v} \in \boldsymbol{V}_0 \\ \text{or} & \\ \int_\Omega \boldsymbol{\varepsilon}_0(\boldsymbol{v}) : \boldsymbol{C}_{eff}^{ep}(t)\,\dot{\boldsymbol{\varepsilon}}_0(\dot{\boldsymbol{u}}_0)\,\mathrm{d}\Omega &= \int_{\partial\Omega_N} \dot{\hat{\boldsymbol{t}}}_0\,\boldsymbol{v}\,\mathrm{d}s + \int_\Omega \dot{\boldsymbol{X}}\boldsymbol{v}\,\mathrm{d}\Omega \qquad \forall \boldsymbol{v} \in \boldsymbol{V}_0 \\ \text{or} & \\ \int_\Omega \boldsymbol{\varepsilon}_0(\boldsymbol{v}) : \dot{\boldsymbol{\sigma}}_0(\boldsymbol{u})\,\mathrm{d}\Omega &= \int_{\partial\Omega_N} \dot{\hat{\boldsymbol{t}}}_0\,\boldsymbol{v}\,\mathrm{d}s + \int_\Omega \dot{\boldsymbol{X}}\boldsymbol{v}\,\mathrm{d}\Omega \qquad \forall \boldsymbol{v} \in \boldsymbol{V}_0 \end{aligned} \tag{2.3}$$

where T denotes the final time of the analysis, $\boldsymbol{V}_0 = \{\boldsymbol{v} \in [H^1(\Omega)]^n,\ \boldsymbol{v} = 0 \text{ on } \partial\Omega_D\}$, $\partial\Omega_D$ and $\partial\Omega_N$ are the Dirichlet and Neumann parts of the boundary, $\partial\Omega_D \cup \partial\Omega_N = \partial\Omega$ and $\partial\Omega_D \cap \partial\Omega_N = \emptyset$. $\dot{\hat{\boldsymbol{t}}}_0$, $\dot{\hat{\boldsymbol{u}}}_0$ are known rates of tractions and displacements along the Neumann and Dirichlet parts of the boundary.

In this work weak formulation in form $(2.3)_1$ was used.

2.3 Micro-scale problem for heterogeneous material

The micro-scale problem is defined over representative volume elements (RVE) associated with selected points of the macro-body. The problem consists of assuming boundary conditions on the basis of strains in homogeneous macro-domain and solution of the initial–boundary value problem defined only in RVE. Body forces are not considered in the equilibrium equations [72]. The micro-scale problem may be formulated in the following form: *find fields of displacements* $\boldsymbol{u}(\boldsymbol{x},t)$*, total strains* $\boldsymbol{\varepsilon}(\boldsymbol{x},t)$*,*

stresses $\boldsymbol{\sigma}(\boldsymbol{x},t)$ *and plastic strains* $\boldsymbol{\varepsilon}^p(\boldsymbol{x},t)$*, such that*

$$\begin{cases} \mathbf{div}\,\dot{\boldsymbol{\sigma}} = 0 & \forall t \in [t_k,\, t_{k+1}], \boldsymbol{x} \in \omega_i \\ \dot{\boldsymbol{\sigma}} = \boldsymbol{C}[\dot{\boldsymbol{\varepsilon}}(\dot{\boldsymbol{u}}) - \dot{\boldsymbol{\varepsilon}}^p] & \forall\, t \in [t_k,\, t_{k+1}], \boldsymbol{x} \in \omega_i \\ \dot{\boldsymbol{\varepsilon}} = \frac{1}{2}[\nabla\dot{\boldsymbol{u}} + (\nabla\dot{\boldsymbol{u}})^T] & \forall t \in [t_k,\, t_{k+1}], \boldsymbol{x} \in \omega_i \\ \dot{\boldsymbol{\varepsilon}}^p = f(\boldsymbol{\sigma}, \boldsymbol{\chi}, \dots) & \forall t \in [t_k,\, t_{k+1}], \boldsymbol{x} \in \omega_i \\ \dot{\boldsymbol{u}} = \hat{\dot{\boldsymbol{u}}} & \forall t \in [t_k,\, t_{k+1}], \boldsymbol{x} \in \Gamma_D \\ \dot{\boldsymbol{\sigma}}\,\boldsymbol{n} = \hat{\dot{\boldsymbol{t}}} & \forall t \in [t_k,\, t_{k+1}], \boldsymbol{x} \in \Gamma_N \\ \dot{\boldsymbol{u}}_- = \dot{\boldsymbol{u}}_+ & \forall t \in [t_k,\, t_{k+1}], \boldsymbol{x} \in \Gamma_0 \\ \dot{\boldsymbol{t}}_- = -\dot{\boldsymbol{t}}_+ & \forall t \in [t_k,\, t_{k+1}], \boldsymbol{x} \in \Gamma_0 \end{cases} \tag{2.4}$$

where ω_i denotes i-th homogeneous subdomain of heterogeneous RVE ($i = 1, \dots, N$), Γ_D and Γ_N are the parts of Dirichlet and Neumann boundary, $\Gamma_D \cup \Gamma_N = \Gamma$ and $\Gamma_D \cap \Gamma_N = \emptyset$, Γ_0 is the interface between various materials. $\hat{\dot{\boldsymbol{t}}}$, $\hat{\dot{\boldsymbol{u}}}$ are the known rates of tractions and displacements along the Neumann and Dirichlet parts of the boundary, f denotes evolution law of inelastic strains. Periodic boundary conditions may be also used and they are discussed in the next section.

The weak formulation, equivalent to (2.4), is as follows: *find field of displacements* $\boldsymbol{u}(\boldsymbol{x},t) \in \boldsymbol{V}_0 + \hat{\boldsymbol{u}}$*, such that for every* $t \in [0,T]$

$$\begin{aligned} &\textstyle\int_{\omega_i} \boldsymbol{\varepsilon}(\boldsymbol{v}) : \boldsymbol{C}\,\dot{\boldsymbol{\varepsilon}}(\dot{\boldsymbol{u}})\,\mathrm{d}\Omega = \int_{\omega_i} \boldsymbol{\varepsilon}(\boldsymbol{v}) : \boldsymbol{C}\,\dot{\boldsymbol{\varepsilon}}^p\,\mathrm{d}\Omega + \int_{\Gamma_N} \hat{\dot{\boldsymbol{t}}}\,\boldsymbol{v}\,\mathrm{d}s \qquad \forall \boldsymbol{v} \in \boldsymbol{V}_0 \\ &\text{or} \\ &\textstyle\int_{\omega_i} \boldsymbol{\varepsilon}(\boldsymbol{v}) : \boldsymbol{C}^{ep}(t)\,\dot{\boldsymbol{\varepsilon}}(\dot{\boldsymbol{u}})\,\mathrm{d}\Omega = \int_{\Gamma_N} \hat{\dot{\boldsymbol{t}}}\,\boldsymbol{v}\,\mathrm{d}s \qquad \forall \boldsymbol{v} \in \boldsymbol{V}_0 \end{aligned} \tag{2.5}$$

where $\boldsymbol{V}_0 = \{\boldsymbol{v} \in [H^1(\Omega)]^n,\, \boldsymbol{v} = 0 \text{ on } \Gamma_D\}$.

In this work weak formulation in form $(2.5)_1$ was used. The classical associative, rate-independent, J_2 flow plasticity with linear kinematic hardening is used for plastic behavior modeling. Thus, the admissible stresses are bounded by the Mises yield surface

$$\phi(\boldsymbol{\sigma}) = \frac{1}{2}\left(\boldsymbol{s} - \frac{2}{3}H\boldsymbol{\varepsilon}^p\right) : \left(\boldsymbol{s} - \frac{2}{3}H\boldsymbol{\varepsilon}^p\right) - k^2 \tag{2.6}$$

where: $\boldsymbol{s}$ is the deviator of stress tensor, H denotes kinematic hardening parameter, $k = \sigma^y/\sqrt{3}$ is the shear yield limit, σ^y denotes yield strength.

Plastic strain rate is given by the associative plastic flow rule

$$\dot{\boldsymbol{\varepsilon}}^p = \gamma\frac{\partial\phi}{\partial\boldsymbol{\sigma}} \tag{2.7}$$

where γ stands for the plastic multiplier. The following Kuhn-Tucker condition (loading/unloading relation) should also be satisfied

$$\gamma \geq 0, \quad \phi \leq 0, \quad \gamma\phi = 0 \tag{2.8}$$

Effective material properties are determined in such a way that the following relation holds

$$\langle \dot{\boldsymbol{\sigma}} \rangle = \boldsymbol{C}^{ep}_{eff} \langle \dot{\boldsymbol{\varepsilon}} \rangle \tag{2.9}$$

where $\langle \cdot \rangle$ denotes the volume average of a quantity over the whole RVE, i.e.

$$\langle \cdot \rangle = \frac{1}{V} \int_V (\cdot) \, \mathrm{d}V$$

Finally, the Hill-Mandel condition (macrohomogeneity condition) is postulated for perfectly bonded microstructure [48]

$$\langle \boldsymbol{\sigma} : \boldsymbol{\varepsilon} \rangle = \langle \boldsymbol{\sigma} \rangle : \langle \boldsymbol{\varepsilon} \rangle \tag{2.10}$$

Integration in time of the problem (2.4) is usually performed by the backward Euler scheme and the radial return algorithm (see e.g. [93]). After converting the rate formulation into the incremental form, the total load history is represented by a sequence of sub-loads. For each sub-load the solution increment is evaluated iteratively by requiring at each Gauss integration point fulfillment of the yield condition and overall momentum equations at the end of each load increment.

The well known algorithm makes use of the decomposition of the stress increment into two parts: the elastic trial component ($\boldsymbol{\sigma}^{trial}$) and the plastic corrector component ($\triangle\boldsymbol{\sigma} = -\boldsymbol{C}\triangle\boldsymbol{\varepsilon}^p$) evaluated by the return mapping method [94] (radial return algorithm for the Mises yield function). The trial part is computed, for fixed plastic strain increment $\triangle\boldsymbol{\varepsilon}^p$, by the momentum Eq. $(2.4)_1$ combined with Eqs. $(2.4)_{2,3}$. Then the plastic flow rule and the yield condition constitute, in the case of constant hardening, the following nonlinear system of equations that is used to define increments of the corrector parts of stress ($\triangle\boldsymbol{\sigma}$) and the plastic multiplier ($\triangle\gamma$)

$$\left\{ \begin{array}{lcl} \boldsymbol{C}^{-1}\triangle\boldsymbol{\sigma} + \triangle\gamma\dfrac{\partial\phi}{\partial\boldsymbol{\sigma}} & = & 0 \\ \phi(\boldsymbol{\sigma}^{trial} + \triangle\boldsymbol{\sigma}) & = & 0 \end{array} \right. \tag{2.11}$$

The system of equations (2.11) is, in general, solved by the Newton-Raphson method. Usually, in order to assure quadratic convergence of the iterative process, the so-called algorithmic tangent modulus is suggested instead of tangent one.

2.4 Boundary conditions

One may use three kinds of boundary conditions applied to RVE: *Dirichlet*, *Neumann* or *periodicity*. The latter one is the most appropriate for a periodic microstructure [45, 66, 110] that is schematically presented in Fig. 2.1.

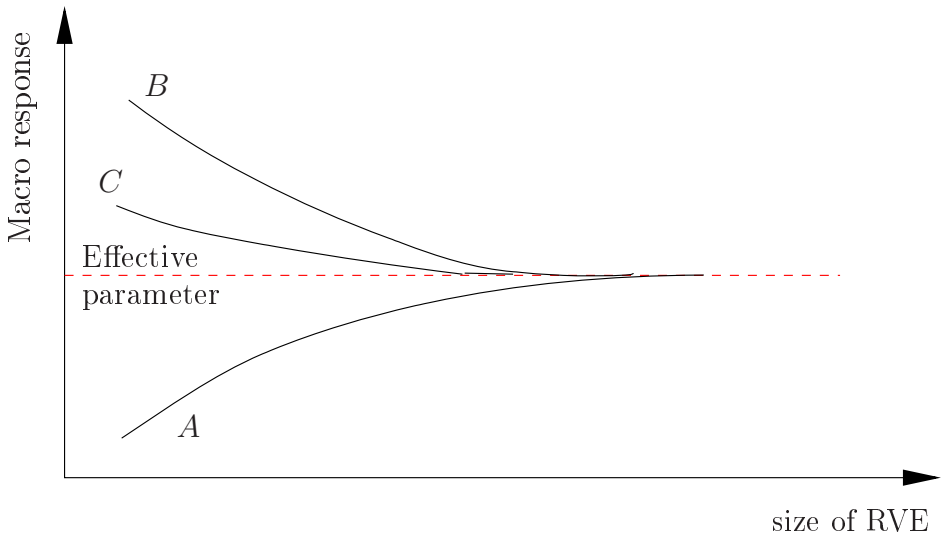

Figure 2.1: Influence of boundary conditions and RVE size on accuracy of effective parameters: A – uniform traction b.c., B – linear displacement b.c., C – periodic b.c.

Periodicity conditions may be imposed either after discretization and assembling the global system of algebraic equations or directly in formulation of the problem.

Let us first consider the global system of equations

$$\boldsymbol{K}\boldsymbol{u} = \boldsymbol{P} \tag{2.12}$$

supplemented with N_C constraints resulting e.g. from assuming periodicity conditions for appropriate degrees of freedom

$$\boldsymbol{A}\boldsymbol{u} = \boldsymbol{b} \tag{2.13}$$

These constraints may be accounted for either by static condensation [57, 67] or by penalty function method [34], where the constraints are imposed by augmenting system of equations (2.12) with penalty terms parameterized by numerical weights W_i ($i = 1, 2, \ldots, N_C$).

$$(\boldsymbol{K} + \boldsymbol{A}^T\boldsymbol{W}\boldsymbol{A})\boldsymbol{u} = \boldsymbol{f} + \boldsymbol{W}\boldsymbol{A}^T\boldsymbol{b} \tag{2.14}$$

or by Lagrange multipliers adjunction, where for each constraint an additional unknown λ_i is adjoined to the global system of equations

$$\begin{bmatrix} \boldsymbol{K} & \boldsymbol{A}^T \\ \boldsymbol{A} & 0 \end{bmatrix} \begin{bmatrix} \boldsymbol{u} \\ \boldsymbol{\lambda} \end{bmatrix} = \begin{bmatrix} \boldsymbol{f} \\ \boldsymbol{b} \end{bmatrix} \tag{2.15}$$

The next possibility is to introduce Lagrange multiplier function to the weak formulation. This approach is preferred for the *hp* finite element method and it is described briefly below.

For plane stress state and RVE denoted by ω, the periodic boundary conditions are schematically presented in Fig. 2.2.

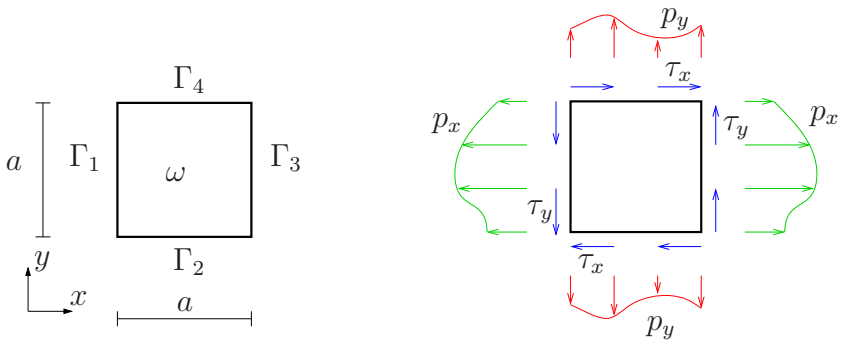

Figure 2.2: RVE. Periodicity conditions.

They may be specified as follows:

- $u_{x|\Gamma_3} = u_{x|\Gamma_1} + d_1, \quad u_{x|\Gamma_4} = u_{x|\Gamma_2} + d_2$
- $u_{y|\Gamma_3} = u_{y|\Gamma_1} + d_3, \quad u_{y|\Gamma_4} = u_{y|\Gamma_2} + d_4$
- $\boldsymbol{t}_{|\Gamma_3} = -\boldsymbol{t}_{|\Gamma_1}, \quad \boldsymbol{t}_{|\Gamma_4} = -\boldsymbol{t}_{|\Gamma_2}$

where $\boldsymbol{t} = \boldsymbol{\sigma}\,\boldsymbol{n}$. Such displacements are called periodic and tractions – antiperiodic [53, 67].

The problem may be formulated in the following weak form: *find the displacement field* $\boldsymbol{u}$ *and the traction components* $p_x, p_y, \tau_x, \tau_y \in \mathbb{W} = L^2(\Gamma)$, *such that:*

$$\begin{cases} \int_{\omega_i} \varepsilon_{ij}(\boldsymbol{v})\, C_{ijkl}\, \varepsilon_{kl}(\boldsymbol{u})\, \mathrm{d}\Omega = \int_{\omega_i} \varepsilon_{ij}(\boldsymbol{v})\, C_{ijkl}\, \varepsilon^p_{kl}\, \mathrm{d}\Omega + \int_\Gamma v_i\, t_i\, \mathrm{d}s \qquad \forall v \in V_0 \\ -\int_0^a u_{x|\Gamma_3}\, q_x\, \mathrm{d}y + \int_0^a u_{x|\Gamma_1}\, q_x\, \mathrm{d}y = -\int_0^a q_x\, d_1\, \mathrm{d}y \qquad \forall q_x \in \mathbb{W} \\ -\int_0^a u_{x|\Gamma_4}\, s_x\, \mathrm{d}y + \int_0^a u_{x|\Gamma_2}\, s_x\, \mathrm{d}y = -\int_0^a s_x\, d_2\, \mathrm{d}y \qquad \forall s_x \in \mathbb{W} \\ -\int_0^a u_{y|\Gamma_3}\, s_y\, \mathrm{d}x + \int_0^a u_{y|\Gamma_1}\, s_y\, \mathrm{d}x = -\int_0^a s_y\, d_3\, \mathrm{d}x \qquad \forall s_y \in \mathbb{W} \\ -\int_0^a u_{y|\Gamma_4}\, q_y\, \mathrm{d}x + \int_0^a u_{y|\Gamma_2}\, q_y\, \mathrm{d}x = -\int_0^a q_y\, d_4\, \mathrm{d}x \qquad \forall q_y \in \mathbb{W} \end{cases} \tag{2.16}$$

where:

$$\int_\Gamma v_i\, t_i\, \mathrm{d}s = -\int_0^a (v_x\, p_x + v_y\, \tau_y)_{|\Gamma_1}\, \mathrm{d}s - \int_0^a (v_x\, \tau_x + v_y\, p_y)_{|\Gamma_2}\, \mathrm{d}s + \\ + \int_0^a (v_x\, p_x + v_y\, \tau_y)_{|\Gamma_3}\, \mathrm{d}s + \int_0^a (v_x\, \tau_x + v_y\, p_y)_{|\Gamma_4}\, \mathrm{d}s \tag{2.17}$$

Lower order shape functions, at least by one, should be used for Lagrange multipliers p_x, p_y, τ_x, τ_y than for displacements $\boldsymbol{u}$ in order to obtain stable finite elements. Presented formulation was verified on simple tests, but was not used in the general code.

Chapter 3

Preliminary tests

1D problem was analyzed to use various approaches to homogenization, verify the algorithm that will be used for 2D and 3D problems and examine influence of discretization, especially compliance of the finite element mesh with material distribution on accuracy of the results.

3.1 Examples of homogenization in 1D

The initial tests were performed for 1D bar benchmark (see Fig. 3.1) in the uniaxial stress state. The bar comprised of two various materials distributed periodically. Both components underwent elastic deformations.

The formulation of the benchmark problem in the macro-scale is stated in the following form: *find the displacement field u, as well as the resulting strain ε and stress σ, that satisfy simultaneously the following equations:*

$$\begin{cases} -\dfrac{\mathrm{d}\sigma}{\mathrm{d}x} & = q(x) & \forall\, l_i \in (0, L) \\ \sigma & = E\,\varepsilon & \forall\, l_i \in (0, L) \\ \varepsilon & = \dfrac{\mathrm{d}u}{\mathrm{d}x} & \forall\, l_i \in (0, L) \\ u(0) & = 0 & \\ \sigma(L) & = \dfrac{P}{A} & \\ u(a_i^-) & = u(a_i^+) & \\ E_1 u'(a_i^-) & = E_2 u'(a_i^+) & \end{cases} \tag{3.1}$$

where: a_i denotes a point of materials interface $i = 1, \ldots, n$,

$$E = \begin{cases} E_1 & \text{(mat.1)} \\ E_2 & \text{(mat.2)} \end{cases}$$

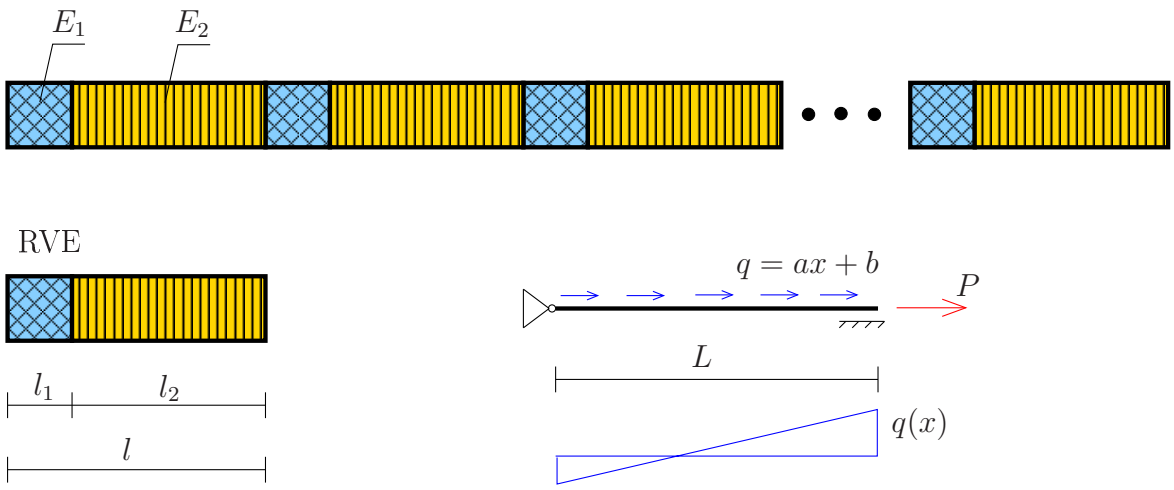

Figure 3.1: Composite bar. Details of the model.

Because deformations of the bar were in the elastic range, the effective Young modulus may be evaluated either by the solution of problem (2.4) and then as the ratio of averaged stresses and total strains

$$E_{eff} = \frac{\langle \sigma \rangle}{\langle \varepsilon \rangle} \tag{3.2}$$

or analytically due to the known displacement at the right hand side bar end

$$\begin{cases} \Delta L = \frac{PL}{AE_{eff}} \\ \\ \Delta L = \frac{PLn_1}{AE_1} + \frac{PLn_2}{AE_2} \end{cases} \Longrightarrow \quad E_{eff} = \frac{E_1 E_2}{n_1 E_2 + n_2 E_1} \tag{3.3}$$

where: $n_1 = \dfrac{l_1}{l}$, $n_2 = \dfrac{l_2}{l}$, l is the RVE size.

The bar benchmark problem was solved for the following data:
$E_1 = 150$ GPa, $E_2 = 50$ GPa, $n_1 = 25\%$, $n_2 = 75\%$, $L = 1$ m, $l = 0.04$ m, $P = -15$ MN, $a = 125$ MN/m^2, $b = -50$ MN/m.

The effective Young modulus was obtained using Eq. (3.3) (see Fig. 3.2). The results were computed with two-scale approach. Solutions for heterogeneous and homogenized material are compared in Figs. 3.3 and 3.4. In this 1D example numerical homogenization in the elastic range gives the same results as the mathematical approach, where one seeks the homogenized solution as the limit of solutions to problem (3.1) when the ratio $\frac{l}{L}$ approaches 0 [97].

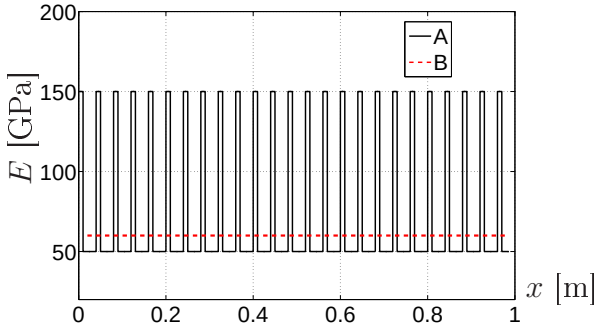

Figure 3.2: Composite bar. Young modulus (A – heterogeneous material {E1,E2}, B – homogenized material $\{E_{eff}\}$).

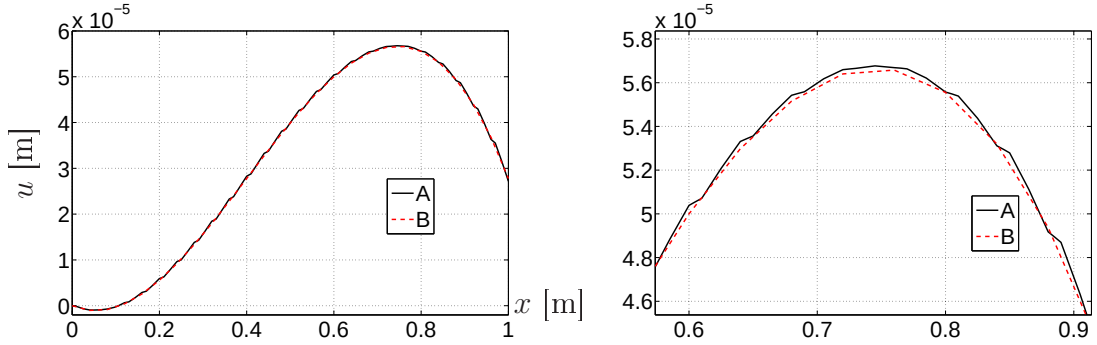

Figure 3.3: Composite bar. Displacement (A – heterogeneous material, B – homogenized material).

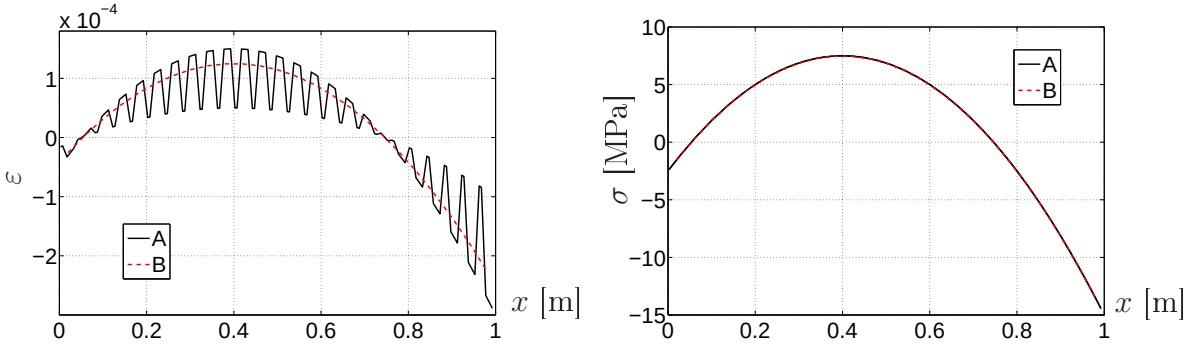

Figure 3.4: Composite bar. Strain and stress (A – heterogeneous material, B – homogenized material).

3.2 Discretization for heterogeneous materials

Preliminary computations in 1D were also performed to determine the influence of the mesh adjustment to material heterogeneity on reliability of the results. The solutions were obtained using meshes, which either did or did not account for material distribution.

Hierarchical error indicator, based on two approximate solutions [26], was used to estimate the error of the solution approximation

$$\eta_k^h = \sqrt{\int_{e_k} (u_h - u_{h/2})^2 \, \mathrm{d}x} \tag{3.4}$$

where u_h denotes coarse mesh solution and $u_{h/2}$ denotes solution obtained by two times smaller elements.

3.2.1 FE mesh adjusted to material distribution

The aforementioned bar with constant cross section, made of two materials in proportions of 50%+50% and the Young moduli E and $3E$, respectively, was analyzed. The bar was fixed on the left hand side, axially loaded by constant loading in interior $(0, L)$ and by concentrated force at the right end. Four finite elements of the same size and linear shape functions were used for discretization. The FE mesh complied with distribution of the material components. In order to estimate approximation error each element was h-refined. Both meshes and material distribution (denoted by the colors) are presented in Fig. 3.5. Computed results were compared with the exact solution (Figs. 3.6 – 3.16), where $||\cdot||_{0,\omega}$ denotes L_2 norm evaluated over domain ω. Distribution of hierarchical error indicators at each element for displacements, strains and stresses presented in Figs. 3.17 – 3.19 shows that this error indicator is a good estimate of the real error rate.

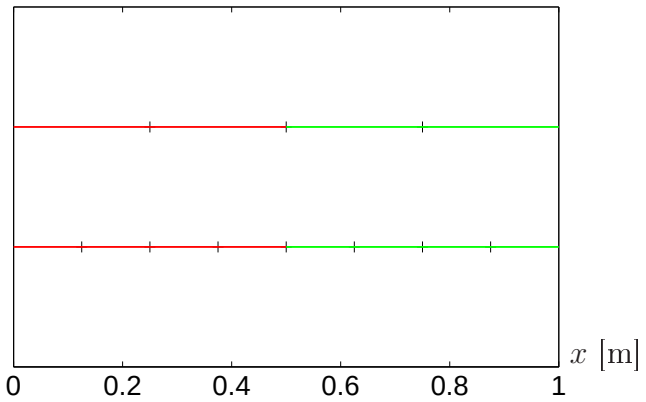

Figure 3.5: TEST I. Material distribution and discretization of initial and refined meshes (red & green colors correspond to various materials).

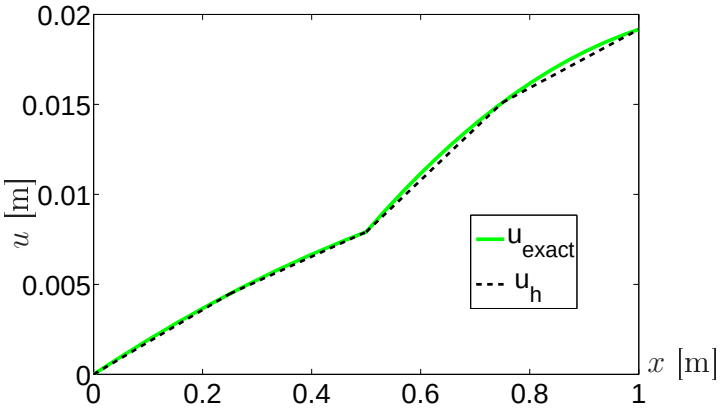

Figure 3.6: TEST I. Exact and FE solutions (4 elements).

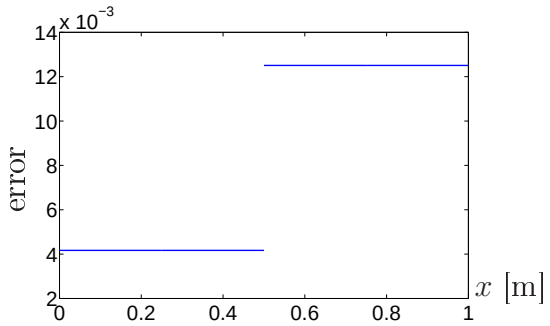

Figure 3.7: TEST I. True relative approximation error $\frac{||u_{exact}-u_h||_{0,e}}{||u_{exact}||_{0,\Omega}}$.

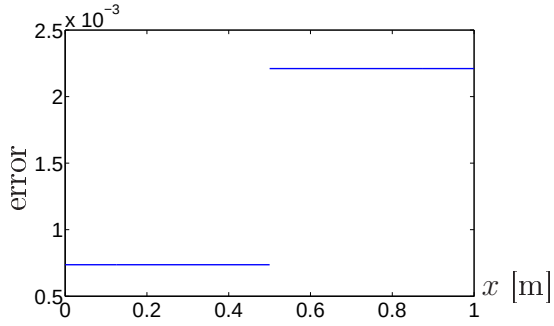

Figure 3.8: TEST I. True relative approximation error $\frac{||u_{exact}-u_{h/2}||_{0,e}}{||u_{exact}||_{0,\Omega}}$.

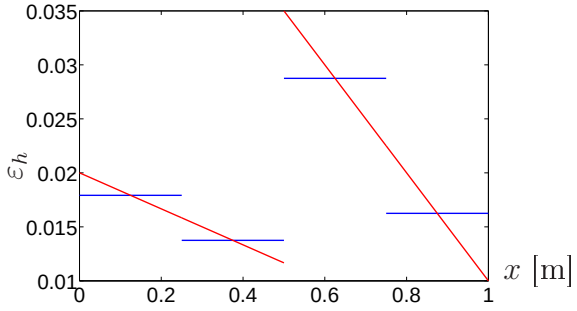

Figure 3.9: TEST I. Strain for elements of size h (the blue line) and exact strain (the red line).

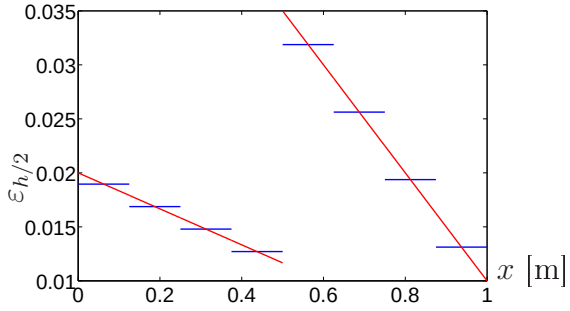

Figure 3.10: TEST I. Strain for elements of size $h/2$ (the blue line) and exact strain (the red line).

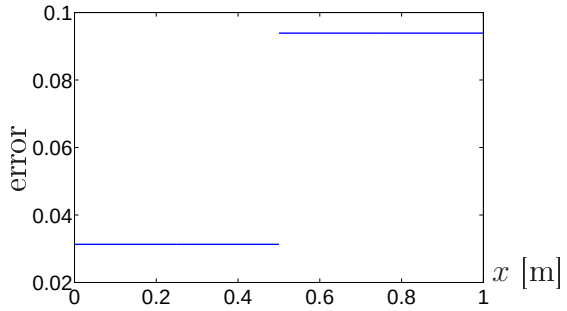

Figure 3.11: TEST I. True strain relative error $\frac{||\varepsilon_{exact}-\varepsilon_h||_{0,e}}{||\varepsilon_{exact}||_{0,\Omega}}$.

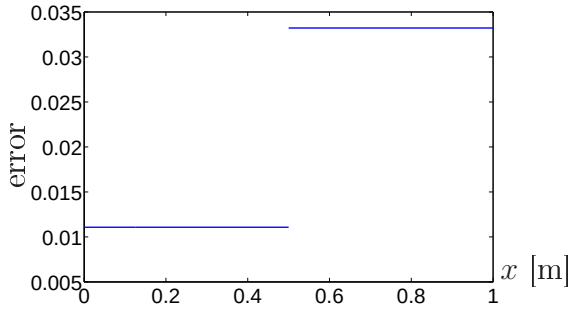

Figure 3.12: TEST I. True strain relative error $\frac{||\varepsilon_{exact}-\varepsilon_{h/2}||_{0,e}}{||\varepsilon_{exact}||_{0,\Omega}}$.

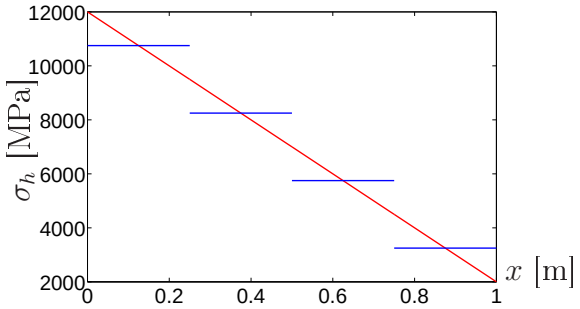

Figure 3.13: TEST I. Stress for elements of size h (the blue line) and exact stress (the red line).

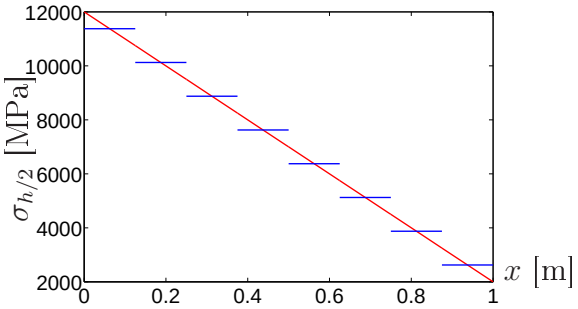

Figure 3.14: TEST I. Stress for elements of size $h/2$ (the blue line) and exact stress (the red line).

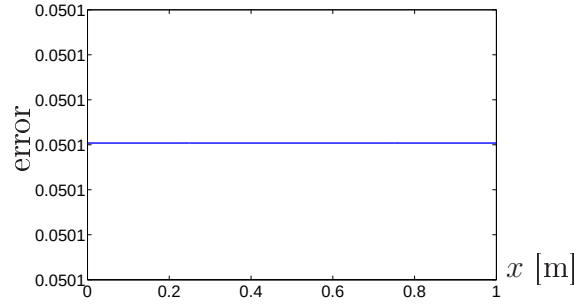

Figure 3.15: TEST I. True stress relative error $\frac{||\sigma_{exact}-\sigma_h||_{0,e}}{||\sigma_{exact}||_{0,\Omega}}$.

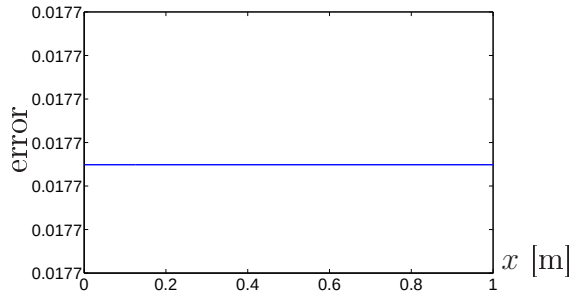

Figure 3.16: TEST I. True stress relative error $\frac{||\sigma_{exact}-\sigma_{h/2}||_{0,e}}{||\sigma_{exact}||_{0,\Omega}}$.

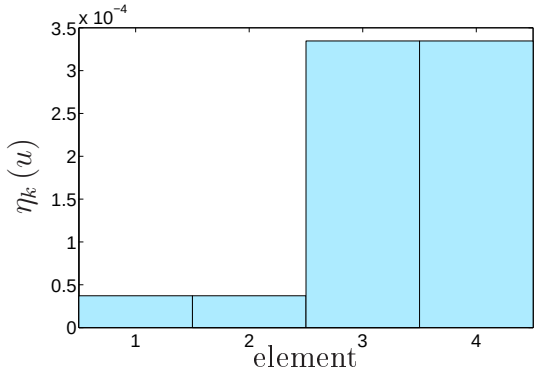

Figure 3.17: TEST I. Error indicator for displacements obtained by hierarchical method $\eta_k(u) = \frac{||u_h - u_{h/2}||_{0,e}}{||u_{h/2}||_{0,\Omega}}$.

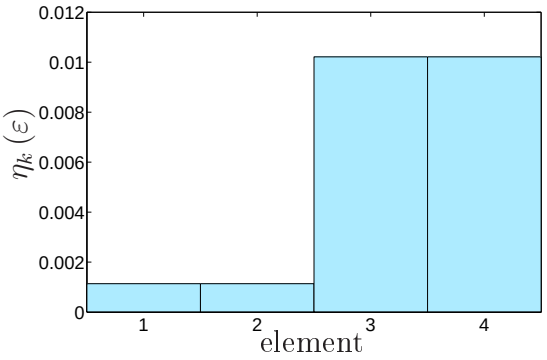

Figure 3.18: TEST I. Error indicator for strains obtained by hierarchical method $\eta_k(\varepsilon) = \frac{||\varepsilon_h - \varepsilon_{h/2}||_{0,e}}{||\varepsilon_{h/2}||_{0,\Omega}}$.

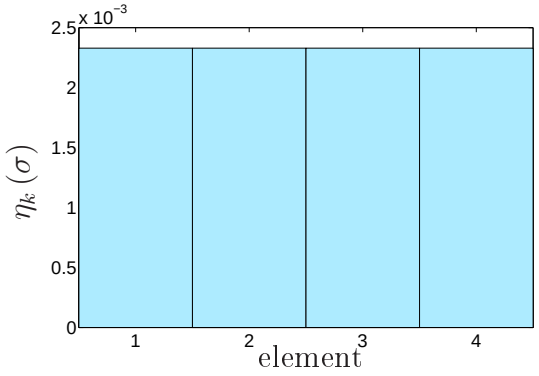

Figure 3.19: TEST I. Error indicator for stresses obtained by hierarchical method $\eta_k(\sigma) = \frac{||\sigma_h - \sigma_{h/2}||_{0,e}}{||\sigma_{h/2}||_{0,\Omega}}$.

3.2.2 FE mesh unadjusted to material distribution

In the second test the same bar as previously was analyzed, but volume rates of material components were 33% and 67%. The domain was initially discretized by four elements with linear shape functions, thus the FE mesh did not comply with distribution of material components (see Fig. 3.20). Obtained results are presented in Figs. 3.21 – 3.31. Figs. 3.32 – 3.34 show distribution of hierarchical error indicator. One may observe that the largest error occurs for strains and stresses in the element, which contains both materials. For solution u we may also notice propagation of the error onto other elements, as a result of mismatch between mesh and material interface.

In 2D and 3D FE mesh, which matches with the distribution of material is often difficult to be generated (especially when the inclusions have irregular shapes). These simple tests confirm that FE mesh should be adjusted to the interface of materials to reduce the error. The error indicator used in these tests gave reliable results.

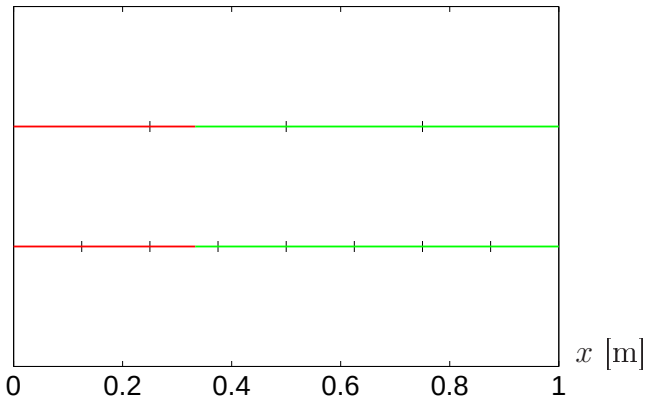

Figure 3.20: TEST II. Material distribution and discretization of initial and refined meshes (red & green colors correspond to various materials).

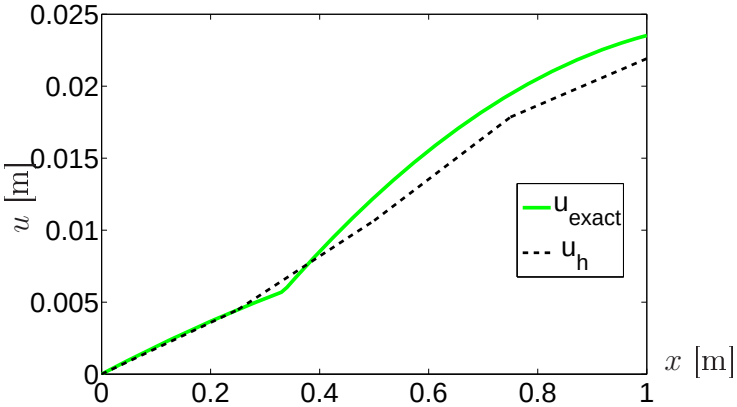

Figure 3.21: TEST II. Exact and FE solutions (4 elements).

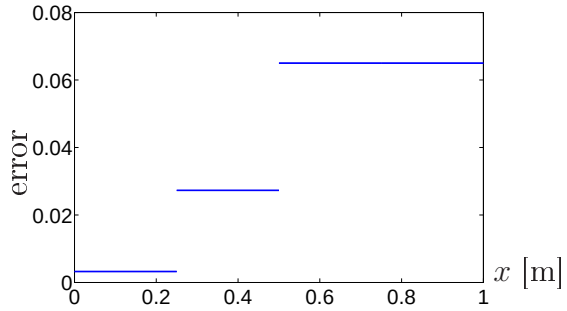

Figure 3.22: TEST II. True relative approximation error $\frac{||u_{exact}-u_h||_{0,e}}{||u_{exact}||_{0,\Omega}}$.

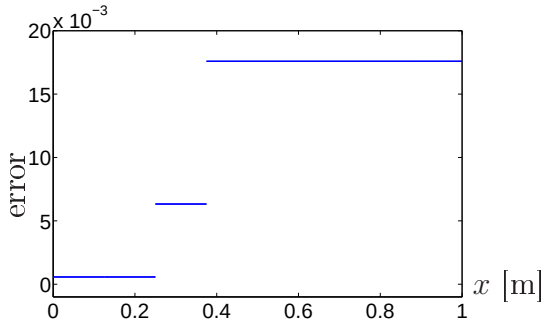

Figure 3.23: TEST II. True relative approximation error $\frac{||u_{exact}-u_{h/2}||_{0,e}}{||u_{exact}||_{0,\Omega}}$.

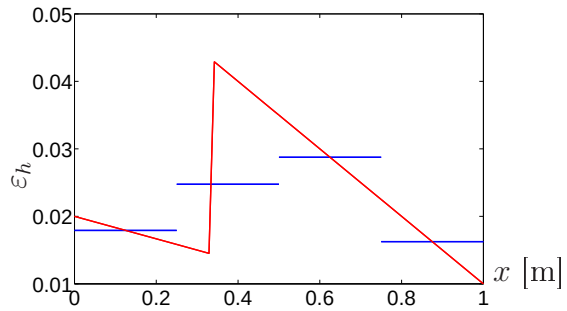

Figure 3.24: TEST II. Strain for elements of size h (the blue line) and exact strain (the red line).

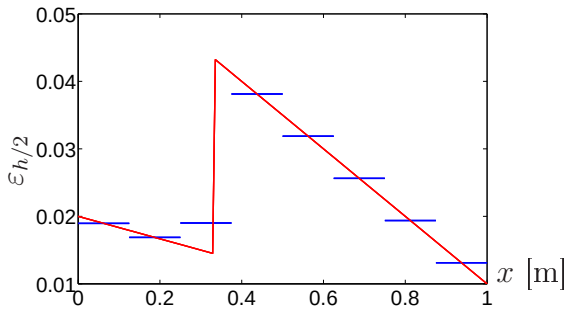

Figure 3.25: TEST II. Strain for elements of size $h/2$ (the blue line) and exact strain (the red line).

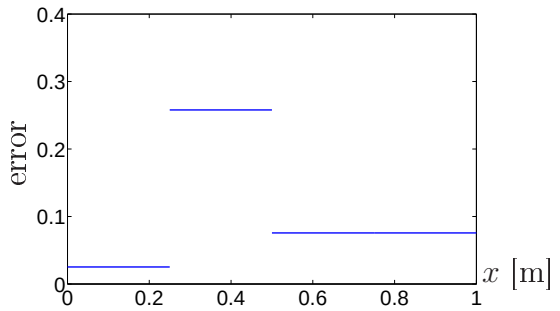

Figure 3.26: TEST II. True strain relative error $\frac{||\varepsilon_{exact}-\varepsilon_h||_{0,e}}{||\varepsilon_{exact}||_{0,\Omega}}$.

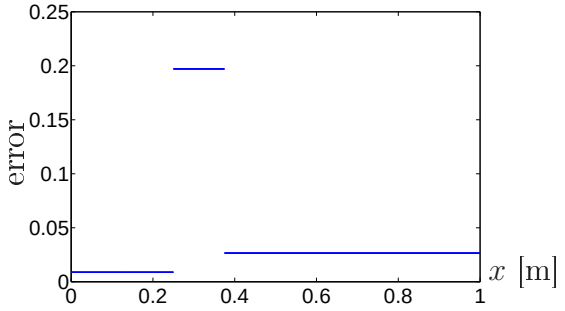

Figure 3.27: TEST II. True strain relative error $\frac{||\varepsilon_{exact}-\varepsilon_{h/2}||_{0,e}}{||\varepsilon_{exact}||_{0,\Omega}}$.

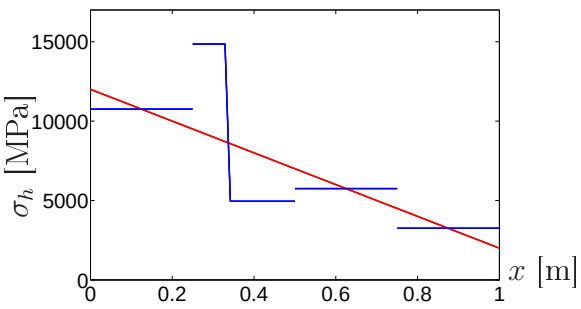

Figure 3.28: TEST II. Stress for elements of size h (the blue line) and exact stress (the red line).

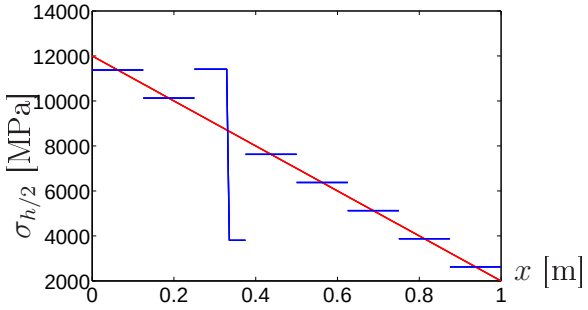

Figure 3.29: TEST II. Stress for elements of size $h/2$ (the blue line) and exact stress (the red line).

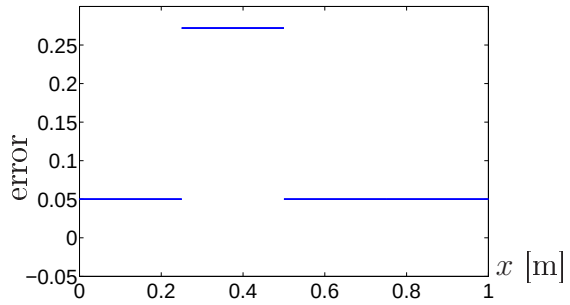

Figure 3.30: TEST II. True stress relative error $\frac{||\sigma_{exact}-\sigma_h||_{0,e}}{||\sigma_{exact}||_{0,\Omega}}$.

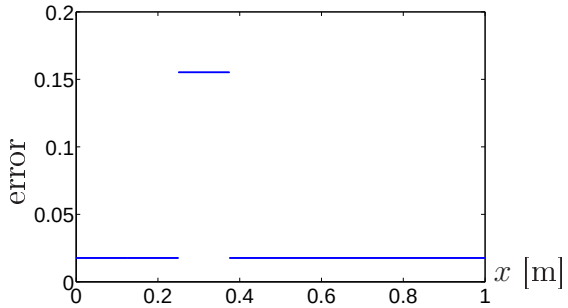

Figure 3.31: TEST II. True stress relative error $\frac{||\sigma_{exact}-\sigma_{h/2}||_{0,e}}{||\sigma_{exact}||_{0,\Omega}}$.

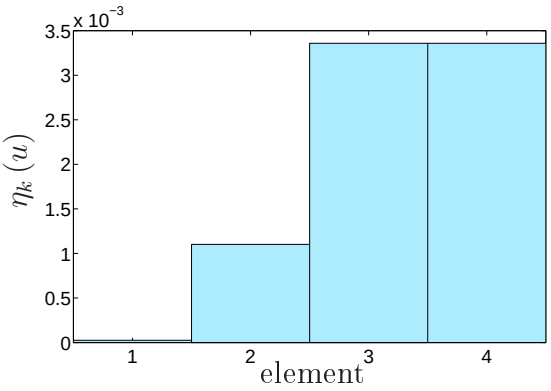

Figure 3.32: TEST II. Error indicator for displacements obtained by hierarchical method $\eta_k(u) = \frac{||u_h-u_{h/2}||_{0,e}}{||u_{h/2}||_{0,\Omega}}$.

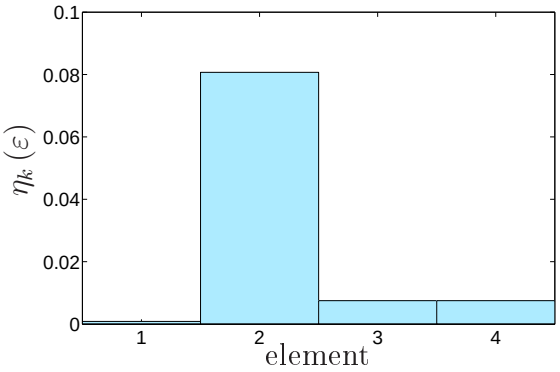

Figure 3.33: TEST II. Error indicator for strains obtained by hierarchical method $\eta_k(\varepsilon) = \frac{||\varepsilon_h - \varepsilon_{h/2}||_{0,e}}{||\varepsilon_{h/2}||_{0,\Omega}}$.

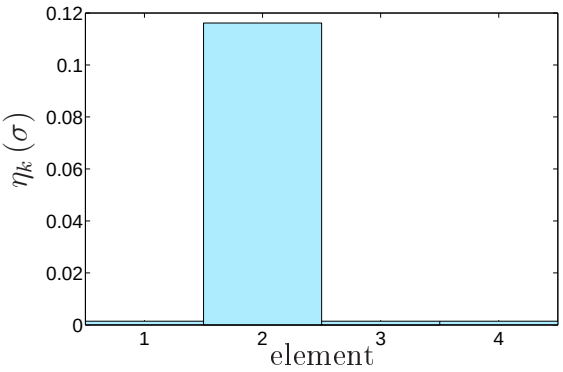

Figure 3.34: TEST II. Error indicator for stresses obtained by hierarchical method $\eta_k(\sigma) = \frac{||\sigma_h - \sigma_{h/2}||_{0,e}}{||\sigma_{h/2}||_{0,\Omega}}$.

Chapter 4

Homogenization of elastic-plastic composites

The objective of homogenization approach is to replace properties of the heterogeneous body by a homogeneous one. For the sake of simplicity periodic distribution of material components was assumed. However, it should be remembered that whenever microstructure of real composite materials is random, RVE can be used only in a statistical sense [79, 86, 99] as the so-called statistical volume element (SVE). It can be identified as the smallest volume element that satisfies certain requirement, e.g. independence of the location in the local microstructure, as well as of the applied loading direction, even for anisotropic material response.

In this section selected possibilities of material properties evaluation (effective Young modulus, Poisson ratio, etc.) are presented.

4.1 Modeling of elastic deformations in micro-scale

If deformations of the material occur in the elastic range and heterogeneous material components are distributed periodically, a single RVE analysis is sufficient to estimate the effective elastic parameters in order to obtain global response of the macro-body. Following [113] usually six independent load cases are enough to compute the tensor relation between average stress and strain

$$S = \left\{ \begin{bmatrix} \beta & 0 & 0 \\ 0 & 0 & 0 \\ 0 & 0 & 0 \end{bmatrix}, \quad \begin{bmatrix} 0 & 0 & 0 \\ 0 & \beta & 0 \\ 0 & 0 & 0 \end{bmatrix}, \quad \begin{bmatrix} 0 & 0 & 0 \\ 0 & 0 & 0 \\ 0 & 0 & \beta \end{bmatrix}, \right. \tag{4.1}$$

$$\left. \begin{bmatrix} 0 & \beta & 0 \\ \beta & 0 & 0 \\ 0 & 0 & 0 \end{bmatrix}, \quad \begin{bmatrix} 0 & 0 & 0 \\ 0 & 0 & \beta \\ 0 & \beta & 0 \end{bmatrix}, \quad \begin{bmatrix} 0 & 0 & \beta \\ 0 & 0 & 0 \\ \beta & 0 & 0 \end{bmatrix} \right\}$$

where S stands for average strain or stress tensors depending on the assumed boundary conditions (pure displacements or pure tractions), β denotes load parameter. For isotropic materials effective parameters may be obtained by one loading test and then the following relations [113]

$$3\kappa_{eff} \stackrel{\text{def}}{=} \frac{\left\langle \frac{\text{tr}\boldsymbol{\sigma}}{3} \right\rangle}{\left\langle \frac{\text{tr}\boldsymbol{\varepsilon}}{3} \right\rangle} \tag{4.2}$$

$$2\mu_{eff} \stackrel{\text{def}}{=} \sqrt{\frac{\langle \boldsymbol{\sigma}' \rangle : \langle \boldsymbol{\sigma}' \rangle}{\langle \boldsymbol{\varepsilon}' \rangle : \langle \boldsymbol{\varepsilon}' \rangle}}, \qquad \boldsymbol{\sigma}' = \boldsymbol{\sigma} - \frac{\text{tr}\boldsymbol{\sigma}}{3}\boldsymbol{I}, \quad \boldsymbol{\varepsilon}' = \boldsymbol{\varepsilon} - \frac{\text{tr}\boldsymbol{\varepsilon}}{3}\boldsymbol{I} \tag{4.3}$$

where $\boldsymbol{I}$ stands for the identity matrix, κ_{eff} and μ_{eff} denote effective bulk and shear moduli, respectively.

In this work initially orthotropic response of composite was assumed. Thus, to determine the following compliance tensor of material parameters (special case)

$$\boldsymbol{C}_{eff}^{-1} = \begin{bmatrix} \frac{1}{E_{eff}} & -\frac{\nu_{eff}}{E_{eff}} & -\frac{\nu_{eff}}{E_{eff}} & 0 & 0 & 0 \\ -\frac{\nu_{eff}}{E_{eff}} & \frac{1}{E_{eff}} & -\frac{\nu_{eff}}{E_{eff}} & 0 & 0 & 0 \\ -\frac{\nu_{eff}}{E_{eff}} & -\frac{\nu_{eff}}{E_{eff}} & \frac{1}{E_{eff}} & 0 & 0 & 0 \\ 0 & 0 & 0 & \frac{1}{\mu_{eff}} & 0 & 0 \\ 0 & 0 & 0 & 0 & \frac{1}{\mu_{eff}} & 0 \\ 0 & 0 & 0 & 0 & 0 & \frac{1}{\mu_{eff}} \end{bmatrix} \tag{4.4}$$

two computer simulations on RVE were enough to obtain effective constants:

- uniaxial tension test that enables computation of Young modulus E_{eff} and Poisson ratio ν_{eff}
- shear test that leads to evolution of rigidity modulus μ_{eff}.

The *hp*-adaptive finite element method with brick elements [27] was used for computation. The first tests in 3D were performed in order to verify the convergence of the solutions for adaptive FEM and heterogeneous material.

Let us consider a composite, in which metal matrix is reinforced by another metallic material (examples of application may be found in [51]). In presented examples ball-like inclusions are distributed periodically in equal distances measured between centers in directions of coordinate system axis. The radii of the balls were $r = 0.3a$. In order to verify how the orientation of RVE influences the effective material parameters, the analysis for various RVE, schematically presented in Fig. 4.1, was performed. The rotated one was also used for orthotropy verification. Properties of both materials (E, ν) are presented in Tab. 4.1.

Material parameters	inclusion	matrix
Young modulus E (GPa)	300	100
Poisson ratio ν	0.3	0.3

Table 4.1: Material parameters.

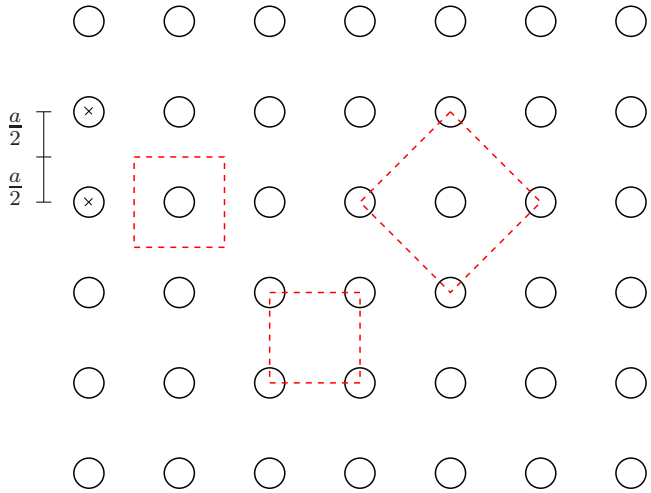

Figure 4.1: Periodic microstructure. A cross section of the body with traces of RVE.

Since these RVE are not at least ten times larger than inclusions the separation scale condition (Eq. 1.1) does not hold. Therefore, the RVE size influence on the results was verified. For two different RVE, schematically presented in Fig. 4.2, it was observed that the size of RVE is irrelevant. Similar observations for materials with particle inclusions are described in [95]. However, for composite material with random microstructure more samples should be examined to select optimal size, which guarantees appropriate statistical representation of material properties [39, 70, 80].

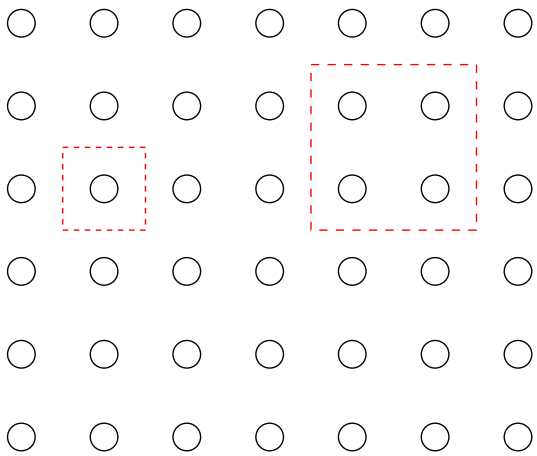

Figure 4.2: Periodic microstructure. A cross section of the body with two RVE.

Cross sections of the first RVE, as well as the initial discretization with 27 node brick elements (second order shape functions) are shown in Fig. 4.3. The initial mesh was very coarse and did not account for material distribution. However, a few (4-5) *hp*-adaptation steps were enough to obtain meshes that were sufficiently refined in the neighborhood of the interface between these two materials.

The mesh, which complies with the material heterogeneity and meshes after few steps of adaptation are shown in Fig. 4.4. However, for various complicated shapes of inclusions such a mesh fitting may be difficult to provide.

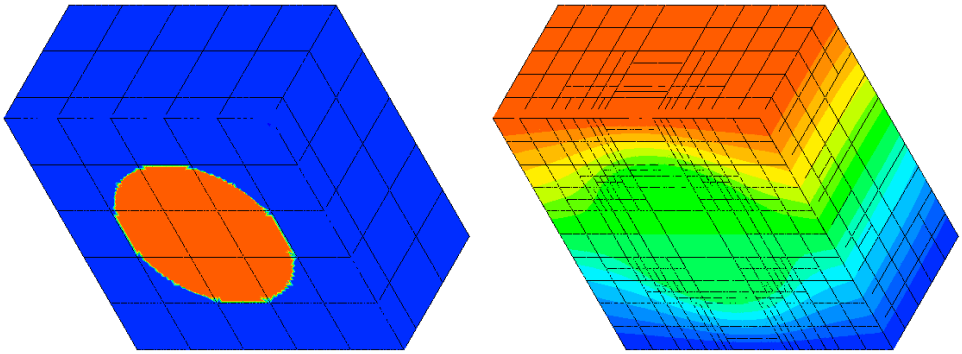

Figure 4.3: 3D RVE cross section. Initial mesh ($\boldsymbol{A}$) that did not comply with material distribution and adaptively refined mesh ($\boldsymbol{A}_1$).

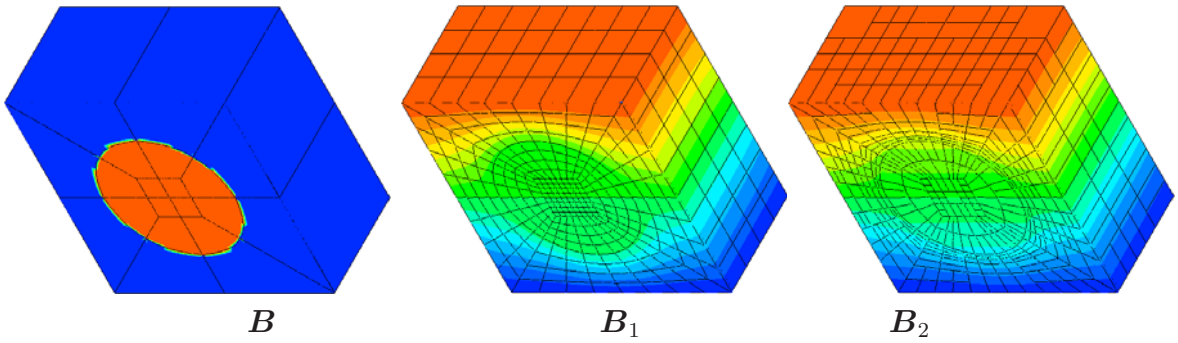

Figure 4.4: 3D RVE cross section. Initial mesh ($\boldsymbol{B}$) that complied with material distribution. Uniformly ($\boldsymbol{B}_1$) and adaptively ($\boldsymbol{B}_2$) refined meshes.

The numerical simulation of the tension test was performed on presented RVE. Convergence of the results is compared in Fig. 4.5. The observed difference that may be treated as an error indicator of effective Young modulus computed by initial, not complying with material distribution mesh, is approximately equal to 2%. A faster reduction of approximation error for adaptively refined meshes may be also observed in that figure.

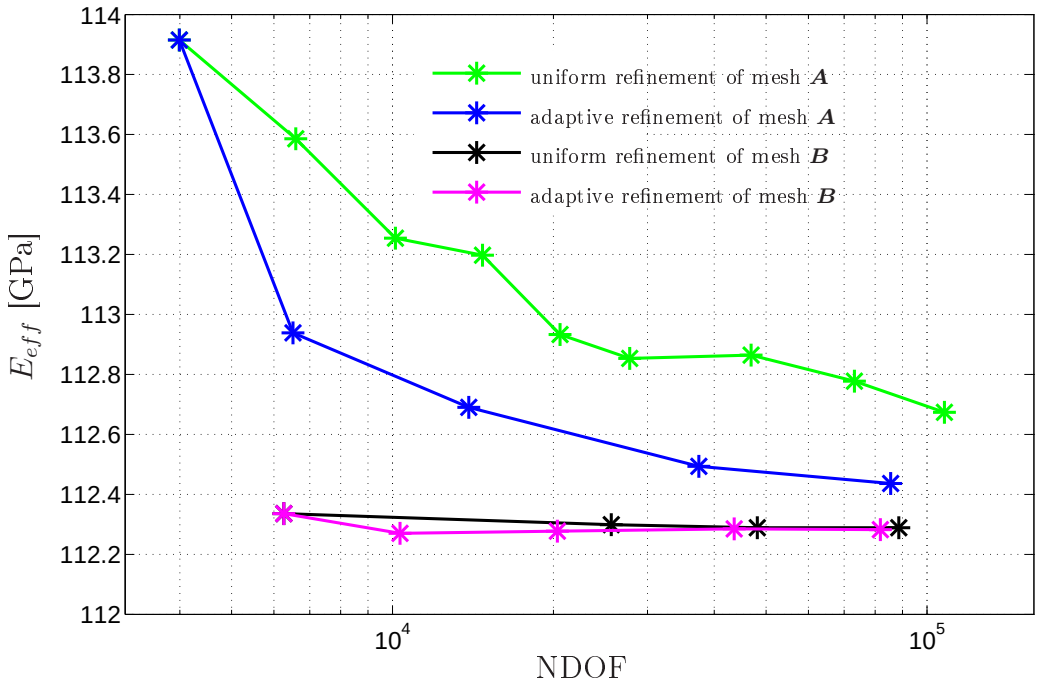

Figure 4.5: 3D test. Convergence of the effective Young modulus for various meshes.

It was also verified how the orientation of RVE (Fig. 4.1) influences the results. Fig. 4.6 presents different material distribution and contour maps of selected displacement and stress components resulted from tension test. Convergence of the effective material parameters obtained during simulation of tension test in x direction with assumed orthotropic response of composite (RVE) for different refinement strategies (uniform refinement, h and hp adaptation) is shown in Fig. 4.7 and compared in Tab. 4.2.

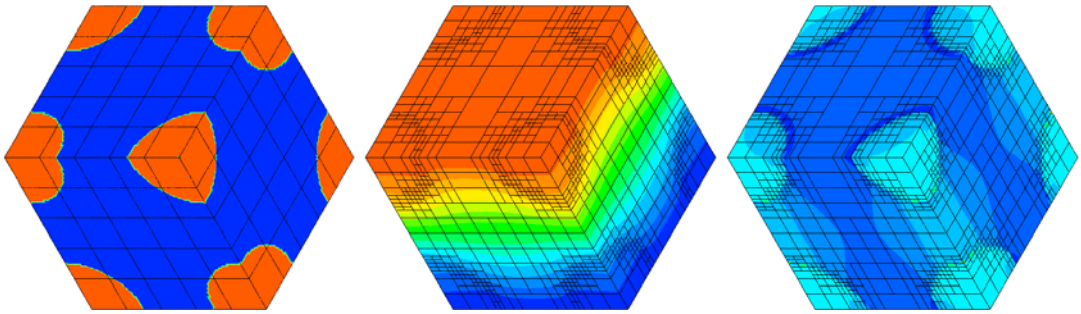

Figure 4.6: 3D test. Material distribution and selected contour maps of the tensile test solution (displacement and stress components – qualitative results).

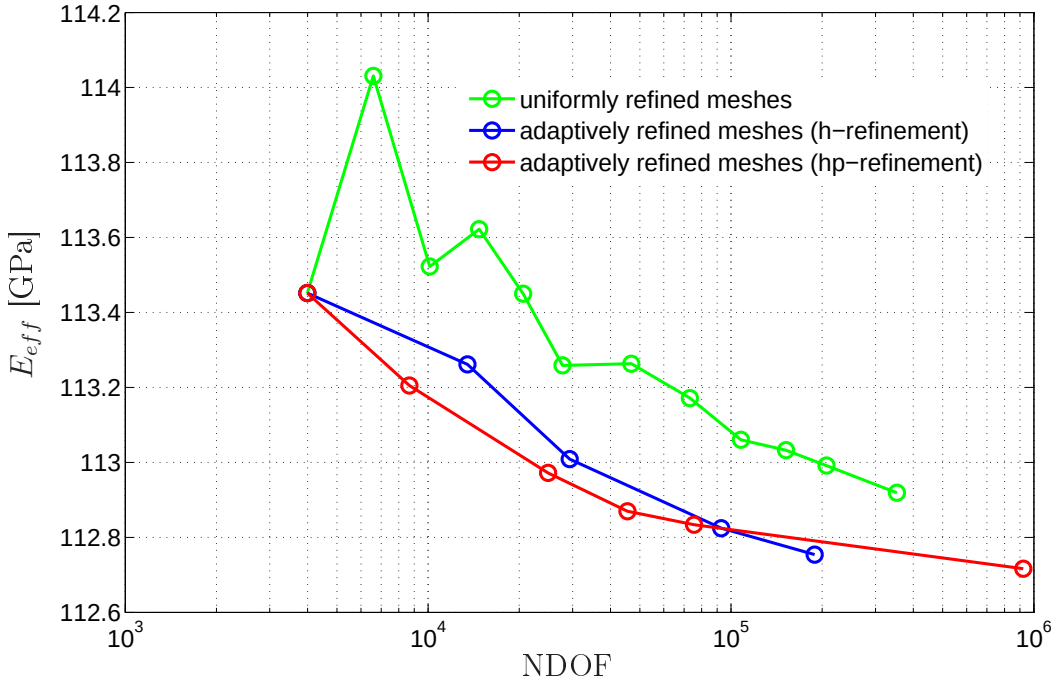

Figure 4.7: 3D test. Convergence of effective elasticity modulus.

Material parameters	RVE:1	RVE:2
E_{eff} (GPa)	112.44	112.80
ν_{eff}	0.3	0.3

Table 4.2: 3D test. Comparison of the results for RVE:1 with a ball-like inclusion located centrally and RVE:2 with balls in the corners.

The RVE rotated by 45^o was used to check whether homogenization of the considered composite results in an orthotropic body (Fig. 4.8).

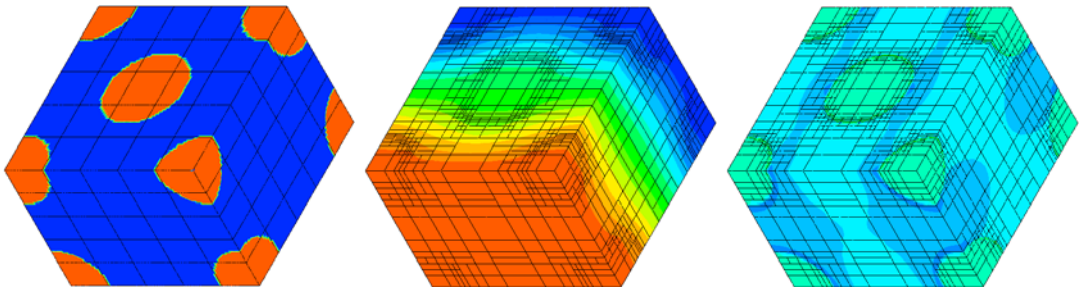

Figure 4.8: 3D test. Material distribution and selected contour maps (displacement and stress components – qualitative results) of the tension test.

Using transformation formulas for orthotropic material

$$E_{eff} = \frac{1}{E_1}\cos^4(\phi) + \left(\frac{1}{\mu_{12}} - 2\frac{\nu_{12}}{E_1}\right) cos^2(\phi)\sin^2(\phi) + \frac{1}{E_2} sin^4(\phi) \tag{4.5}$$

$$\mu_{eff} = 2\left(\frac{2}{E_1} + \frac{2}{E_2} + 4\frac{\nu_{12}}{E_1} - \frac{1}{\mu_{12}}\right)\cos^2(\phi)\sin^2(\phi) + \frac{1}{\mu_{12}}(\cos^4(\phi) + \sin^4(\phi)) \tag{4.6}$$

where: $E_1 = 112.44$ GPa, $E_2 = E_1$, $\nu_{12} = 0.298$, $\mu_{12} = 42.96$ GPa, with different angles changing from 0 to 90^o one may obtain the effective Young modulus and the shear modulus, presented in Fig. 4.9. The stars denote the same moduli computed independently from tension and shear tests performed in x and y directions using the rotated RVE. One may observe that a small change in the values of these parameters when changing the angle proves that the material is almost isotropic. The difference between these two results is an indicator of the error of our analysis. Since both results for the angle of 45^o are close one may also conclude that the modeling error is small.

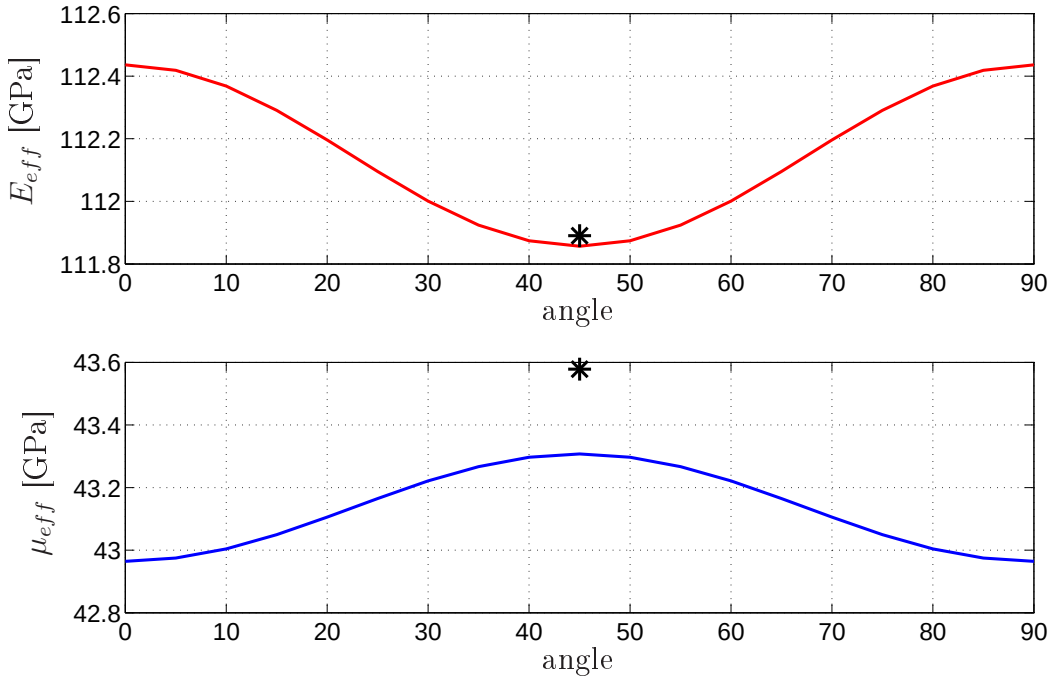

Figure 4.9: 3D test. Orthotropy verification.

The results obtained by computational homogenization were also compared with a few recalled below direct formulas, which are used for two-phase elastic bodies with isotropic effective response.

1. Mixture rule

$$E_{eff} = E_1 \cdot n_1 + E_2 \cdot n_2 \tag{4.7}$$

where: $n_i = v_i/V$, v_i - material volume, V - total volume, $i = 1, 2$.

2. Inverse mixture rule

$$E_{eff} = \frac{E_1 \cdot E_2}{n_1 \cdot E_2 + n_2 \cdot E_1} \tag{4.8}$$

3. Hashin - Shtrikman bounds [43, 113]

$$\kappa_1 + \frac{v_2}{\frac{1}{\kappa_2 - \kappa_1} + \frac{3(1-v_2)}{3\kappa_1 + 4\mu_1}} \leq \kappa_{eff} \leq \kappa_2 + \frac{1 - v_2}{\frac{1}{\kappa_1 - \kappa_2} + \frac{3v_2}{3\kappa_2 + 4\mu_2}} \tag{4.9}$$

$$\mu_1 + \frac{v_2}{\frac{1}{\mu_2 - \mu_1} + \frac{6(1-v_2)(\kappa_1+2\mu_1)}{5\mu_1(3\kappa_1+4\mu_1)}} \leq \mu_{eff} \leq \mu_2 + \frac{1 - v_2}{\frac{1}{\mu_1 - \mu_2} + \frac{6v_2(\kappa_2+2\mu_2)}{5\mu_2(3\kappa_2+4\mu_2)}} \tag{4.10}$$

$$\kappa_2 \geq \kappa_1, \quad \mu_2 \geq \mu_1$$

where:
κ_1, κ_2, κ_{eff} - bulk moduli for matrix, inclusion and effective, respectively
μ_1, μ_2, μ_{eff} - shear moduli for matrix, inclusion and effective, respectively.

4. Maxwell formulas [58]

$$\frac{1}{\kappa_{eff}} = \frac{\frac{4\mu_1}{\kappa_1\kappa_2} + \frac{3v_1}{\kappa_1} + \frac{3v_2}{\kappa_2}}{4\mu_1\left(\frac{v_2}{\kappa_1} + \frac{v_1}{\kappa_2} + \frac{3}{4\mu_1}\right)} \tag{4.11}$$

$$\mu_{eff} = \mu_1\left[1 + \frac{15(1-\nu_1)(\mu_2 - \mu_1)v_2}{2(4-5\nu_1)(v_1\mu_2 + v_2\mu_1) + (7-5\nu_1)\mu_1}\right] \tag{4.12}$$

where: ν_1 - Poisson ratio of matrix.

The effective Young modulus for RVE with a ball-like inclusion, calculated by various methods, is summarized in Tab. 4.3.

Method	E_{eff} (GPa)
Mixture method	122.62
Inverse mixture method	108.15
HASHIN - SHTRIKMAN lower/upper bound	112.06/115.73
Maxwell method	112.06
Computational homogenization	112.44

Table 4.3: Effective Young modulus obtained by different methods.

This comparison shows that the result obtained by the *hp*-adaptive FEM during numerical simulation of tensile test is reliable, because it is bounded by Hashin - Shtrikman solutions. Maxwell method also enables obtaining reasonable solution. The simplest methods (mixture rule and its inverse) gave rough estimation that may be used to define the limits of solutions (min, max).

The tests were also performed for metal matrix composites reinforced with ellipsoidal (Fig. 4.10) or cylinder (fibers) (Fig. 4.14) metallic inclusions.

The exemplary FE meshes for ellipsoidal-shape inclusion obtained by h-adaptation method are shown in Fig. 4.11. One may observe concentration of the smallest elements near border of two materials. In this example material parameters are the same as in the previous examples with a ball-like inclusion.

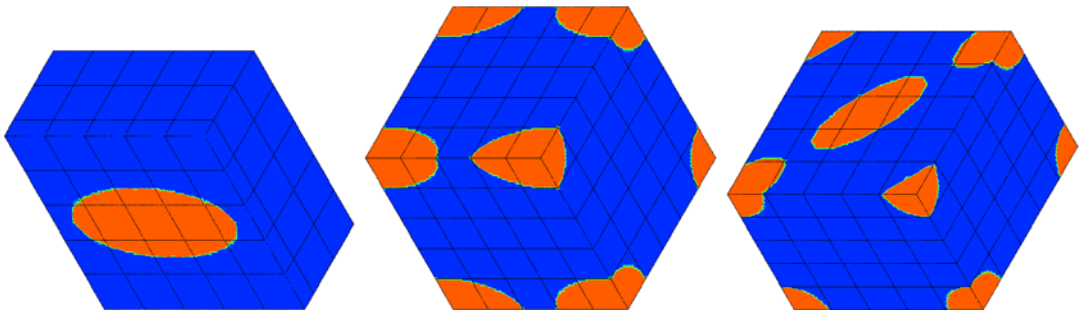

Figure 4.10: 3D test. RVE with ellipsoidal inclusion. Material distribution and initial meshes.

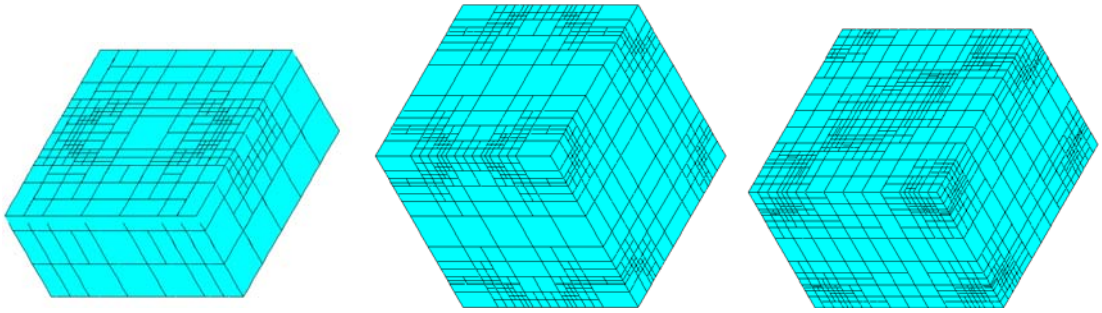

Figure 4.11: 3D test. RVE with ellipsoidal inclusion. h-adaptively refined meshes.

Convergence of effective material parameters for uniformly and adaptively refined meshes is presented in Figs. 4.12 and 4.13. In all presented graphs of convergence of the effective Young modulus it can be observed that the most accurate results with the smallest number of degrees of freedom were obtained for the hp-strategy of mesh refinement.

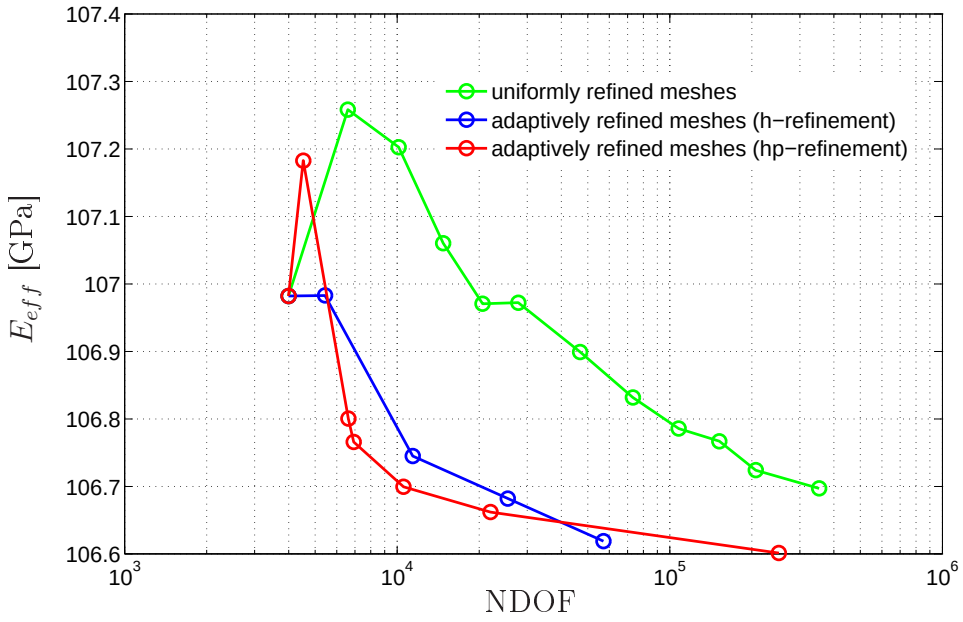

Figure 4.12: 3D test. Convergence of effective elasticity modulus for RVE with centrally located ellipsoidal inclusion.

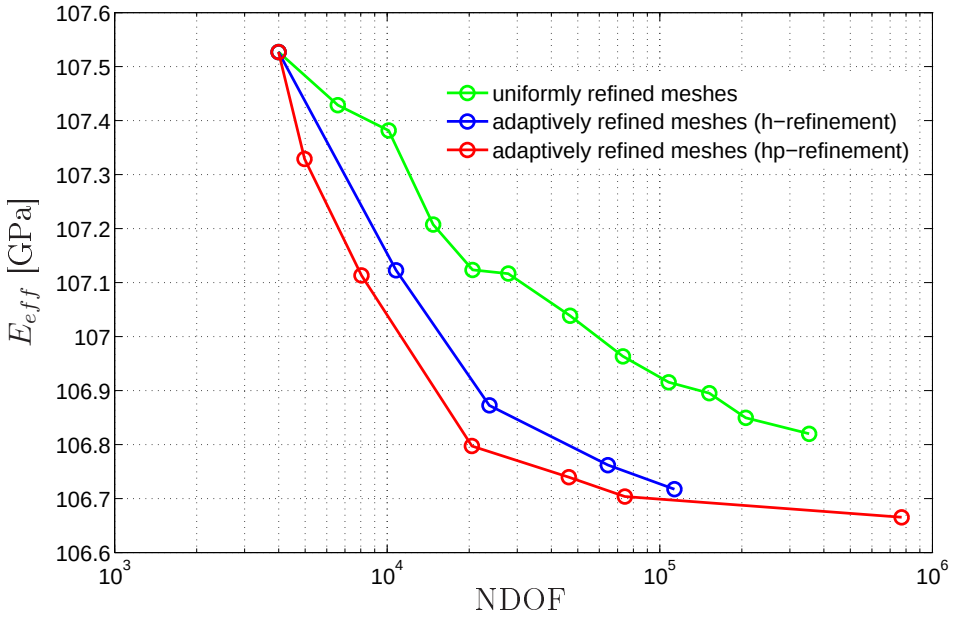

Figure 4.13: 3D test. Convergence of effective elasticity modulus for RVE with vertex located ellipsoidal inclusions.

In another example reinforcement with cylindrical fibers was used. Material data are collected in Tab. 4.4, on the basis of publication [110]. Material distribution and adaptively refined meshes are shown in Figs. 4.14 and 4.15.

Material parameters	fibers (boron)	matrix (aluminum)
Young modulus E (GPa)	379.3	68.3
Poisson ratio ν	0.1	0.3

Table 4.4: Material parameters.

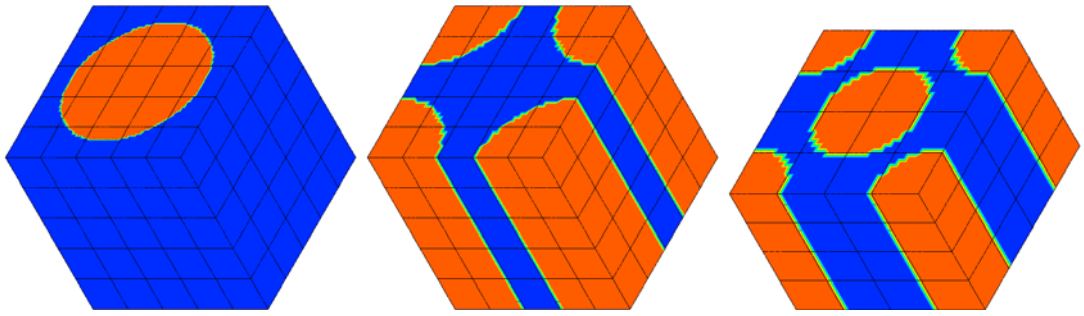

Figure 4.14: 3D test. RVE with fiber inclusion. Material distribution and initial meshes.

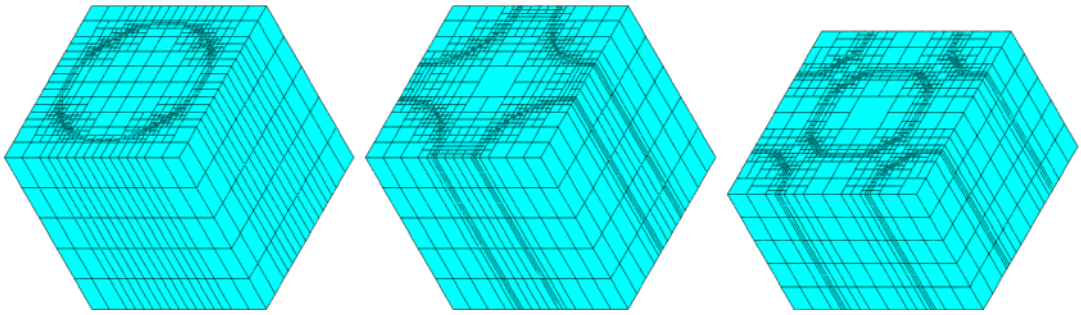

Figure 4.15: 3D test. RVE with fiber inclusion. h-adaptively refined meshes.

Computed results are summarized in Tab. 4.5 and compared with numerical, as well as experimental tests for fiber volume fraction $V_f = 0.47$ as in paper [110]. The results of computer simulation coincide very well with the results known from the literature, obtained both by calculation and experiment.

Material parameter	(min; max)	mean value	own result
E_1 (GPa)	(214; 216)	215	215
E_2 (GPa)	(123; 156)	139	138
G_{12} (GPa)	(51.1; 62.6)	55	55
G_{23} (GPa)	(43.6; 52.3)	47	47
ν_{12}	(0.19; 0.29)	0.2	0.195
ν_{23}	(0.253; 0.31)	0.29	0.27

Table 4.5: Comparison of the results published in [110] and computed by numerical simulation of tensile test performed on RVE.

4.2 Single RVE analysis for inelastic deformations

Analysis of inelastic problems is very time-consuming, even if homogenization is used, because the calculation at the micro-level must be performed repeatedly. In the classical computational homogenization an RVE should correspond to each Gauss integration point, but it is actually ineffective approach to practical problems, even for high-speed computers. The first reason is that in 3D the FE model has a lot of Gauss integration points. Another drawback of attributing RVE to every quadrature point has to be overcome when adaptive FEM is used. Since the history of deformation is stored only at integration points after mesh adaptation new Gauss points occur without information of the history. Then necessary information may be transfered from surrounding points, but only at the macro-scale. It is not possible to approximate e.g. distribution of plastic strains in a new RVE. To avoid such problems other possibilities of the two-scale homogenization are presented in this section.

The first option is based on a single RVE solution. We assume that in elastic-plastic range global response of the body in the macro-scale may be derived from the analysis of a single RVE. Numerically simulated tensile tests over RVE with different loading paths leads to a relation between averaged strains and stresses. Then effective plastic parameters (yield strength limit, hardening coefficient, etc.) are evaluated and global response of the inelastic macro-model is determined. The proposed method is presented more precisely for the following example.

It was assumed that for metallic composites both in the micro- and macro-scales the stresses are bounded by the Mises yield surface using relation (2.6) and rates of strains are given by the associative plastic flow rule in the form (2.7) that may be modified for orthotropic material according to [18].

For the test purpose the same composite, as in section 4.1 with cross section presented in Fig. 4.1, was used. The RVE with a ball-like inclusion located centrally was assumed. Both materials underwent elastic-plastic deformations with kinematic hardening. Properties of both composite components are presented in Tab. 4.6. On the basis of the tensile test simulated numerically dependency between averaged stress and strain was obtained (Fig. 4.16). It enables estimation of effective Young modulus, Poisson ratio and kinematic hardening parameter.

Material parameters	inclusion	matrix
Young modulus E (GPa)	300	100
Poisson ratio ν	0.3	0.3
yield strength σ^y (MPa)	300	200
hardening coefficient H (GPa)	$0.1E$	$0.1E$

Table 4.6: Material parameters.

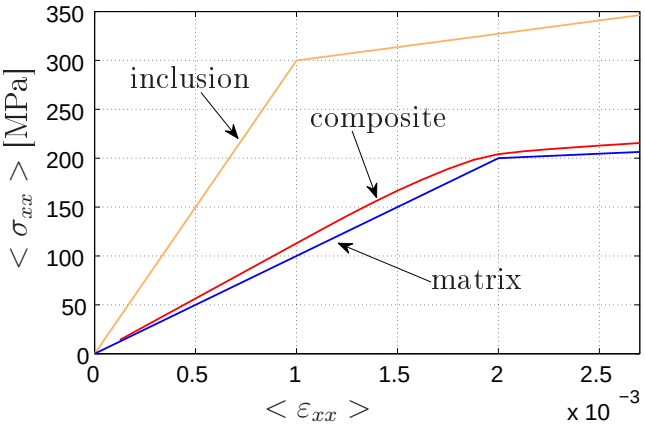

Figure 4.16: Single RVE analysis. Tensile tests.

The yield strength limit is estimated as an y-coordinate of the intersection of the tangents to the elastic and plastic parts of the tensile curve (Fig. 4.17). Then, based on tests carried out for other loading paths, the points, where the first yielding occurred, were detected. They are marked by the red circles in Fig. 4.18.

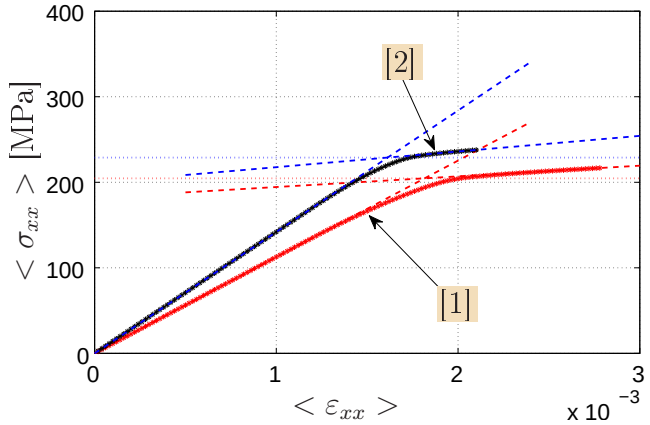

Figure 4.17: Single RVE analysis. Relation between $< \sigma_{xx} >$ and $< \varepsilon_{xx} >$ for various loading paths (see Fig. 4.18) and yield limit estimation.

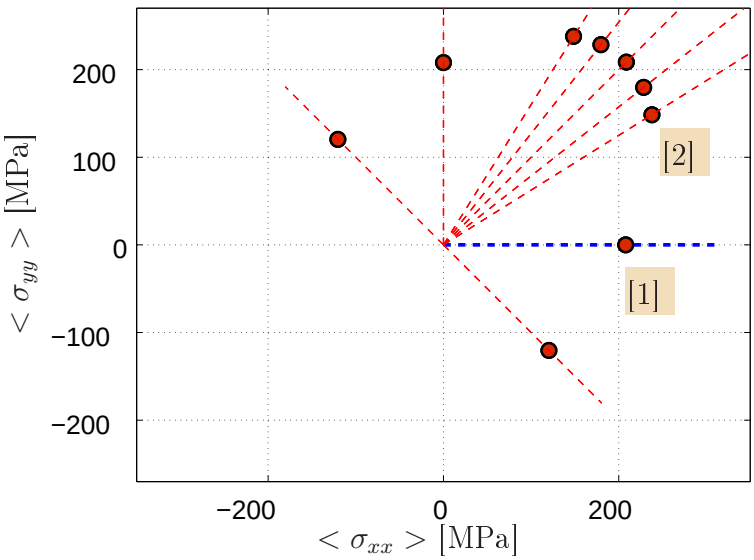

Figure 4.18: Single RVE analysis. Yield limit for various loading paths.

All these points belong (with a small tolerance) to a certain Mises yield surface, as it is shown in Fig. 4.19. After unloading and re-loading selected stress states evaluated by RVE analysis also fitted the shifted surface (Fig. 4.20), what validates kinematic hardening at the macro-scale.

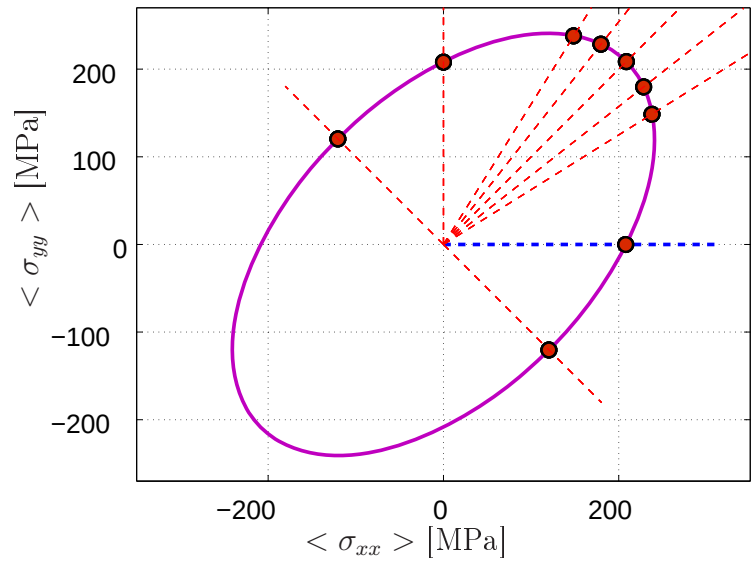

Figure 4.19: Single RVE analysis. Fitting of a Mises yield surface (the continuous violet line).

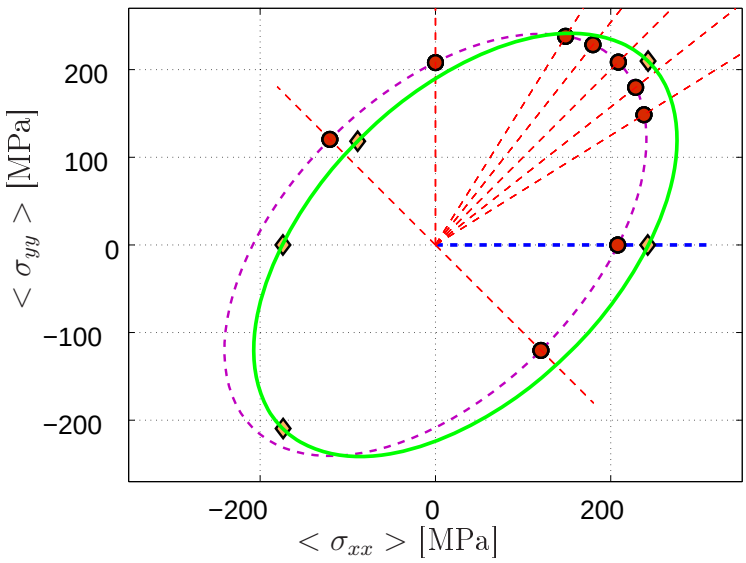

Figure 4.20: Single RVE analysis. Validation of kinematic hardening (the continuous green line).

Thus, on the basis of the analysis performed on a single RVE, one may define a Mises yield surface of the homogenized material in the macro-scale with effective parameters (yield limit σ^y_{eff}, shear yield limit k_{eff} and kinematic hardening parameter H_{eff}) and postulate associated plastic flow rule

$$\dot{\boldsymbol{\varepsilon}}^p_0 = \lambda \frac{\partial \phi}{\partial \boldsymbol{\sigma}_0} \tag{4.13}$$

$$\phi(\boldsymbol{\sigma}_0) = \frac{1}{2}\left(\boldsymbol{s}_0 - \frac{2}{3}H_{eff}\boldsymbol{\varepsilon}^p_0\right) : \left(\boldsymbol{s}_0 - \frac{2}{3}H_{eff}\boldsymbol{\varepsilon}^p_0\right) - k^2_{eff} \tag{4.14}$$

$$\gamma \geq 0, \quad \phi \leq 0, \quad \gamma\phi = 0 \tag{4.15}$$

where "0" denotes solutions for homogenized material.

4.2.1 Micro-scale analysis

The same composite type, as in section 4.1, was considered. The elastic-plastic properties of the components are defined in Tab. 4.6. At the micro-level the analysis was performed for three different RVE shown in Figs. 4.21, 4.24 and 4.26 to verify influence of RVE orientation on the global effective parameters. Figs. 4.22, 4.23, 4.25 and 4.27 present qualitative solution for different RVE in tensile test simulation in y direction.

- RVE 1: centrally located inclusion

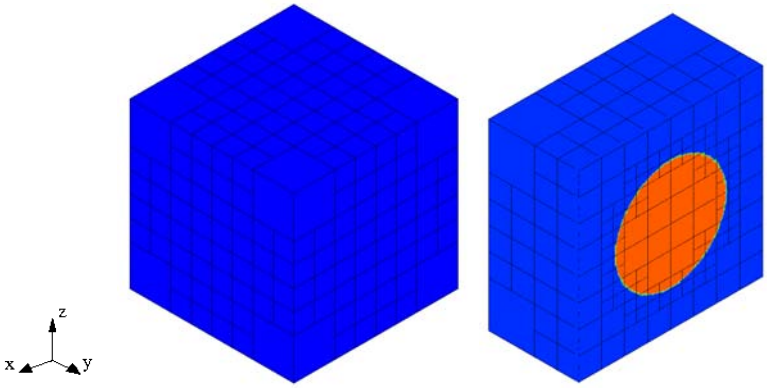

Figure 4.21: RVE 1. Material distribution.

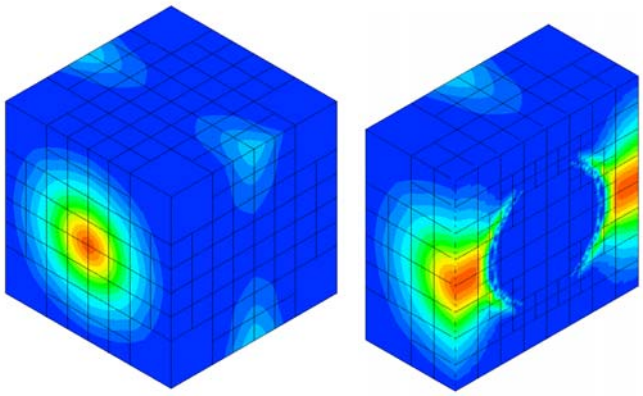

Figure 4.22: RVE 1. Component ε^p_{xx} of plastic strain tensor.

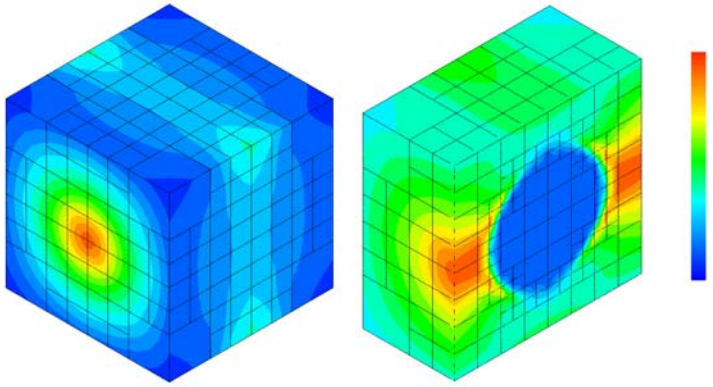

Figure 4.23: RVE 1. Component ε_{xx} of total strain tensor.

- RVE 2: inclusion located at vertexes

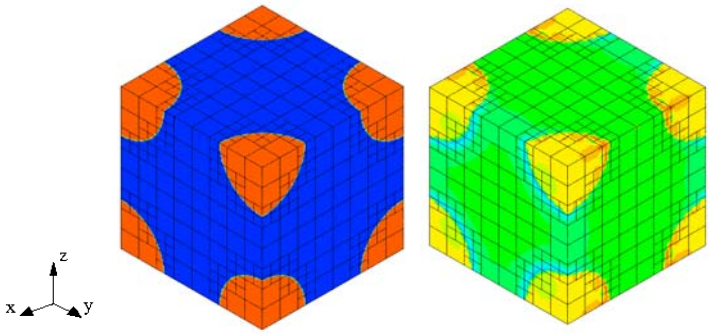

Figure 4.24: RVE 2. Material distribution and component σ_{xx} of stress tensor.

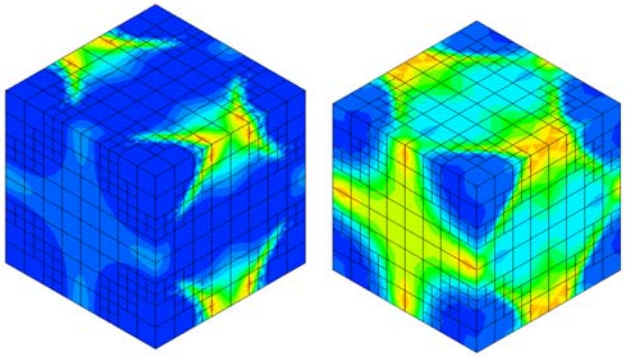

Figure 4.25: RVE 2. Component ε_{yy} of total strain tensor and component ε^p_{yy} of plastic strain tensor.

- RVE 3: domain rotated by 45^o

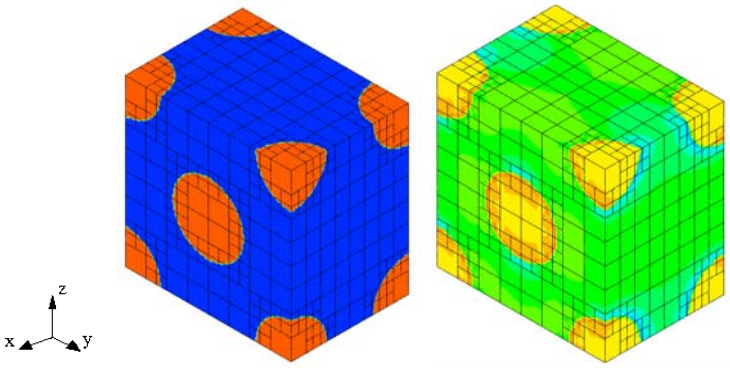

Figure 4.26: RVE 3. Material distribution and component σ_{yy} of stress tensor.

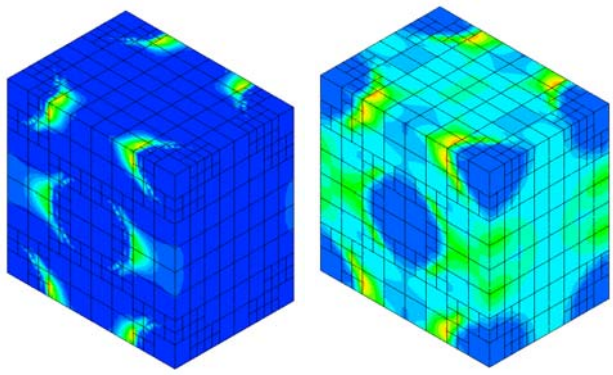

Figure 4.27: RVE 3. Component ε_{xx} of total strain tensor and component ε^p_{xx} of plastic strain tensor.

Tensile test results for the three described above RVE are compared in Fig. 4.28. One may notice that the size and orientation of RVE practically does not change the results.

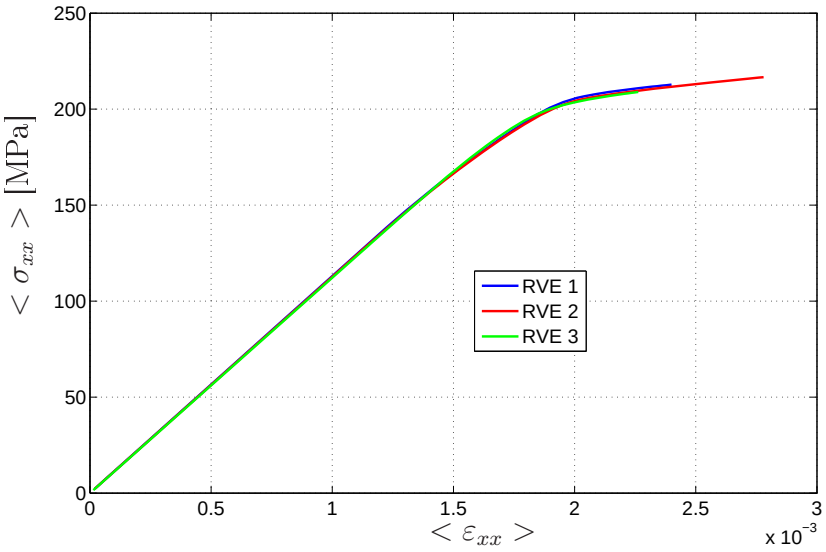

Figure 4.28: RVE test. Comparison of the tensile test results for different RVE.

4.2.2 Macro-scale analysis

Since normality rule may not be valid for heterogeneous materials [61], two numerical tests were performed in order to validate this assumption.

Analysis at the macro-scale was performed for the following elastic-plastic effective parameters determined by numerical analysis of tensile test for RVE:
$E_{eff} = 112.44$ GPa, $\nu_{eff} = 0.3$, $H_{eff} = 0.104 E_{eff}$, $\sigma^y_{eff} = 208.03$ MPa.
Simultaneously, for comparison purposes, much more time-consuming calculation for a heterogeneous material without homogenization was carried out.

Numerical example – L-shaped domain

The 3D L-shaped domain was considered. Assumed boundary conditions, a cross section and selected segment AB that is used for post-processing purposes, are schematically presented in Fig. 4.29.

On the walls parallel to the plane yz no penetration boundary conditions were assumed, while the wall marked by the black color was fixed. The upper horizontal part of the boundary was subjected to kinematic enforcing $u_z = \delta = 0.16\,a$ and zero horizontal traction. On the remaining boundary part the homogeneous Neumann boundary conditions were imposed. Finite element discretizations, generated by hp-adaptive method for homogenized material and exclusively h-adaptation for fully heterogeneous material, are shown in Fig. 4.30. To provide a better compliance between mesh and shapes of inclusions additional refinements of elements with different material parameters were used.

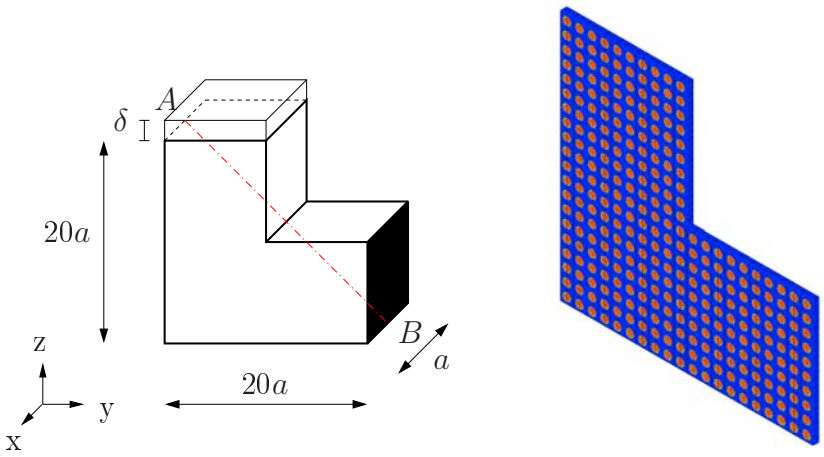

Figure 4.29: L-shaped domain. Boundary conditions and a cross section.

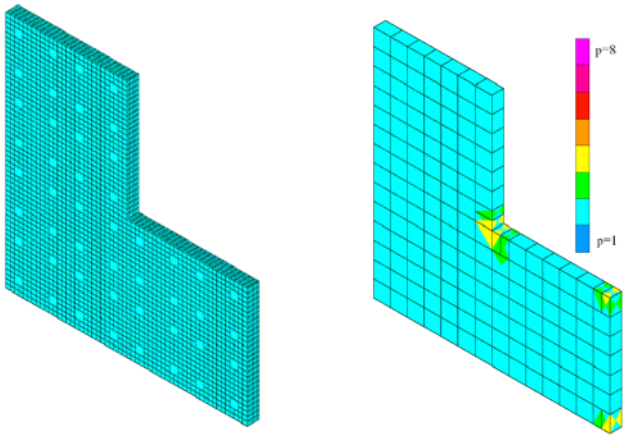

$NDOFS \approx 460\,000$ $NDOFS \approx 7\,000$

Figure 4.30: L-shaped domain. Descretization of heterogeneous and homogenized materials.

The results are presented in Figs. 4.31 and 4.32. They were also compared along the segment AB in Figs. 4.33 – 4.36.

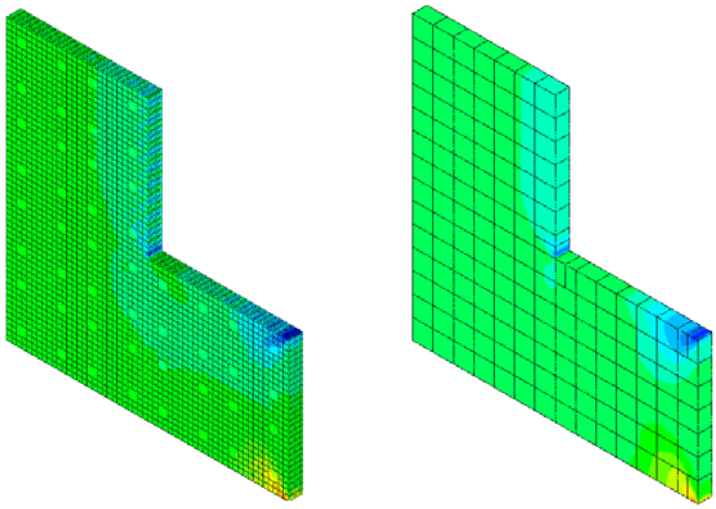

Figure 4.31: L-shaped domain. Contour map of component ε^p_{yy} of plastic strain tensor for heterogeneous and homogenized materials. Color scales match approximately.

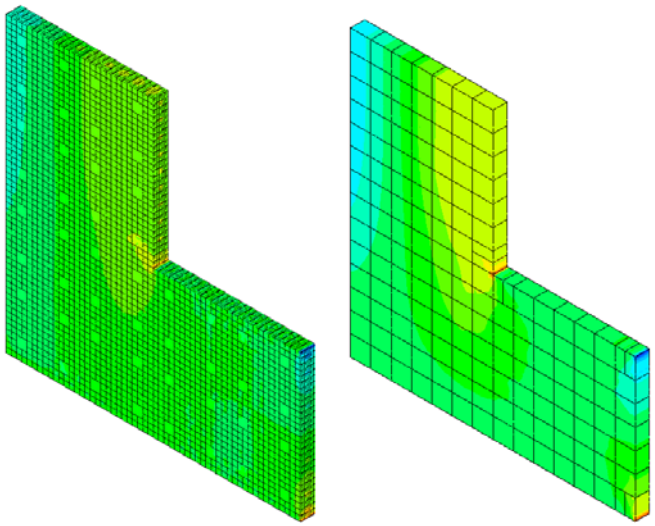

Figure 4.32: L-shaped domain. Contour map of component σ_{zz} of stress tensor for heterogeneous and homogenized materials. Color scales match approximately.

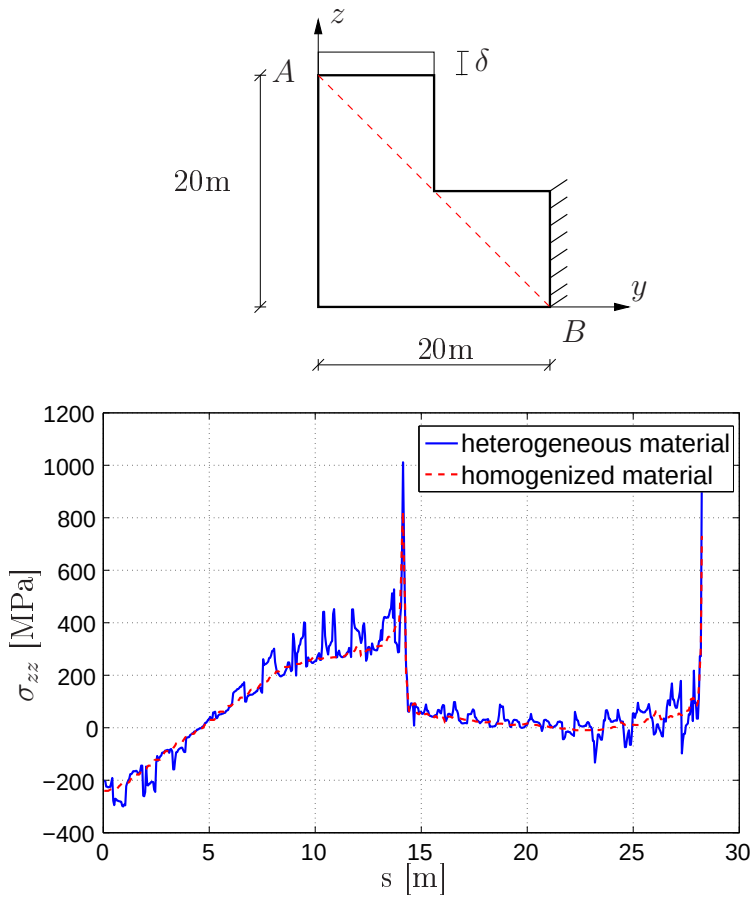

Figure 4.33: L-shaped domain. Comparison of component σ_{zz} of stress tensor for heterogeneous and homogenized material along segment AB.

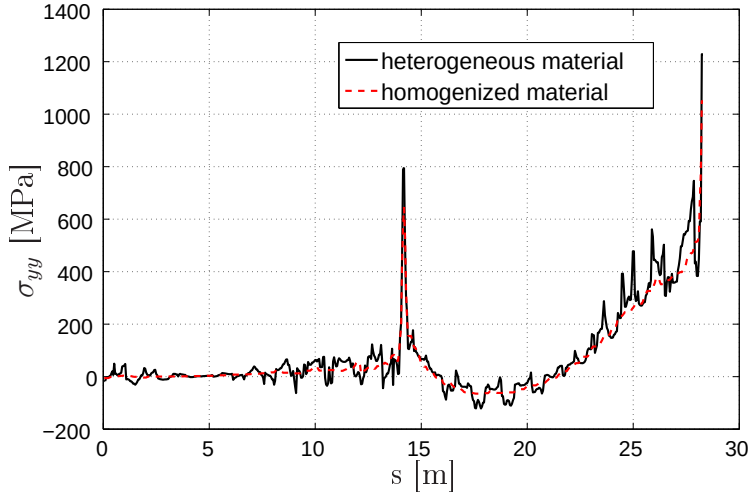

Figure 4.34: L-shaped domain. Comparison of component σ_{yy} of stress tensor for heterogeneous and homogenized material along segment AB.

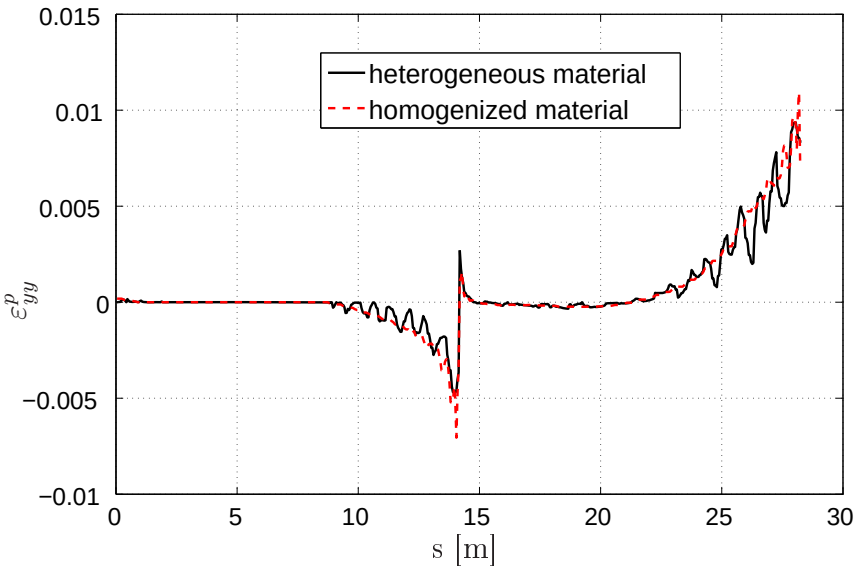

Figure 4.35: L-shaped domain. Comparison of component ε^p_{yy} of plastic strain tensor for heterogeneous and homogenized material along segment AB.

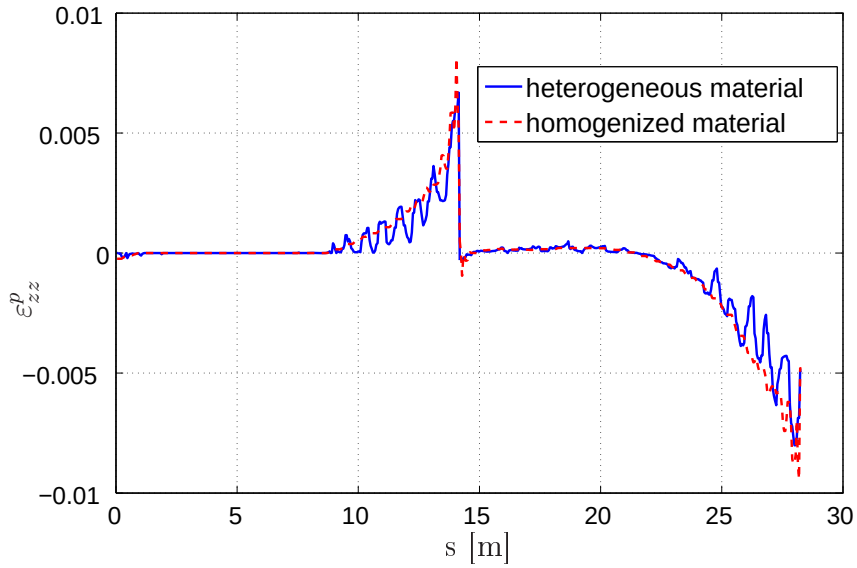

Figure 4.36: L-shaped domain. Comparison of component ε^p_{xx} of plastic strain tensor for heterogeneous and homogenized material along segment AB.

Stress component σ_{yy} was also compared along another segment CD (Fig. 4.37). In this example one may observe a good approximation of heterogeneous solution using single RVE approach with postulated associative plastic flow rule in the macro-scale. Computation time after homogenization was reduced three times.

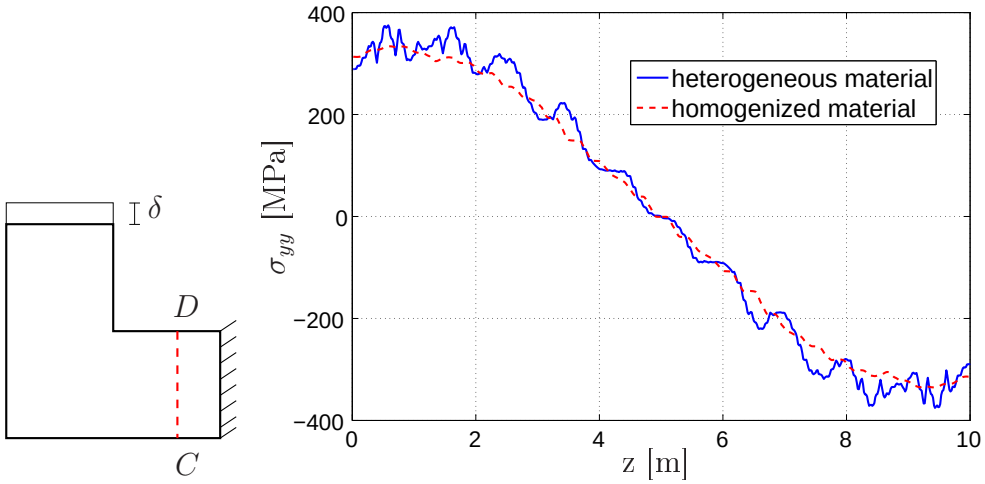

Figure 4.37: L-shaped domain. Comparison of component σ_{yy} of stress tensor for heterogeneous and homogenized material along segment CD.

Numerical example – cantilever beam

In the next test a cantilever beam, shown in Fig. 4.38, was considered as a 3D body. The beam was fixed on the wall in the plane xz and subjected to the constant distributed load $q = 80$ kN$/m^2$, perpendicular to the upper wall. On the other parts of the boundary homogeneous Neumann conditions were assumed.

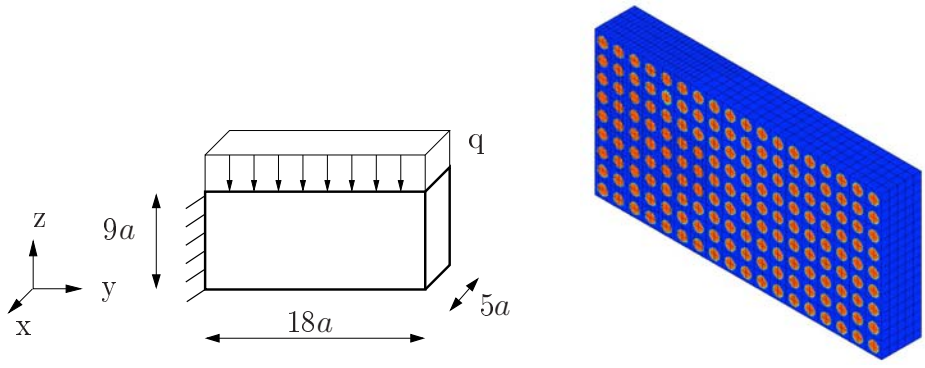

Figure 4.38: Cantilever beam. Boundary conditions and a cross section.

Finite element discretizations for heterogeneous and homogenized materials are shown in Fig. 4.39. The results of the analysis are shown in Figs. 4.40 – 4.41 and relevant components of stress and strain obtained for homogenized and heterogeneous material are compared along the segment EF in Figs. 4.42 – 4.44.

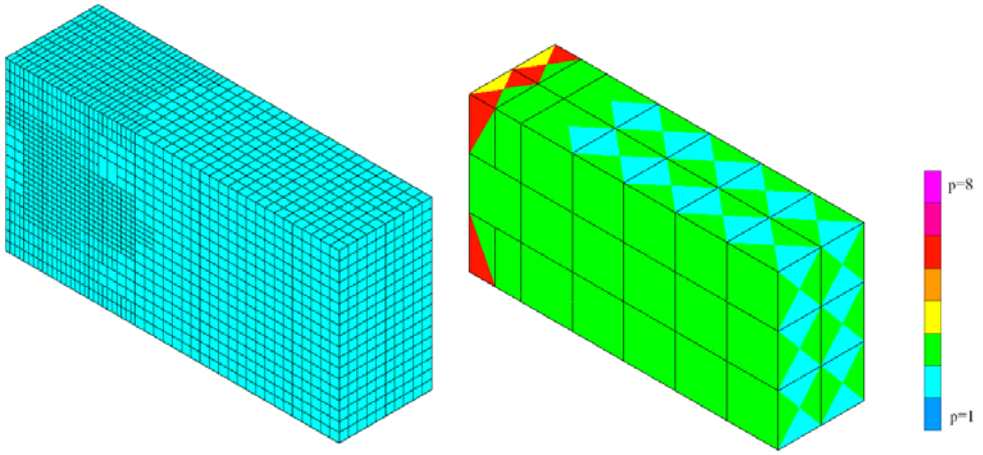

$NDOFS \approx 280\,000$ $NDOFS \approx 5\,000$

Figure 4.39: Cantilever beam. Descretization of model with heterogeneous and homogenized material.

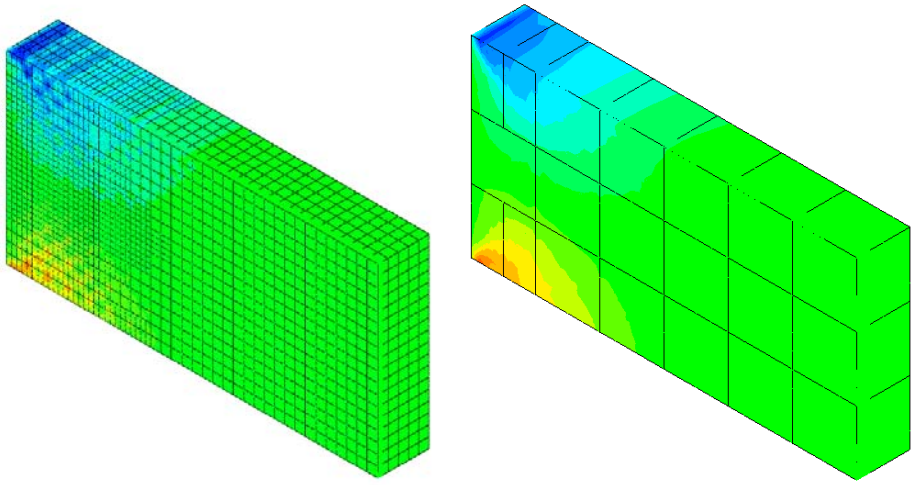

Figure 4.40: Cantilever beam. Contour map of component ε^p_{zz} of plastic strain tensor for heterogeneous and homogenized domain in cross section. Color scales match approximately.

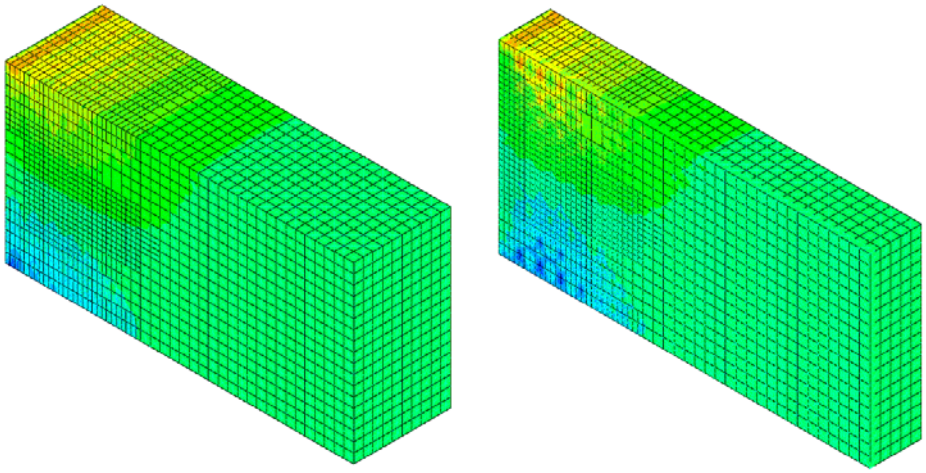

Figure 4.41: Cantilever beam. Contour map of component ε^p_{yy} of plastic strain tensor for heterogeneous domain and in its cross section. Color scales match approximately.

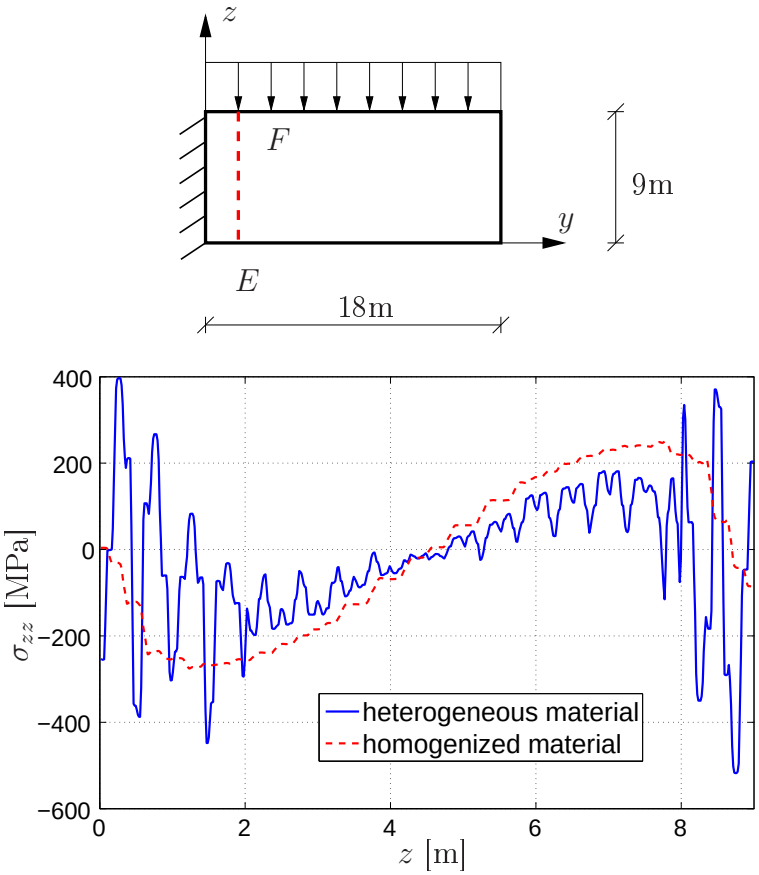

Figure 4.42: Cantilever beam. Comparison of component σ_{zz} of stress tensor for heterogeneous and homogenized material along segment EF.

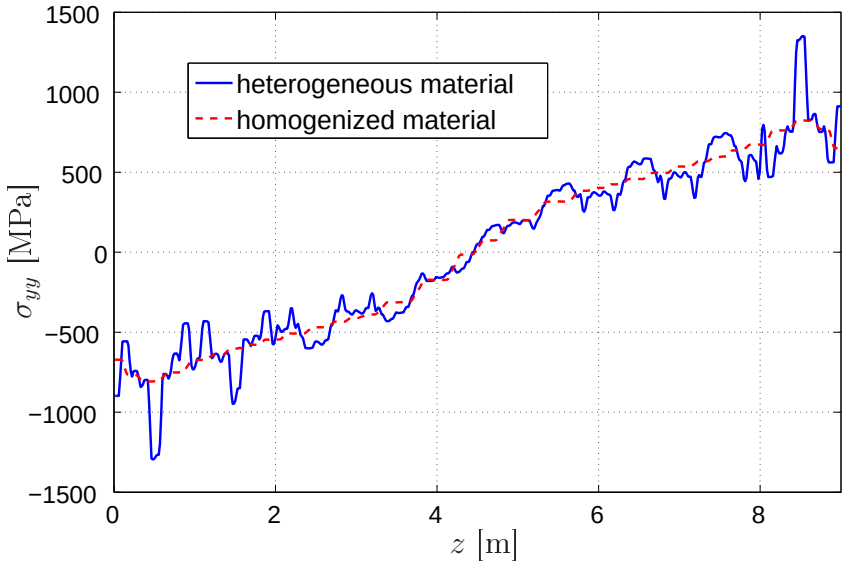

Figure 4.43: Cantilever beam. Comparison of component σ_{yy} of stress tensor for heterogeneous and homogenized material along segment EF.

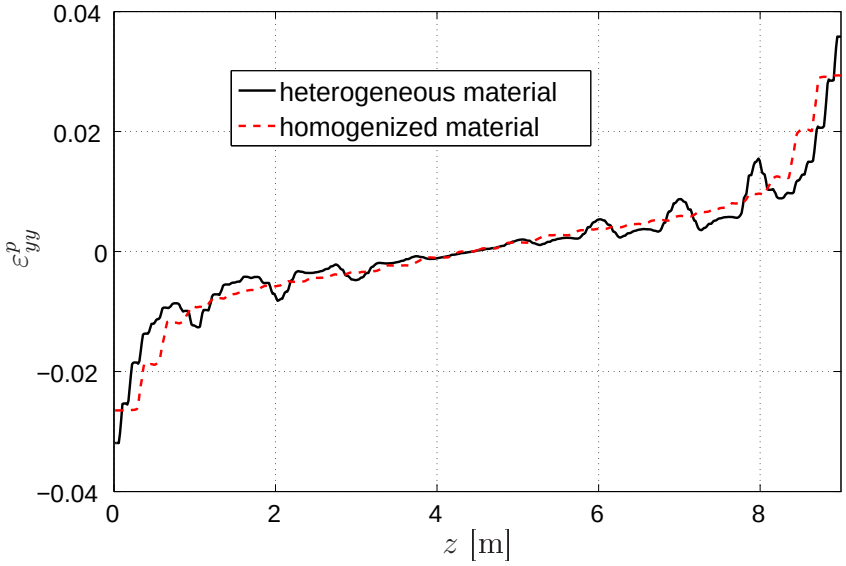

Figure 4.44: Cantilever beam. Comparison of component ε^p_{yy} of plastic strain tensor for heterogeneous and homogenized material along segment EF.

One may notice that a single RVE approach with associative plasticity assumed in the macro-scale for periodic microstructures approximates the heterogeneous solution with a good accuracy for considered examples.

4.3 Fixed set of RVE

The single RVE approach resulted in a good solution approximation of a real heterogeneous material for examples considered in the previous section. However, if the material properties after homogenization are not the same in the whole domain, more than one RVE should be used in order to guarantee an accurate solution. In classical homogenization approach each Gauss integration point is associated to RVE but, as it was previously mentioned, such an analysis is rarely possible to perform for 3D domain.

The approach proposed in this section is based on the idea of fixed RVE positions, independent of the integration points [91, 64, 65]. Data transfer between fixed and Gauss points is performed by simple MLS (*moving least square*) approximation [92].

The numerical test of such an approach was conducted for the composite, where both components may deform in elastic-plastic range. The L-shaped domain, schematically presented in Fig. 4.45, was considered. One wall, marked by the black color, was fixed. The wall in the plane xz was subjected to a constant loading q in horizontal direction, for walls parallel to yz plane no penetration conditions are enforced. For the other parts of the boundary homogeneous Neumann conditions were assumed.

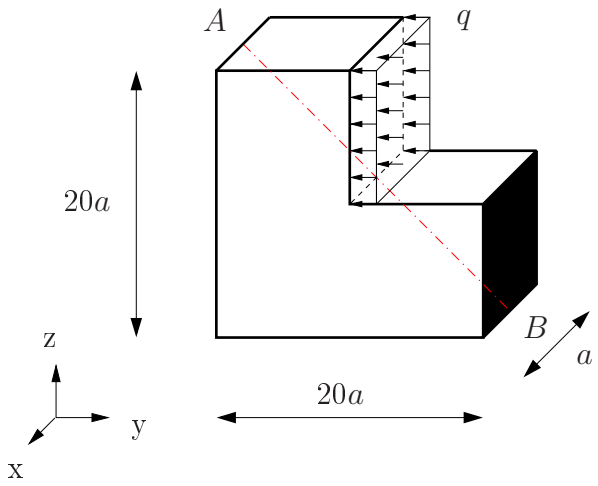

Figure 4.45: L-shaped domain. Boundary conditions of a model.

Initial computations were performed in the elastic range for the homogenized material with effective Young modulus and Poisson ratio in order to determine places, where the Mises equivalent stresses reached the largest values. The finite element discretization is shown in Fig. 4.46 and contour maps of the stress tensor components σ_{yy} and σ_{zz} are plotted in Fig. 4.47.

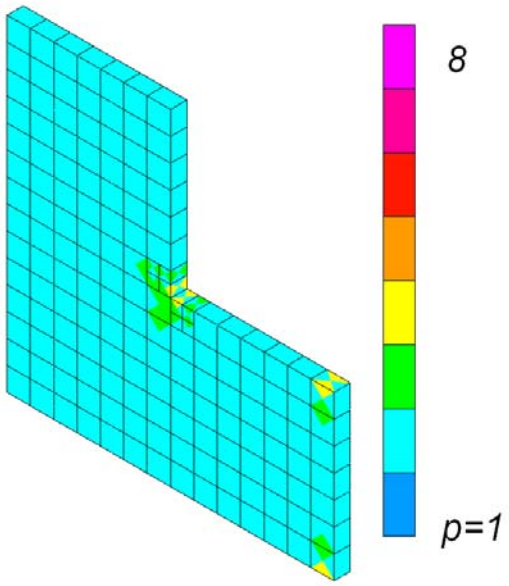

Figure 4.46: L-shaped domain. FE discretization.

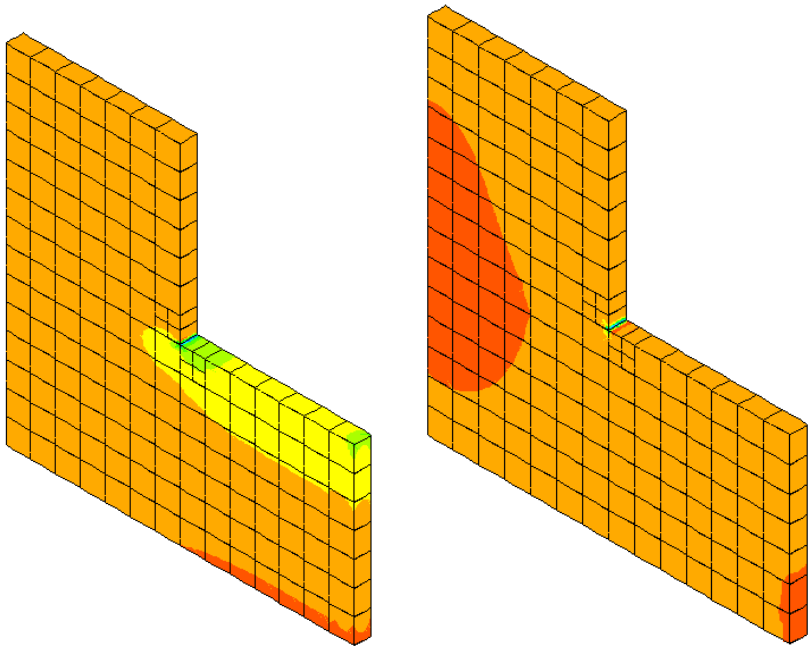

Figure 4.47: L-shaped domain. Contour maps of σ_{yy} and σ_{zz} components of stress tensor for homogenized domain. Color scales match approximately.

Distribution of fixed points in the macro-scale was established on the basis of the Mises equivalent stresses distribution. The results shown that the plastic yield limit was reached in vicinity of the reentrant corner of the domain. Thus, 16 fixed points (RVE), 8 for each wall (shown in Fig. 4.48) were assumed and parallel elastic-plastic computation was performed in the micro-scale. These points were selected manually. However, in practice they may be regularly distributed in the plastic zone.

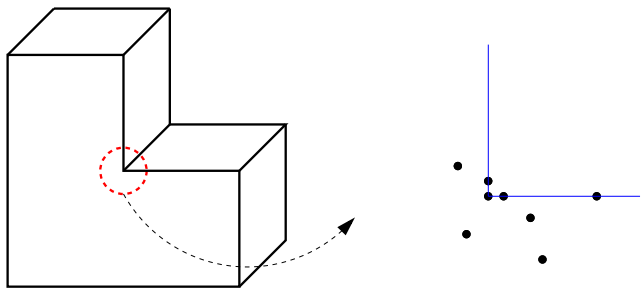

Figure 4.48: L-shaped domain. RVE distribution.

For each RVE the boundary conditions were assumed on the basis of averaged strains from the macro-scale. Contour maps defining the state of stresses in each RVE are shown in Fig. 4.49.

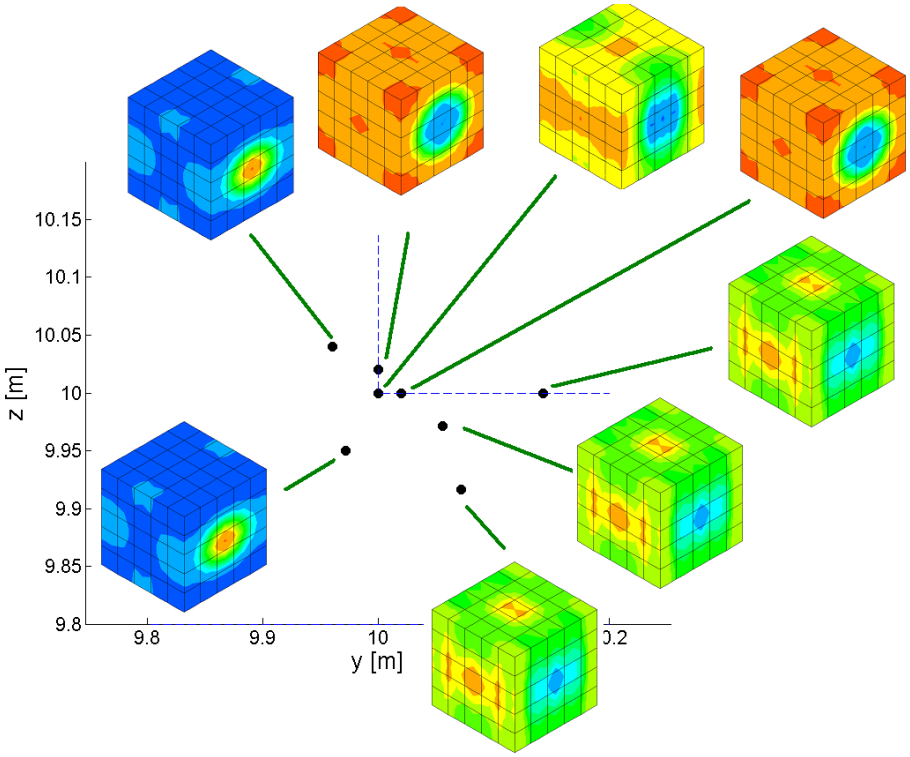

Figure 4.49: L-shaped domain. Contour maps of component σ_{yy} of stress tensor in fixed number of RVE near reentrant corner (color scales are different for different RVE).

In the next step the increments of plastic strains $\langle \Delta\boldsymbol{\varepsilon}^p \rangle$ obtained by RVE analysis were transfered to the Gauss integration points by MLS approximation method [59, 92] constructed on the approximate solution at m (here all 16) points $P_1(x_1, y_1), P_2(x_2, y_2), \ldots, P_m(x_m, y_m)$. Using, for the sake of simplicity, notation $f_i = \sigma_{kl}(P_i)$, $f^* = \sigma_{kl}(P^*)$ for arbitrary $k, l \in \{1, 2, 3\}$ and the Taylor formula with neglected second order reminder term (the Taylor formula with higher order terms may be used in the same way resulting in better approximation properties), one obtains an expression for the known values f_i in terms of the unknown quantities at i-th point (x^*, y^*) in the form

$$f_i = f^* + h_i f^*_{,x} + k_i f^*_{,y}, \quad h_i = x^* - x_i, \quad k_i = y^* - y_i \tag{4.16}$$

Minimization of the weighted sum of squared differences between known values and computed using Eq. (4.16)

$$S(f^*, f^*_{,x}, f^*_{,y}) = \sum_{i=1}^{m} w_i (f_i - f^* - h_i f^*_{,x} - k_i f^*_{,y})^2 \tag{4.17}$$

is the condition used to define the values of f^* and its derivatives $f^*_{,x}$, $f^*_{,y}$ at point P^*. If weights w_i in Eq. (4.17) are singular, then approximation $f^*(x, y)$ becomes an interpolation. There was assumed after [62]

$$w_i = \frac{1}{r_i^4}, \qquad r_i^2 = h_i^2 + k_i^2 \tag{4.18}$$

If only the first term is used in Eq. (4.16) the technique is called the Shepard approximation [92]. Such a simple version of the MLS approximation was used in this work.

Computed results were compared with a single RVE approach, presented in the previous section. The qualitative comparison of stress components σ_{yy} and σ_{zz} are presented in Figs. 4.50 and 4.51. Their distributions along segment AB are compared in Figs. 4.52 and 4.53.

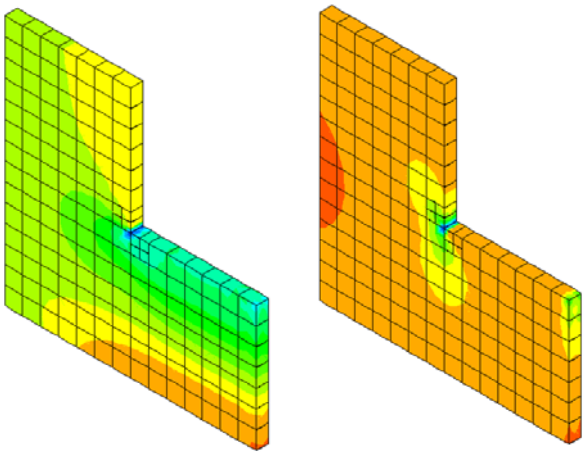

Figure 4.50: L-shaped domain. Contour map of components σ_{yy} and σ_{zz} of stress tensor obtained from the homogenization based on a single RVE (qualitative comparison).

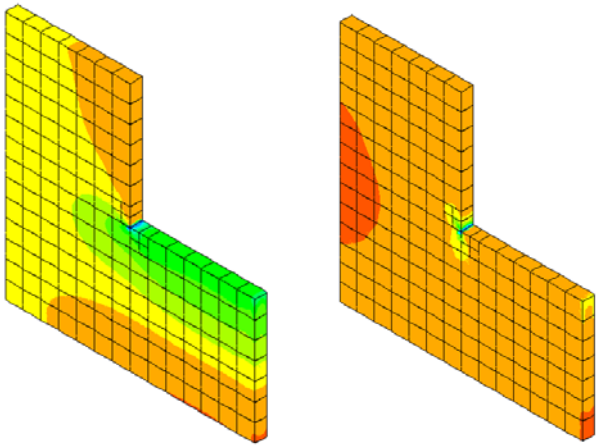

Figure 4.51: L-shaped domain. Contour map of components σ_{yy} and σ_{zz} of stress tensor obtained from the homogenization based on a limited number of RVE (qualitative comparison).

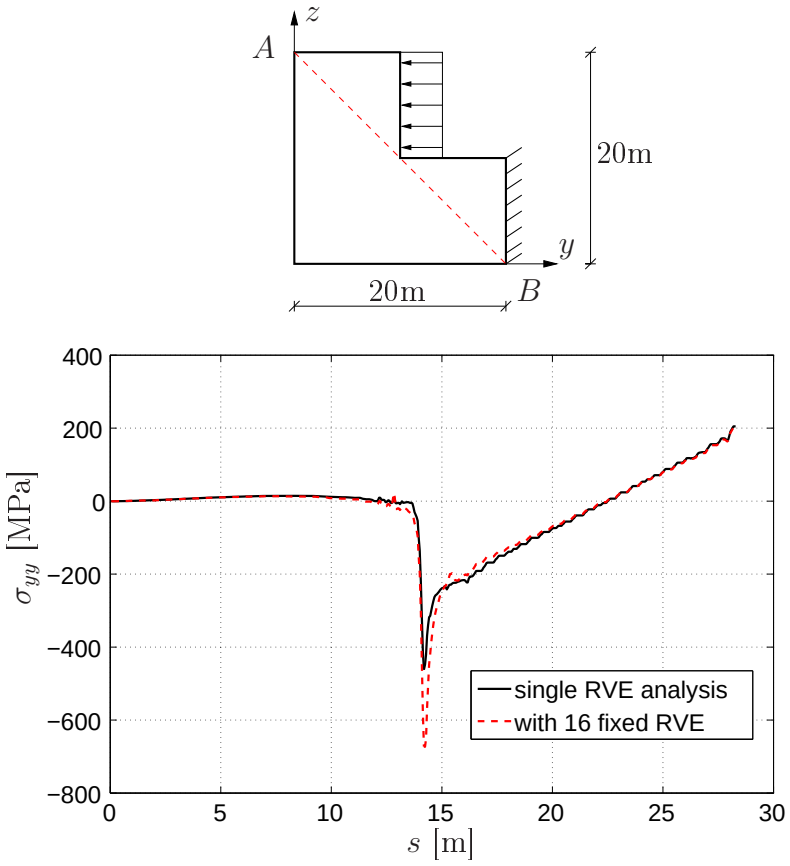

Figure 4.52: L-shaped domain. Component σ_{yy} of stress tensor along segment AB.

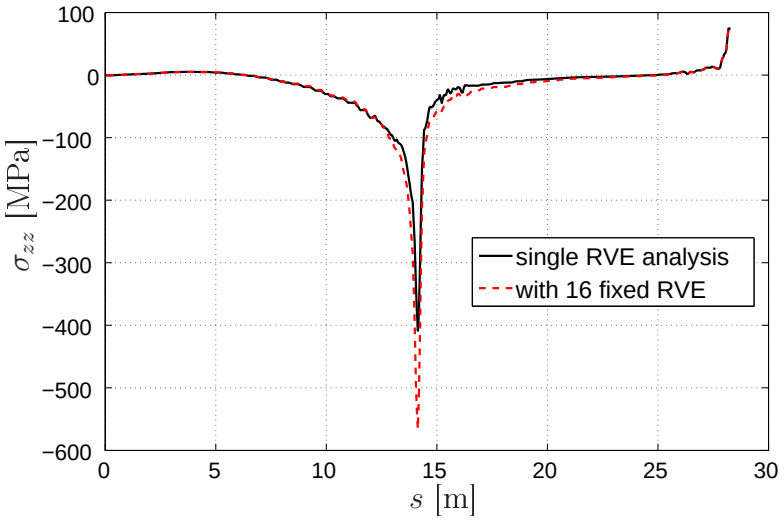

Figure 4.53: L-shaped domain. Component σ_{zz} of stress tensor along segment AB.

The presented tests shown that both computations based on a single RVE approach and a small number of RVE located in the appropriate area, give a good approximation of heterogeneous solution. One may conclude that for uniformly distributed inclusions we may avoid cumbersome analysis related to each Gauss integration point.

Chapter 5

Homogenization error estimation

Replacement of heterogeneous body by a homogenized one with effective material parameters introduces an error, related to incomplete information about the microstructure. Thus, it may happen that the homogenization should not be used for certain part of the domain. Therefore, estimation of homogenization (modeling) error is discussed in this chapter. The concepts of modeling error is also employed in a different setting, where one assesses the adequacy of relatively inexpensive models [76].

A global explicit estimate using the homogenized (coarse) elasticity tensor and the actual fine-scale elasticity tensor was proposed by Zohdi et al. [112]. However, it is not able to capture local error.

A scale adaptation strategy developed by Temizer and Wriggers [101] was used to account for loss of accuracy for the finite deformation analysis of macrostructures. In that method the adaptation zones that correspond to regions with high strain-gradients, are identified based on a post-processing step on the homogenized solution. Subsequently, for critical zones, exact microstructural representation is introduced, without intermediate models.

In this section an upper bound approach [77, 105, 106] is presented, as well as other possibilities of modeling error estimation, since this issue is essential for reliability of the results.

5.1 Upper bound approach

This method of the homogenization error assessment is the following upper bound proposed in [77, 105, 106]

$$\mathscr{I}_0 = \boldsymbol{I} - \boldsymbol{C}^{-1}\boldsymbol{C}_{eff} \tag{5.1}$$

$$||\boldsymbol{u} - \boldsymbol{u}_0||_E \leq \zeta_{\text{upp}} \stackrel{\text{def}}{=} \left\{ \int_\Omega \mathscr{I}_0 \nabla \boldsymbol{u}_0 : \boldsymbol{C}\mathscr{I}_0 \nabla \boldsymbol{u}_0 \, \mathrm{d}\boldsymbol{x} \right\}^{1/2} \tag{5.2}$$

where $\boldsymbol{u}$ and $\boldsymbol{u}_0$ stand for heterogeneous and homogenized solution, respectively; $\boldsymbol{C}$ and $\boldsymbol{C}_{eff}$ denote elasticity tensor for heterogeneous domain and effective elasticity tensor for homogenized body. This approach was verified on the 1D example.

Numerical example - bar benchmark

The bar benchmark and assumed material distribution are schematically presented in Figs. 5.1 and 5.2.

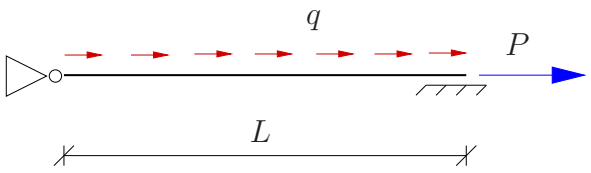

Figure 5.1: Bar model.

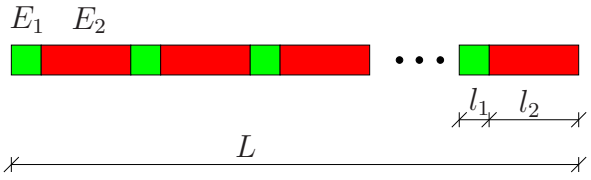

Figure 5.2: Bar benchmark. Material distribution.

The following data were assumed: $L = 1$ m, $P = -60$ kN, $q = 10x + 20$ kN/m, $E1 = 50$ GPa, $E2 = 0.1 \cdot E1$

In this 1D example effective Young modulus may be computed as [97]

$$E_{eff} = \frac{E_1 E_2}{n_1 E_2 + n_2 E_1}, \qquad n_1 = \frac{l_1}{l}, \quad n_2 = \frac{l_2}{l} \tag{5.3}$$

Thus, one may obtain derivatives of the exact solution for homogenized (u_0) and heterogeneous (u) materials:

$$u_0' = \frac{1}{AE_{eff}}(-qx + P + qL) \tag{5.4}$$

$$u' = \frac{1}{AE}(-qx + P + qL) \tag{5.5}$$

where: $E = \begin{cases} E_1 & \text{(mat.1)} \\ E_2 & \text{(mat.2)} \end{cases}$

Since the following relations hold

$$||u - u_0||_E^2 = \int_a^b (u' - u_0')^2 E \, \mathrm{d}x \tag{5.6}$$

$$\zeta_{\text{upp}}^2 = \int_a^b \left(1 - \frac{E_{eff}}{E}\right)^2 E (u_0')^2 \, \mathrm{d}x \tag{5.7}$$

after a few simplifications one obtains that in this example the inequality (5.2) simplifies to the relation

$$||u - u_0||_E^2 = \zeta_{\text{upp}}^2 \tag{5.8}$$

Thus, this error bound in 1D example gives exact error. Moreover, it is independent of the large difference between matrix and inclusion material data.

5.2 Estimation by subdomain solutions

Another possibility of modeling error estimation is based on the solution of heterogeneous problem in selected subdomains with boundary conditions assumed on the basis of homogenized solution. Such an error estimate consists of a few steps:

STEP 1: Compute the homogenized solution in domain Ω.

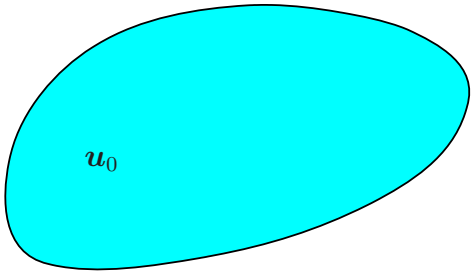

Figure 5.3: Homogenization error. Homogenized domain.

STEP 2: Select a part of the body, where the error should be estimated and consider heterogeneous material in this subdomain.

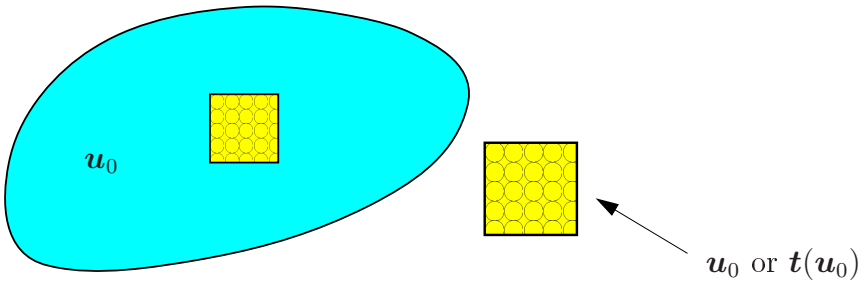

Figure 5.4: Homogenization error. Cut-off part of heterogeneous domain.

STEP 3: Solve the boundary value problem for cut-off heterogeneous subdomain with boundary conditions resulted from homogenized solution. Obtain the solution and consider it ($\boldsymbol{u}_I$) in a smaller truncated part of the selected heterogeneous domain (subdomain A denoted by the red rectangle). Estimate the error between solution $\boldsymbol{u}_I$ and homogenized one $\boldsymbol{u}_0$ in subdomain A

$$\eta = \frac{||\boldsymbol{u}_I - \boldsymbol{u}_0||_A}{||\boldsymbol{u}_0||_A} \tag{5.9}$$

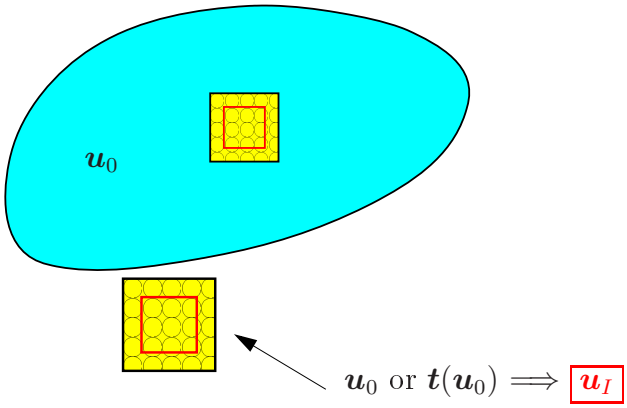

Figure 5.5: Homogenization error. Analysis of cut-off part of heterogeneous domain.

One may also use two additional steps.

(STEP 4:) Increase the heterogeneous cut-off part and once more solve the boundary value problem with boundary conditions resulted from homogenized solution in order to examine the influence of imposed boundary conditions to solution. Obtain the solution $\boldsymbol{u}_{II}$ and consider it for the same truncated area A as previously.

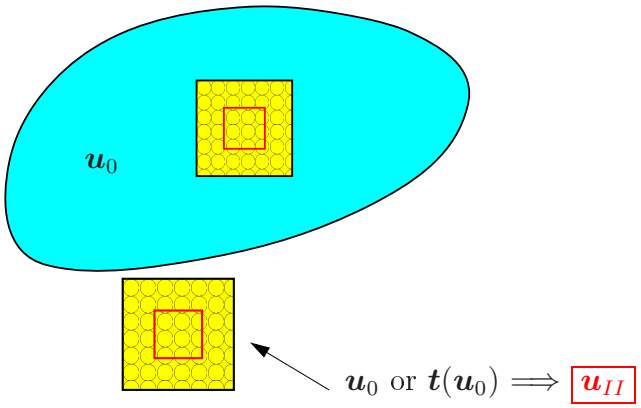

Figure 5.6: Homogenization error. Second cut-off part of heterogeneous domain.

(STEP 5:) If you want to estimate the quality of solution $\boldsymbol{u}_I$ compute the difference between both solutions

$$\gamma = ||\boldsymbol{u}_I - \boldsymbol{u}_{II}||_A \tag{5.10}$$

Numerical example – bar benchmark

Finite element solution for bar benchmark (Fig. 5.1) is shown below.

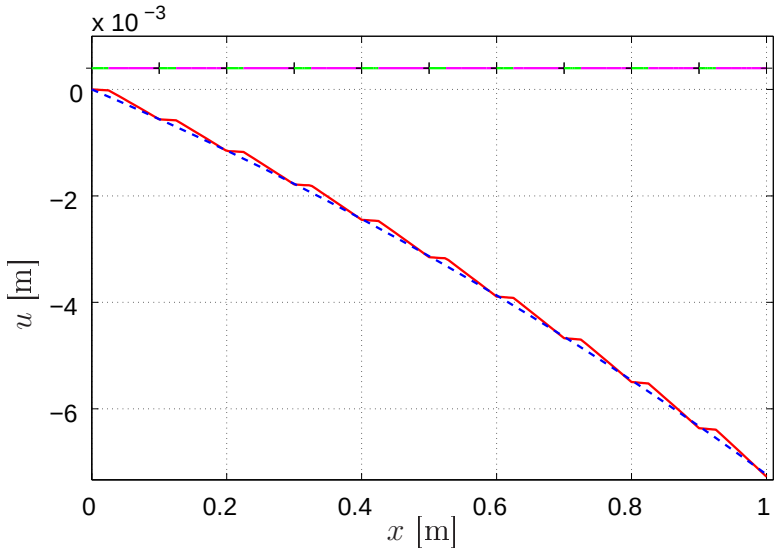

Figure 5.7: Bar benchmark. Material distribution (the horizontal line). Solution for heterogeneous u (the continuous line) and homogenized u_0 (the dashed line) material.

For homogenized domain a part of the body where material is heterogeneous was assumed and, after that, the problem with kinematic boundary conditions from homogenized solution was solved. The results may be observed in Fig. 5.8 (the green line). The solution, which was used for error estimation u_I, is denoted by the violet line.

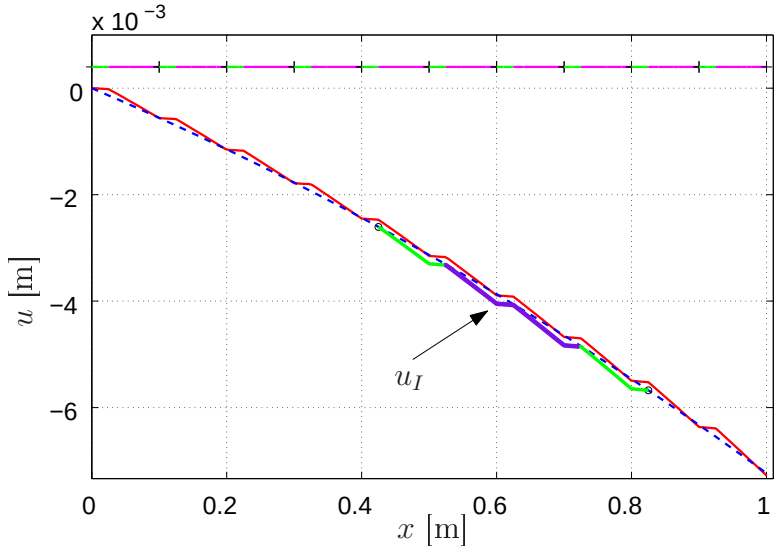

Figure 5.8: Bar benchmark. Solution u_I in the selected subdomain A (the violet line).

In the next step the heterogeneous part was increased and the new solution u_{II} was computed (presented in Fig. 5.9).

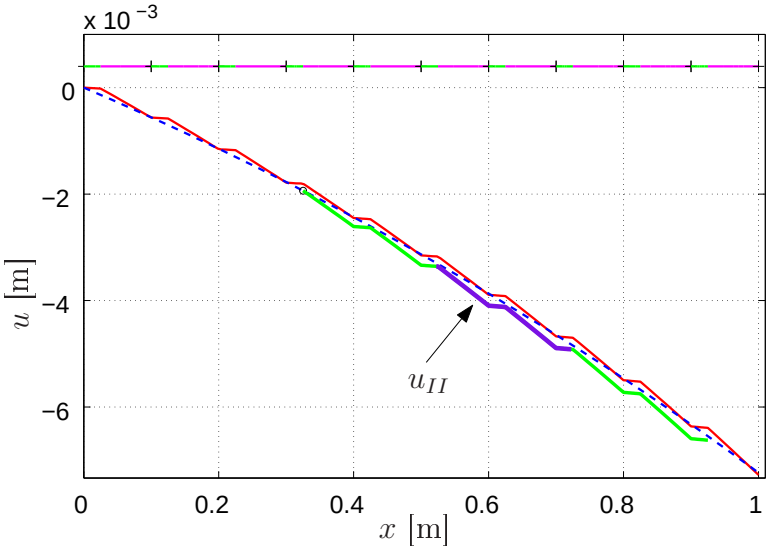

Figure 5.9: Bar benchmark. Solution u_{II} in the selected subdomain A (the violet line).

Few possibilities of this type of error estimation were considered. The results are compared below

$$\frac{||u_I - u_0||_{0,A}}{||u||_{0,[0,l]}} \approx 2.57\% \tag{5.11}$$

$$\frac{||u_{II} - u_0||_{0,A}}{||u||_{0,[0,l]}} \approx 2.82\% \tag{5.12}$$

$$\frac{||u - u_0||_{0,[0,l]}}{||u||_{0,[0,l]}} \approx 2.04\% \quad \text{(true error)} \tag{5.13}$$

Influence of boundary conditions to the solution quality

$$\frac{||u_I - u_{II}||_{0,A}}{||u||_{0,[0,l]}} \approx 0.28\% \tag{5.14}$$

One may observe that influence of boundary conditions to the solution can be neglected in this 1D example and the formulas (5.11), (5.12) give the reasonable homogenization error estimate.

Numerical example – plane strain problem 1

The L-shaped domain in plane strain state was considered. The metal matrix was reinforced by cylinder-like inclusions, distributed uniformly. Material parameters ale collected in Tab. 4.1. Assumed boundary conditions, as well as material distribution, are shown in Fig. 5.10.

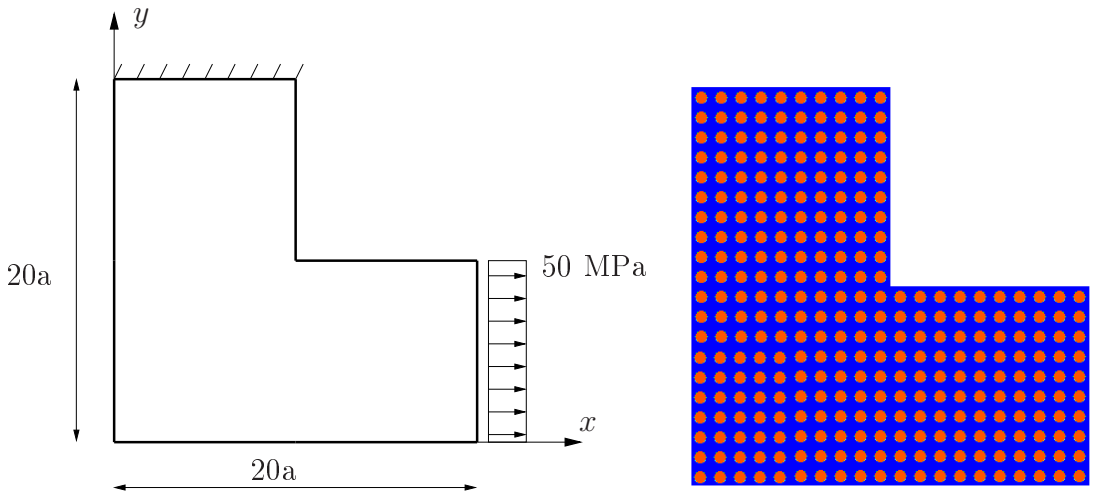

Figure 5.10: Boundary conditions for L-shaped domain. Material distribution.

In the first step effective material parameters were determined during tension test performed on two RVE of sizes $a \times a$ and $2a \times 2a$. The radius of cylinder-like inclusion was $r = 0.3a$. Finite element meshes obtained in adaptation processes are presented in Fig. 5.11.

Computed effective material parameters are: $E_{ff} = 129.09$ GPa, $\nu_{eff} = 0.2977$ (the same result for both RVE). They are used for solution of homogeneous problem.

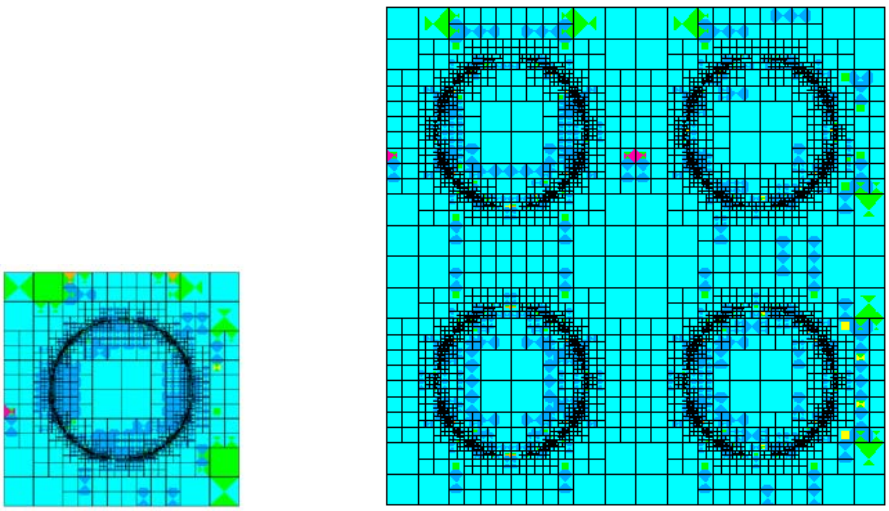

Figure 5.11: RVE meshes (colors indicate order of approximation).

In the macro-scale, for the test purposes, the computations were performed for homogenized material with effective material data, as well as for fully heterogeneous domain to verify the proposed error estimation approach.

The finite element discretization for heterogeneous and homogenized material are shown in Fig. 5.12. The FE mesh for homogenized domain was generated in automatic *hp* adaptation process. However, for heterogeneous domain only *h*-refinements were used at the interface of both materials. Contour maps of displacement vector components for homogenized material, denoted by $\boldsymbol{u}_0^L$, are presented in Fig. 5.13.

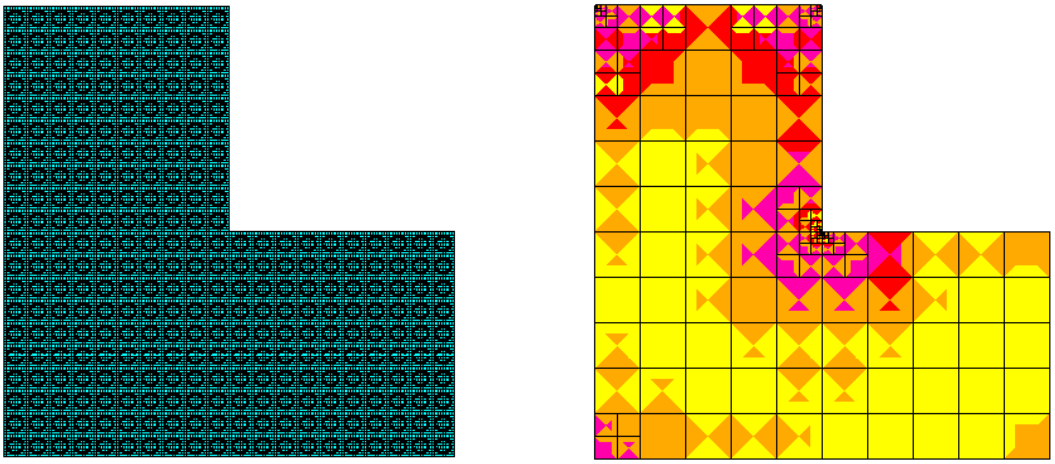

Figure 5.12: L-shaped domain 1. FE meshes for heterogeneous and homogenized material.

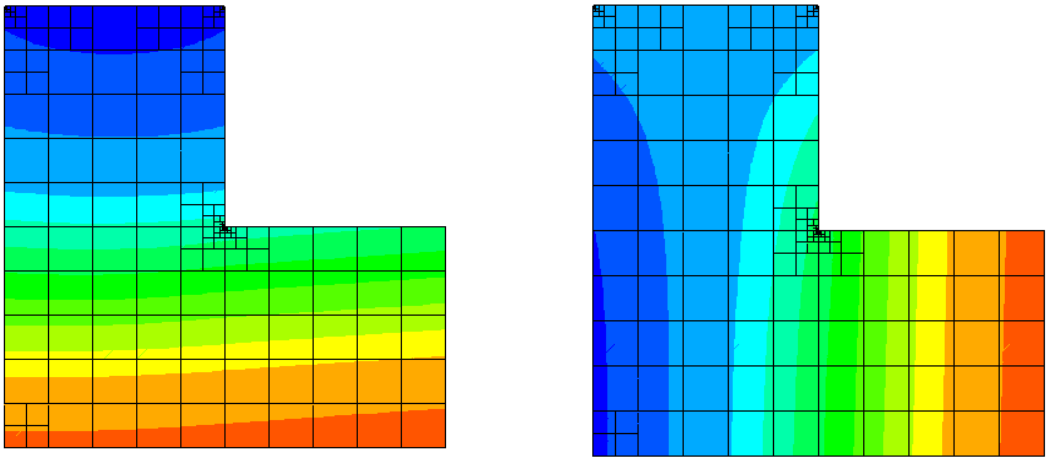

Figure 5.13: L-shaped domain 1. Contour maps of displacement vector components $u_x \in [0,\ 0.094\ \text{m}]$ and $u_y \in [-0.024\ \text{m},\ 0.078\ \text{m}]$ of homogenized domain.

The entire domain was used to obtain true error in L_2 norm. The displacement solution of complex heterogeneous domain is denoted by $\boldsymbol{u}^L$, $\boldsymbol{u}_0^L$ stands for homogenized solution. Similar convention was assumed for stresses, as well as strains. The results are presented below

$$\frac{||\boldsymbol{u}^L - \boldsymbol{u}_0^L||_{0,\Omega}}{||\boldsymbol{u}^L||_{0,\Omega}} \approx 1.08\% \quad \text{(true error in L-shaped domain)} \tag{5.15}$$

$$\frac{||\boldsymbol{\sigma}^L - \boldsymbol{\sigma}_0^L||_{0,\Omega}}{||\boldsymbol{\sigma}^L||_{0,\Omega}} \approx 24.22\% \quad \text{(true error in L-shaped domain)} \tag{5.16}$$

$$\frac{||\boldsymbol{\varepsilon}^L - \boldsymbol{\varepsilon}_0^L||_{0,\Omega}}{||\boldsymbol{\varepsilon}^L||_{0,\Omega}} \approx 33.86\% \quad \text{(true error in L-shaped domain)} \tag{5.17}$$

In the first case heterogeneous subdomain A (see Fig. 5.14) was cut-off from domain Ω with boundary conditions (displacements) resulted from homogenized solution, approximated along edges of selected subdomain A by 8-*th* order Legendre polynomials (Figs. 5.14 and 5.15).

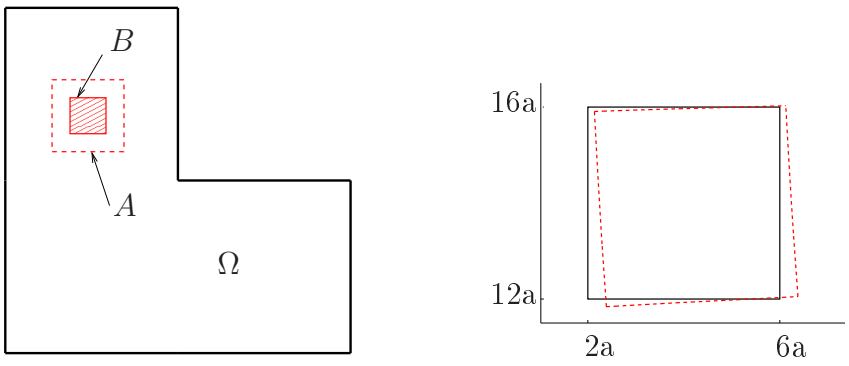

Figure 5.14: L-shaped domain 1. Boundary displacement for heterogeneous subdomain A resulted from homogenized solution (rescaled values).

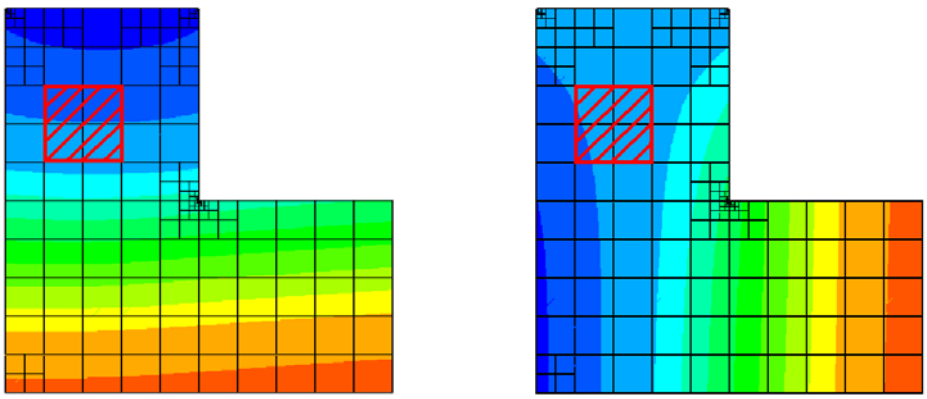

Figure 5.15: L-shaped domain 1. Contour maps of displacement vector components u_x and u_y with selected subdomain A.

For the cut-off subdomain A heterogeneous material was assumed. The corresponding FE mesh is shown in Fig. 5.16. The red line shows part B of the subdomain A, where the solution was considered.

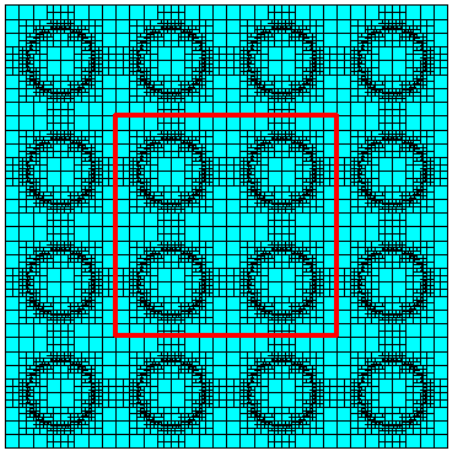

Figure 5.16: FE mesh for domain A and smaller truncated part B of the selected heterogeneous domain (denoted by the red rectangle).

The Dirichlet boundary conditions (see Fig. 5.14), resulted from solution of homogenized body, were imposed to the subdomain A. The solution is shown in Fig. 5.17. Distribution of stress component σ_{xx} in zoomed part of L-shaped with heterogeneity that enclosed cut-off domain A and solution obtained for independent subdomain A with kinematic boundary conditions are compared in Fig. 5.18.

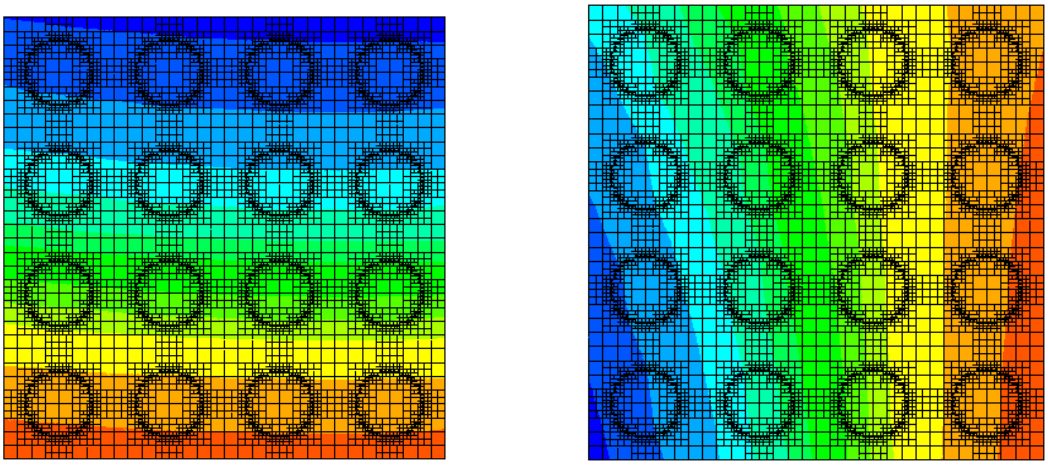

Figure 5.17: Contour maps of displacement vector components $u_x \in [0.008\text{ m}, 0.026\text{ m}]$ and $u_y \in [-0.011\text{ m}, 0.003\text{ m}]$ of domain A.

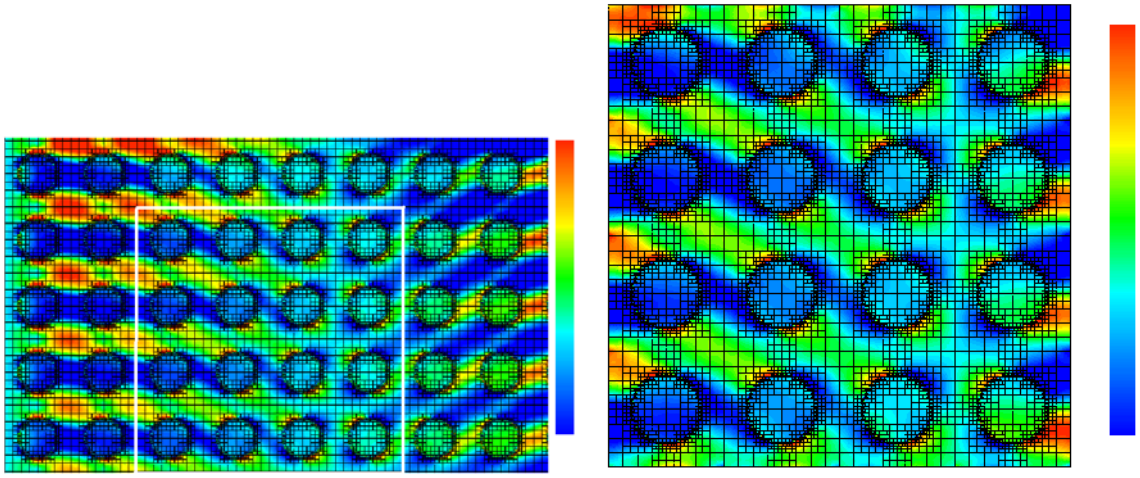

Figure 5.18: Contour maps of stress component $\sigma_{xx} \in$ [–20 MPa, 40 MPa] for zoomed part of L-shaped domain and domain A.

Estimates of modeling error are collected below, where $\boldsymbol{u}$, $\boldsymbol{\sigma}$ and $\boldsymbol{\varepsilon}$ stand for the solutions in subdomain B obtained by analysis in subdomain A

$$\frac{||\boldsymbol{u} - \boldsymbol{u}_0^L||_{0,B}}{||\boldsymbol{u}_0^L||_{0,B}} \approx 0.91\% \quad \text{(error in subdomain } B\text{)} \tag{5.18}$$

$$\frac{||\boldsymbol{\sigma} - \boldsymbol{\sigma}_0^L||_{0,B}}{||\boldsymbol{\sigma}_0^L||_{0,B}} \approx 22.08\% \quad \text{(error in subdomain } B\text{)} \tag{5.19}$$

$$\frac{||\boldsymbol{\varepsilon} - \boldsymbol{\varepsilon}_0^L||_{0,B}}{||\boldsymbol{\varepsilon}_0^L||_{0,B}} \approx 35.73\% \quad \text{(error in subdomain } B\text{)} \tag{5.20}$$

$$\frac{||\boldsymbol{u}^L - \boldsymbol{u}_0^L||_{0,B}}{||\boldsymbol{u}^L||_{0,B}} \approx 0.64\% \quad \text{(true error in selected part of L-shaped domain)} \tag{5.21}$$

$$\frac{||\boldsymbol{\sigma}^L - \boldsymbol{\sigma}_0^L||_{0,B}}{||\boldsymbol{\sigma}^L||_{0,B}} \approx 21.68\% \quad \text{(true error in selected part of L-shaped domain)} \tag{5.22}$$

$$\frac{||\boldsymbol{\varepsilon}^L - \boldsymbol{\varepsilon}_0^L||_{0,B}}{||\boldsymbol{\varepsilon}^L||_{0,B}} \approx 34.13\% \quad \text{(true error in selected part of L-shaped domain)} \tag{5.23}$$

In the next case heterogeneous subdomain C (see Fig. 5.19) was cut-off from domain Ω. The corresponding boundary conditions resulted from homogenized solution are shown in Figs. 5.19 and 5.20.

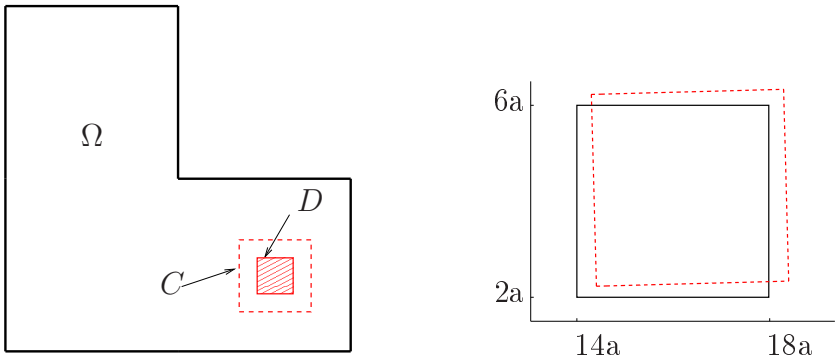

Figure 5.19: L-shaped domain 1. Boundary displacement for heterogeneous subdomain C resulted from homogenized solution (rescaled values).

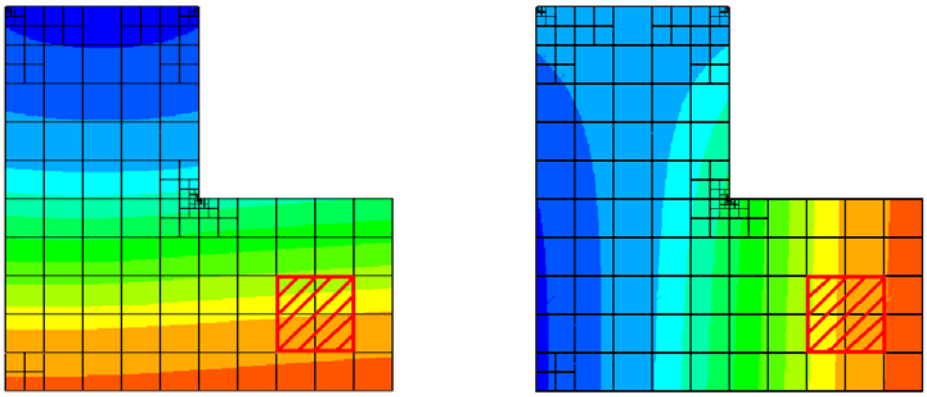

Figure 5.20: Contour maps of displacement vector components u_x and u_y with selected subdomain C.

The solution resulted from prescribed Dirichlet boundary conditions is shown in Fig. 5.21. Contour maps of stress component are presented in Fig. 5.22.

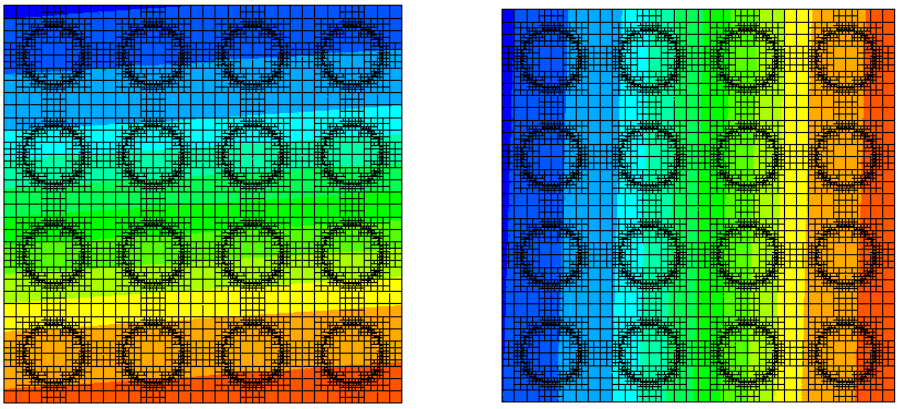

Figure 5.21: Contour maps of displacement vector components $u_x \in [0.06\text{ m}, 0.08\text{ m}]$ and $u_y \in [0.045\text{ m}, 0.067\text{ m}]$ in domain C.

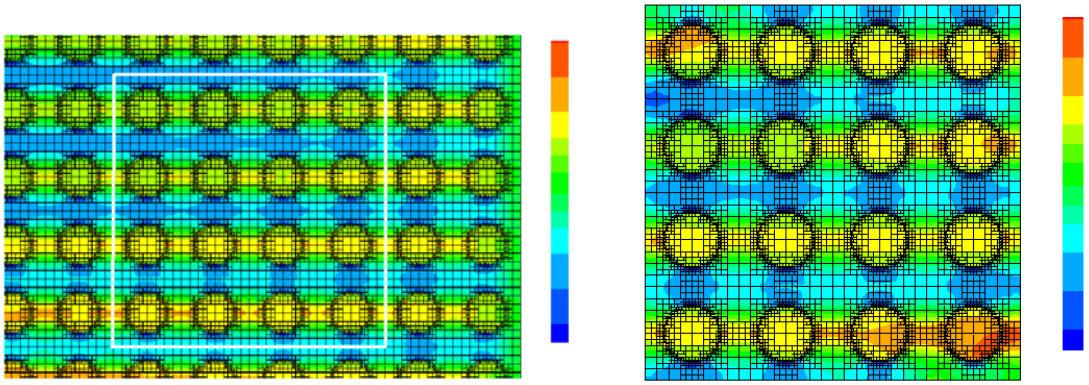

Figure 5.22: Contour maps of stress component $\sigma_{xx} \in [20\text{ MPa}, 80\text{ MPa}]$ for zoomed part of L-shaped domain and subdomain C.

Estimated modeling errors in subdomain D are as follows

$$\frac{||\boldsymbol{u} - \boldsymbol{u}_0^L||_{0,D}}{||\boldsymbol{u}_0^L||_{0,D}} \approx 0.03\% \quad \text{(error in subdomain } D\text{)} \tag{5.24}$$

$$\frac{||\boldsymbol{\sigma} - \boldsymbol{\sigma}_0^L||_{0,D}}{||\boldsymbol{\sigma}_0^L||_{0,D}} \approx 28.43\% \quad \text{(error in subdomain } D\text{)} \tag{5.25}$$

$$\frac{||\boldsymbol{\varepsilon} - \boldsymbol{\varepsilon}_0^L||_{0,D}}{||\boldsymbol{\varepsilon}_0^L||_{0,D}} \approx 36.20\% \quad \text{(error in subdomain } D\text{)} \tag{5.26}$$

$$\frac{||\boldsymbol{u}^L - \boldsymbol{u}_0^L||_{0,D}}{||\boldsymbol{u}^L||_{0,D}} \approx 1.18\% \quad \text{(true error in selected part of L-shaped domain)} \tag{5.27}$$

$$\frac{||\boldsymbol{\sigma}^L - \boldsymbol{\sigma}_0^L||_{0,D}}{||\boldsymbol{\sigma}^L||_{0,D}} \approx 25.8\% \quad \text{(true error in selected part of L-shaped domain)} \tag{5.28}$$

$$\frac{||\boldsymbol{\varepsilon}^L - \boldsymbol{\varepsilon}_0^L||_{0,D}}{||\boldsymbol{\varepsilon}^L||_{0,D}} \approx 33.44\% \quad \text{(true error in selected part of L-shaped domain)} \tag{5.29}$$

The vicinity of reentrant corner was also considered (see Figs. 5.23, 5.24). The known Neumann boundary conditions were taken into account on two edges, however the Dirichlet boundary conditions resulted from the homogenized solution may be also considered.

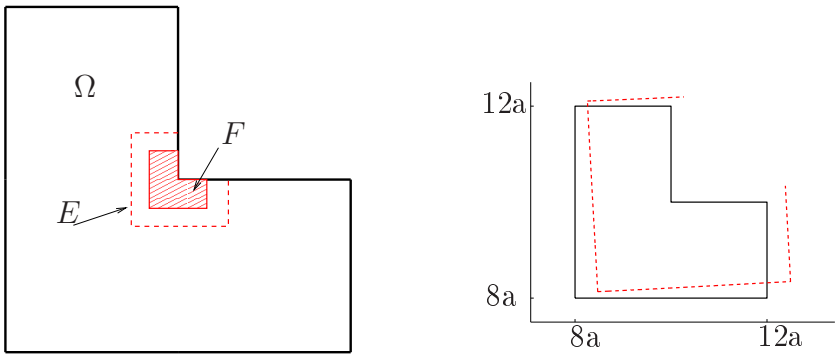

Figure 5.23: L-shaped domain 1. Boundary displacement for heterogeneous subdomain E resulted from homogenized solution (rescaled values).

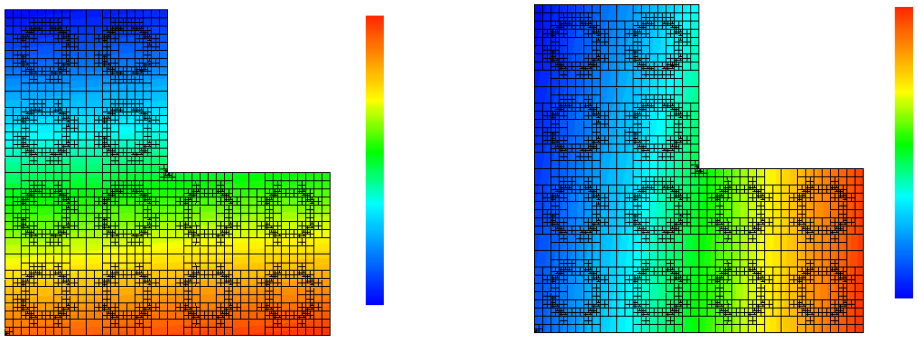

Figure 5.24: L-shaped domain 1. Contour maps of displacement components $u_x \in [0.026\text{ m}, 0.049\text{ m}]$ and $u_y \in [0.011\text{ m}, 0.034\text{ m}]$ in domain E.

The corresponding modeling errors are presented below

$$\frac{||\boldsymbol{u} - \boldsymbol{u}_0^L||_{0,F}}{||\boldsymbol{u}_0^L||_{0,F}} \approx 0.13\% \quad \text{(error in subdomain } F\text{)} \tag{5.30}$$

$$\frac{||\boldsymbol{\sigma} - \boldsymbol{\sigma}_0^L||_{0,F}}{||\boldsymbol{\sigma}_0^L||_{0,F}} \approx 28.12\% \quad \text{(error in subdomain } F\text{)} \tag{5.31}$$

$$\frac{||\boldsymbol{\varepsilon} - \boldsymbol{\varepsilon}_0^L||_{0,F}}{||\boldsymbol{\varepsilon}_0^L||_{0,F}} \approx 34.52\% \quad \text{(error in subdomain } F\text{)} \tag{5.32}$$

One may observe that the modeling error for stresses or strains is larger than for displacements. This is a consequence of stress concentration at material interfaces and large changes in material parameters for heterogeneous body.

Numerical example – plane strain problem 2

In the next example the L-shaped domain with different boundary conditions (see Fig. 5.25) was analyzed. Distribution of heterogeneity (cylinder-like inclusions), material data and corresponding material parameters (also effective ones) were the same as in the previous example.

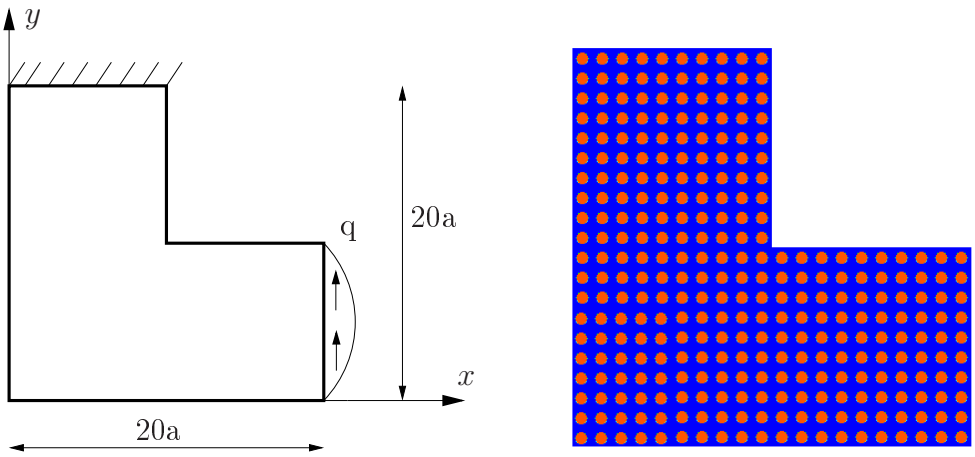

Figure 5.25: Boundary conditions for L-shaped domain, q=$-2y(y-10a)$ MPa.

Finite element mesh obtained during automatic adaptation process for domain with homogeneous material is presented in Fig. 5.26. Displacement solution is shown in Fig. 5.27.

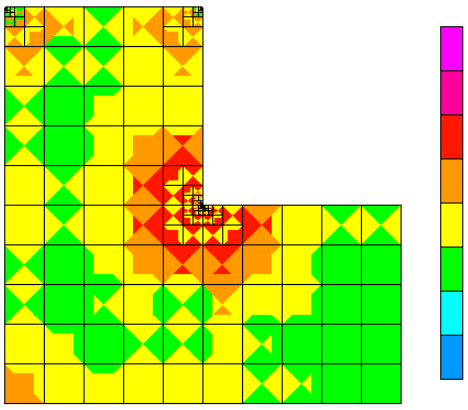

Figure 5.26: L-shaped domain 2. FE meshes for homogenized material (colors indicate order of approximation).

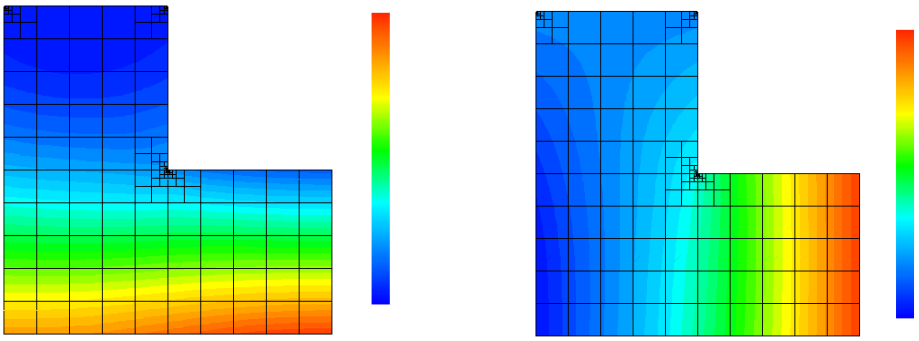

Figure 5.27: L-shaped domain 2. Contour maps of displacement vector components $u_x \in$ [–0.0002 m,0.092 m] and $u_y \in$ [–0.025 m, 0.114 m] of homogenized domain.

The subdomain C (see Fig. 5.28) was cut-off from L-shaped body and subjected to the kinematic boundary conditions resulted from homogenized solution.

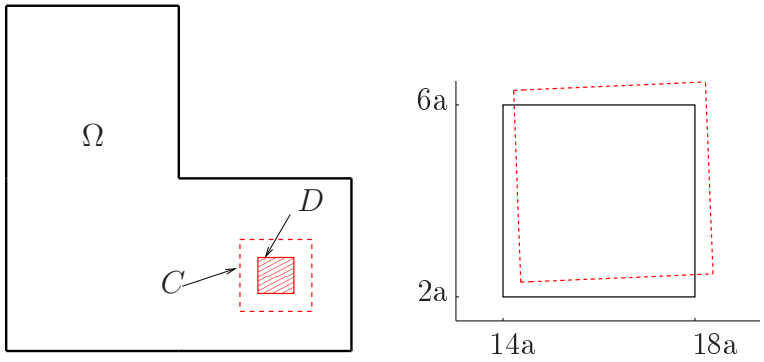

Figure 5.28: L-shaped domain 2. Boundary conditions for heterogeneous subdomain C resulted from homogenized solution.

The following modeling error norms were evaluated

$$\frac{||\boldsymbol{u} - \boldsymbol{u}_0^L||_{0,D}}{||\boldsymbol{u}_0^L||_{0,D}} \approx 0.05\% \quad \text{(error in subdomain } D\text{)} \tag{5.33}$$

$$\frac{||\boldsymbol{\sigma} - \boldsymbol{\sigma}_0^L||_{0,D}}{||\boldsymbol{\sigma}_0^L||_{0,D}} \approx 19.7\% \quad \text{(error in subdomain } D\text{)} \tag{5.34}$$

$$\frac{||\boldsymbol{\varepsilon} - \boldsymbol{\varepsilon}_0^L||_{0,D}}{||\boldsymbol{\varepsilon}_0^L||_{0,D}} \approx 36.7\% \quad \text{(error in subdomain } D\text{)} \tag{5.35}$$

In the next case surrounding of the reentrant corner E (see Fig. 5.29) was cut-off from the L-shaped domain. The corresponding kinematic boundary conditions resulted from homogenized solution were assumed.

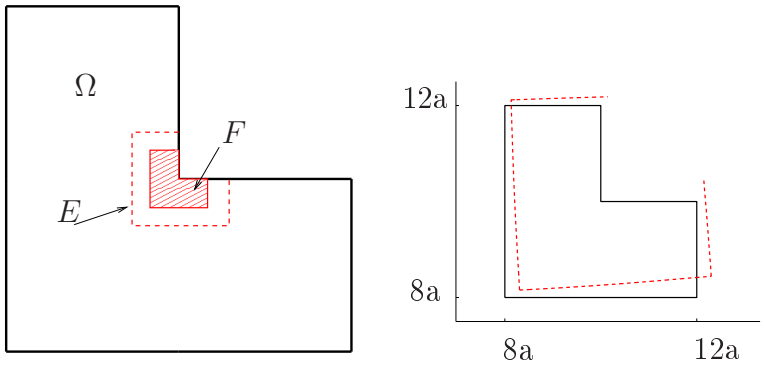

Figure 5.29: L-shaped domain 2. Boundary conditions for heterogeneous subdomain E resulted from homogenized solution.

In this example computed errors are:

$$\frac{||\boldsymbol{u} - \boldsymbol{u}_0^L||_{0,F}}{||\boldsymbol{u}_0^L||_{0,F}} \approx 0.5\% \quad \text{(error in subdomain } F) \tag{5.36}$$

$$\frac{||\boldsymbol{\sigma} - \boldsymbol{\sigma}_0^L||_{0,F}}{||\boldsymbol{\sigma}_0^L||_{0,F}} \approx 18.56\% \quad \text{(error in subdomain } F) \tag{5.37}$$

$$\frac{||\boldsymbol{\varepsilon} - \boldsymbol{\varepsilon}_0^L||_{0,F}}{||\boldsymbol{\varepsilon}_0^L||_{0,F}} \approx 36.28\% \quad \text{(error in subdomain } F) \tag{5.38}$$

Stress and strain errors are at the same level, while displacement error is ten times larger.

The above described method of homogenization error estimation additionally delivers information about solution at the micro-level that may be necessary e.g. for debonding or crack propagation analysis. The algorithm was verified on linear examples only, however, it can be also used for inelastic analysis.

5.3 Estimation based on residuum

By analogy to the explicit residual error indicator for FEM solution [7, 8] the residuum, i.e. the difference between left and right hand sides of the governing differential equation, when the solution approximation is plugged into the equation, is used to bound the solution error.

The proposed algorithm of homogenization error estimation may be stated in the following way:

1. Compute effective material parameters for homogenized domain.
2. Solve homogenized problem with effective properties $\rightarrow \boldsymbol{u}^0$ (Eq. (2.2)).
3. Compute residuum $\boldsymbol{R}$ of Eq. (2.1) for heterogeneous body substituting homogenized solution $\boldsymbol{u}^0$ in selected sub-domains, e.g. in each finite element in the macro-scale.

   Residuum of the equation

   $$L(\boldsymbol{u}) = \boldsymbol{f} \quad \text{has the form} \quad \boldsymbol{R} = L(\boldsymbol{u}_h^0) - \boldsymbol{f} \tag{5.39}$$

   where: $L(\cdot)$ is a differential operator, $\boldsymbol{u}_h^0$ is a finite element approximation of the solution. In fact, $\boldsymbol{R}$ is a distribution. Its norm, which we are interested in, may be bounded by the norms of regular part of $\boldsymbol{R}$ and jumps of the first derivatives of solution.

   For the linear elasticity problem the regular part

   $$r_i = \mu(u^0_{i,jj} + u^0_{j,ij}) + \lambda u^0_{k,kj}\delta_{ij} - f_i \qquad \text{in } \omega_k \qquad i,j = 1,2,3 \tag{5.40}$$

   where μ and λ are the material parameters for heterogeneous domain, $\boldsymbol{u}^0$ is a homogenized solution, ω_k stands for a union of a finite element and a domain with continuous material properties.
4. Compute jumps of tractions at interfaces of finite elements (denoted by J_i^e) and material components (denoted by J_i^m)

   $$J_i^e = t_i^+ - t_i^- \qquad \text{on } \partial\omega_k \qquad i,j = 1,2,3 \tag{5.41}$$

   $$J_i^m = t_i^{m1} - t_i^{m2} \qquad \text{on } \partial\omega_m \subset \omega_k \qquad i,j = 1,2,3 \tag{5.42}$$

   where $\partial\omega_k$ denotes common edge of adjacent elements, $\partial\omega_m$ stands for material (m1, m2) interfaces.
5. Wherever

   $$\eta_R = h||\boldsymbol{R}||_0 + h^{1/2}||\boldsymbol{J}^e||_0 + h^{1/2}||\boldsymbol{J}^m||_0 \tag{5.43}$$

   is large, homogenization should not be used.

A reasoning of this estimation for linear problems may be explained on a simple 1D problem. Let us consider the differential equation for the bar problem (section 3.1)

$$-\frac{\mathrm{d}}{\mathrm{d}x}\left(E\frac{\mathrm{d}u}{\mathrm{d}x}\right) = \frac{q(x)}{A} \tag{5.44}$$

Its residuum for function u_0 has the form

$$r = \frac{\mathrm{d}}{\mathrm{d}x}\left(E\frac{\mathrm{d}u_0}{\mathrm{d}x}\right) + \frac{q(x)}{A} = \frac{\mathrm{d}}{\mathrm{d}x}(Eu_0') + \frac{q(x)}{A} \tag{5.45}$$

The term $E\frac{\mathrm{d}u_0}{\mathrm{d}x}$ may be discontinuous due to a jump of either the first derivative of u_0 at element interfaces or material parameters at material interfaces.

Therefore

$$r = \frac{q(x)}{A} + \begin{cases} Eu_0'' & \text{inside element and material component} \\ \Delta(Eu_0')\,\delta(x-a_j) & \text{on element interfaces} \\ u_0'(a_i)\,\Delta E\,\delta(x-a_i) & \text{on material interfaces} \end{cases} \tag{5.46}$$

where $\Delta E = E_2 - E_1$, δ denotes Dirac delta pseudo-function, $\Delta(Eu_0')$ denotes jump of the term (Eu_0'). Consequently, the residual error indicator is computed using Eq. (5.43).

Selected numerical examples will illustrate the proposed method.

Numerical example – plane strain problem 1

The proposed residual approach was examined on the same L-shaped examples, as in the previous section.

First, example with the L-shaped domain with boundary conditions presented in Fig. 5.10 was considered. Contour map of selected stress component, both for heterogeneous and homogenized material, is shown in Fig. 5.30.

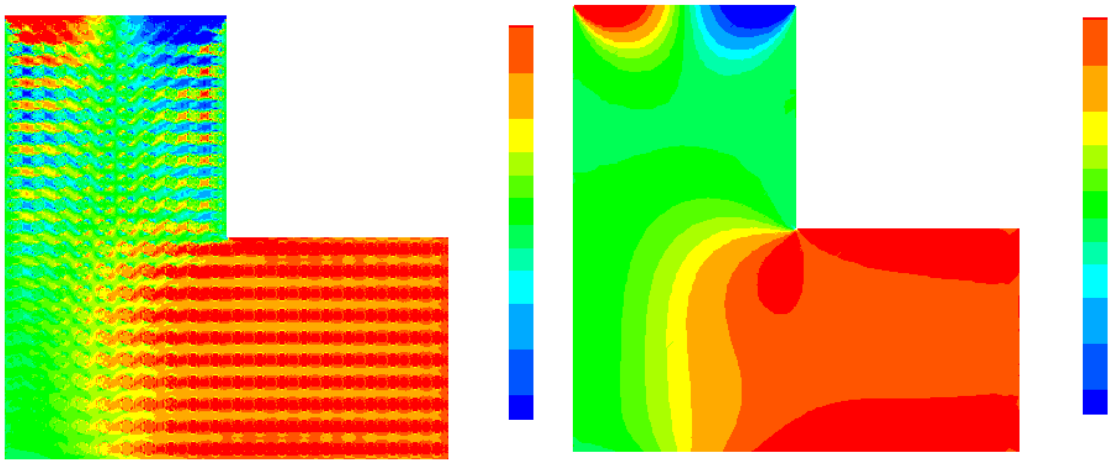

Figure 5.30: L-shaped domain 1. Contour maps of stress component σ_{xx} in truncated range [–50 MPa, 50 MPa] for heterogeneous and homogenized materials.

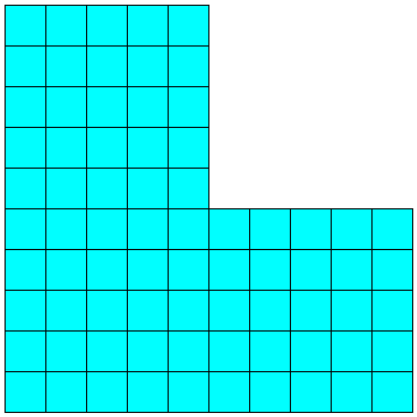

Figure 5.31: L-shaped domain 1. Initial discretization (second order shape functions) for homogenized material.

Error indicator with neglected, for the sake of simplicity, traction jumps at the element interfaces, i.e. $\eta_R = h||\boldsymbol{R}|| + h^{1/2}||\boldsymbol{J}^m||$, was calculated for each element and the admissible error level of 2000 MN/$\sqrt{\text{m}}$ was assumed. Its distribution allowed to localize parts of the domain, where homogenization introduced the largest error (Fig. 5.32). For 5 finite elements η_R exceeded an acceptable limit value, thus in these elements heterogeneous material was considered with new mesh discretization shown in Fig. 5.33. That mesh should account for material heterogeneity in specified region with, as fast as possible, coarsening for the remaining homogenized part.

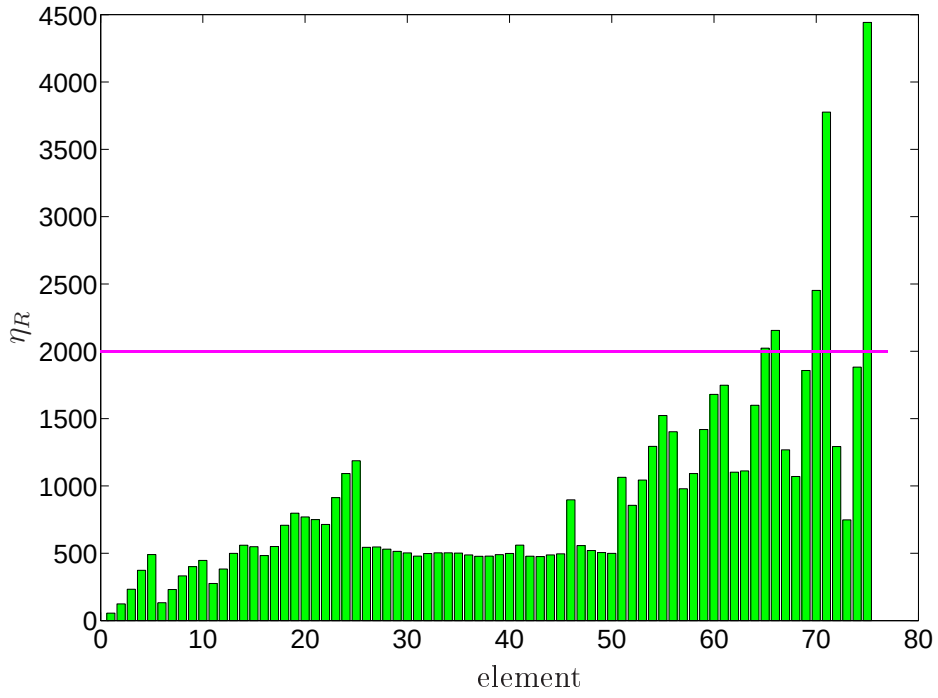

Figure 5.32: L-shaped domain 1. Distribution of error indicator.

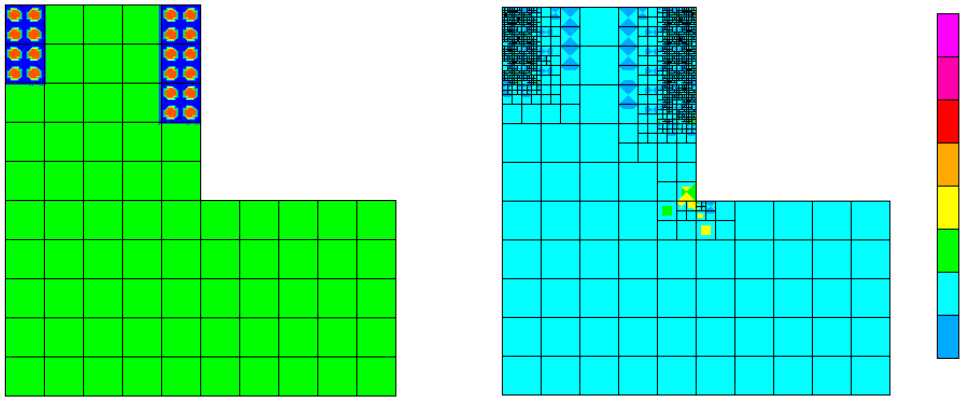

Figure 5.33: L-shaped domain 1. New material distribution. Finite element mesh after 10 *hp*-adaptation steps (colors indicate order of approximation).

The results obtained for homogenized domain and partially heterogeneous body (Fig. 5.33) are compared in Figs. 5.34 – 5.41 along selected segments and in Tab. 5.1. The fully heterogeneous solution was also calculated to verify approximated results. One may observe that partially homogenized solution gave better adjustment to real heterogeneous domain in parts of the body, where the material was considered as heterogeneous.

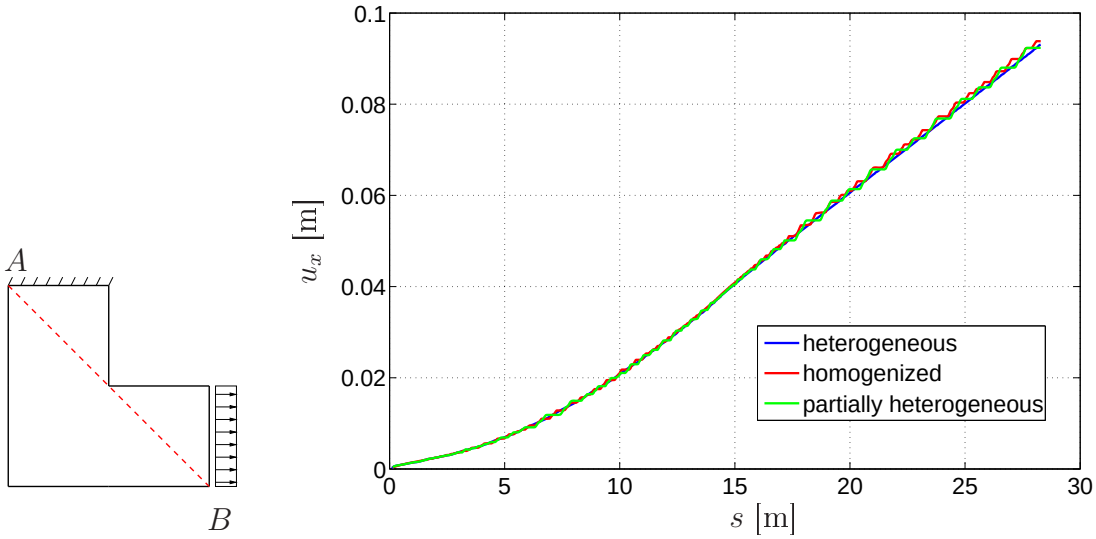

Figure 5.34: L-shaped domain 1. Displacement component u_x along segment AB.

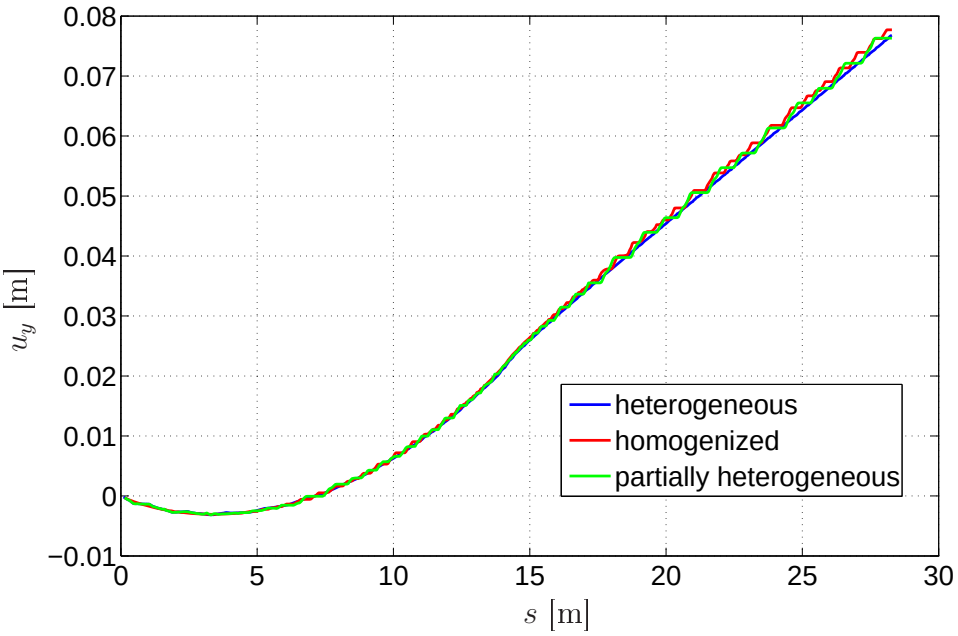

Figure 5.35: L-shaped domain 1. Displacement component u_y along segment AB.

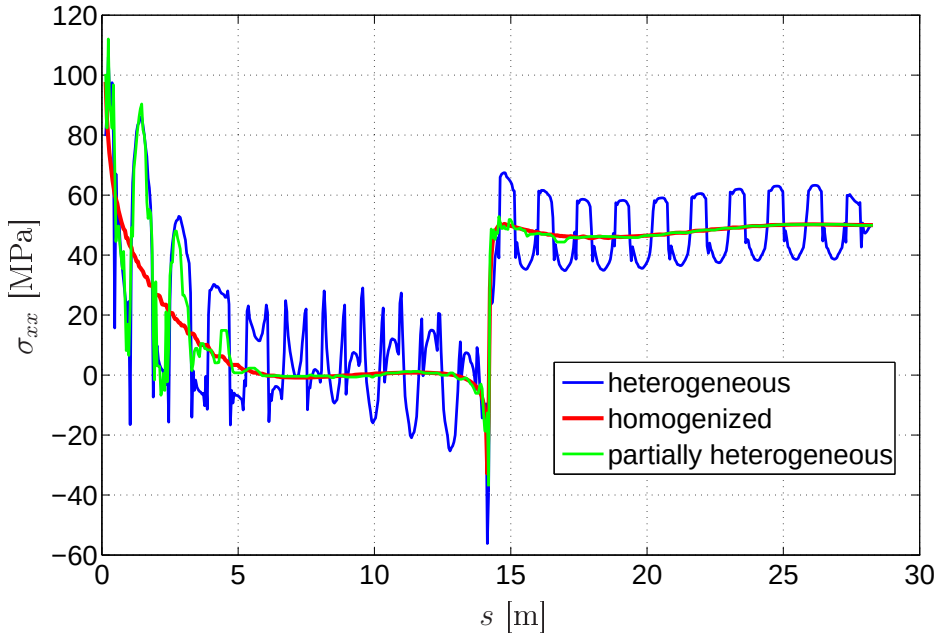

Figure 5.36: L-shaped domain 1. Stress component σ_{xx} along segment AB.

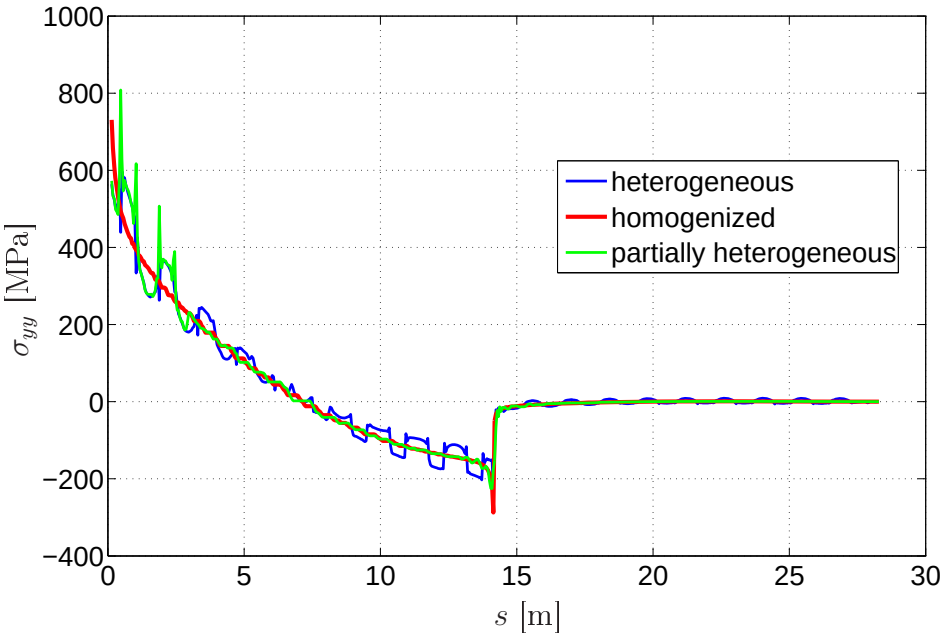

Figure 5.37: L-shaped domain 1. Stress component σ_{yy} along segment AB.

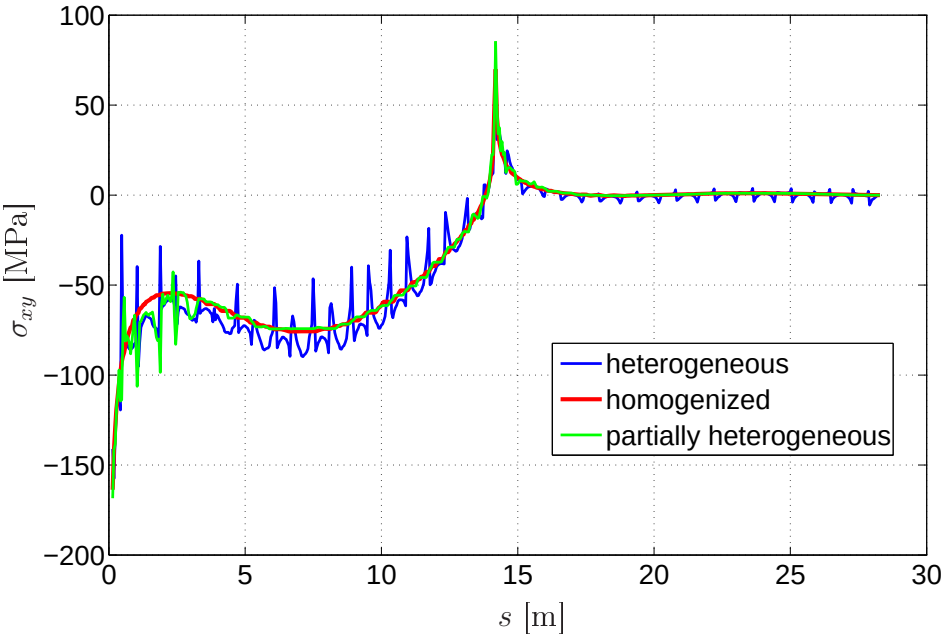

Figure 5.38: L-shaped domain 1. Stress component σ_{xy} along segment AB.

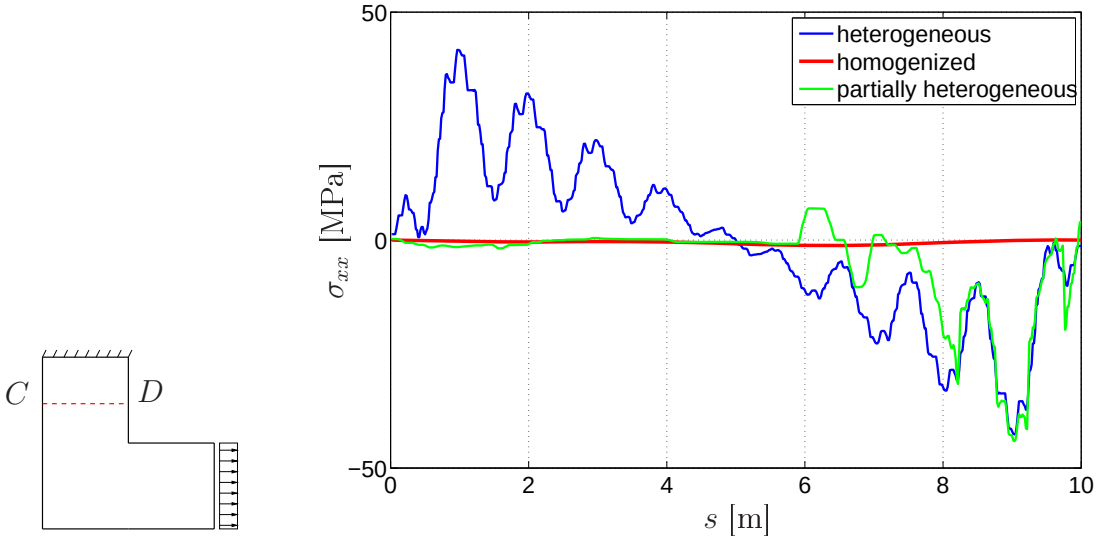

Figure 5.39: L-shaped domain 1. Stress component σ_{xx} along segment CD.

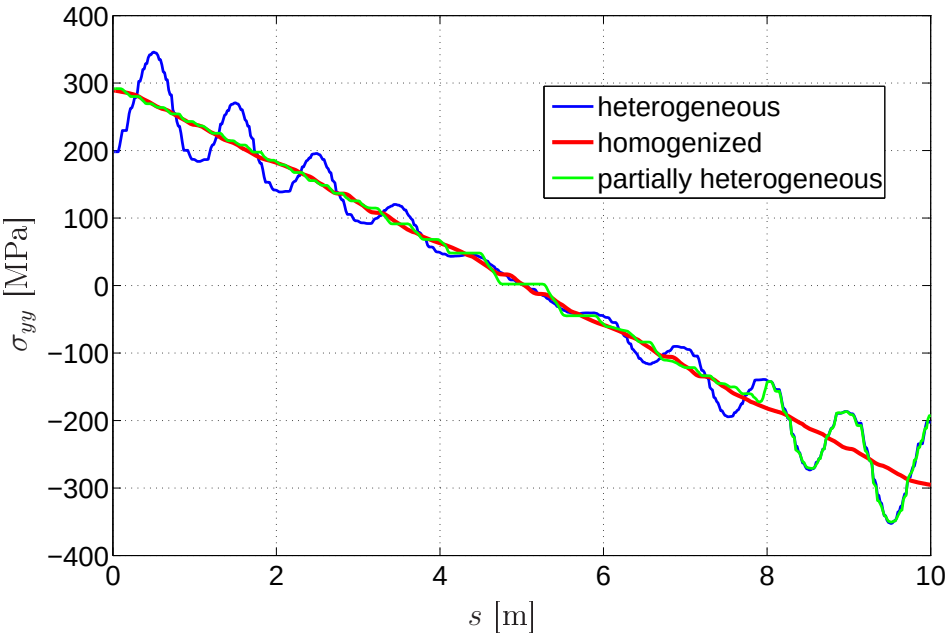

Figure 5.40: L-shaped domain 1. Stress component σ_{yy} along segment CD.

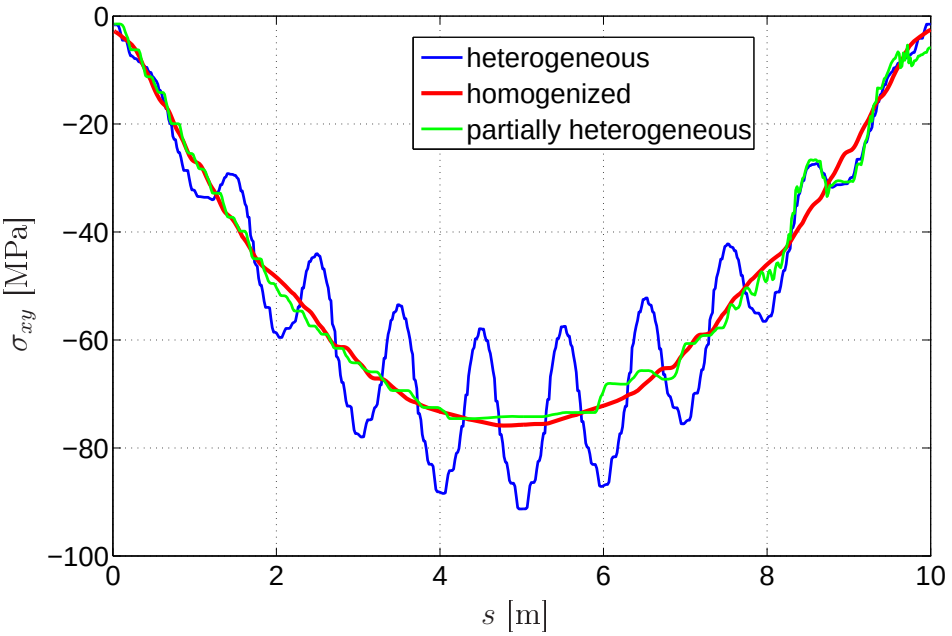

Figure 5.41: L-shaped domain 1. Stress component σ_{xy} along segment CD.

method	formula	homogenization error estimate
homogenization	$\frac{\|\|\boldsymbol{\sigma}^a-\boldsymbol{\sigma}^b\|\|_{0,[C,D]}}{\|\|\boldsymbol{\sigma}^a\|\|_{0,[C,D]}}$	20.4%
partially homogenization	$\frac{\|\|\boldsymbol{\sigma}^a-\boldsymbol{\sigma}^c\|\|_{0,[C,D]}}{\|\|\boldsymbol{\sigma}^a\|\|_{0,[C,D]}}$	16.5%

Table 5.1: L-shaped domain. Estimation of modeling error. $\boldsymbol{\sigma}^a$, $\boldsymbol{\sigma}^b$, $\boldsymbol{\sigma}^c$ denote stress tensors for heterogeneous, homogeneous and partially heterogeneous materials, respectively.

Numerical example – plane strain problem 2

In the next example the L-shaped domain with the boundary conditions, schematically presented in Fig. 5.25, was analyzed. Contour maps of stress component σ_{xx} in the L-shaped domain with heterogeneous and homogenized material are shown in Fig. 5.42. Distribution of error indicator $\eta_R = h||\boldsymbol{R}|| + h^{1/2}||\boldsymbol{J}^m||$ for discretization shown in Fig. 5.31 was calculated (see Fig. 5.43). Similarly, as in the previous example $\boldsymbol{J}^e$, for the sake of simplicity, was neglected. The admissible error level of 2500 $\mathrm{MN}/\sqrt{\mathrm{m}}$, was assumed. For partially heterogeneous domain new mesh discretization was obtained (Fig. 5.44). Solutions for homogenized, partially heterogeneous and fully heterogeneous domain were compared along selected segments. Their comparison is shown in Figs. 5.45 – 5.47. One may notice a good compliance of the true heterogeneous solution with results calculated for partially homogenized domain.

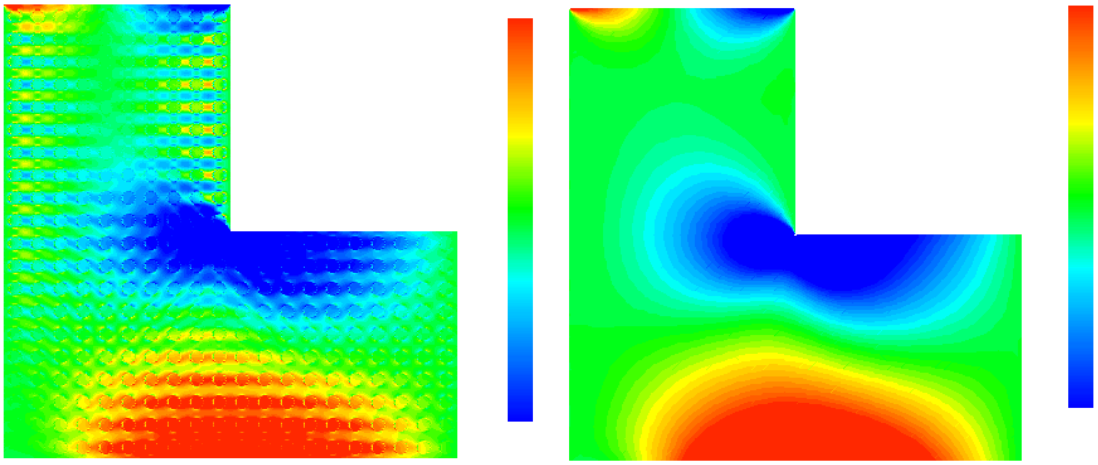

Figure 5.42: L-shaped domain 2. Contour maps of stress component σ_{xx} in truncated range [–80 MPa, 80 MPa] for heterogeneous and homogenized materials.

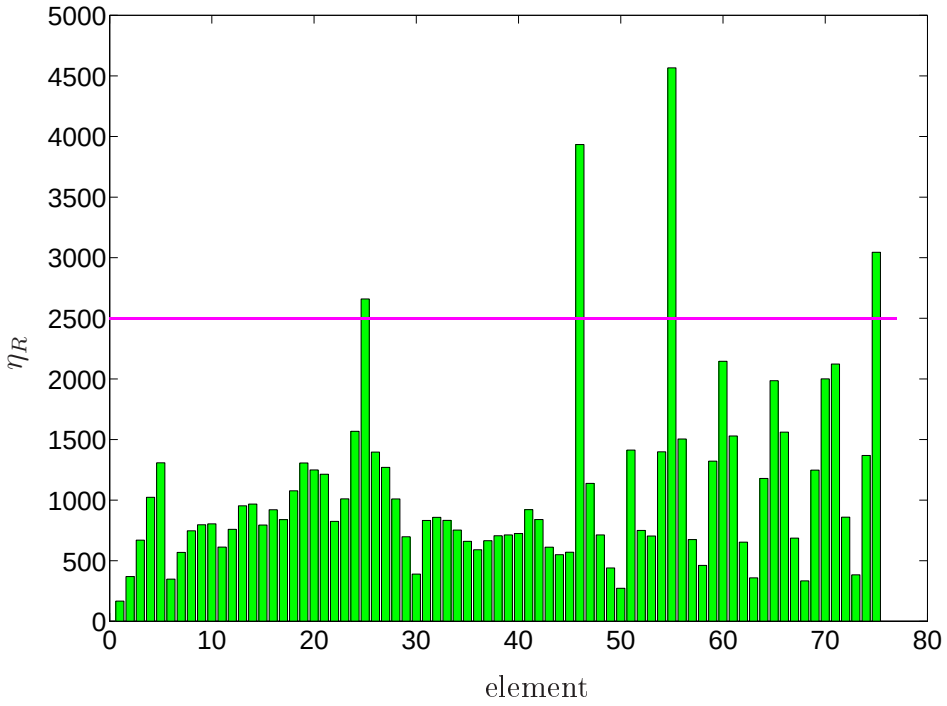

Figure 5.43: L-shaped domain 2. Distribution of error indicator for each element.

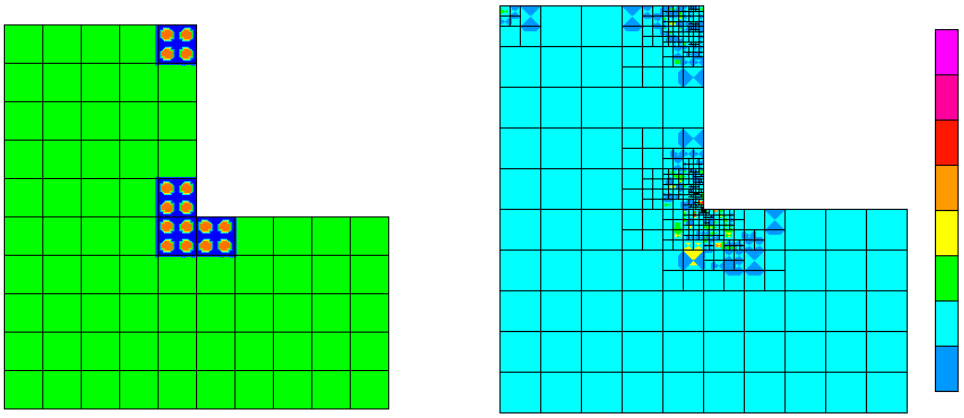

Figure 5.44: L-shaped domain 2. Assumed material distribution and finite element mesh after 10 *hp*-adaptation steps (colors indicate order of approximation).

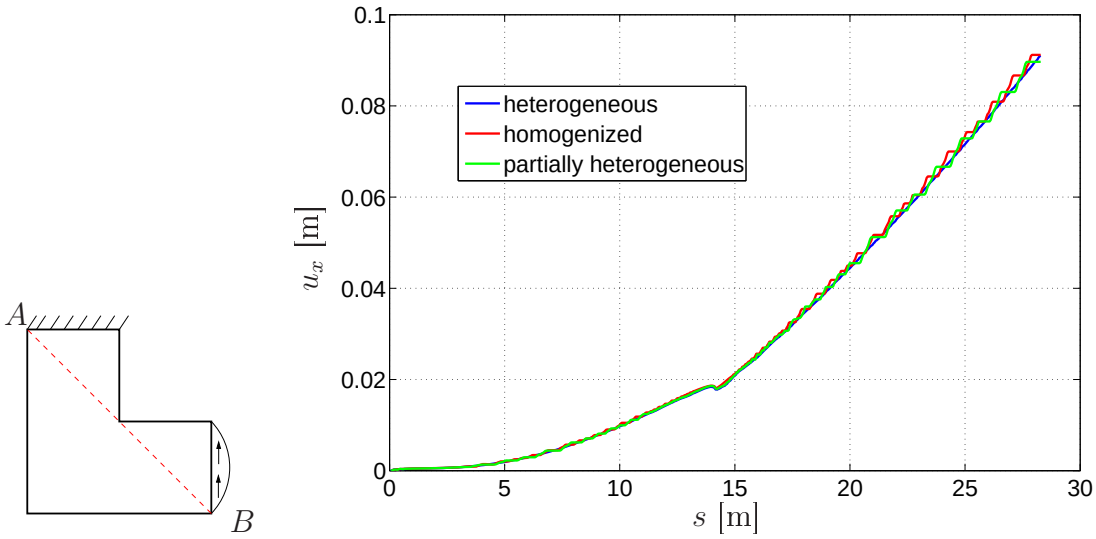

Figure 5.45: L-shaped domain 2. Displacement component u_x along segment AB.

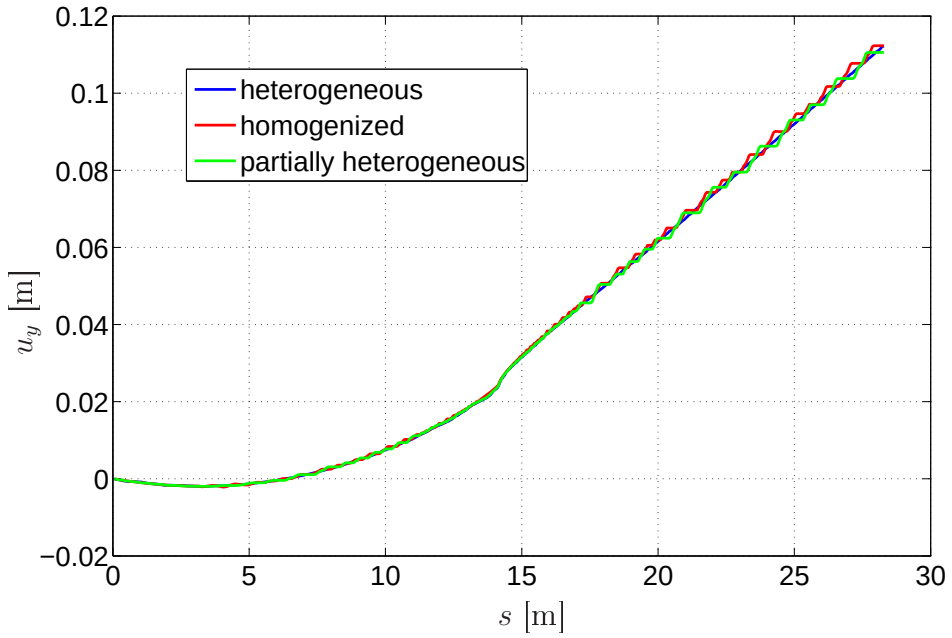

Figure 5.46: L-shaped domain 2. Displacement component u_y along segment AB.

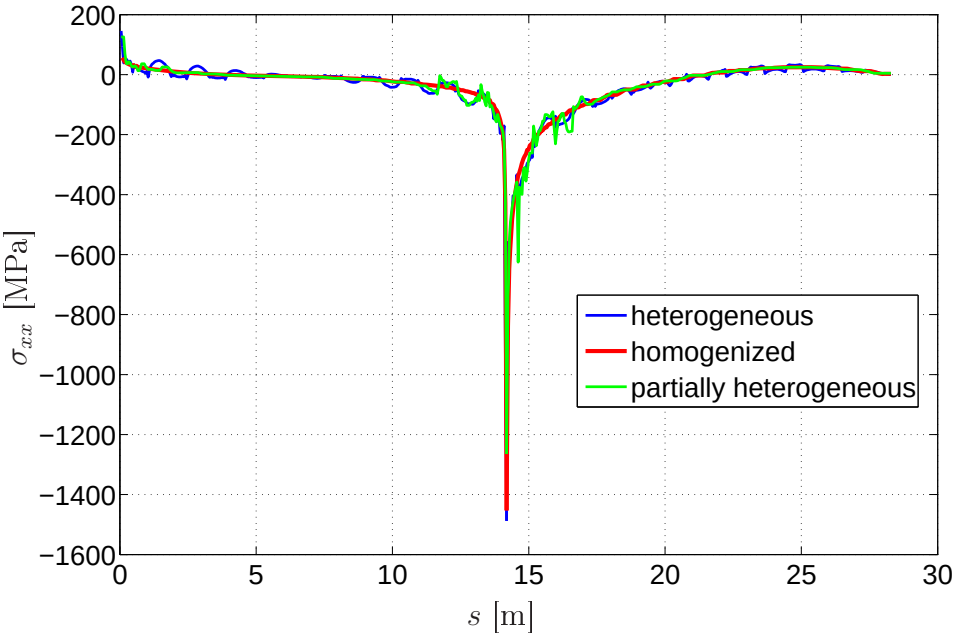

Figure 5.47: L-shaped domain 2. Stress component σ_{xx} along segment AB.

Numerical example – L-shaped domain in 3D

Computations were also performed in 3D for the composite with periodic microstructure (matrix reinforced with ball-like inclusions) in elastic range (material parameters are presented in Tab. 4.1). The considered problem is schematically presented in Fig. 5.48. One wall, denoted by black color, was clamped. The model was loaded tangentially in y direction. The homogeneous Neumann boundary conditions were assumed on the other parts of the boundary.

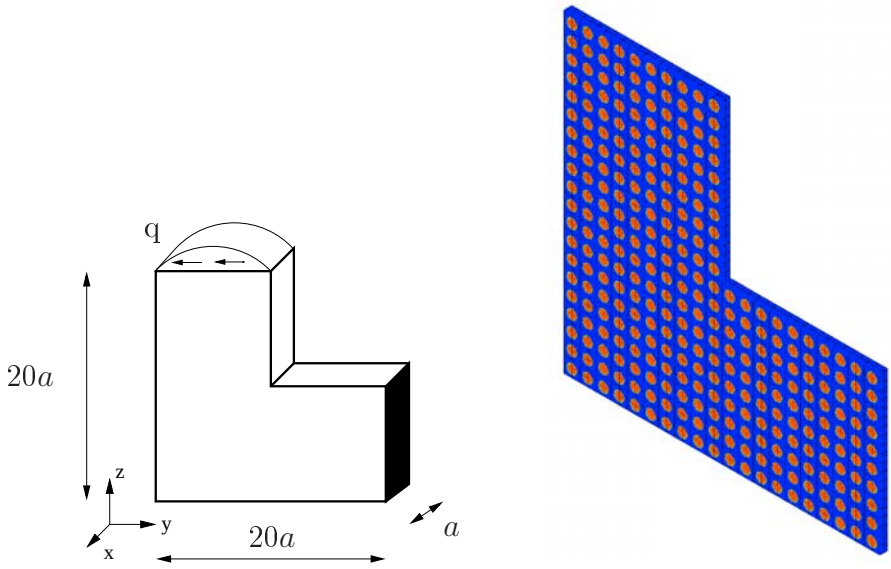

Figure 5.48: L-shaped domain 3. Boundary conditions and a cross section.

Similarly, as for the 2D problems, the following three cases were considered:

1. the full heterogeneous domain with ball-like inclusions regularly distributed in the volume (analyzed by brute force method to obtain a reference solution)
2. homogenized domain with effective material parameters obtained during RVE analysis
3. partially heterogeneous domain after error estimation.

1. Computations for heterogeneous domain

The model was discretized by brick elements with second order shape functions (Fig. 5.49).

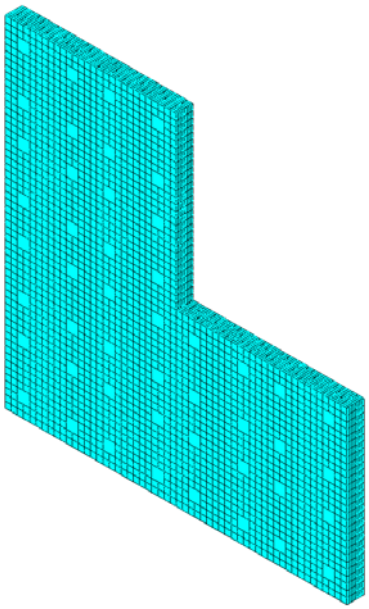

Figure 5.49: L-shaped domain 3. FE discretization (second order shape functions).

Contour maps of the solution u_y and stress component σ_{yy} are shown in Figs. 5.50 and 5.51, respectively. The maximum value of stress σ_{yy} is about 800 MPa (near the point of singularity), minimal value is approximately equal to –550 MPa.

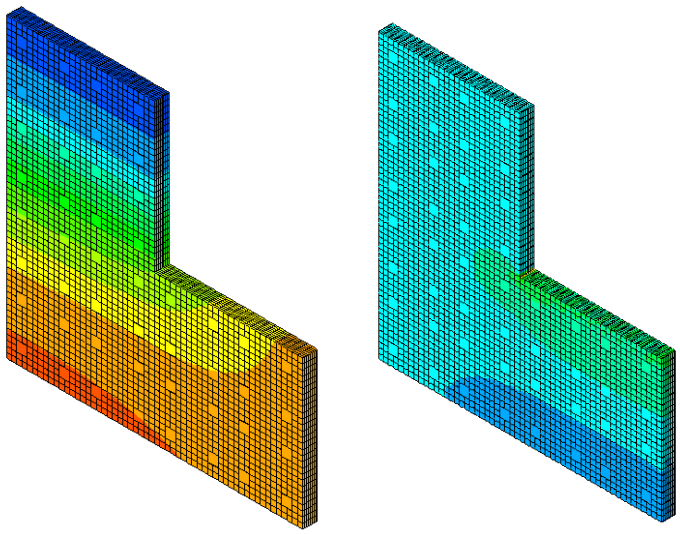

Figure 5.50: L-shaped domain 3. Contour maps of solution component u_y and stress component σ_{yy}.

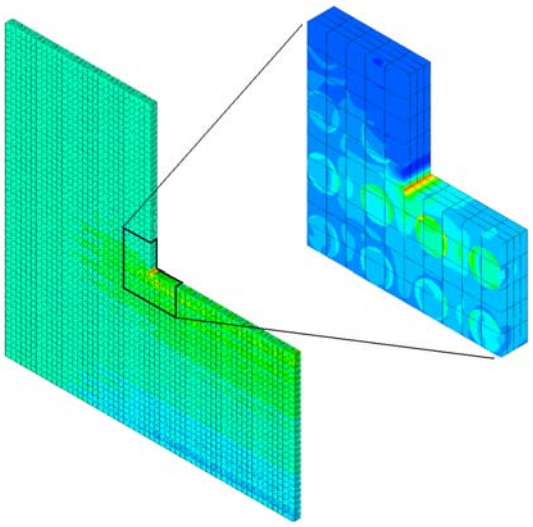

Figure 5.51: L-shaped domain 3. Contour map of stress component σ_{yy} in cross section and in selected subdomain.

2. Computations for homogenized domain

In the next step computations were carried out for the homogenized material. Effective material parameters were obtained by numerical simulations of tensile test performed on RVE in the micro-scale (described in chapter 4). Finite element mesh was obtained in the process of automatic *hp*-adaptation (Fig. 5.52). Contour map of the stress component σ_{yy} is shown in Fig. 5.53.

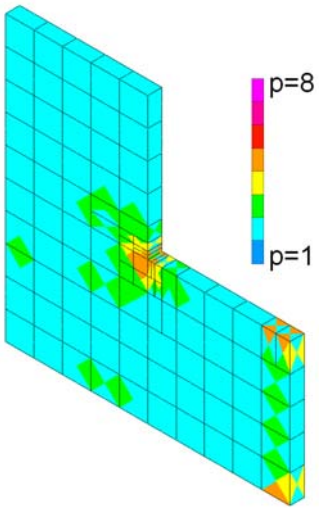

Figure 5.52: L-shaped domain 3. Discretization.

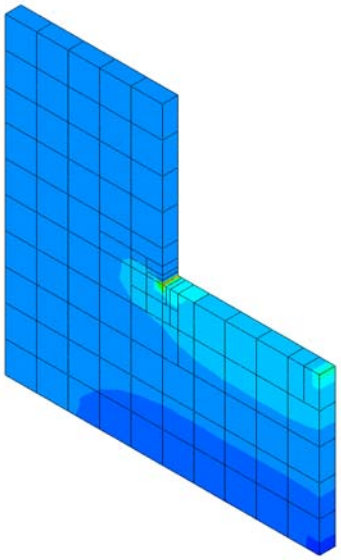

Figure 5.53: L-shaped domain 3. Contour map of stress component $\sigma_{yy} \in [-300 \text{ MPa}, 1200 \text{ MPa}]$.

3. Computations for partially heterogeneous domain

In order to estimate the modeling error, residuum of the equilibrium equation fulfillment was calculated using formula (5.40) (no jumps of tractions were taken into account). Its distribution allowed to localize parts of the domain, where the solution was the most inaccurate. Two cases with different limit value of accepted residuum, were considered. Initial mesh for homogenized domain that was used for residuum estimation, is shown in Fig. 5.54. Two cases of further analysis are presented below.

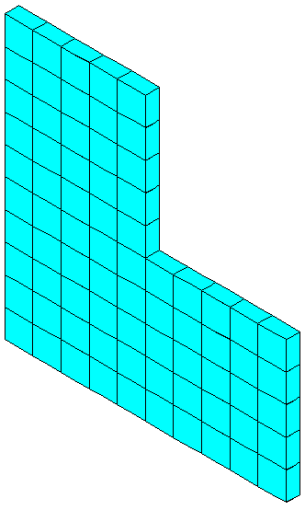

Figure 5.54: L-shaped domain 3. Discretization (second order shape functions).

CASE I

After calculating the error indicator of each element, shown in Fig. 5.55, the admissible residuum level, which equals 10 MN/$\sqrt{\text{m}}$, was assumed. For the 5 finite elements residuum exceeded an acceptable limit value. Thus, in these subdomains heterogeneous material was assumed with new mesh discretization shown in Fig. 5.56. The corresponding contour maps of stress tensor component σ_{yy} are shown in Figs. 5.57 and 5.58.

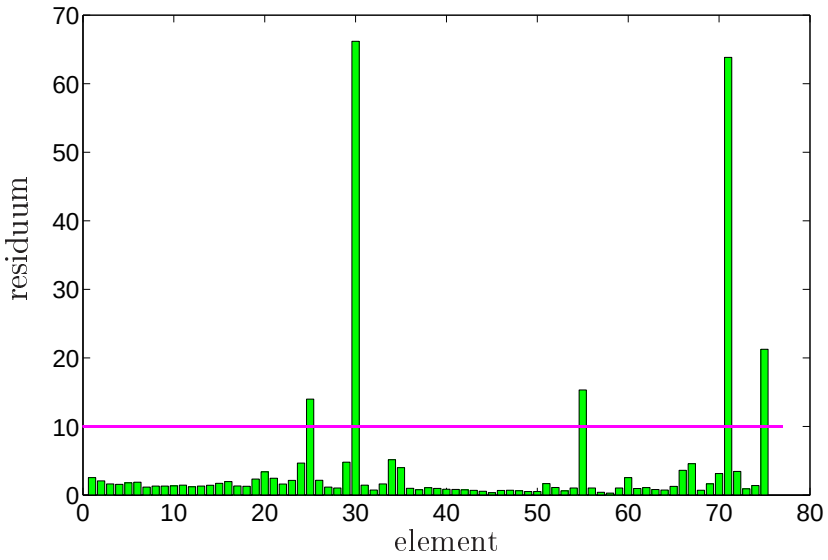

Figure 5.55: L-shaped domain 3. Residuum of each element.

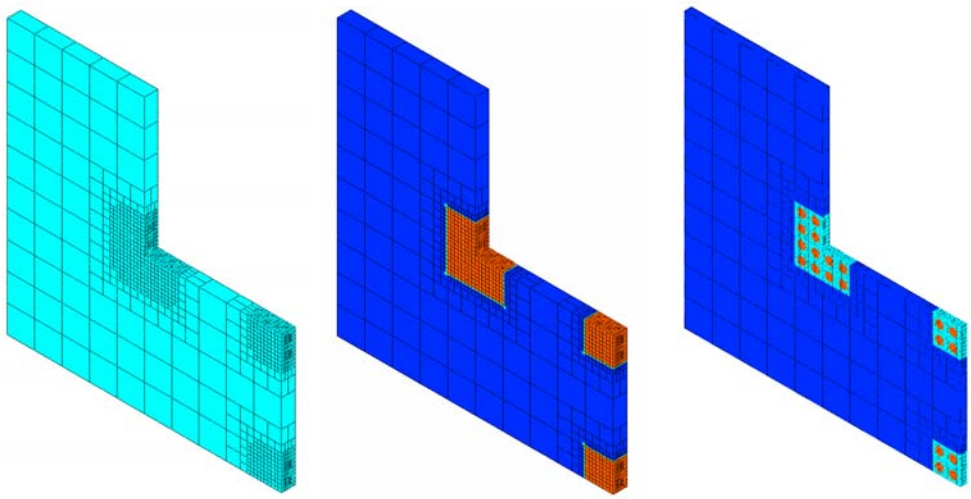

Figure 5.56: L-shaped domain 3. Finite element mesh after h-adaptation. Material distribution in domain and its cross section.

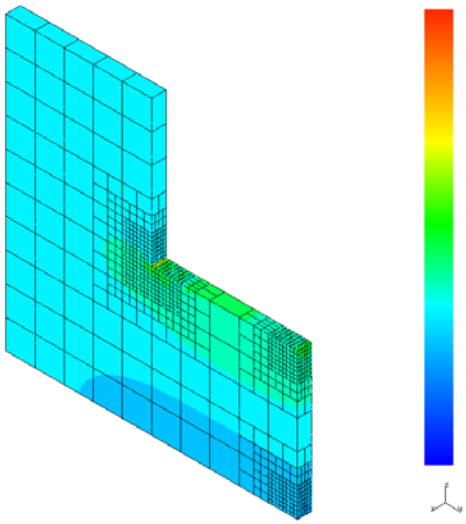

Figure 5.57: L-shaped domain 3. Contour map of stress component $\sigma_{yy} \in$ [–500 MPa, 1000 MPa].

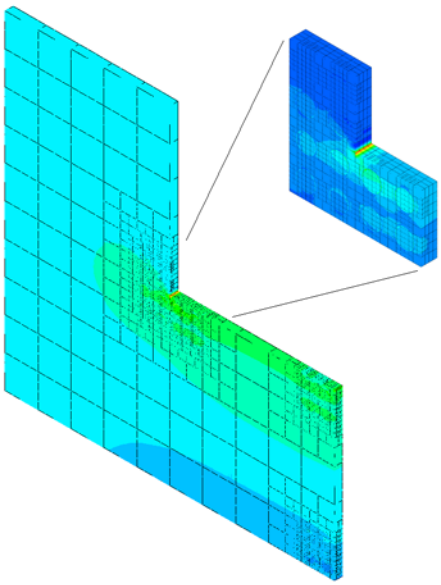

Figure 5.58: L-shaped domain 3. Contour maps of stress component σ_{yy} in cross section and in selected subdomain.

CASE II

In the second case admissible residuum level equal 4 MN/$\sqrt{\text{m}}$ was assumed (Fig. 5.59). Consequently, residuum exceeded the limit value for 9 finite elements and in these subdomains the exact microstructure was assumed. The resulting partially heterogeneous domain and finite element discretization are presented in Fig. 5.60. Contour map of stress component σ_{yy} is shown in Fig. 5.61.

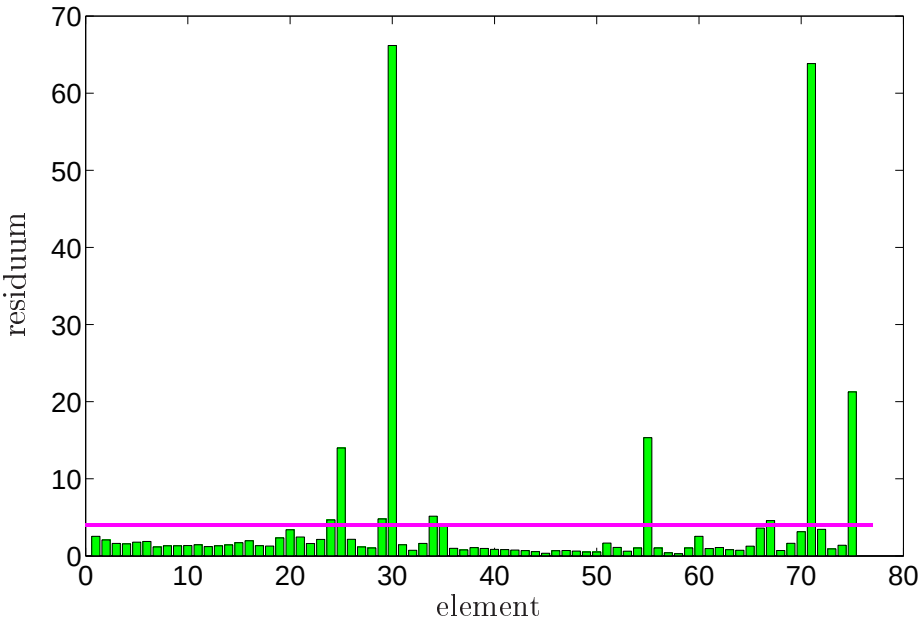

Figure 5.59: L-shaped domain 3. Residuum of each element.

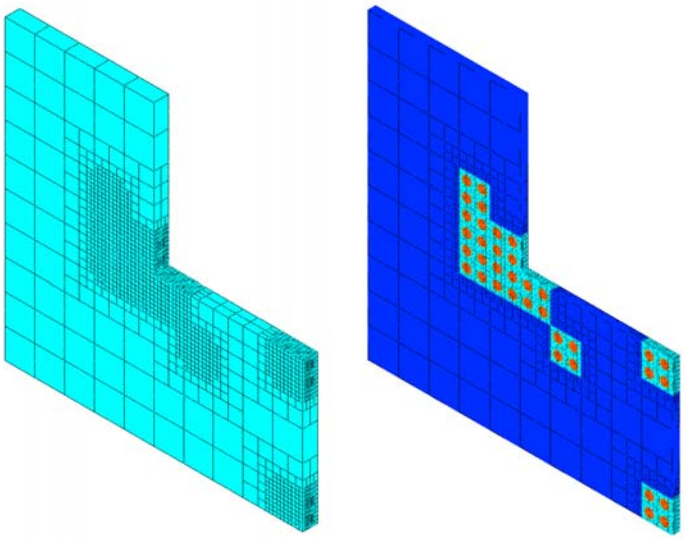

Figure 5.60: L-shaped domain 3. Finite element mesh after h-adaptation. Material distribution.

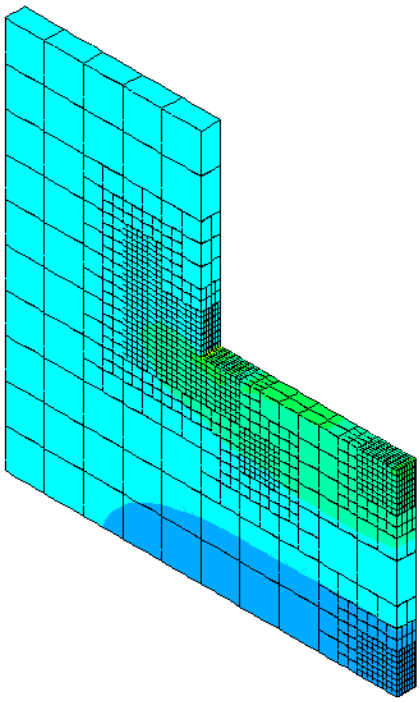

Figure 5.61: L-shaped domain 3. Contour map of stress component $\sigma_{yy} \in [-450 \text{ MPa}, 960 \text{ MPa}]$.

The results obtained by discussed approaches for one component of the stress tensor along the selected segment AB are compared in Fig. 5.62. Modeling error estimation for various cases of this example is summarized in Tab. 5.2.

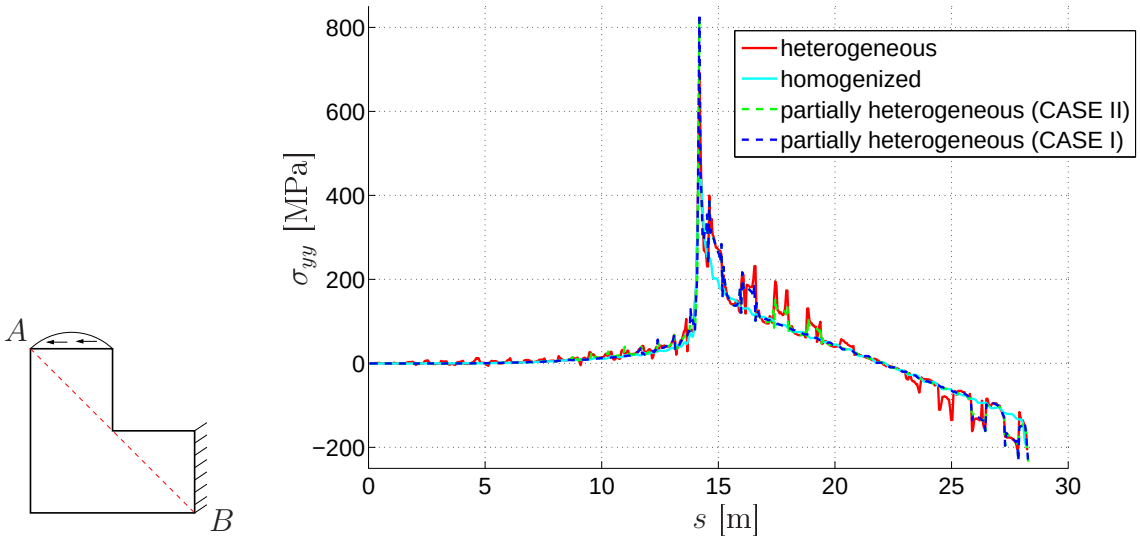

Figure 5.62: L-shaped domain 3. Stress component σ_{yy} along segment AB.

method	formula	homogenization error estimate
homogenization	$\frac{\|\|\sigma^a_{yy}-\sigma^b_{yy}\|\|_{0,[A,B]}}{\|\|\sigma^a_{yy}\|\|_{0,[A,B]}}$	27.6%
partially homogenization (CASE I)	$\frac{\|\|\sigma^a_{yy}-\sigma^c_{yy}\|\|_{0,[A,B]}}{\|\|\sigma^a_{yy}\|\|_{0,[A,B]}}$	19.8%
partially homogenization (CASE II)	$\frac{\|\|\sigma^a_{yy}-\sigma^c_{yy}\|\|_{0,[A,B]}}{\|\|\sigma^a_{yy}\|\|_{0,[A,B]}}$	18.1%

Table 5.2: L-shaped domain. Estimation of modeling error. σ^a_{yy}, σ^b_{yy}, σ^c_{yy} denote stress component σ_{yy} for heterogeneous, homogeneous and partially heterogeneous materials, respectively.

Numerical example – cantilever beam with extra layers

In the next test a cantilever beam with extra layers, presented in Fig. 5.63, was analyzed as a 3D body. Metal matrix was reinforced by ball-like metallic inclusions, distributed periodically (material parameters assumed for this composite are presented in Tab. 4.1). The layers were made of homogeneous, weaker than the other components material.

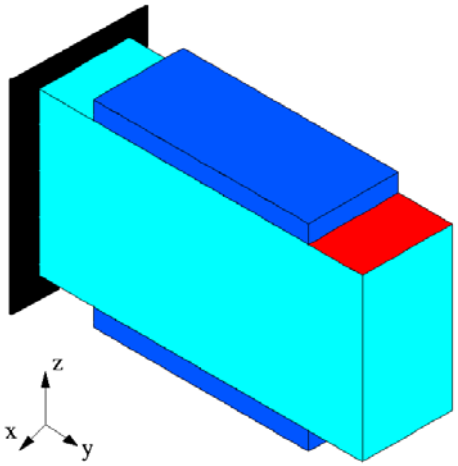

Figure 5.63: Cantilever beam. Boundary conditions (black – fixed face, red – vertical downward loading of 80 kN/m^2, other faces - zero loading).

1. Computations for heterogeneous domain

Fig. 5.64 illustrates heterogeneous domain and finite element discretization. Computed displacement component u_z and the stress component σ_{yy} are shown in Figs. 5.65 and 5.66.

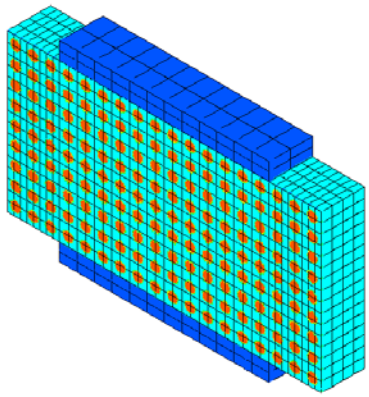

Figure 5.64: Cantilever beam. Material distribution.

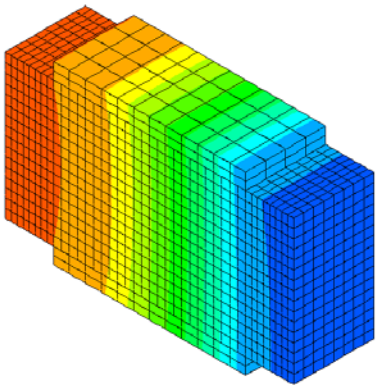

Figure 5.65: Cantilever beam. Displacement component u_z (qualitative result).

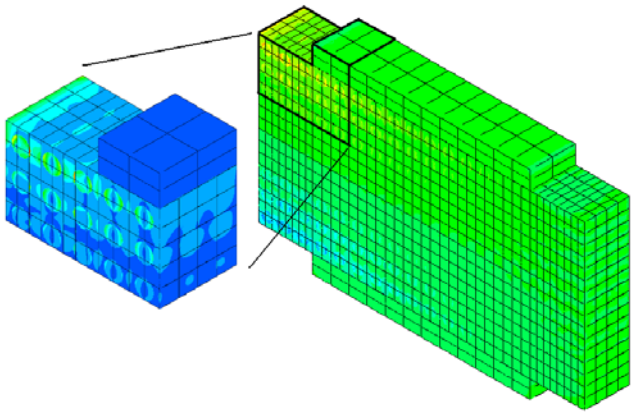

Figure 5.66: Cantilever beam. Contour map of stress component $\sigma_{yy} \in [-918 \text{ MPa}, 918 \text{ MPa}]$ in cross section and in selected subdomain.

2. Computations for homogenized domain

Finite element discretization for homogenized domain is shown in Fig. 5.67. Computed stress component σ_{yy} is presented in Fig. 5.68.

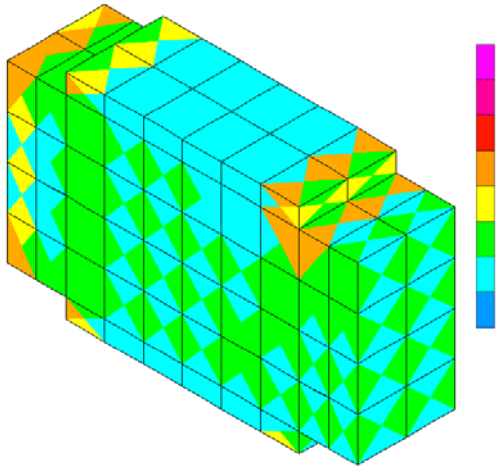

Figure 5.67: Cantilever beam. Discretization.

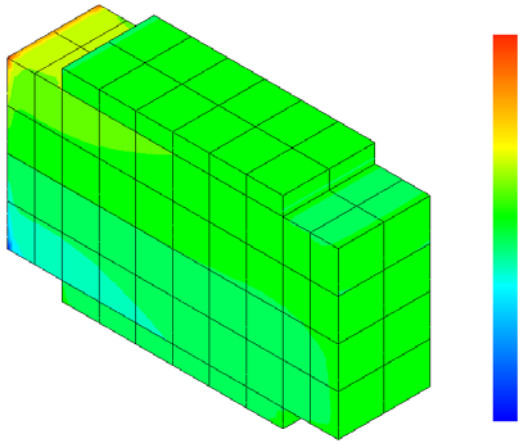

Figure 5.68: Cantilever beam. Contour map of stress component $\sigma_{yy} \in$ [–870 MPa, 870 MPa].

3. Computations for partially heterogeneous domain

The initial discretization for homogenized material is shown in Fig. 5.69. After solution of homogenized problem the residuum (5.40) was estimated for each finite element (no jumps of tractions were considered). Its distribution is shown in Fig. 5.70. In the elements, where residuum reached value 4 MN/$\sqrt{\text{m}}$ and more it was assumed that the homogenization would introduce too high error.

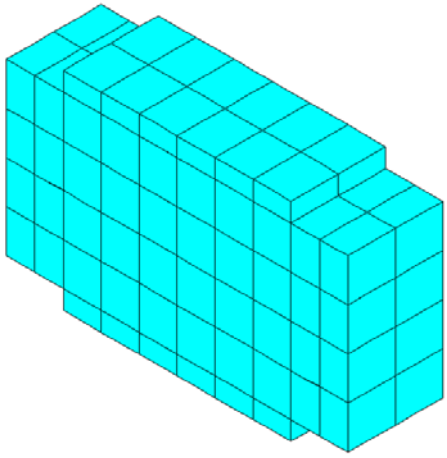

Figure 5.69: Cantilever beam. Discretization of a model.

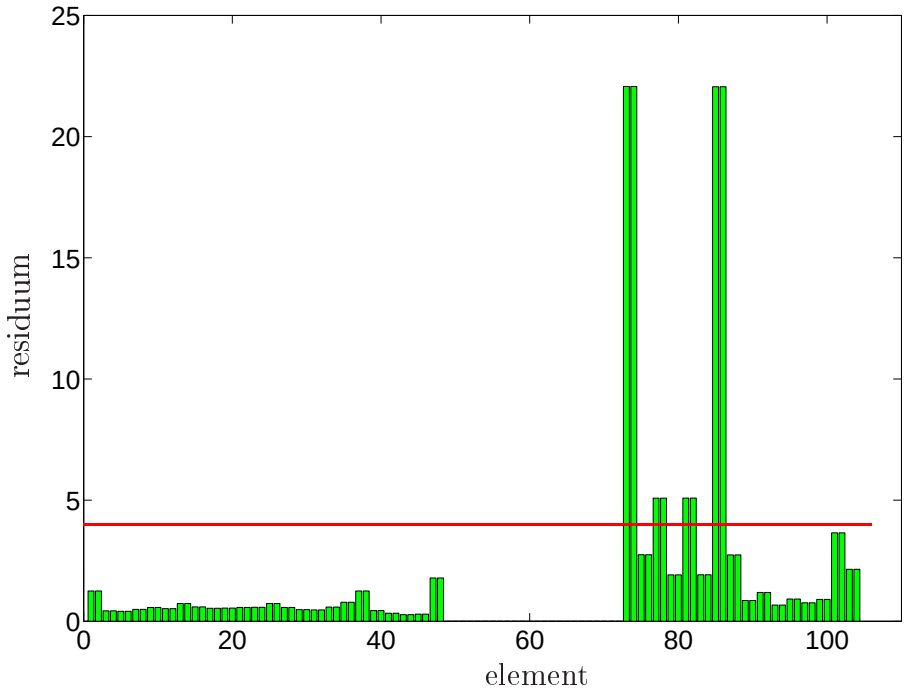

Figure 5.70: Cantilever beam. Distribution of residuum in finite elements.

Part of the domain (8 elements), where the material should have been modeled as heterogeneous one, was selected and new discretization was assumed (Fig. 5.71). For component of stress tensor σ_{yy} (Fig. 5.72) extreme values are similar to results obtained for fully homogenized domain (see Fig. 5.68).

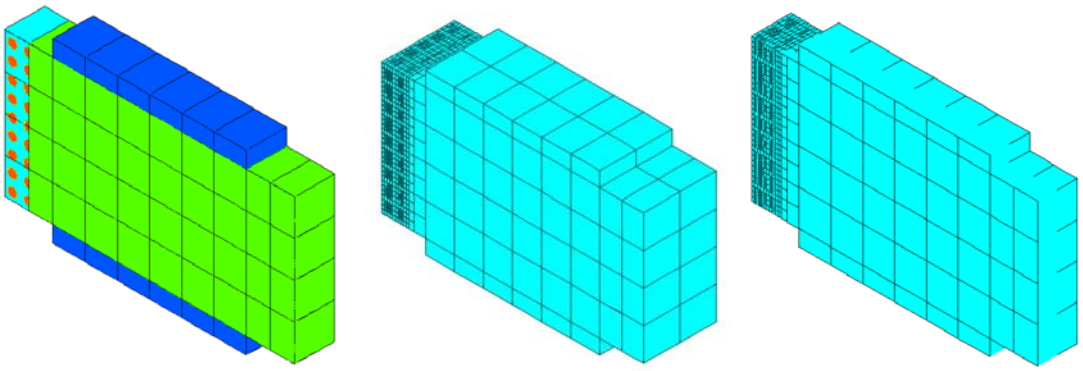

Figure 5.71: Cantilever beam. Material distribution in the cross section. h-adaptive refinement of the domain and its cross section.

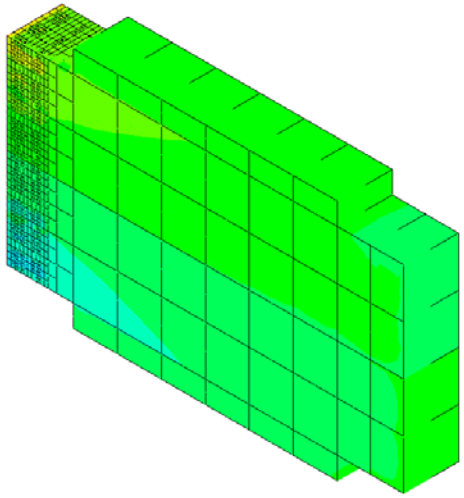

Figure 5.72: Cantilever beam. Contour map of stress component $\sigma_{yy} \in$ [–962 MPa, 962 MPa] in cross section.

Comparison of stress component σ_{yy} along selected segment EF obtained in different ways is shown in Fig. 5.73 and in Tab. 5.3. It may be concluded that computations based on homogenization approach are slightly overestimated, so they are on the safe side and require much less computational time than the direct approach.

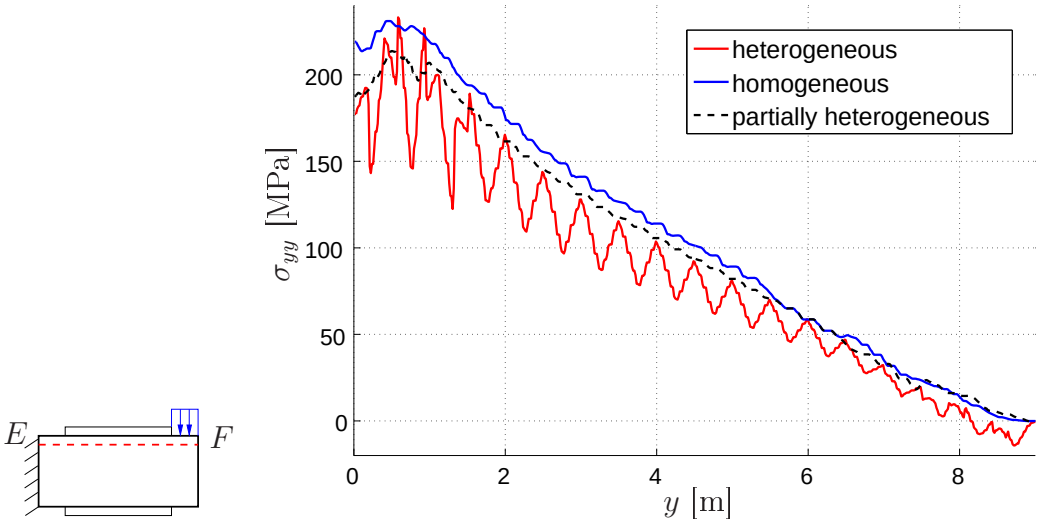

Figure 5.73: Cantilever beam. Component of stress tensor σ_{yy} along segment EF.

method	formula	homogenization error estimate
homogenization	$\frac{\|\|\sigma^a_{yy}-\sigma^b_{yy}\|\|_{0,[E,F]}}{\|\|\sigma^a_{yy}\|\|_{0,[E,F]}}$	25.5 %
partially homogenization	$\frac{\|\|\sigma^a_{yy}-\sigma^c_{yy}\|\|_{0,[E,F]}}{\|\|\sigma^a_{yy}\|\|_{0,[E,F]}}$	18.0 %

Table 5.3: Cantilever beam. Estimation of modeling error. σ^a_{yy}, σ^b_{yy}, σ^c_{yy} denote stress component σ_{yy} for heterogeneous, homogeneous and partially heterogeneous materials, respectively.

One may observe in this case improvement of solution accuracy in a larger domain than the area, where heterogeneous material was assumed, even though the solution in this area is still inaccurate. The residual modeling error estimate gave reasonable results, even though not all terms of Eq. 5.43 were used.

Chapter 6

Automatic *hp* adaptation for inelastic problems

It was already mentioned that the automatic *hp* mesh adaptation, developed by Demkowicz and coworkers [26, 27, 29, 102], was successfully used for various linear problems. In this section convergence of *hp* adaptation strategy for elastic-plastic problems is examined and some modifications of the algorithm are proposed.

Applications of the adaptive meshing in plasticity were initiated in the eighties. Cheng [20], as well as Zienkiewicz and coworkers [111], developed this approach to metal forming processes. Peric, Dutko and Owen [81, 82] presented adaptive FEM solutions for large strain plasticity, Cramer et al. [24] applied partitioning of elements to associative and non-associative plasticity. The *p*-adaptive FEM was reported to be efficient approximation to physically nonlinear problems by Düster and Rank [30]. The *rp*-adaptive approach was used by Nübel and coworkers [73] to adjust finite element mesh to elastic-plastic border in order to take into account the loss of regularity.

According to reported in literature experience [11, 19, 37, 83], inelastic deformations should be accounted for in a special way in a-posteriori error estimates in order to obtain appropriate stress approximation accuracy. In this section modification of *hp*-mesh refinement by additional *h*-refinement along the elastic-plastic interface, which is a place of lower solution regularity, is studied.

In all the examples described in this work loading was applied in one step. Therefore, there was no need for solution transfer. However, if more steps were used the solution transfer might be comparatively easily performed since the mesh is refined by subdivision of the elements [109].

6.1 1D numerical examples

First 1D numerical tests were performed for the following problem modeling a homogeneous bar subject to axial body force: *find displacement* $u(x,t) \in C^0(0,1)$ *(piecewise* C^2*), total strain* $\varepsilon(x,t)$*, stress* $\sigma(x,t)$*, plastic multiplier* $\gamma(x,t)$ *(*$\gamma(x,t) = 0$ in ω_e*) and*

inelastic strain $\varepsilon^p(x,t) \in C^0$, *such that*

$$\begin{cases} \frac{\mathrm{d}\dot{\sigma}}{\mathrm{d}x} = -\dot{q}(x) & \forall x \in \omega_e \text{ or } \omega_p \\ \dot{\sigma} = E\left(\dot{\varepsilon} - \dot{\varepsilon}^p\right) & \forall x \in \omega_e \text{ or } \omega_p \\ \dot{\varepsilon} = \frac{\mathrm{d}\dot{u}}{\mathrm{d}x} & \forall x \in \omega_e \text{ or } \omega_p \\ \dot{\varepsilon}^p = \frac{2}{3}\gamma(\sigma - H\varepsilon^p) & \forall x \in \omega_e \text{ or } \omega_p \\ \gamma \geq 0, \quad \phi \leq 0, \quad \gamma\phi = 0 & \forall x \in \omega_e \text{ or } \omega_p \\ \phi(\sigma) = (\sigma - H\varepsilon^p)^2 - (\sigma^y)^2 & \forall x \in \omega_e \text{ or } \omega_p \\ u(0) = 0 & \\ E\frac{\mathrm{d}u}{\mathrm{d}x}_{|x=L} = 0 & \end{cases} \tag{6.1}$$

supplemented with initial conditions and standard compatibility conditions at elastic-plastic interfaces. The axial loading was assumed as

$$q(x) = -\sin(2\pi x)\, 2\sigma^y \pi$$

Accuracy of integration in semi-time τ depends primarily on accuracy of stress approximation in space, since both plastic multiplier and plastic strain rate are determined by stress rate. It is worth to notice that incremental application of loading reduces number of iterations and prevents numerical solution from coming too far away from the true one.

The following material properties were assumed: Young modulus $E = 200$ GPa, Poisson ratio $\nu = 0.3$, yield stress limit $\sigma^y = 200$ MPa and hardening parameter $H = 0.2\ E$; $L = 1$ m.

Exact solution of this problem is presented in Figs. 6.1 and 6.2 in order to illustrate lower solution regularity at the elastic-plastic interface. Exact displacements and stresses are given by the formulas presented below

$$\begin{cases} u(x) = -\frac{\sigma^y}{E}\left[\left(\sin\frac{2\pi x}{L}\right)\frac{L}{2\pi} - x\right] & \forall x \in [0,\, \frac{L}{4}) \text{ (elastic part)} \\ u(x) = -\frac{\sigma^y L}{2\pi E_T}\sin\frac{2\pi x}{L} + \varepsilon^y x + M & \forall x \in [\frac{L}{4},\, \frac{3L}{4}] \text{ (plastic part)} \\ u(x) = -\frac{\sigma^y L}{2\pi E}\sin\frac{2\pi x}{L} + \varepsilon^y\left(x + \frac{3}{4}L\right) + M + \sigma^y L\left(\frac{-3}{4E} + \frac{E^*}{2\pi}\right) & \forall x \in (\frac{3L}{4},\, L] \text{ (elastic part)} \end{cases} \tag{6.2}$$

$$\sigma = -\sigma^y\left(\cos\frac{2\pi x}{L} - 1\right)$$

where:

$$\varepsilon^y = \frac{\sigma^y}{E}, \qquad E_T = \frac{EH}{E+H}, \qquad E^* = \frac{1}{E_T} - \frac{1}{E}, \quad M = \frac{\sigma^y L}{2\pi}E^*\sin\left(\frac{\pi}{2L}\right)$$

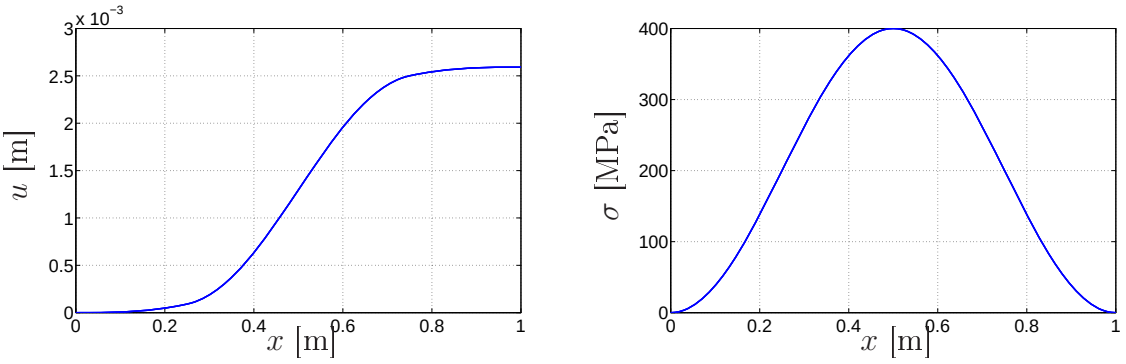

Figure 6.1: 1D example. Exact displacement and stress.

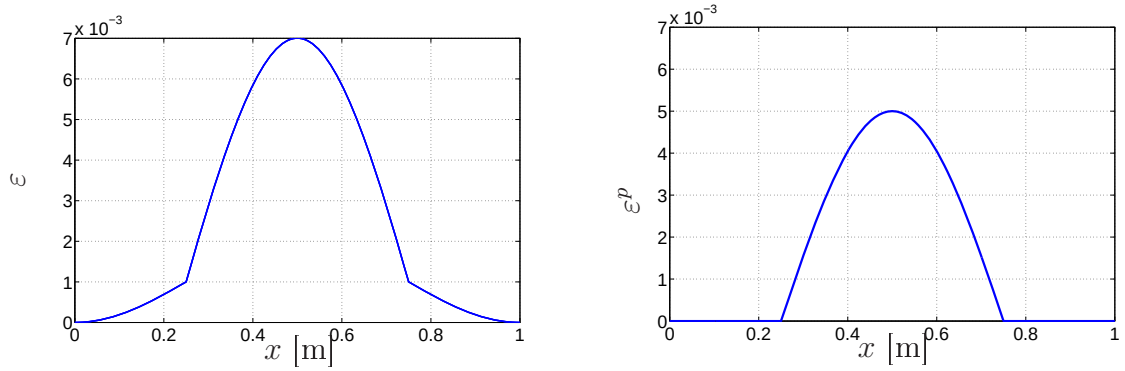

Figure 6.2: 1D example. Exact strain and plastic strain.

First, p-stability for presented example was verified and the results presented in Fig. 6.3 indicate that p-enrichment is reasonable for our problem since it reduces the error. We may observe limit of convergence for p-stability, but it is caused by set of yield condition fulfillment accuracy.

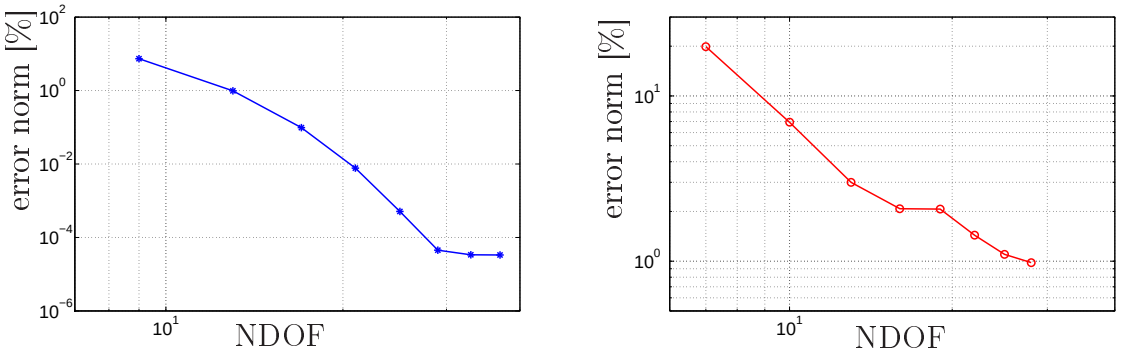

Figure 6.3: First 1D example. p-stability for meshes that initially did or did not comply with elastic-plastic zones.

The main objective of the tests was verification whether the fully automatic *hp*-refinements should be complemented with additional *h*-refinements (or *p*-enrichment) in vicinity of the elastic-plastic zone.

Since the rate of convergence is much better for the meshes that initially comply with the elastic-plastic interface, the numerical analysis with two initial meshes was performed in order to examine the adaptation process for inelastic problems. In the first case the initial finite element mesh complied with a-priori known elastic and plastic zones, while in the second case initial mesh was independent of yielding. In the second case we have observed that after few automatic adaptation steps the mesh accommodated to elastic-plastic interfaces at points $x = 0.25$ and $x = 0.75$ (first 1D example), as may be observed in Fig. 6.4. Convergences of the error norm for various refinement strategies are compared in Figs. 6.5, 6.6. One may observe that in the first case, i.e. with initially detected elastic-plastic interface, the results are better.

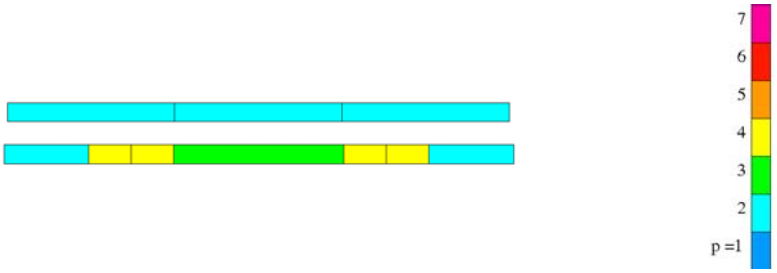

Figure 6.4: First 1D example. Initial and *hp*-refined meshes.

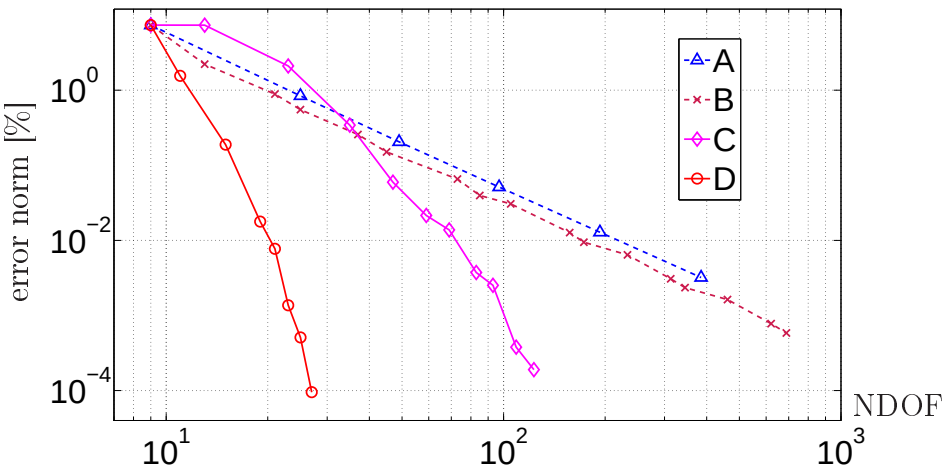

Figure 6.5: First 1D example. Convergence test for the mesh that initially complied with elastic-plastic zone. A – uniform refinement, B – *h*-adaptation, C – automatic *hp*-adaptation with additional *h*-refinements of neighboring elements, D – automatic *hp*-adaptation.

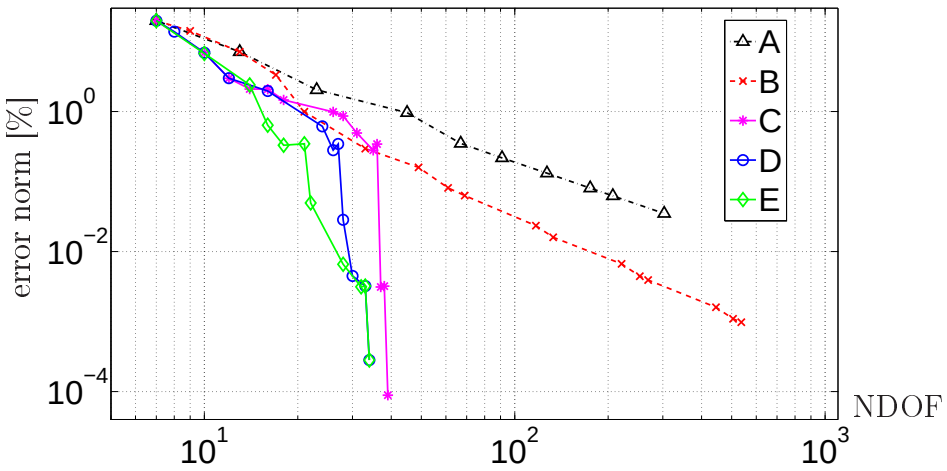

Figure 6.6: First 1D example. Convergence test for the mesh that did not comply with elastic-plastic zone. A – uniform refinement, B – *h*-adaptation, C – automatic *hp*-adaptation with additional *p*-enrichment, D – automatic *hp*-adaptation, E – automatic *hp*-adaptation with additional *h*-refinements.

To make an example more realistic the elastic-plastic interfaces at arbitrary points $x = 0.23456789$ and $x = 0.703703670$ were assumed (second 1D example). Obviously, in this case only meshes that did not comply with elastic-plastic interface were used. The corresponding plastic strain distribution and the resulting mesh refinements are presented in Fig. 6.7. In this example the *p*-stability was also observed (Fig. 6.8) and convergence of error norm for different refinements is presented in Fig. 6.9.

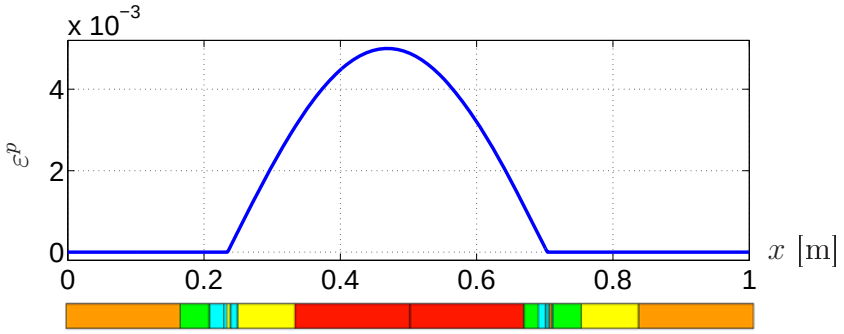

Figure 6.7: Second 1D example. Plastic strain and mesh after few steps of *hp*-adaptation.

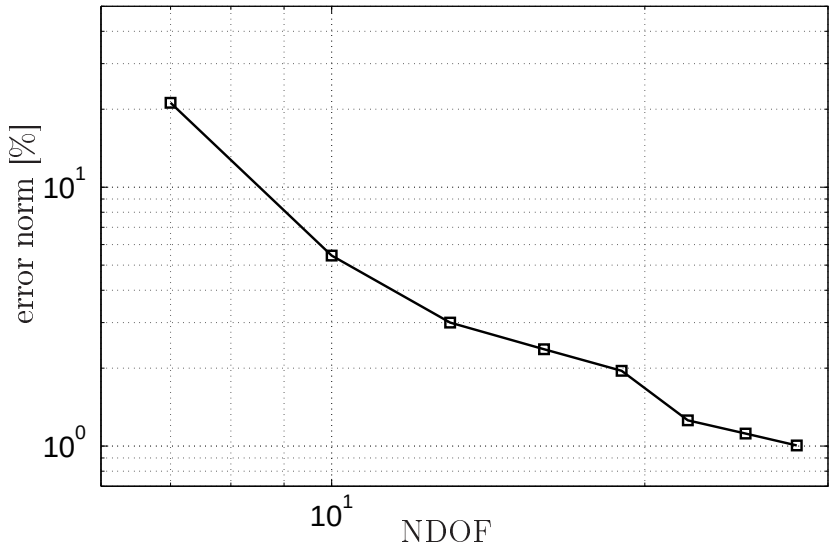

Figure 6.8: Second 1D example. *p*-stability.

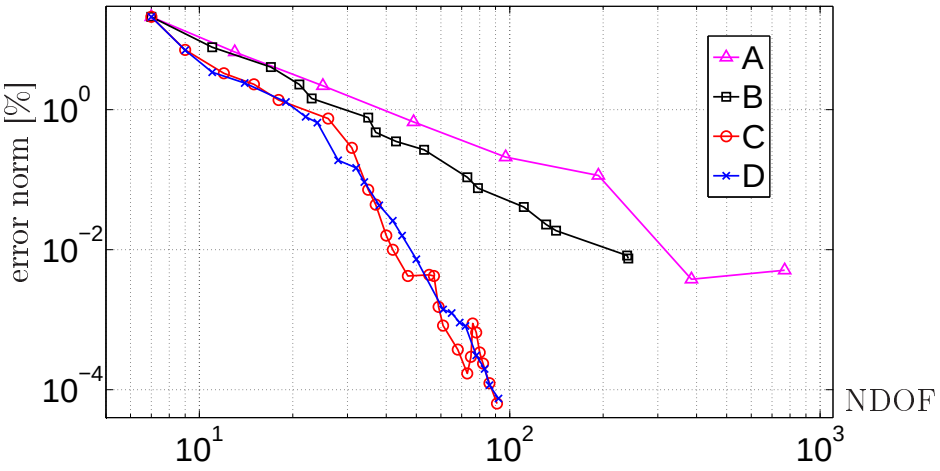

Figure 6.9: Second 1D example. Convergence test for mesh that did not account for elastic-plastic zone. A – uniform refinement, B – *h*-adaptation, C – automatic *hp*-adaptation with additional *h*-refinements, D – automatic *hp*-adaptation.

Since 1D problems may exhibit super convergence properties the further tests were performed for 2D examples.

6.2 2D numerical examples

To verify the proposed modification the computations were performed also in 2D for homogeneous and heterogeneous (RVE) materials. For considered examples the plane strain state was assumed. In 2D examples additional *h*-refinements for elements with both elastic and plastic zones were performed uniformly or in an anisotropic way in order to better fit to the zones.

Let us consider four closest to vertices Gauss integration points. If only at two of those points located near one common edge (marked by the red color in Fig. 6.10) material yields, then the element is partitioned in the direction perpendicular to that common edge, otherwise uniform refinement is performed.

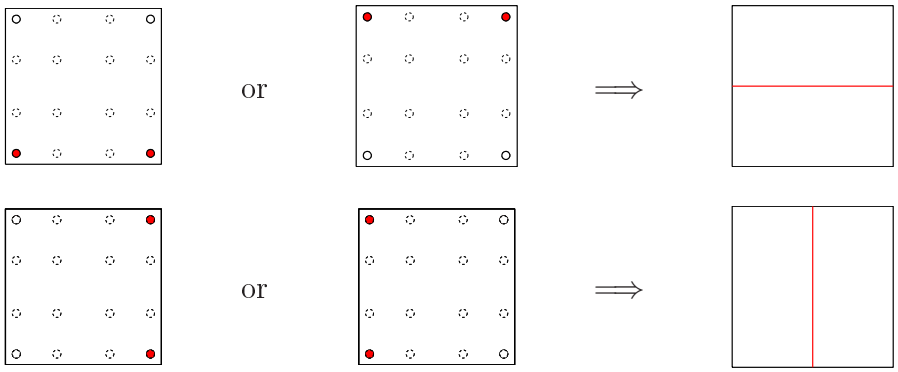

Figure 6.10: Cases of additional anisotropic element refinement.

Homogeneous domain – thick-walled cylinder test

A quarter of a thick-walled cylinder with radii 1 m and 2 m, loaded by internal pressure $p = 120$ MPa that resulted in yielding at points in distance smaller then ~ 1.226 m from the center was analyzed. The following material data were assumed for heterogeneous domain: Young modulus E=200 GPa, Poisson ratio $\nu = 0.3$, yield limit $\sigma^y = 200$ MPa, hardening parameter $H = 0.1E$.

The finite element mesh initially did not comply with the elastic-plastic interface and consisted of 8 second order isoparametric elements (2 in the radial and 4 in the hoop directions). Automatic *hp*-adaptation was performed in the standard way (FE mesh after a few steps of adaptations is shown in Fig. 6.11) and it was compared with some other possible refinements (Fig. 6.14). In one of them *hp*-adaptation was augmented with additional *h*-refinements in the radial direction for elements, which contain points of both elastic and plastic zones (Fig. 6.12). It may be observed that automatic mesh adaptation (Fig. 6.11) gave FE mesh with smaller element concentration near edges. Presumably, this is a consequence of the no penetration symmetry conditions enforcement by penalty function. The proposed modification, based on additional refinements, resulted in better convergence and higher order approximation in the elastic zone. For comparison, finite element mesh, which complies with elastic-plastic interface was assumed (Fig. 6.13) and automatically refined. As one may expect in such a situation the best convergence was observed.

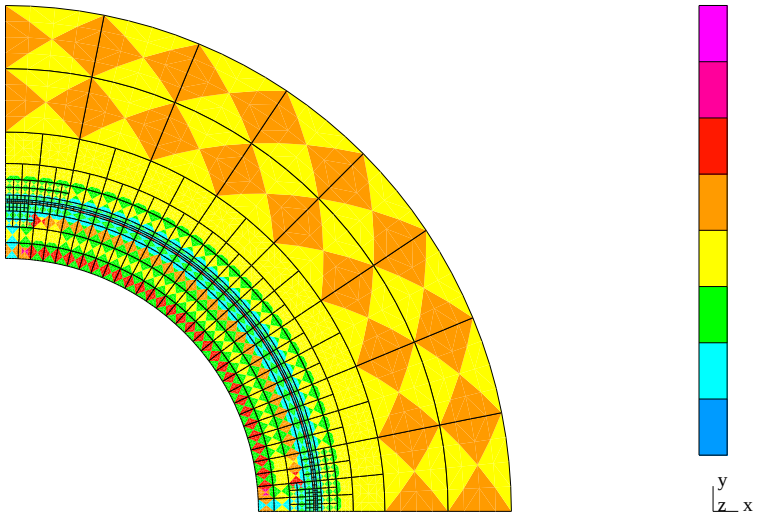

NDOF=9554

Figure 6.11: Cylinder test. Mesh after 20 steps of *hp*-refinements.

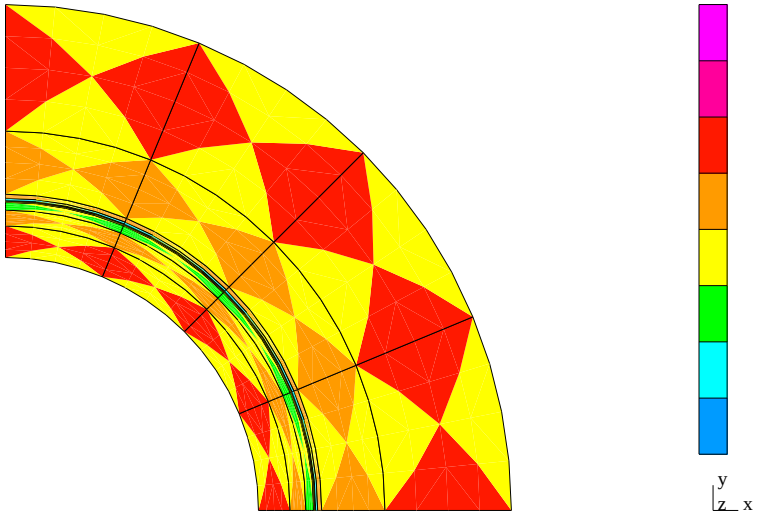

NDOF=2082

Figure 6.12: Cylinder test. Mesh after 14 steps of modified *hp*-refinements.

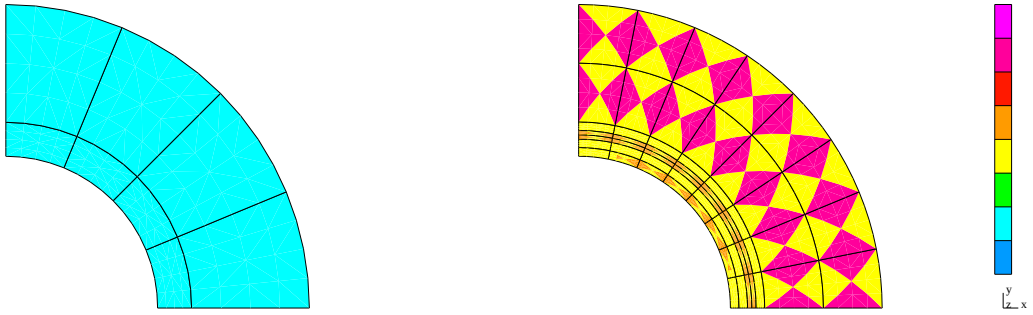

NDOF=90 NDOF=2158

Figure 6.13: Cylinder test. Initial and refined (in 13 *hp*-steps) meshes.

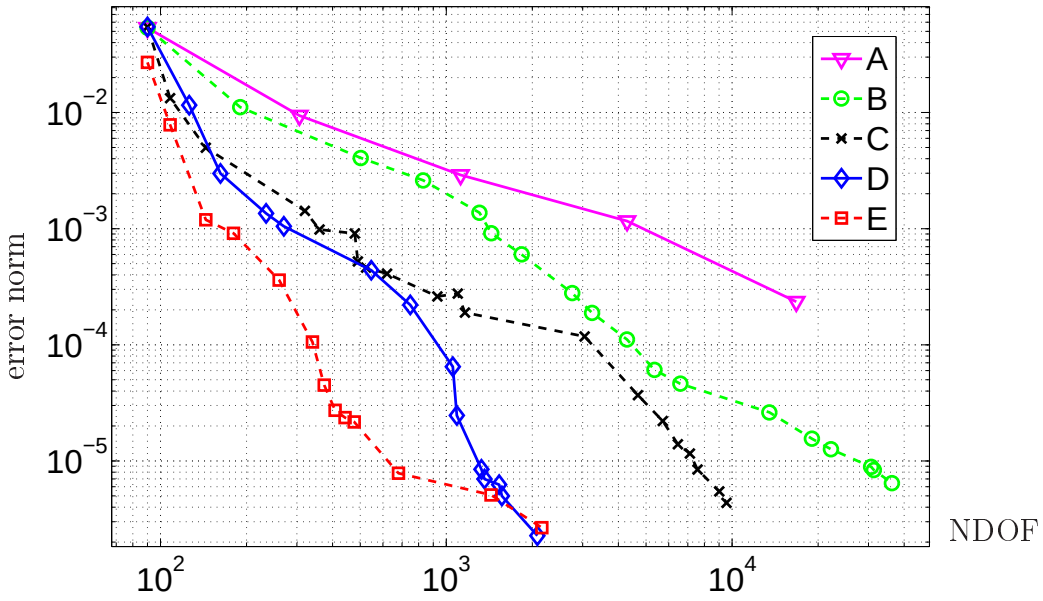

Figure 6.14: Cylinder test. Convergence of error norm. A – uniform refinement, B – *h*-adaptation, C – original automatic *hp*-adaptation, D – automatic *hp*-adaptation with additional *h*-refinements of elements containing elastic-plastic interfaces, E – automatic *hp*-adaptation for mesh, which initially complies with known elastic-plastic interface.

Homogeneous domain – perforated plate

A quarter of a perforated plate in the plane strain state with constant loading was analyzed as a next test. Material parameters were the same as in the previous test. Assumed boundary conditions and loading are shown in Fig. 6.15. The next figures present meshes obtained by fully automatic refinement of *hp* and *h*-type (Fig. 6.16), as well as after additional *h*-refinements along elastic-plastic interface (Fig. 6.17). In this example such a modification of adaptation process did not improve error convergence and the best one was observed for the original algorithm. However, the number of necessary adaptation steps that guarantees results with assumed accuracy was reduced. The overall time of computation is shown in Fig. 6.18. One may conclude that the original automatic *hp* adaptation is faster than the modified one.

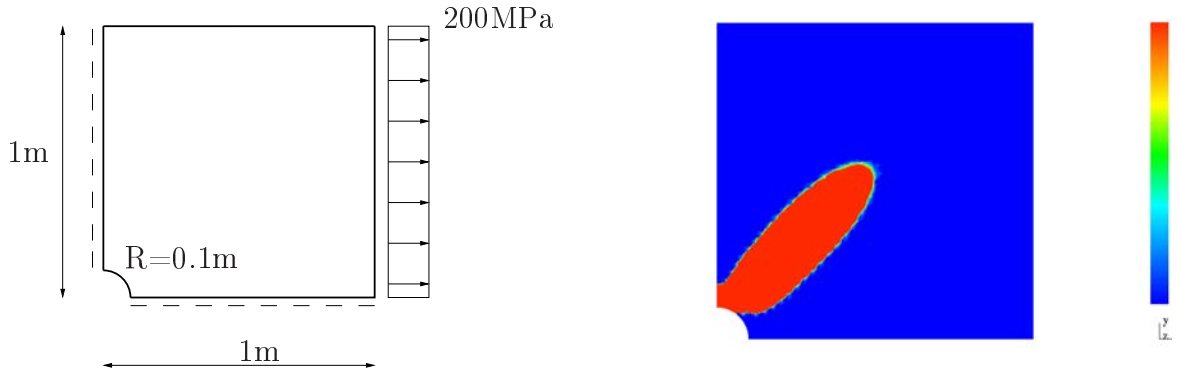

Figure 6.15: Perforated plate. Boundary conditions, elastic and plastic zones.

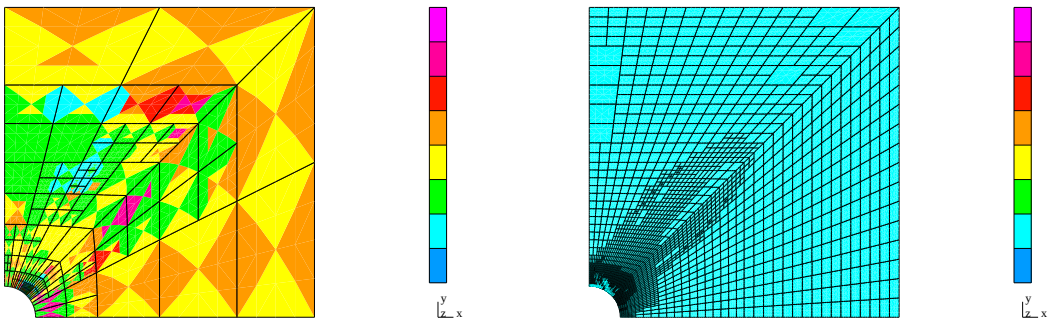

NDOF=3944 NDOF=18358

Figure 6.16: Perforated plate. Meshes after 20 steps of *hp*-refinements and 16 exclusively *h*-refinements.

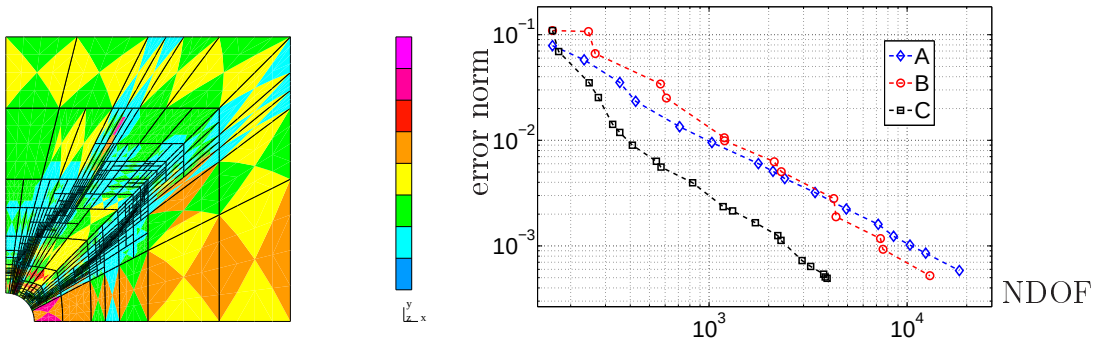

Figure 6.17: Perforated plate. Mesh after 15 steps of modified *hp*-refinements and convergence history (A – adaptive *h*-refinement, B – automatic *hp*-adaptation with additional *h*-refinements, C – original automatic *hp*-adaptation).

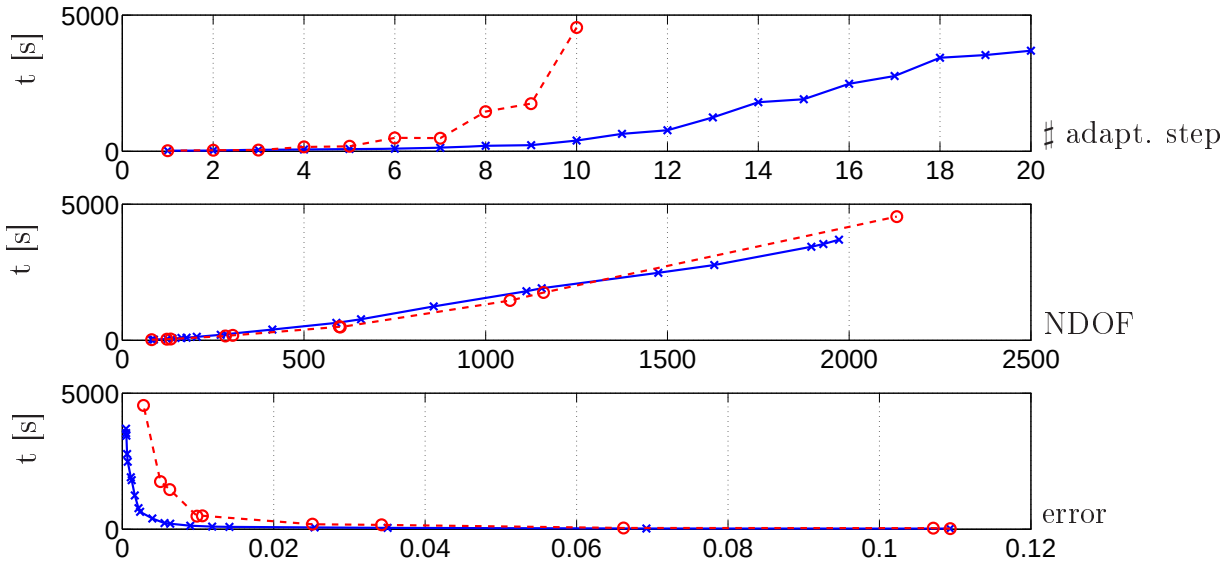

Figure 6.18: Perforated plate. Comparison of computation time (the continuous blue line – original *hp*-adaptation process, the dashed red line – original *hp*-adaptation process modified by additional *h*-refinements).

Heterogeneous domain – RVE with a cylinder-like inclusion

In the next test RVE with a cylinder-like inclusion was considered. Both materials underwent elastic-plastic deformations with kinematic hardening (Tab. 4.6). The model was loaded by constant loading $q = 220$ MPa. Boundary conditions and equivalent plastic strain distribution are shown in Fig. 6.19. The initial mesh and mesh after h-adaptive refinements are presented in Fig. 6.20. Using additional refinement the interface between elastic and plastic zones was successfully detected (see Fig. 6.21). Convergence history is shown in Fig. 6.22. Similarly as in the previous plate example the additional anisotropic refinements of elements with elastic-plastic borders reduced the number of necessary steps of refinements.

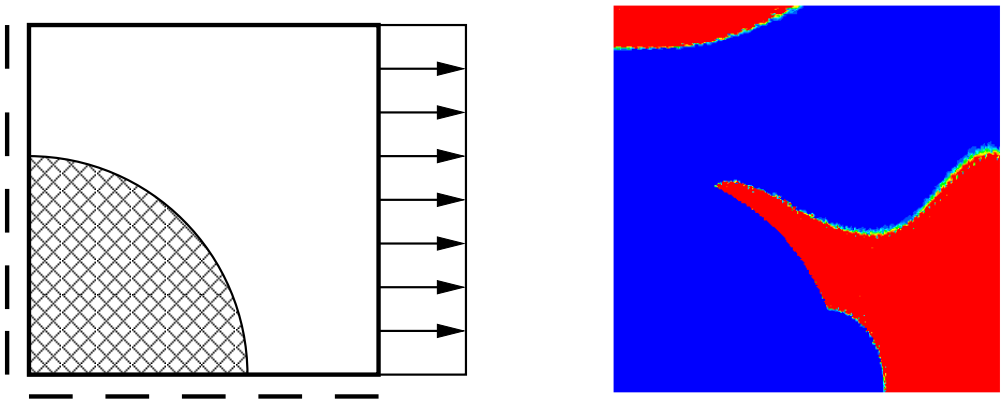

Figure 6.19: RVE. Boundary conditions, elastic and plastic zones.

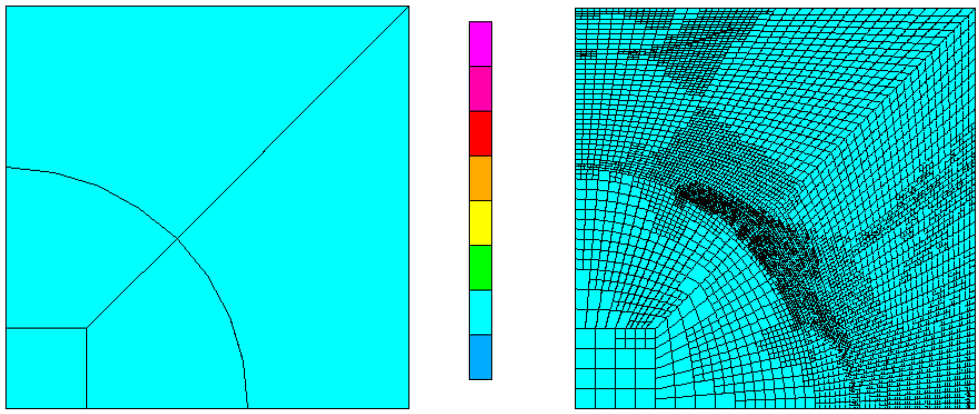

Figure 6.20: RVE. Initial mesh and after 20 steps of adaptive h-refinements.

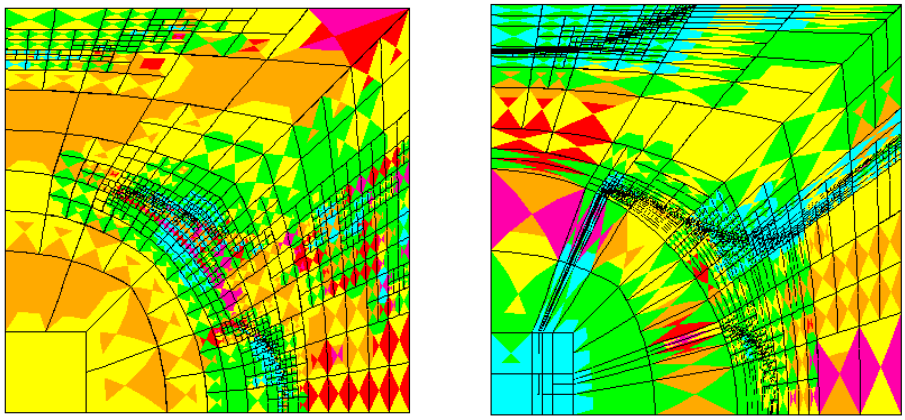

NDOF= 21048 NDOF= 54052

Figure 6.21: RVE. Mesh after 40 steps of original and 20 steps of modified *hp*-refinements.

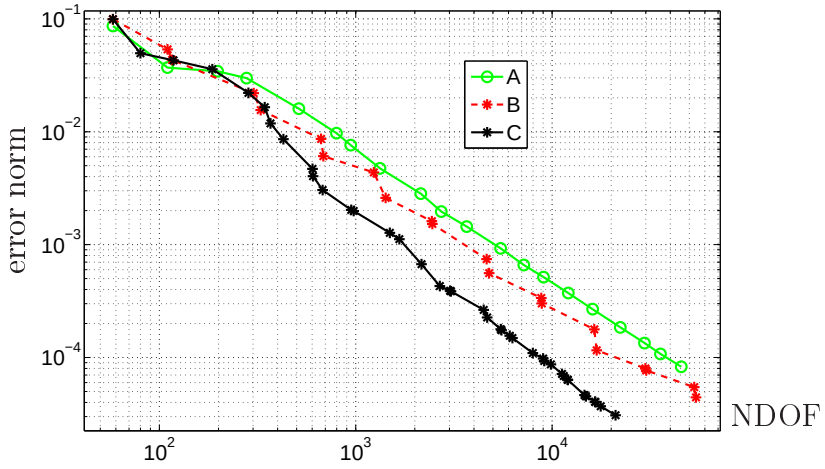

Figure 6.22: RVE. Convergence history (A – adaptive *h*-refinement, B – automatic *hp*-adaptation with additional *h*-refinements, C – original automatic *hp*-adaptation).

6.3 Sequel of tests

Only in the case of a cylinder modification of the fully automatic *hp*-adaptation resulted in a speed up of the convergence. Presumably the reason for significant improvement only in this case was the shape of the elastic-plastic interface, which could have been relatively easily captured in the cylinder. Therefore, the proposed modification of the fully automatic *hp* mesh refinement for elastic-plastic problems should probably be supplemented with the *r*-adaptation, similarly as it was done for *p*-refinements [73]. In all these nonlinear problems the automatic *hp*-adaptivity resulted in the fastest convergence but of algebraic rather than exponential type.

Chapter 7

Mixed finite element method

The finite element method, in which at least two fields e.g. displacements and stresses are approximated independently, is called the mixed method. One introduces stresses to a formulation in order to improve their convergence and obtain well-posed formulation for incompressible materials. Independent approximation of stresses is useful in multiscale computations, where homogenization is based on evaluation of stress solutions in the lower scale.

Applications of mixed finite elements have been developed since the seventies, especially by Brezzi [16], Crouzeix and Raviart [25], Raviart and Thomas [87] or Arnold [2, 3, 4].

Stable mixed finite elements for solid mechanics are very difficult to construct. They have to provide symmetry of stress tensor and continuity of only traction across interelement boundaries rather than all the stress components.

7.1 Problem formulation

The equations of linear elasticity can be written in the following form:

$$\begin{cases} \boldsymbol{\varepsilon}(\boldsymbol{u}) = \boldsymbol{C}^{-1}\boldsymbol{\sigma} & \text{in } \Omega \\ \mathbf{div}\,\boldsymbol{\sigma} = -\boldsymbol{b} & \text{in } \Omega \\ \boldsymbol{u} = \hat{\boldsymbol{u}} & \text{on } \partial\Omega_D \\ \boldsymbol{\sigma}\boldsymbol{n} = \hat{\boldsymbol{t}} & \text{on } \partial\Omega_N \end{cases} \tag{7.1}$$

where $\boldsymbol{C}$ is a tensor of elastic material parameters and $\boldsymbol{b}$ denotes body forces.

In order to formulate the elasticity problem weakly let us multiply Eq. $(7.1)_1$ and Eq. $(7.1)_2$ by test functions $\boldsymbol{\tau} \in \mathrm{L}^2(\Omega, \mathbb{S})$ and $\boldsymbol{v} \in \mathrm{L}^2(\Omega, \mathbb{V})$, respectively. Here $\mathbb{S}$ is the space of second order symmetric tensors $\mathbf{R}^{\mathbf{n}\times\mathbf{n}}_{\mathbf{sym}}$ and $\mathbb{V}$ is the vector space $\mathbf{R}^{\mathbf{n}}$. Integration by parts of the first equation results in the following weak formulation that is a counterpart of the Hellinger–Reissner principle: *find* $\boldsymbol{\sigma} \in \mathrm{H}_{\hat{t}}(\mathrm{div}, \Omega, \mathbb{S})$ *and* $\boldsymbol{u} \in \mathrm{L}^2(\Omega, \mathbb{V})$, *such that:*

$$\begin{cases} \int\limits_\Omega \boldsymbol{\tau} : \boldsymbol{C}^{-1}\boldsymbol{\sigma}\,\mathrm{d}\Omega + \int\limits_\Omega \mathbf{div}\,\boldsymbol{\tau}\cdot\boldsymbol{u}\,\mathrm{d}\Omega &= \int\limits_{\partial\Omega} \boldsymbol{\tau}\boldsymbol{n}\cdot\hat{\boldsymbol{u}}\,\mathrm{d}s \\ \int\limits_\Omega \boldsymbol{v}\cdot\mathbf{div}\,\boldsymbol{\sigma}\,\mathrm{d}\Omega &= -\int\limits_\Omega \boldsymbol{v}\cdot\boldsymbol{b}\,\mathrm{d}\Omega \end{cases} \tag{7.2}$$

$$\forall\, \boldsymbol{\tau} \in \mathrm{H}_0(\mathrm{div}, \Omega, \mathbb{S}), \quad \forall\, \boldsymbol{v} \in \mathrm{L}^2(\Omega)$$

where $\mathrm{H}_0(\mathrm{div}, \Omega, \mathbb{S})$ and $\mathrm{H}_{\hat{t}}(\mathrm{div}, \Omega, \mathbb{S})$ stand for stresses with square integrable divergence and vanishing or equal to $\boldsymbol{q}$ tractions on $\partial\Omega_N$, $\mathbb{S}$ is the space of second order symmetric tensors, $\hat{\boldsymbol{u}}$ is displacement known on $\partial\Omega_D$, $\partial\Omega_D \cup \partial\Omega_N = \partial\Omega$, $\partial\Omega_D \cap \partial\Omega_N = \emptyset$.

The choice of the shape function spaces for such a formulation is not trivial. E.g., considering the resulting system of algebraic equations

$$\begin{bmatrix} \boldsymbol{A}_{m\times m} & \boldsymbol{B}_{m\times n} \\ (\boldsymbol{B}^T)_{n\times m} & \boldsymbol{0} \end{bmatrix} \begin{bmatrix} \boldsymbol{u} \\ \boldsymbol{\sigma} \end{bmatrix} = \begin{bmatrix} \boldsymbol{c} \\ \boldsymbol{0} \end{bmatrix} \tag{7.3}$$

the relation $m \geq n$ must be satisfied to avoid singularity. More precise conditions are specified by the *inf–sup* theorem [5], recalled below.

Assuming denotations

$$a(\boldsymbol{\tau}, \boldsymbol{\sigma}) = \int_\Omega \boldsymbol{\tau} : \boldsymbol{C}^{-1}\boldsymbol{\sigma}\, \mathrm{d}\Omega, \qquad b(\boldsymbol{\tau}, \boldsymbol{u}) = \int_\Omega \mathbf{div}\boldsymbol{\tau} \cdot \boldsymbol{u}\, \mathrm{d}\Omega \tag{7.4}$$

it states that if:

1. $a(\boldsymbol{\tau}, \boldsymbol{\sigma}) = a(\boldsymbol{\sigma}, \boldsymbol{\tau})$ *(symmetry)*
2. $\exists M > 0 : a(\boldsymbol{\tau}, \boldsymbol{\sigma}) \leq M\, ||\boldsymbol{\tau}||\, ||\boldsymbol{\sigma}||$ *(continuity)*
3. $\exists \alpha > 0 : a(\boldsymbol{\tau}, \boldsymbol{\tau}) \geq \alpha ||\boldsymbol{\tau}||^2$ *(coercivity)*
4. $\exists N > 0 : b(\boldsymbol{\tau}, \boldsymbol{u}) \leq N\, ||\boldsymbol{\tau}||\, ||\boldsymbol{u}||$ *(continuity)*
5. $\exists \beta > 0 : \sup_{\boldsymbol{\tau} \in H_0^1(\mathrm{div},\Omega)} \frac{||b(\boldsymbol{\tau},\boldsymbol{v})||}{||\boldsymbol{v}||} \geq \beta\, ||\boldsymbol{v}|| \qquad \forall \boldsymbol{v} \in (L_0(\Omega))^2$

then there exists a unique solution of problem (7.2).

Usually, it is more convenient to verify commutativity of the de Rham diagram [17]

$$\begin{array}{ccc} \boldsymbol{C}^\infty(\Omega, \mathbb{S}) & \xrightarrow{\mathrm{div}} & \boldsymbol{C}^\infty(\Omega, \mathbb{R}^2) \\ \downarrow \boldsymbol{\Pi_h} & & \downarrow \boldsymbol{P}_h \\ \boldsymbol{\Sigma}_h & \xrightarrow{\mathrm{div}} & \boldsymbol{V}_h \end{array}$$

where $\boldsymbol{\Pi_h}$, $\boldsymbol{P}_h$ are projections defined by the finite element degrees of freedom. It guarantees stability and convergence of the mixed model (fulfillment of the *inf–sup* theorem).

Summing up the main features of the approximation should be as follows:

- continuity requirement for traction ($\boldsymbol{\sigma n}$) across the interelement boundaries
- discontinuous approximation of displacement field $\boldsymbol{u}$
- the relation between orders of approximation should be determined by the exact sequence ($\boldsymbol{\Sigma_h} \xrightarrow{\mathrm{div}} \boldsymbol{V_h} \longrightarrow \boldsymbol{0}$ [33])

- de Rham diagram should commute
- *hp* refinements should be possible.

Since enforcement of symmetry together with traction continuity is a very difficult task for arbitrary order and shape of finite elements, one may use a modified weak formulation [4, 85] with build in condition of stress tensor symmetry.

The problem may be formulated in the following way: *find* $\boldsymbol{\sigma} \in \mathrm{H}_{\hat{t}}(\mathrm{div}, \Omega, \mathbb{M})$, $\boldsymbol{u} \in \mathrm{L}^2(\Omega, \mathbb{V})$ *and* $\boldsymbol{p} \in \mathrm{L}^2(\Omega, \mathbb{K})$ *such that:*

$$\begin{cases} \int\limits_{\Omega} \boldsymbol{\tau} : \boldsymbol{C}^{-1}\boldsymbol{\sigma}\,\mathrm{d}\Omega + \int\limits_{\Omega} \mathbf{div}\,\boldsymbol{\tau} \cdot \boldsymbol{u}\,\mathrm{d}\Omega + \int\limits_{\Omega} \boldsymbol{\tau} \cdot \boldsymbol{p}\,\mathrm{d}\Omega = \int\limits_{\partial\Omega} \boldsymbol{\tau}\,\boldsymbol{n} \cdot \hat{\boldsymbol{u}}\,\mathrm{d}s \\ \int\limits_{\Omega} \boldsymbol{v} \cdot \mathbf{div}\,\boldsymbol{\sigma}\,\mathrm{d}\Omega = -\int\limits_{\Omega} \boldsymbol{v} \cdot \boldsymbol{b}\,\mathrm{d}\Omega \\ \int\limits_{\Omega} \boldsymbol{q} \cdot \boldsymbol{\sigma}\,\mathrm{d}\Omega = 0 \end{cases} \tag{7.5}$$

$$\forall\, \boldsymbol{\tau} \in \mathrm{H}_0(\mathrm{div}, \Omega, \mathbb{M}), \quad \forall\, \boldsymbol{v} \in \mathrm{L}^2(\Omega, \mathbb{V}), \quad \forall\, \boldsymbol{q} \in \mathrm{L}^2(\Omega, \mathbb{K})$$

where $\mathbb{M}$ is the space of second order (now, not necessary symmetric) tensors, $\mathbb{K}$ is the space of skew-symmetric tensors.

7.2 Discretization

The last formulation was used for 2D problems and discretization described below. 9 node quadrilateral elements, shown schematically in Fig.7.1, were used. The nodes are ordered in the following way:

- vertex nodes: a_1, a_2, a_3, a_4 (used only for geometry)
- edge nodes: a_5, a_6, a_7, a_8
- middle node: a_9.

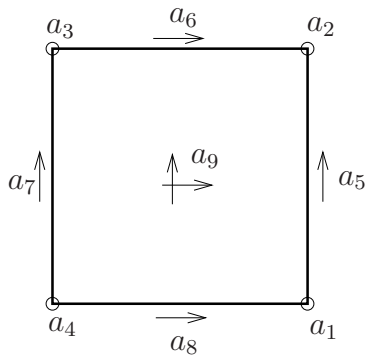

Figure 7.1: Master finite element $\hat{\mathrm{K}}$.

The master element $\hat{\mathrm{K}}$ is defined as $\hat{\mathrm{K}} = \{(\xi, \eta) \in \mathbb{R}^2 : \xi, \eta \in (0, 1)\}$. The transformation that maps $\hat{\mathrm{K}}$ onto a particular finite element K is assumed in the standard form

$$x = \sum_{i=1}^{8} x_i\, \hat{g}_i(\xi, \eta), \qquad y = \sum_{i=1}^{8} y_i\, \hat{g}_i(\xi, \eta) \tag{7.6}$$

where: $\hat{g}_i$ are at most second order shape functions; x_i and y_i are the geometrical degrees of freedom.

All shape functions are defined as products of the following two sets of 1D functions that contain integrated Legendre polynomials

$$\begin{array}{rclcrcl} \hat{\psi}_1(t) & = & 1 & \text{or} & \hat{\varphi}_1(t) & = & 1-t \\ \hat{\psi}_2(t) & = & t-\frac{1}{2} & & \hat{\varphi}_2(t) & = & t \end{array} \tag{7.7}$$

supplemented with the following higher order shape functions

$$\begin{array}{rcl} \hat{\psi}_3(t) = \hat{\varphi}_3(t) & = & t(t-1) \\ \hat{\psi}_4(t) = \hat{\varphi}_4(t) & = & t(t-1)(t-2) \\ \ldots & & \end{array} \tag{7.8}$$

where $t \in [0,1]$.

Scalar shape functions $\hat{g}_1, \ldots, \hat{g}_9$ related to nodes $a_1, \ldots, a_9$ (see Fig.7.1) are constructed in the following way

$$\begin{array}{rcl} \hat{g}_1(\xi,\eta) & = & \hat{\varphi}_2(\xi)\,\hat{\varphi}_1(\eta) \\ \hat{g}_2(\xi,\eta) & = & \hat{\varphi}_2(\xi)\,\hat{\varphi}_2(\eta) \\ \hat{g}_3(\xi,\eta) & = & \hat{\varphi}_1(\xi)\,\hat{\varphi}_2(\eta) \\ \hat{g}_4(\xi,\eta) & = & \hat{\varphi}_1(\xi)\,\hat{\varphi}_1(\eta) \\ \hat{g}_5(\xi,\eta) & = & \hat{\varphi}_2(\xi)\,\hat{\varphi}_3(\eta) \\ \hat{g}_6(\xi,\eta) & = & \hat{\varphi}_3(\xi)\,\hat{\varphi}_2(\eta) \\ \hat{g}_7(\xi,\eta) & = & \hat{\varphi}_1(\xi)\,\hat{\varphi}_3(\eta) \\ \hat{g}_8(\xi,\eta) & = & \hat{\varphi}_3(\xi)\,\hat{\varphi}_1(\eta) \\ \hat{g}_9(\xi,\eta) & = & \hat{\varphi}_3(\xi)\,\hat{\varphi}_3(\eta) \end{array} \tag{7.9}$$

Additionally, bilinear shape functions that are used for approximation of stresses, are defined in the following way:

$$\begin{array}{rcl} \hat{e}_1(\xi,\eta) & = & \hat{\varphi}_2(\xi)\,\hat{\psi}_1(\eta) \\ \hat{e}_2(\xi,\eta) & = & \hat{\varphi}_2(\xi)\,\hat{\psi}_2(\eta) \\ \hat{e}_3(\xi,\eta) & = & \hat{\psi}_1(\xi)\,\hat{\varphi}_2(\eta) \\ \hat{e}_4(\xi,\eta) & = & \hat{\psi}_2(\xi)\,\hat{\varphi}_2(\eta) \\ \ldots & & \end{array} \tag{7.10}$$

One of the shape functions used for stress approximation, is shown in Fig. 7.2. Such an approximation enables enforcement of only tractions continuity. There is no assumption about stress tensor continuity.

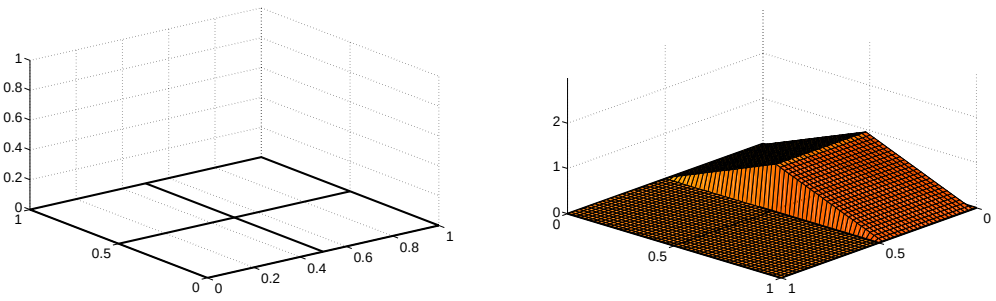

Figure 7.2: FE discretization. A basis shape function for stress approximation.

The general form of approximation for stress field that enforces continuity of traction, is assumed in the following form

$$\boldsymbol{\sigma}_h = \boldsymbol{\sigma}^X \sum_{i \in I_X} \alpha_i \, e_i^X + \boldsymbol{\sigma}^Y \sum_{i \in I_Y} \beta_i \, e_i^Y + \boldsymbol{\sigma}^{XY} \sum_{i \in I_{XY}} \gamma_i \, e_i^X + \boldsymbol{\sigma}^{YX} \sum_{i \in I_{YX}} \delta_i \, e_i^Y \tag{7.11}$$

where:

$$\boldsymbol{\sigma}^X = \begin{pmatrix} x_{,\xi}\, y_{,\eta} & y_{,\xi}\, y_{,\eta} \\ -x_{,\xi}\, x_{,\eta} & -y_{,\xi}\, x_{,\eta} \end{pmatrix} / \det \boldsymbol{J} \tag{7.12}$$

$$\boldsymbol{\sigma}^{XY} = \begin{pmatrix} x_{,\xi}\, x_{,\eta} & y_{,\xi}\, x_{,\eta} \\ x_{,\xi}\, y_{,\eta} & y_{,\xi}\, y_{,\eta} \end{pmatrix} / \det \boldsymbol{J} \tag{7.13}$$

$$\boldsymbol{\sigma}^{Y} = \begin{pmatrix} -x_{,\eta}\, y_{,\xi} & -y_{,\eta}\, y_{,\xi} \\ x_{,\xi}\, x_{,\eta} & y_{,\eta}\, x_{,\xi} \end{pmatrix} / \det \boldsymbol{J} \tag{7.14}$$

$$\boldsymbol{\sigma}^{YX} = \begin{pmatrix} -x_{,\eta}\, x_{,\xi} & -y_{,\eta}\, x_{,\xi} \\ -x_{,\eta}\, y_{,\xi} & -y_{,\eta}\, y_{,\xi} \end{pmatrix} / \det \boldsymbol{J} \tag{7.15}$$

α_i, β_i, γ_i, δ_i denote degrees of freedom, I_X, I_Y, I_{XY}, I_{YX} are sequences of appropriate indices, $\boldsymbol{J}$ is the determinant of the Jacobi matrix. Formulas (7.12) – (7.15) were obtained satisfying appropriate conditions, e.g.

$$\boldsymbol{\sigma}^X \boldsymbol{n} = \boldsymbol{n} \quad \text{or} \quad \boldsymbol{0} \qquad \text{(dependent on the edge)} \tag{7.16}$$

The resulting traction continuity for tensor $\boldsymbol{\sigma}^X$ for linear approximation is shown in Fig. 7.3.

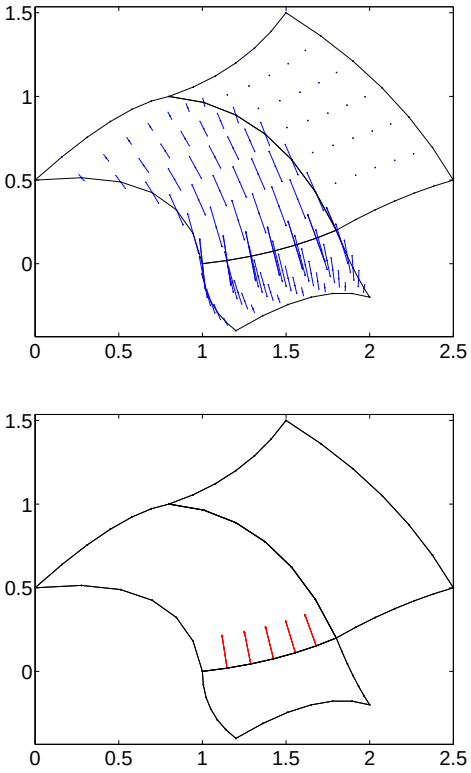

Figure 7.3: Principal directions of stress tensor $\boldsymbol{\sigma}^X$. Traction continuity.

Another approach that also enables obtaining stress tensors with tractions coinciding at every point of the element interfaces, is based on the Piola transform for matrices [23], which transforms functions from master $\hat{\mathrm{K}}$ to physical finite element K by relation

$$\boldsymbol{\sigma}_h = \hat{\boldsymbol{\sigma}}_h \boldsymbol{B}^T, \qquad \mathrm{div}\boldsymbol{\sigma}_h = (\det \boldsymbol{J})\, \mathrm{div}\hat{\boldsymbol{\sigma}}_h \tag{7.17}$$

where: $\boldsymbol{B} = \dfrac{\boldsymbol{J}}{\det \boldsymbol{J}}$ and e.g. $\boldsymbol{\sigma}^X$ as a mapping of $\hat{\boldsymbol{\sigma}}_h = \begin{pmatrix} 1 & 0 \\ 0 & 0 \end{pmatrix}$

has the form

$$\boldsymbol{\sigma}^X = \begin{pmatrix} x_{,\xi} & y_{,\xi} \\ 0 & 0 \end{pmatrix} / \det \boldsymbol{J} \tag{7.18}$$

The above mentioned transformation is suggested in [3, 15] and guarantees that the Rham diagram commutes. Comparison of traction continuity obtained by both possible methods and contour maps of tensor fields are shown in Figs. 7.4 – 7.6.

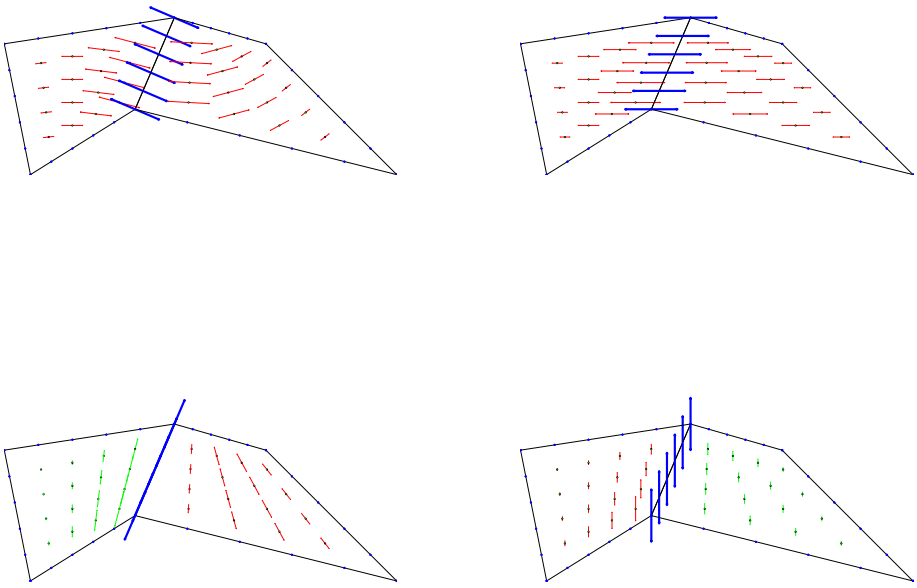

Figure 7.4: Traction components continuity for Eq. (7.12) (left) and Eq. (7.18) (right).

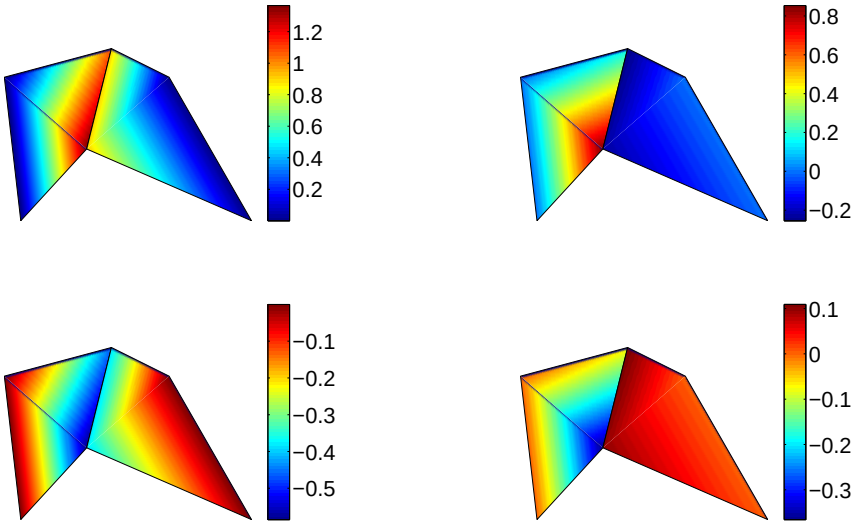

Figure 7.5: Tensor field components of $\boldsymbol{\sigma}^X$ for Eq. (7.12). Top left: σ^X_{11}, top right: σ^X_{12}, bottom left: σ^X_{21}, bottom right: σ^X_{22}.

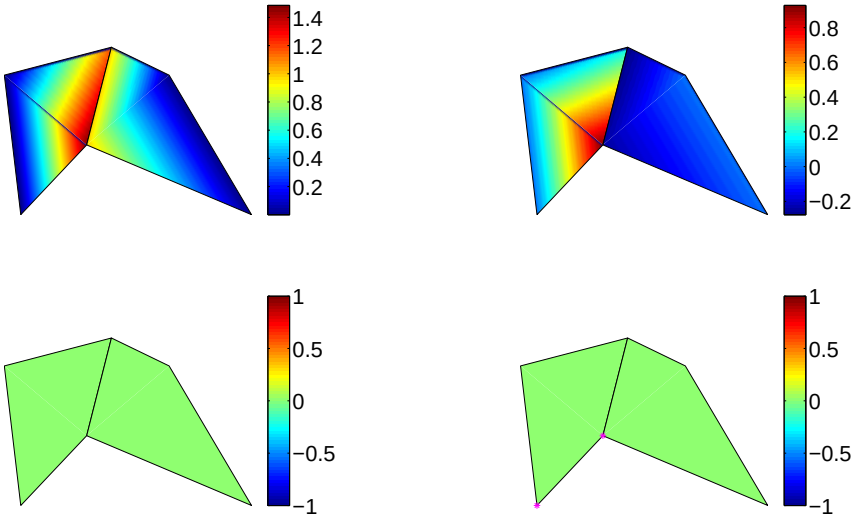

Figure 7.6: Tensor field components of $\boldsymbol{\sigma}^X$ for Eq. (7.18). Top left: σ^X_{11}, top right: σ^X_{12}, bottom left: σ^X_{21}, bottom right: σ^X_{22}.

In general for plane state problems there are N_σ degrees of freedom related to tensor field, where assuming orders of approximation p_1 and p_2 in two directions

$$N_\sigma = \underbrace{4(p_1+1)+4(p_2+1)}_{\text{edge nodes}} + \underbrace{6(p_1-1)+6(p_2-1)}_{\text{middle node}}$$

These degrees of freedom correspond to edge nodes (a_5, a_6, a_7, a_8) and middle node (a_9) (see Fig. 7.1).

In order to satisfy the exact sequence condition the shape functions used for approximation of displacements should contain polynomials of order lower by one in each direction. Thus, for $p_1 = p_2 = 2$, they are in the form:

$$\begin{array}{rcl} f_1(\xi,\eta) & = & \psi_1(\xi)\,\psi_1(\eta) \\ f_2(\xi,\eta) & = & \psi_1(\xi)\,\psi_2(\eta) \\ f_3(\xi,\eta) & = & \psi_2(\xi)\,\psi_1(\eta) \\ f_4(\xi,\eta) & = & \psi_2(\xi)\,\psi_2(\eta) \end{array} \tag{7.19}$$

Discontinuous approximation for displacements is as follows

$$\boldsymbol{u}_h = \begin{pmatrix} 1 \\ 0 \end{pmatrix} \sum_{i=1}^{3} c_i\, f_i + \begin{pmatrix} 0 \\ 1 \end{pmatrix} \sum_{i=1}^{3} d_i\, f_i \tag{7.20}$$

Discontinuous approximation for Lagrange multiplier of $p_1 - 1$, $p_2 - 1$ orders has a form:

$$\boldsymbol{p}_h = \begin{pmatrix} 0 & 1 \\ -1 & 0 \end{pmatrix} \sum_{i=1}^{I_p} e_i\, f_i \tag{7.21}$$

Example of shape functions that are used for discontinuous approximation is shown in Fig. 7.7.

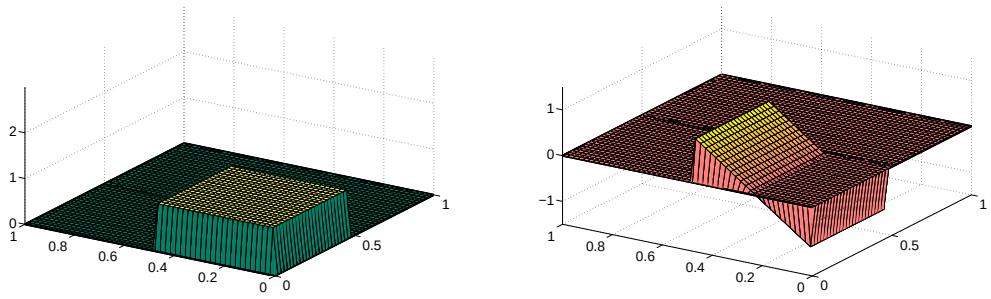

Figure 7.7: Shape functions for displacements.

Therefore, there are N_u degrees of freedom for displacement approximation

$$N_u = 2p_1p_2$$

and N_p unknown parameters for Lagrange multipliers (skew-symmetric tensor field)

$$N_p = p_1p_2$$

Appropriate degrees of freedom for displacements and Lagrange multipliers are associated with middle node a_9 (see Fig. 7.1).

All together there are N degrees of freedom in each element

$$N = N_\sigma + N_u + N_p$$

2D finite element for plane stress problem with the second order of approximation for stresses and the linear approximation both for displacements and Lagrange multipliers has 48 degrees of freedom.

The proposed approximation was verified on selected examples presented in the next section.

7.3 Numerical examples

Cooke membrane

The first test was performed to validate the formulation and the proposed approximations for stresses and displacements. The considered plate in plane stress state was fixed on the left side and subjected to tangential parabolic loading q on the right hand side (schematically shown in Fig. 7.8), with resultant force equal to -100 kN. Deformation of the area and contour maps of the stress tensor components are shown in Figs. 7.9 – 7.12. They confirm correctness of the applied approximation.

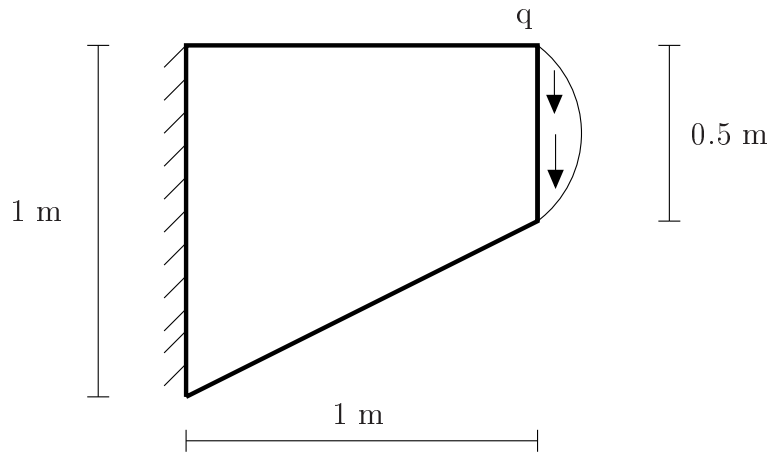

Figure 7.8: Cooke membrane. Boundary conditions.

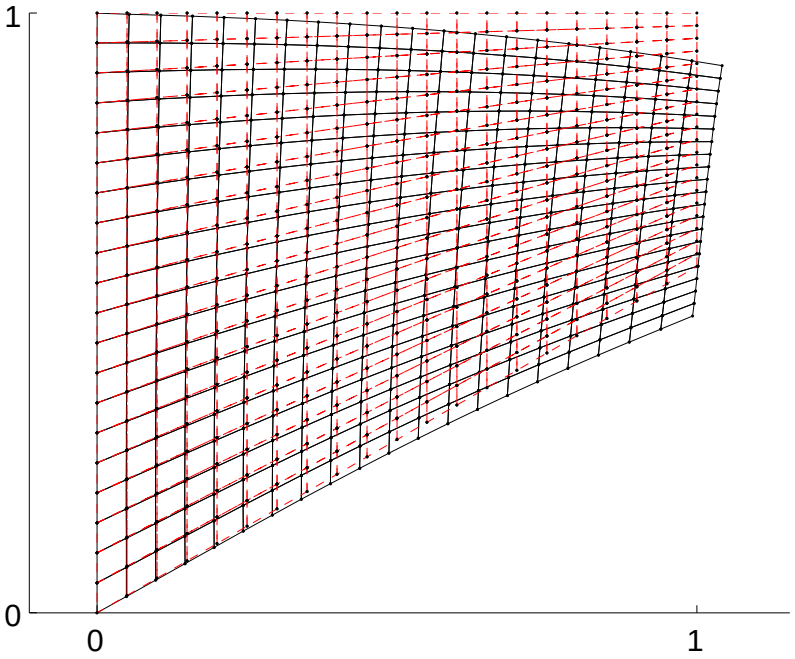

Figure 7.9: Cooke membrane. Deformation.

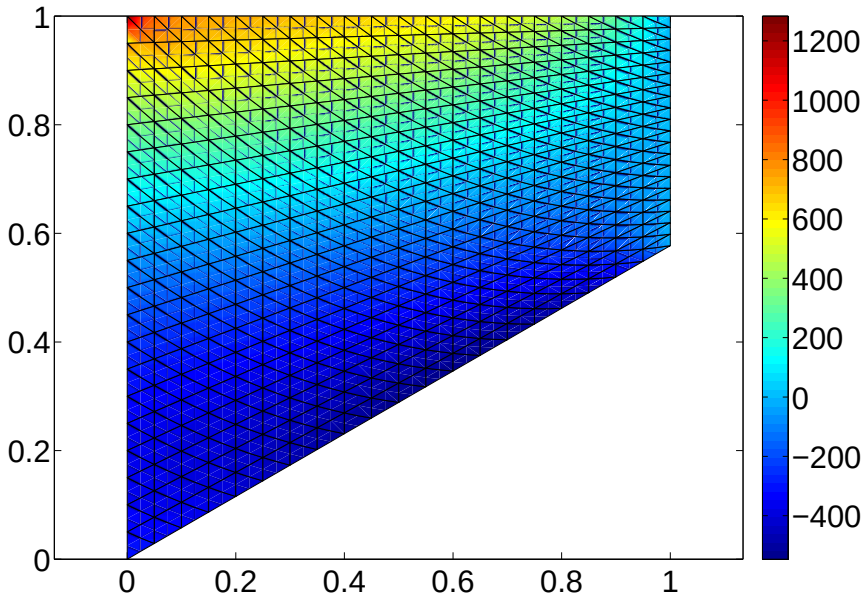

Figure 7.10: Cooke membrane. Contour map of component σ_{xx} of the stress tensor.

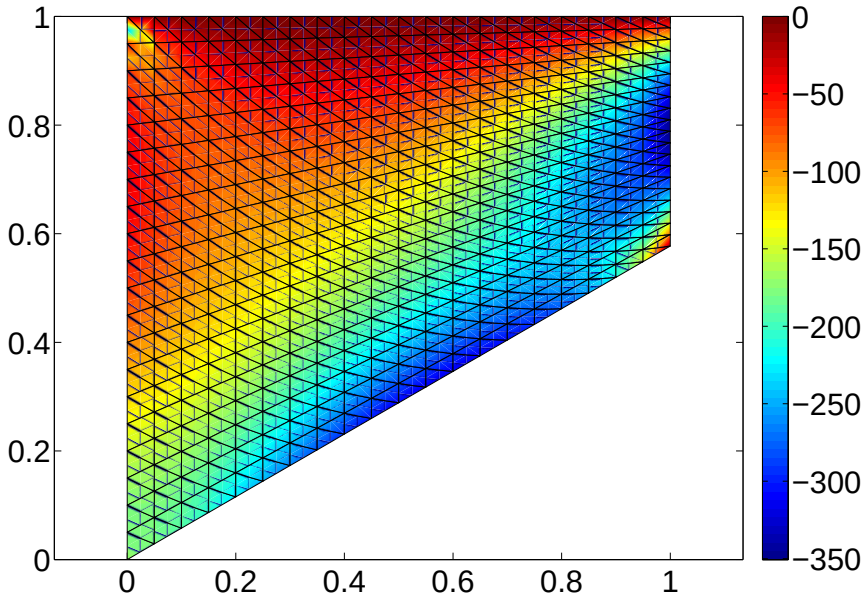

Figure 7.11: Cooke membrane. Contour map of component σ_{yx} of the stress tensor.

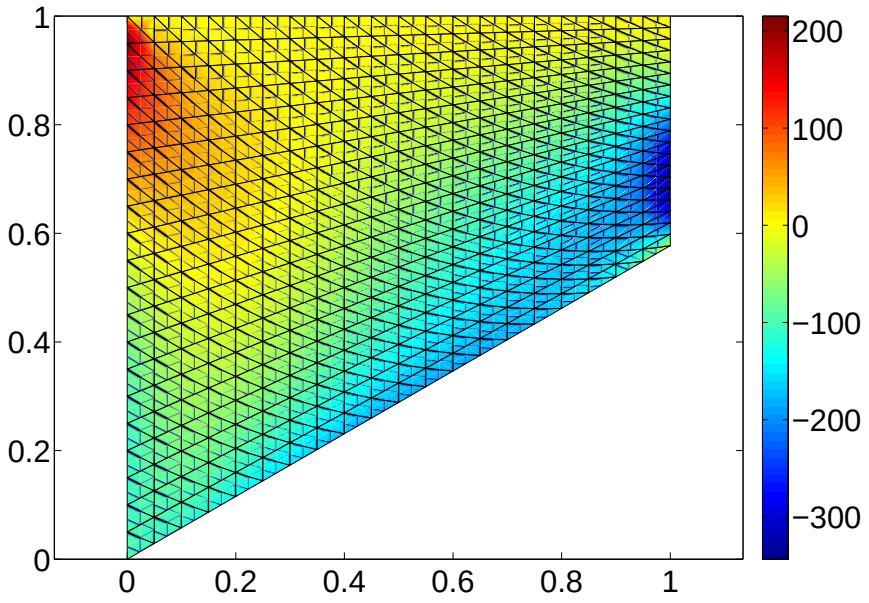

Figure 7.12: Cooke membrane. Contour map of component σ_{yy} of the stress tensor.

Heterogeneous material

Further tests were performed for a problem considered at the micro-level to calculate the effective material parameters on the basis of the tensile test simulations.

The first test was performed for a square RVE (2 mm × 2 mm) with square inclusion (1 mm × 1 mm) located in the central part. The model was subjected to constant loading $q = 100$ kN/m. Due to the symmetry only 1/4 part of the area was analyzed (see Fig. 7.13). All material data are collected in Tab. 7.1.

Material parameters	matrix	inclusion
E (GPa)	200	0.002
ν	0.3	0.3

Table 7.1: Material parameters for RVE:1 with square inclusion.

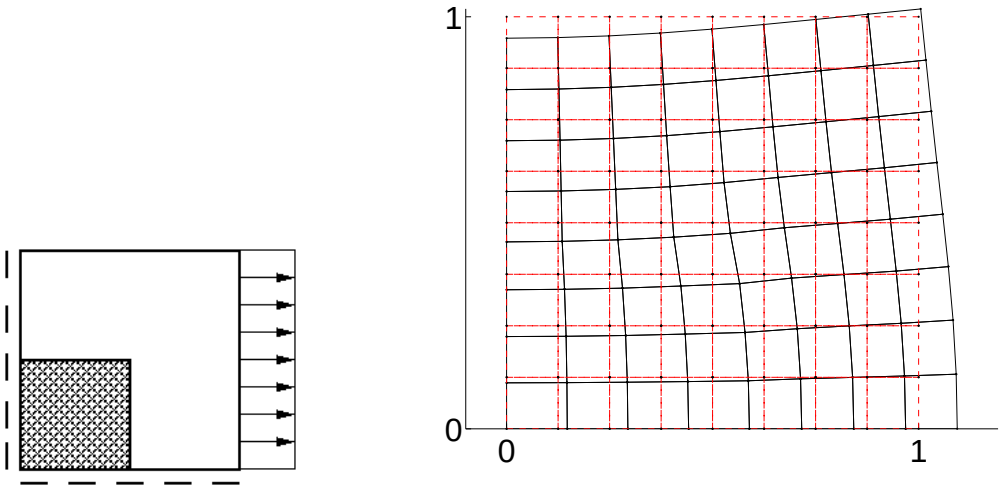

Figure 7.13: RVE:1 with square inclusion. Boundary conditions and deformation.

For discretization by 324 quadrilateral elements (11880 DOF) the principal stress directions are shown in Fig. 7.14, contour maps of selected stress and strain components are presented in Figs. 7.15 – 7.17.

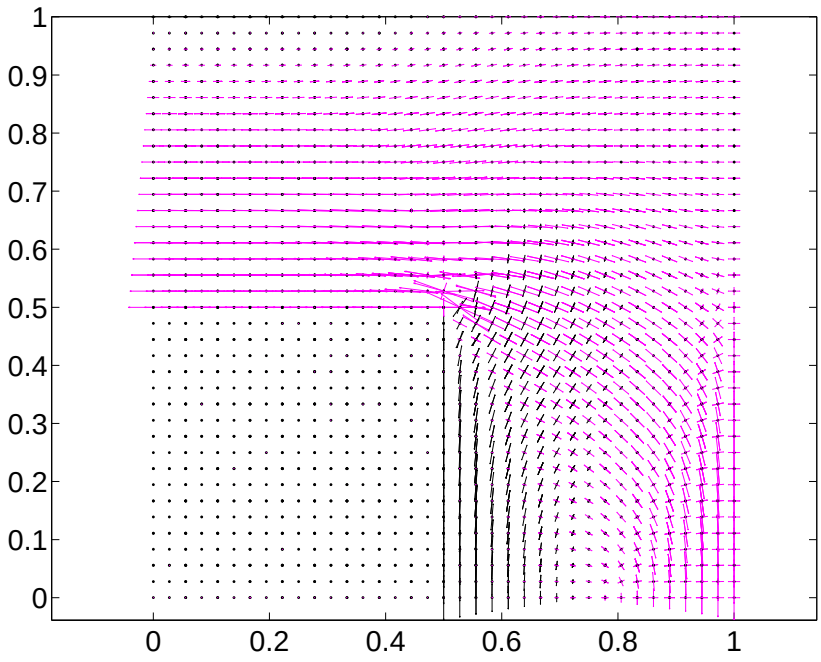

Figure 7.14: RVE:1 with square inclusion. Principal stress directions.

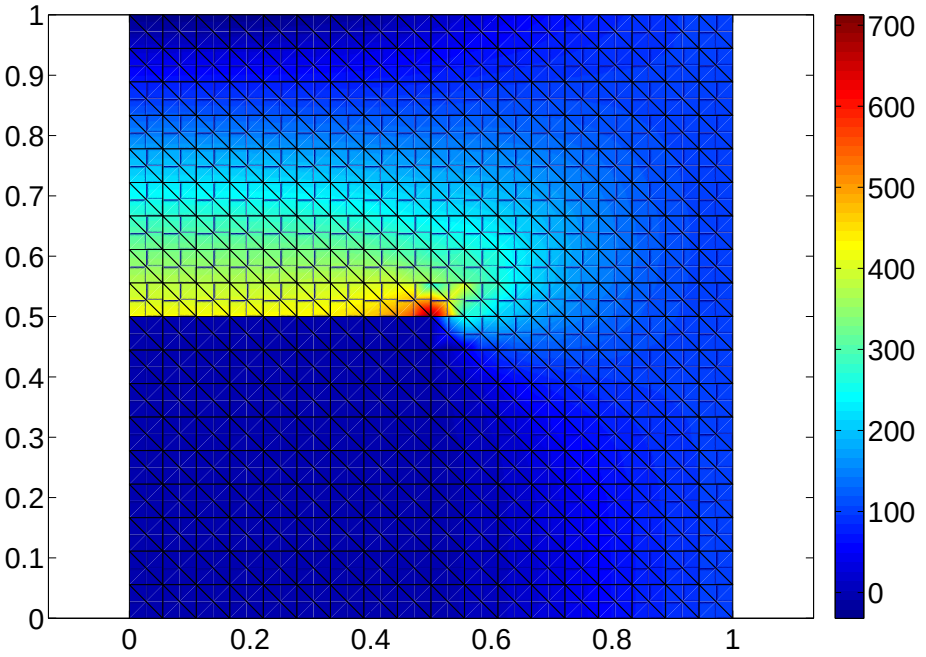

Figure 7.15: RVE:1 with square inclusion. Component σ_{xx} of stress tensor.

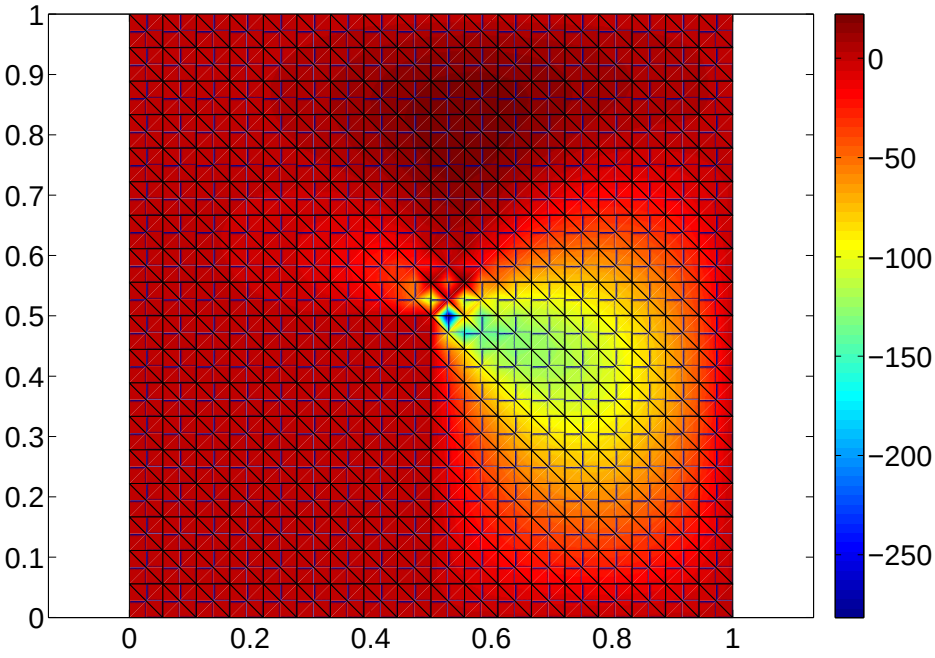

Figure 7.16: RVE:1 with square inclusion. Component σ_{yx} of stress tensor.

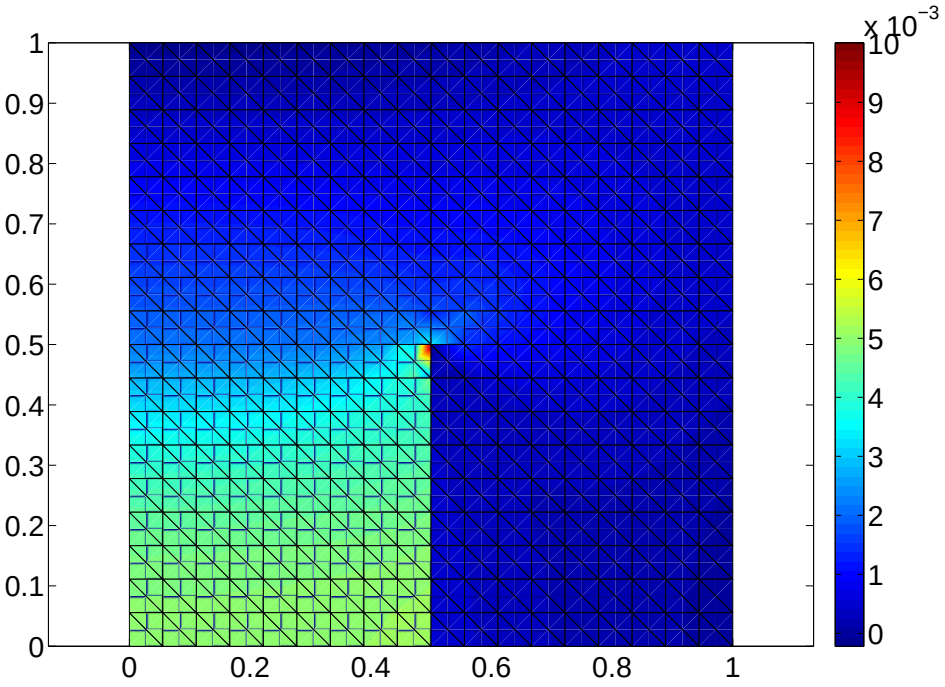

Figure 7.17: RVE:1 with square inclusion. Component ε_{xx} of strain tensor.

Performing uniform refinements of finite element mesh a comparison of stress and displacement results obtained by the mixed and the standard (displacement) formulations was done. The effects are summarized in Fig. 7.18.

Also effective Young modulus and Poisson ratio were determined by formulas

$$E_{eff} = \frac{\langle \sigma_{xx} \rangle}{\langle \varepsilon_{xx} \rangle} \tag{7.22}$$

$$\nu_{eff} = -\frac{\langle \varepsilon_{yy} \rangle}{\langle \varepsilon_{xx} \rangle} \tag{7.23}$$

Convergence of the effective parameters computed on the basis of displacement and mixed formulations are shown in Fig. 7.19. It may be noticed that each formulation provides good either upper or lower bound. Therefore, presumably both formulations can be used for a small number of degrees of freedom, then s mean value may be treated as an estimate of the effective parameters.

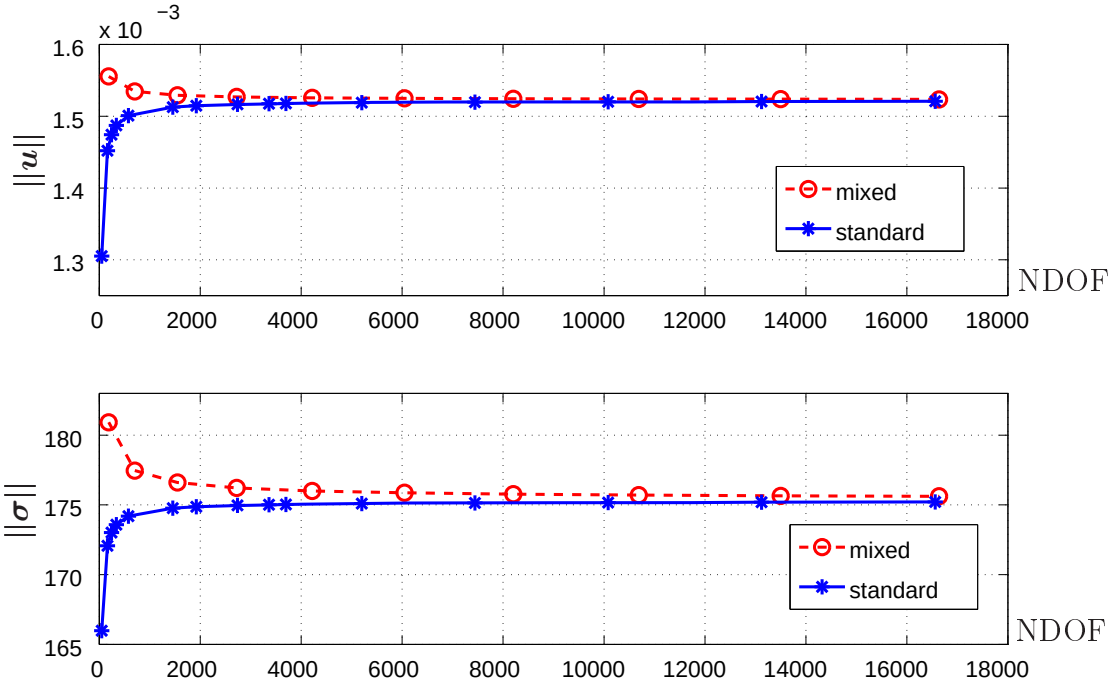

Figure 7.18: RVE:1 with square inclusion. Norms of the solution.

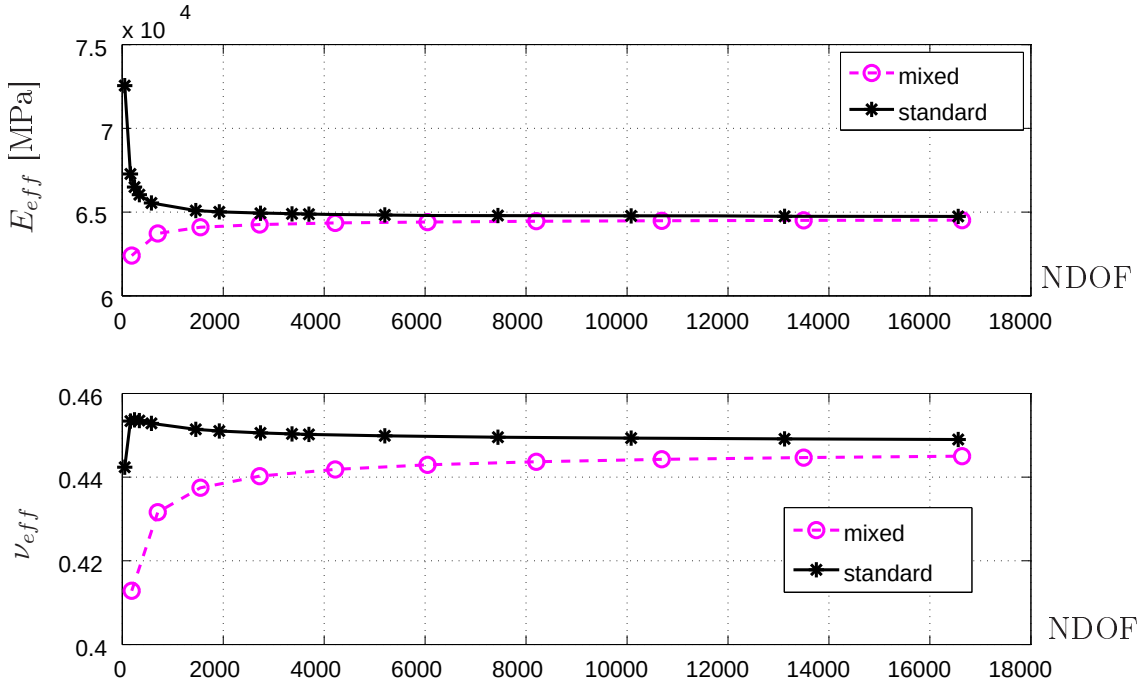

Figure 7.19: RVE:1 with square inclusion. Effective material parameters.

A similar test, for RVE with the same size and shape as previous, was performed with another material parameters, collected in Tab 7.2.

Material parameters	matrix	inclusion
E (GPa)	100	300
ν	0.3	0.3

Table 7.2: Material parameters for RVE:2 with square inclusion.

Convergence of solution norms and effective material parameters for uniform mesh refinements are shown in Figs. 7.20 and 7.21.

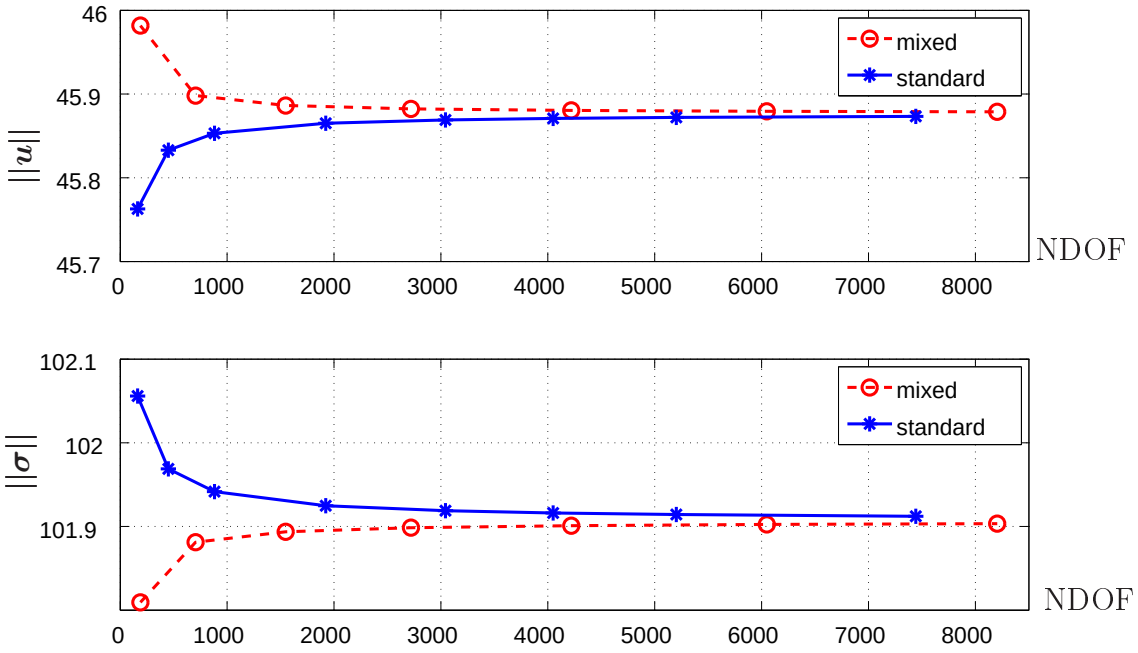

Figure 7.20: RVE:2 with square inclusion. Norms of the solution.

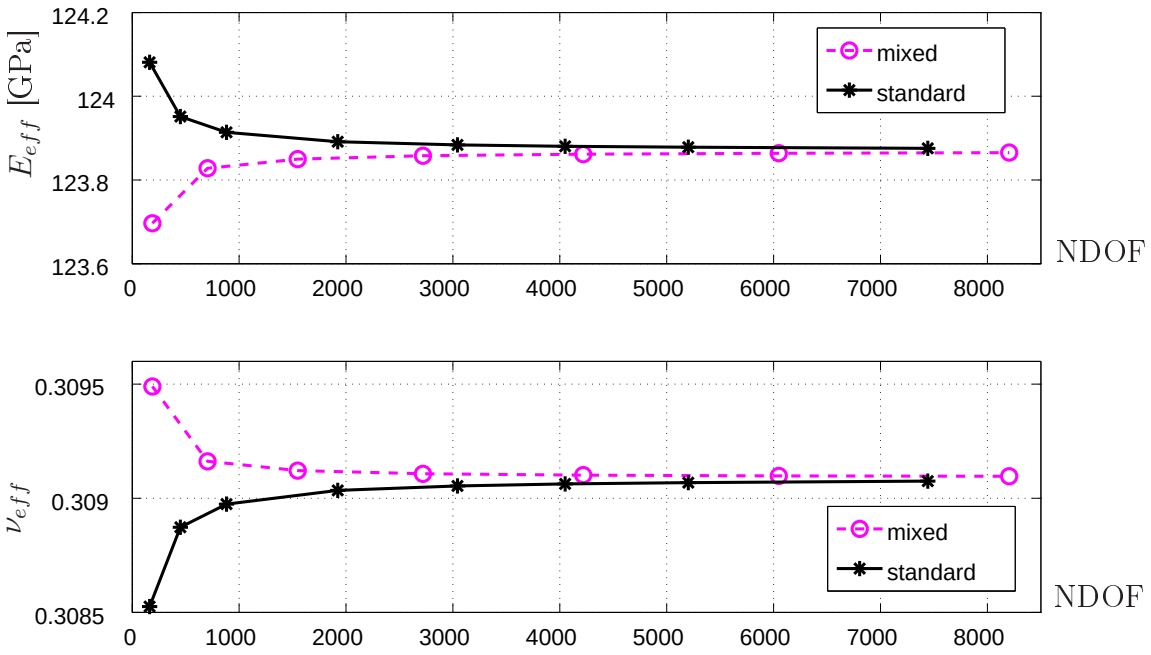

Figure 7.21: RVE:2 with square inclusion. Effective material parameters.

In the next example the square RVE 2 mm × 2 mm with circle-like inclusion (radius $r = 0.7$ mm) located centrally was tested. Numerical tensile test was analyzed with constant loading $q = 100$ kN/m. Because of the symmetry only a quarter of the plate was analyzed (Fig. 7.22). Material data were the same as for RVE:1 (summarized in Tab. 7.1). Principal directions of stresses are shown in Fig. 7.23. Contour maps of selected results are presented in Figs. 7.24 – 7.26.

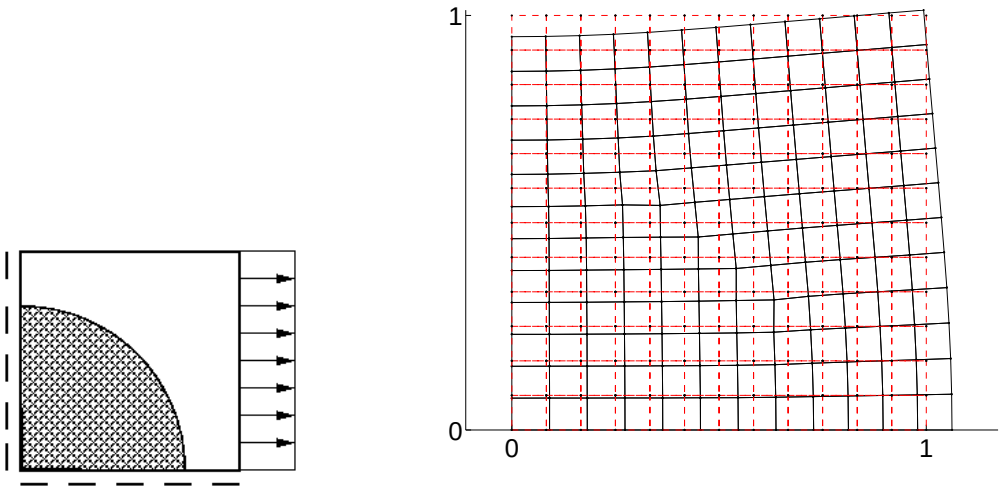

Figure 7.22: RVE:3 with circle inclusion. Boundary conditions and deformation.

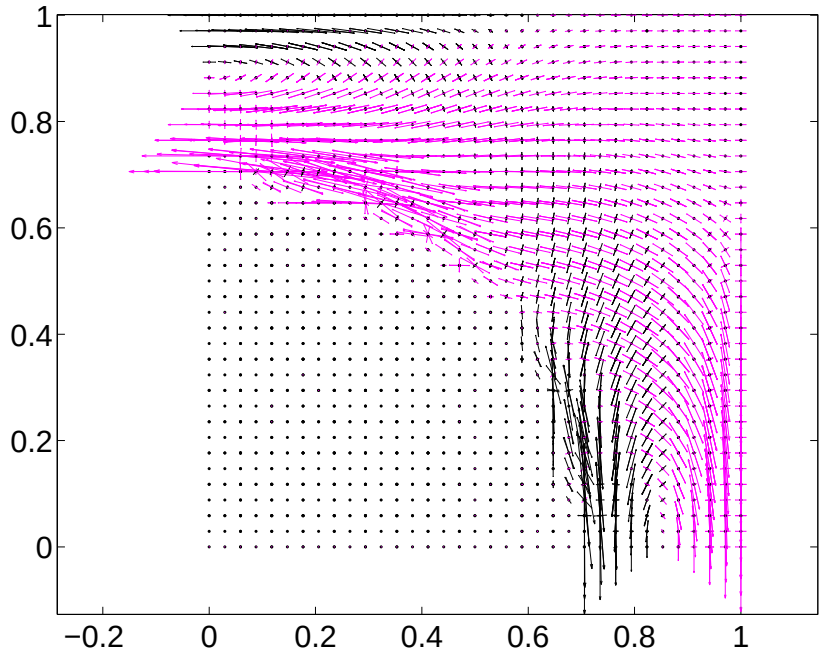

Figure 7.23: RVE:3 with circle inclusion. Principal stress directions.

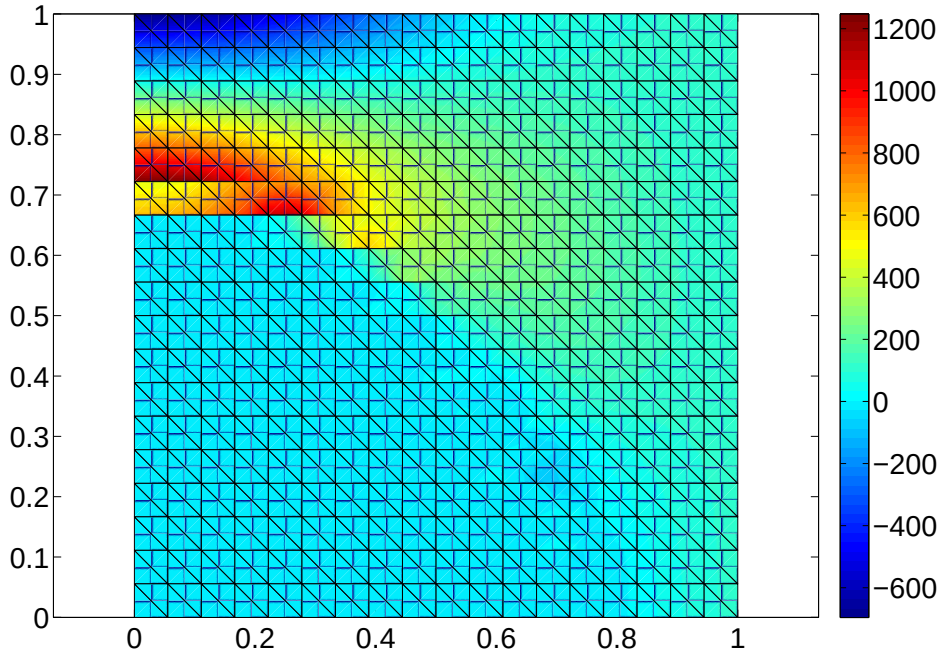

Figure 7.24: RVE:3 with circle inclusion. Component σ_{xx} of stress tensor.

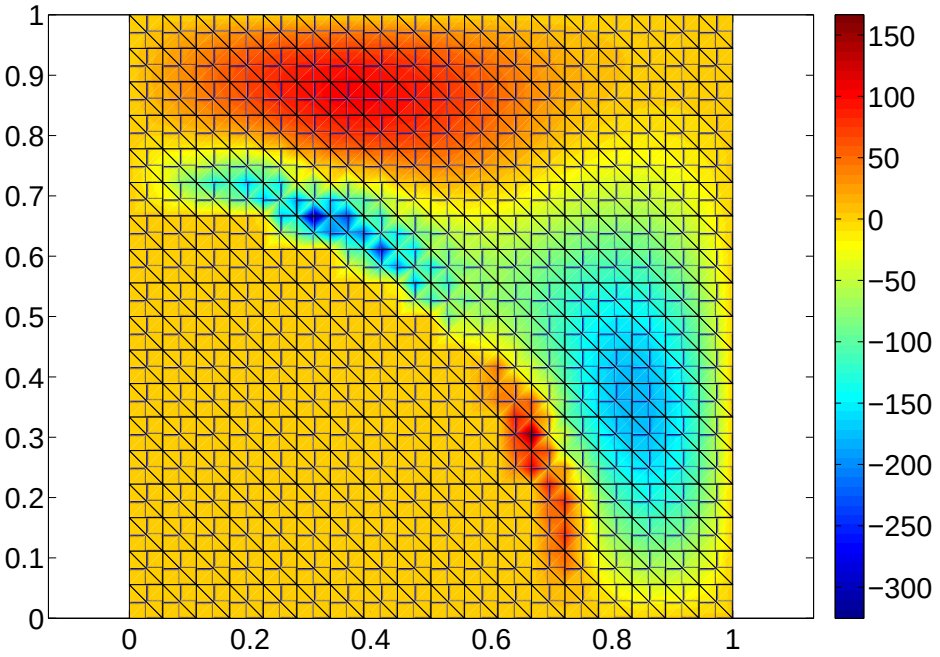

Figure 7.25: RVE:3 with circle inclusion. Component σ_{yx} of stress tensor.

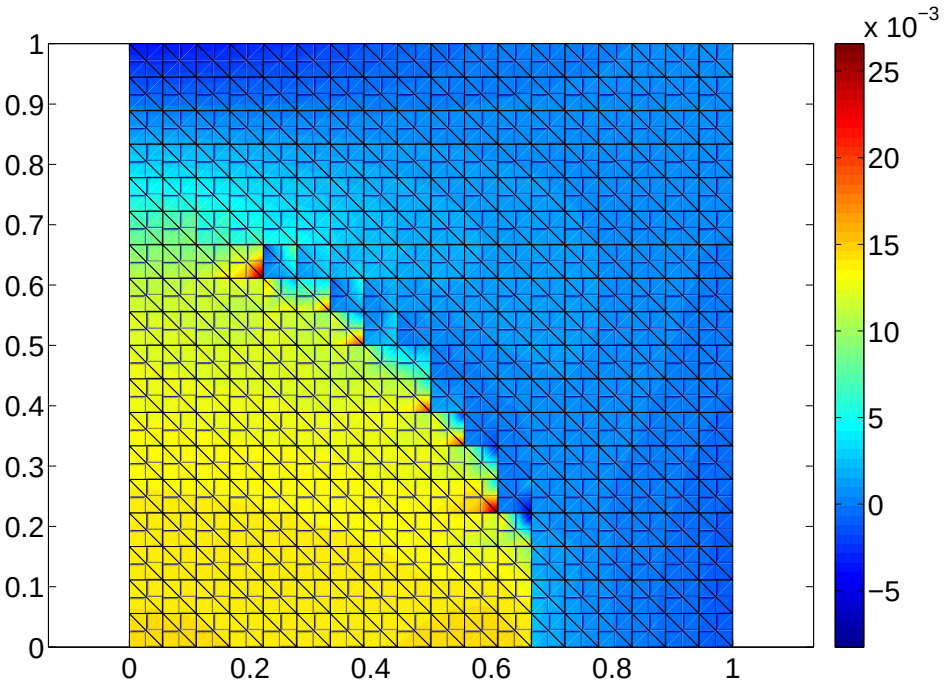

Figure 7.26: RVE:3 with circle inclusion. Component ε_{xx} of strain tensor.

Similarly, as in the previous tests, comparison of effective parameters and solution was carried out. The results are shown in Figs. 7.27 and 7.28.

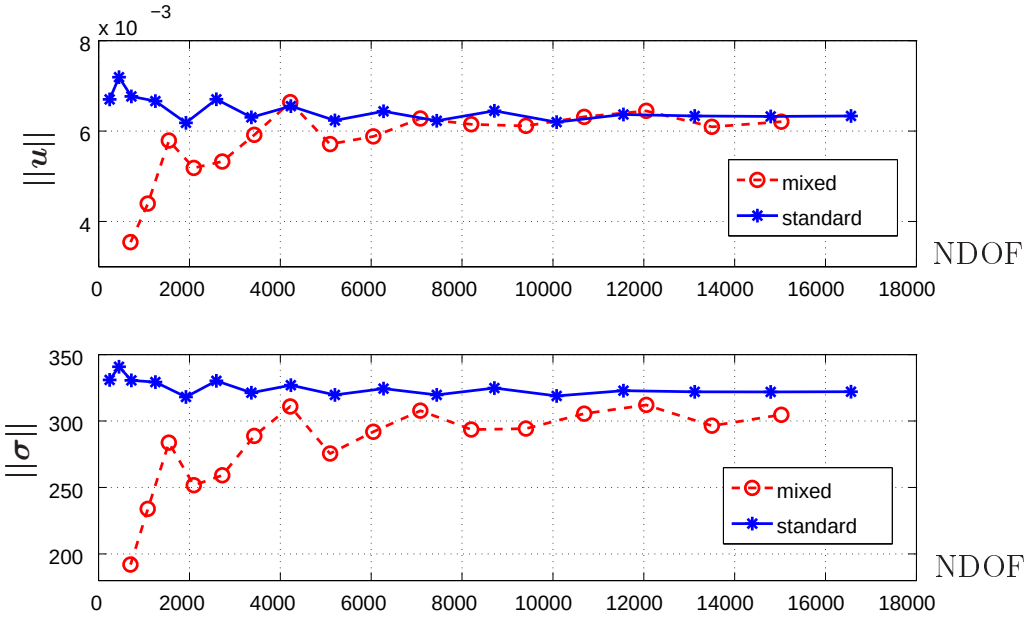

Figure 7.27: RVE:3 with circle inclusion. Norm of solutions.

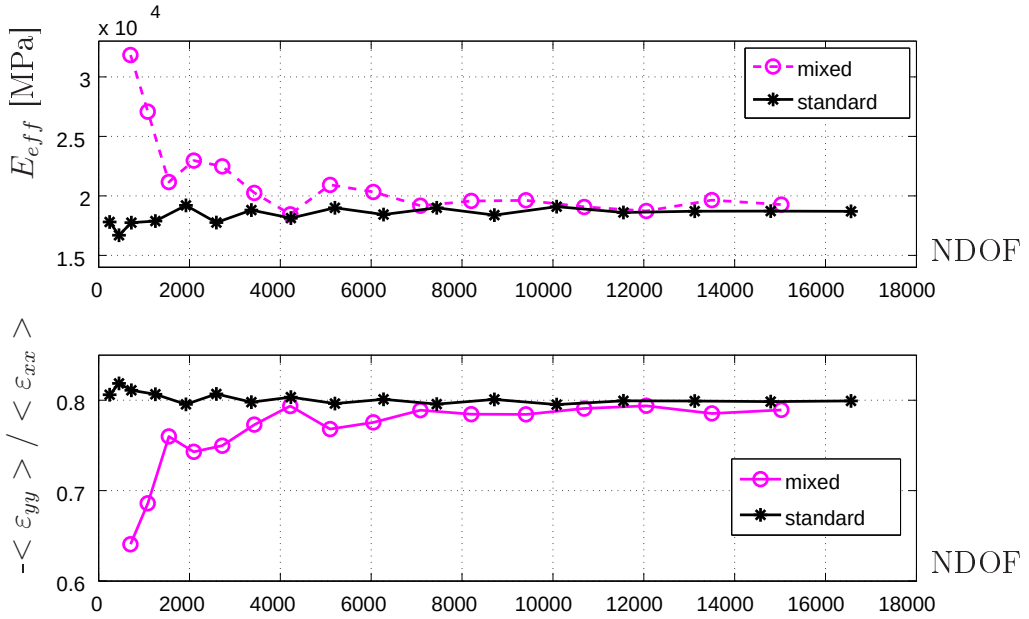

Figure 7.28: RVE:3 with circle inclusion. Effective material parameters.

Values greater than 0.5, obtained in the last test (Fig. 7.28) indicate that elastic continuum theory cannot be used at the macro-scale (non-homogeneous material).

In the next test square RVE 2 mm× 2 mm with circle inclusion ($r = 0.6$ mm) was tested. Material constants were the same as for RVE:2 (summarized in Tab. 7.2). Constant loading $q = 100$ kN/m was assumed for simulation of tensile test. Comparison of the results is shown in Figs. 7.29 and 7.30. The numerical comparison of the results is collected in Tab. 7.3.

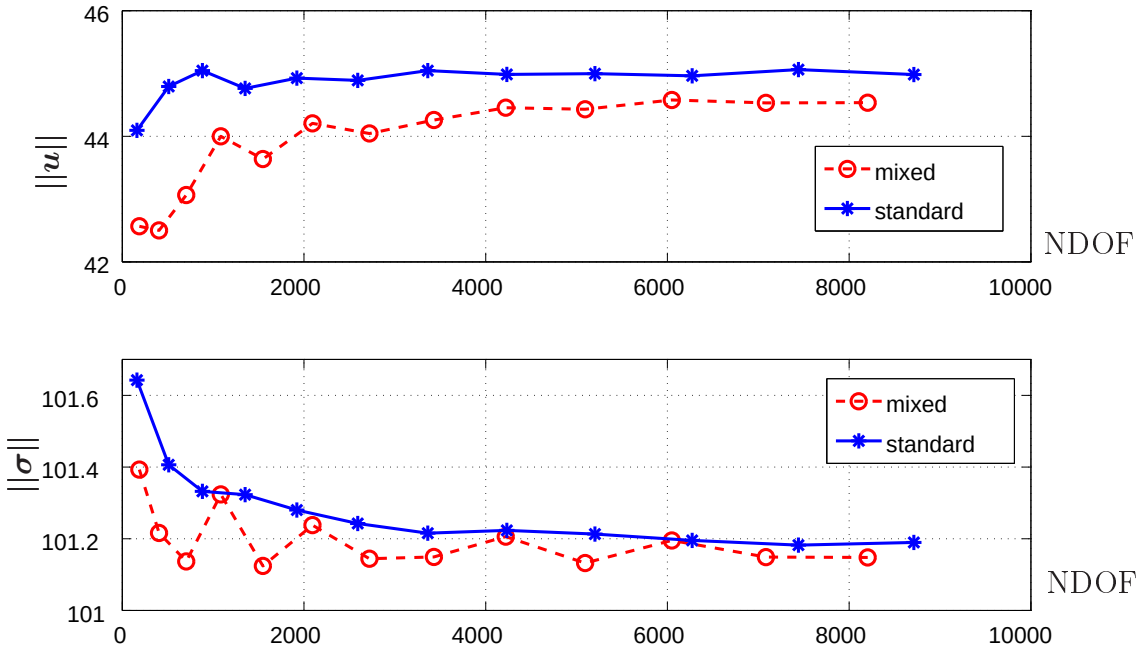

Figure 7.29: RVE:4 with circle inclusion. Norm of solutions.

Material parameters	mixed formulation	standard formulation
E_{eff} (GPa)	127.5	126.4
ν_{eff}	0.31	0.31

Table 7.3: Effective material parameters for RVE:4 with circle inclusion.

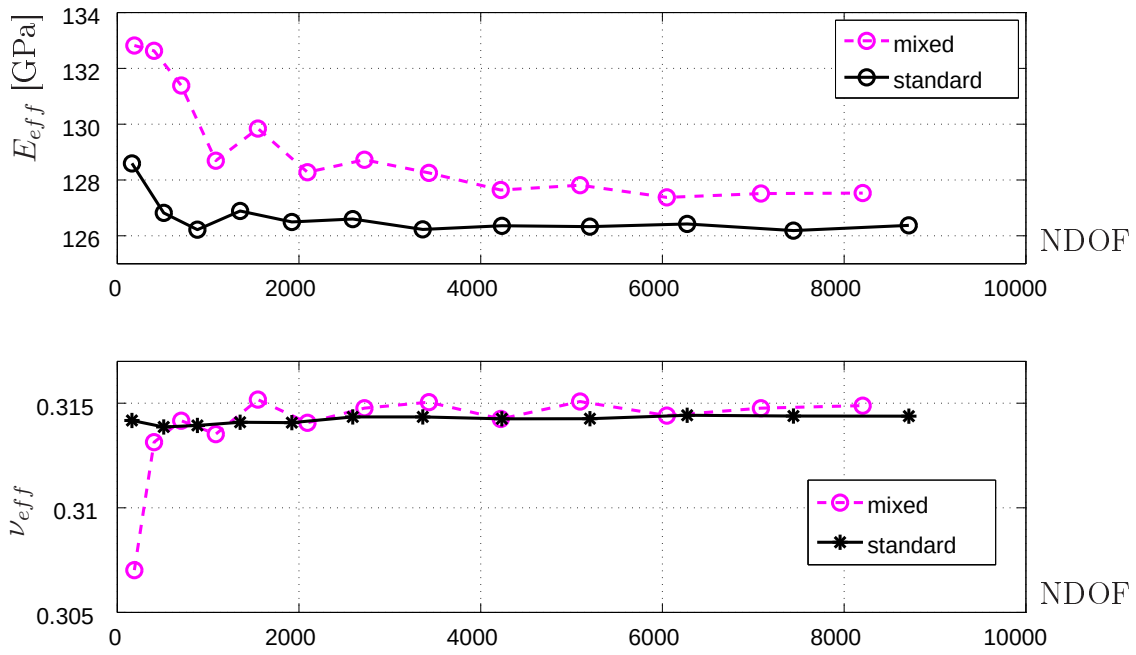

Figure 7.30: RVE:4 with circle inclusion. Effective material parameters.

The results confirm that simultaneous use of the standard and mixed approaches enables obtaining the effective parameters more precisely and faster than using only one of these FEM versions.

Chapter 8

Conclusions

The purpose of the presented research was to apply the *hp*-adaptive finite element method to modeling of inelastic heterogeneous materials (metal matrix composites) with periodic microstructure by two-scale approach. The thesis contains theoretical basis of inelastic, RVE based computational homogenization, mathematical formulations, details of the algorithms and many numerical examples (1D, 2D and 3D problems) that illustrate the proposed approaches.

Computations, both in the macro and micro-scale, were performed using automatic *hp* FEM that enables obtaining accurate results in a reasonable time. In each adaptation step appropriate anisotropic h, p or hp mesh refinements are performed to find optimal mesh for the assumed accuracy. This technique, used so far only for linear problems, is especially efficient in analysis of heterogeneous materials, when FE mesh should fit, in the best possible way, the material boundaries.

In the classical algorithm of computational homogenization each quadrature point is associated to RVE. However, if inelastic behavior occurs such an analysis is rarely possible to perform, even using parallel computations. In this work two other possibilities of two-scale homogenization were presented. The first one was based on the single RVE analysis used for evaluation of effective parameters, both for elastic and plastic material behavior. These parameters were later on applied to evaluate the macro-scale global response of homogenized body. The second approach was more similar to classical homogenization algorithm. However, the set of RVE was restricted to certain number and they were associated to selected fixed points, independent of the Gauss integration abscissas. This way the number of RVE was significantly reduced and the results were accurate enough.

Sometimes homogenization may introduce too large error resulting from the loss of information about microstructure. Thus, it is necessary to determine the subdomains, where homogenization should not be used. In this work three possibilities of homogenization error estimation, based on the upper bound approach, residuum of equilibrium equation and subdomain analysis, were used. Assessment of homogenization error and detailed microstructure consideration in selected parts allow improvement of modeling reliability and accuracy.

In this work the automatic *hp* adaptive FEM was tested for inelastic problems. The obtained results enable one to confirm that the original algorithm works correctly, even for inelastic problems. Additional refinement of finite elements with both elastic and plastic zones introduced in order to better adjust the mesh to elastic-plastic interface

did not improve the convergence.

From engineering point of view correct estimation of stresses is necessary for the safety of structures. In classical FEM the primary unknowns are displacements, while stresses are computed during post-processing. A mixed method, where both displacement and stress are approximated independently, seems to be a better approach. In this work mixed formulation based on the modified Hellinger–Reissner principle with weakly enforced symmetry of stress tensor and new shape functions were used and validated on several examples. Direct stress approximation is certainly an advantage of this method. However, special requirements that guarantee stability of approximation, have to be fulfilled.

In this research numerical analysis was performed using three adaptive FE computer codes, developed by Demkowicz group, written in $Fortran95$ ($hp1D$, $hp2D$ and $hp3D$). They had to be modified and supplemented with a number of own routines that enable e.g.:

- definition of material distribution for RVE
- computation of average values of strains, stresses, effective material parameters, verification of Hill-Mandel condition
- driving integration of the plasticity problem
- post-processing (dumping data, plotting graphs of functions along a segment or in a domain)
- detection of various materials or plastic zones in elements
- estimation of modeling error and determination of subregions with large error
- modification of adaptation process for inelastic problems.

Certain computations were carried out by independent codes prepared in either Fortran (especially mixed method) or Matlab environment (for initial tests and additional post-processing of results). All of the self prepared routines contain more than 20000 lines.

The main original contributions of the work are:

- application of automatic *hp*-adaptive FEM to inelastic two-scale homogenization
- elastic-plastic two-scale analysis based on limited number of RVE (either one or a few assumed independently of Gauss integration points) with continuous approximation of effective material parameters
- modeling error estimation to select parts of the domain where homogenization should not be used
- modification and testing of *hp*-adaptation algorithm for inelastic problems
- application of a mixed FEM with new shape functions

The new approaches developed in this work might be applied to many engineering problems, such as: predicting the properties and thus efficient design of new metallic composites, calculation of deformations and stresses in bodies made of such composites. Future work on development of this approach may by focused in particular on further tests and mathematical proofs for modeling error estimates, adaptive distribution of fixed RVE, implementation of other constitutive laws at the micro-level, analysis of random distribution of inclusions, detection of debonding of materials, comparison of the results with experimental results.

List of Figures

List of Tables

Bibliography

[1] J. Aarnes and T.Y.Hou. Multiscale domain decomposition methods for elliptic problems with high aspect ratios. *Acta Mathematicae Applicatae Sinica, English Series*, 18(1):63–76, 2002.

[2] D. N. Arnold, G. Awanou, and R. Winther. Finite elements for symmetric tensors in three dimensions. *Mathematics of Computations*, 77(263):1229–1251, 2008.

[3] D. N. Arnold, D. Boffi, and R. Falk. Quadrilateral H(div) finite elements. *SIAM J.Numer.Anal.*, 42(6):2429–2451, 2005.

[4] D. N. Arnold, R. Falk, and R. Winther. Mixed finite element methods for linear elasticity with weakly imposed symmetry. *Mathematics of Computations*, 76(260):1699–1723, 2007.

[5] I. Babuška. The finite element method with Lagrangian multipliers. *Numer. Math.*, 20:179–192, 1973.

[6] I. Babuška, R. B. Kellogg, and J. Pitkaranta. Direct and inverse error estimates for finite elements with mesh refinement. *Numer. Math.*, 33:447–471, 1979.

[7] I. Babuška and A. Miller. A feedback finite element method with a posteriori error estimation. Part 1. *Comp. Meth. Appl. Mech. Engng*, 61:1–40, 1987.

[8] I. Babuška and W. C. Rheinboldt. Error estimates for adaptive finite element computations. *Int. J. Num. Meth. Engng*, 12:1597–1615, 1978.

[9] I. Babuška and M. Suri. The p and hp versions of the finite element methods, basic principles and properties. *SIAM rev.*, 36:578–632, 1994.

[10] I. Babuška, B. A. Szabo, and I. N. Katz. The p-version of the finite element method. *SIAM J. Numer. Anal.*, 18:515–545, 1981.

[11] F. Barthold, M. Schmidt, and E. Stein. Error indicators and mesh refinements for finite-element-computations of elastoplastic deformations. *Computational Mechanics*, 22(225-238), 1998.

[12] P. K. Basu and A. G. Peano. Adaptivity in p-version finite element analysis. *J. of Struct. Engng.*, 109:2310–2324, 1983.

[13] A. Bensoussan, J. L. Lions, and G. Papanicolaou. *Asymptotic Analysis for Periodic Structures*. Elsevier, North-Holland, 1978.

[14] S. Boucher. On the effective moduli of isotropic two-phase elastic composites. *Journal of Composite Materials*, 8:82–89, 1974.

[15] L. Boulaajinea, S. Nicaise, L. Paquet, and Rafilipojaona. Dual mixed finite element methods for the elasticity problem with Lagrange multipliers. *Journal of Computational and Applied Mathematics*, 221:234–260, 2008.

[16] F. Brezzi. On the existence, uniqueness and approximation of saddle-point problems arising from lagrangian multipliers. *Rev. Francaise Automat. Informat. Recherche Operationnelle Ser. Rouge*, 8(151):129–211, 1974.

[17] F. Brezzi and L.D. Marini. A survey on mixed finite element methods. *IEEE Transactions on Magnetics*, 30(5):3547–3551, 1994.

[18] O. Cazacu. *Multiscale Modeling of Heterogenous Materials.* Eisenbrauns Inc., 2008.

[19] W. Cecot. Adaptive FEM analysis of selected elastic-visco-plastic problems. *Comp. Meth. Appl. Mech. Engng*, 196:3859–3870, 2007.

[20] J. H. Cheng. Automatic adaptive remeshing for finite element simulation of forming processes. *Int. J. Num. Meth. Engng*, 26:1–18, 1988.

[21] R. M. Christensen and K. H. Lo. Solutions for effective shear properties in three phase sphere and cylinder models. *J. Mech. Phys. Solids*, 27:315–330, 1979.

[22] M. Chrzanowski and K. Nowak. Cellular automata in damage mechanics: creep rupture case. *Arch. Mech.*, 59:329–339, 2007.

[23] P. G. Ciarlet. *Mathematical Elasticity: Three-Dimensional Elasticity.* North-Holland, 1994.

[24] H. Cramer, R. Findeiss, G. Steinl, and W. Wunderlich. An approach to the adaptive finite element analysis in associated and non-associated plasticity considering localization phenomena. *Comp. Meth. Appl. Mech. Engng*, 176:187–202, 1999.

[25] M. Crouzeix and P. A. Raviart. Conforming and nonconforming finite element methods for solving the stationary Stokes equations. *R.A.I.R.O. R3*, 7:33–76, 1973.

[26] L. Demkowicz. *Computing with* hp-*Adaptive Finite Elements. Vol. 1. One and Two Dimensional Elliptic and Maxwell Problems.* Chapman & Hall/CRC, 2006.

[27] L. Demkowicz, J. Kurtz, D. Pardo, M. Paszynski, W. Rachowicz, and A. Zdunek. *Computing with hp Finite Elements. Vol 2. Frontiers: Three-Dimensional Elliptic and Maxwell Problems with Applications.* Chapman & Hall/CRC, 2007.

[28] L. Demkowicz, J. T. Oden, W. Rachowicz, and O. Hardy. Toward a universal *hp*-adaptive finite element strategy. Part 1: Constrained approximation and data structure. *Comp. Meth. Appl. Mech. Engng*, 77:79–112, 1989.

[29] L. Demkowicz, W. Rachowicz, and Ph. Devloo. A fully automatic *hp*-adaptivity. *Journal of Scientific Computing*, 17:127–155, 2002.

[30] A. Düster and E. Rank. A p-version finite element approach for two- and three-dimensional problems of the J2 flow theory with non-linear isotropic hardening. *Int. J. Numer. Meth. Engng*, 53:49–63, 2002.

[31] J. Engström. *Some Developments of the Homogenization Theory and Related Questions*. PhD thesis, Luleå University of Technology, Department of Mathematics, Luleå, Sweden, 2005.

[32] J. D. Eshelby. The determination of the elastic field of an ellipsoidal inclusion, and related problems. *Proc. R. Soc. Lond. A*, 241:376–396, 1957.

[33] R. Falk. Finite elements methods for linear elasticity. In D. Boffi et al., editors, *Mixed Finite Elements, Compatibility Conditions, and Applications*, pages 159–194. Springer, 2008.

[34] C. A. Felippa. Introduction to finite element methods. Online course materials, Chapter 9, 2007.

[35] F. Feyel. A multilevel finite element method (FE^2) to describe the response of highly non-linear structures using generalized continua. *Comput. Methods Appl. Mech. Engrg.*, 192:3233–3244, 2003.

[36] J. Fish and Z. Yuan. Multiscale enrichment based on partition of unity. *Int. J. Numer. Meth. Engng*, 62:1341–1359, 2005.

[37] L. Gallimard, P. Ladeveze, and J. P. Pelle. Error estimation and adaptivity in elastoplasticity. *Int. J. Numer. Meth. Engng*, 39:189–217, 1996.

[38] J. Gawąd, P. Macioł, and M. Pietrzyk. Multiscale modelling of microstructure and macroscopic properties in thixoforming process using cellular automation technique. *Archives of Metallurgy and Materials*, 50:549–562, 2005.

[39] I. Gitman. *Representative Volumes and Multi-scale Modelling of Quasi-brittle Materials*. PhD thesis, Delft University of Technology, 2006.

[40] W. Gui and I. Babuška. The h, p and hp versions of the finite element method in one dimension. Parts 1,2,3. *Numer. Math.*, 49:577–683, 1986.

[41] B. Guo and I. Babuška. The $h - p$ Version of the Finite Element Method, Part 1: The Basic Approximation Results. *Comp. Mech.*, 1:22–41, 1986.

[42] Z. Hashin and S. Shtrikman. A variational approach to the theory of the elastic behaviour of polycrystals. *J Mech Phys Solids*, 10:343–352, 1962.

[43] Z. Hashin and S. Shtrikman. A variational approach to the elastic behaviour of multiphase materials. *J. Mech. Phys. Solids*, 11:127–140, 1963.

[44] J. Haslinger, P. Neittaanmaki, and K. Salmenjoki. On FE-grid relocation in solving unilateral boundary value problems by FEM. *Applications of Mathematics*, 37:105–122, 1992.

[45] B. Hassani. A direct method to derive the boundary conditions of the homogenization equation for symmetric cells. *Comm. in Num. Meth. in Engng*, 12:185–196, 1996.

[46] R. Hill. Elastic properties of reinforced solids: some theoreticel principles. *Journal of the Mechanics and Physics of Solids*, 11(357-372), 1963.

[47] R. Hill. A self-consistent mechanics of composite materials. *J. Mech. Phys. Solids*, 13(189-198), 1965.

[48] R. Hill. The essential structure of constitutive laws for metal composites and polycrystals. *Journal of the Mechanics and Physics of Solids*, 15(79-95), 1967.

[49] C. K. Jhurani. *Multiscale Modeling Using Goal-oriented Adaptivity and Numerical Homogenization*. PhD thesis, The University of Texas at Austin, 2009.

[50] C. K. Jhurani and L. Demkowicz. A goal-oriented hp-adaptive dimensional reduction method for one-dimensional network of linear springs. Technical report, The University of Texas at Austin, ICES, 2006.

[51] J. Kaczmar, K. Pietrzak, and W. Wlosinski. The production and application of metal matrix composite materials. *Journal of Materials Processing Technology*, 106:58–67, 2000.

[52] L. Kaczmarczyk. *Numeryczna analiza wybranych problemów mechaniki ośrodków niejednorodnych*. PhD thesis, Cracow University of Technology, 2006.

[53] L. Kaczmarczyk, C. Pearce, and N. Bicanic. Scale transition and enforcement of rve boundary conditions in second-order computational homogenization. *Int. J. Numer. Meth. Engng*, 74:506–522, 2008.

[54] P. Kanoute, D. P. Boso, J. L. Chaboche, and B. A. Schrefler. Multiscale methods for composites: A review. *Arch Comput Methods Eng*, 16:31–75, 2009.

[55] M. Klimczak and W. Cecot. Local homogenization in modeling of asphalt pavement structures. *Czasopismo Techniczne*, 3(1-B):87–94, 2011.

[56] V. G. Kouznetsova, M. G. D. Geers, and W. A. M. Brekelmans. Multi-scale second-order computational homogenization of multi-phase materials: a nested finite element solution strategy. *Comput. Methods Appl. Mech. Engrg.*, 193:5525–5550, 2004.

[57] V. G. Kouznetsova, M. G. D. Geers, and W. A. M. Brekelmans. Size of a representative volume element in a second-order computational homogenization framework. *International Journal for Multiscale Computational Engineering*, 2(4):575–598, 2004.

[58] Y. W. Kwon, D. H. Allen, and R. R. Talreja. *Multiscale Modeling and Simulation of Composite Materials and Structures*. Springer, 2008.

[59] P. Lancaster and K. Salkauskas. Surface generated by moving least squares methods. *Mathematics of Computation*, 155(37):141–158, 1981.

[60] T. Lewiński and J. J. Telega. *Plates, laminates, and shells : asymptotic analysis and homogenization*, volume 52 of *Advances in Mathematics for Applied Sciences*. World Scientific Publishing, 1999.

[61] W. Li and M. Ostoja-Starzewski. Yield of random elasto-plastic materials. *Journal of Mechanics of Materials and Structures*, 1:1055–1073, 2006.

[62] T. Liszka and J. Orkisz. The finite difference method at arbitrary irregular grids and its applications in applied mechanics. *Comp. & Struct.*, 11:83–95, 1980.

[63] S. P. MacLachlan. *Improving Robustness in Multiscale Methods*. PhD thesis, University of Colorado, Department of Applied Mathematics, 2004.

[64] L. Madej, P. D. Hodgson, and M. Pietrzyk. Multi-scale rheological model for discontinuous phenomena in materials under deformation conditions. *Computational Materials Science*, 38:685–691, 2007.

[65] L. Madej, P. D. Hodgson, and M. Pietrzyk. The validation of a multiscale rheological model of discontinuous phenomena during metal rolling. *Computational Materials Science*, 41:236–241, 2007.

[66] J. C. Michel, H. Moulinec, and P. Suquet. Effective properties of composite materials with periodic microstructure: a computational approach. *Comput. Methods Appl. Mech. Engrg*, 172:109–143, 1999.

[67] C. Miehe and A. Koch. Computational micro-to-macro transitions of discretized microstructures undergoing small strains. *Archive of Applied Mechanics*, 72(300-317), 2002.

[68] C. Miehe, J. Schröder, and J. Schotte. Computational homogenization analysis in finite plasticity simulation of texture development in polycrystalline materials. *Comput. Methods Appl. Mech. Engrg.*, 171:387–418, 1999.

[69] N. Moes, J. Dolbow, and T. Belytschko. A finite element method for crack growth without remeshing. *International Journal for Numerical Methods in Engineering*, 46:131–150, 1999.

[70] I. Monetto and W. J. Drugan. A micromechanics-based nonlocal constitutive equation and minimum RVE size estimates for random elastic composites containing aligned spheroidal heterogeneities. *Journal of the Mechanics and Physics of Solids*, 57:1578–1595, 2009.

[71] T. Mori and K. Tanaka. Average stress in the matrix and average elastic energy of materials with misfitting inclusions. *Acta metall.*, 21:571–574, 1973.

[72] S. Nemat-Nasser and M. Hori. *Micromechanics: Overall Properties of Heterogeneous Solids*. Elsevier Science Publishers, 2 edition, 1999.

[73] V. Nübel, A. Düster, and E. Rank. An rp-adaptive finite element method for the deformation theory of plasticity. *Comput. Mech.*, 39:557–574, 2007.

[74] J. T. Oden, L. Demkowicz, W. Rachowicz, and T. A. Westermann. Toward a universal *hp*-adaptive finite element strategy. Part 2: A posteriori error estimation. *Comp. Meth. Appl. Mech. Engng*, 77:113–180, 1989.

[75] J. T. Oden and S. Prudhomme. Goal-oriented error estimation and adaptivity for the finite element method. *Computers and Mathematics with Applications*, 41:735–756, 2001.

[76] J. T. Oden and S. Prudhomme. Estimation of modeling error in computational mechanics. *J. Comput. Phys.*, 182:496–515, 2002.

[77] J. T. Oden and K. S. Vemaganti. Estimation of local modeling error and goal-oriented adaptive modeling of heterogeneous materials. Part I. Error estimates and adaptive algorithms. *Journal of Computational Physics*, 164:22–47, 2000.

[78] M. Ostoja-Starzewski. Material spatial randomness: from statistical to representative volume element. *Probabilist. Engrg. Mech.*, 21:112–132, 2006.

[79] M. Ostoja-Starzewski. *Microstructural Randomness and Scaling In Mechanics Of Materials*. Chapman & Hall/CRC, 2008.

[80] C. Pelissou, J. Baccou, Y. Monerie, and F. Perales. Determination of the size of the representative volume element for random quasi-brittle composites. *International Journal of Solids and Structures*, 46:2842–2855, 2009.

[81] D. Peric, M. Dutko, and D. Owen. Aspects of adaptive strategies for large deformation problems at finite inelastic strains. In P. Ladeveze and J. T. Oden, editors, *Advances in Adaptive Computational Methods in Mechanics*, pages 349–363. Elsevier, 1998.

[82] D. Peric, Ch. Hochard, M. Dutko, and D. Owen. Transfer operators for evolving meshes in small strain elasto-plasticity. *Comp. Meth. Appl. Mech. Engng*, 137:331–344, 1996.

[83] D. Peric, J. Yu, and D. Owen. On error estimates and adaptivity in elastoplastic solids. *Int. J. Num. Meth. Engng*, 37:1351–1379, 1994.

[84] S. Prudhomme and J. T. Oden. On goal oriented error estimation for elliptic problems. *Comp. Meth. Appl. Mech. Engng*, 176:313–331, 1999.

[85] W. Qiu and L. Demkowicz. Mixed hp-finite element method for linear elasticity with weakly imposed symmetry. *Comp. Meth. Appl. Mech. Engng*, 198:3682–3701, 2009.

[86] P. Raghavan, S. Li, and S. Ghosh. Two scale response and damage modeling of composite materials. *Finite Elements in Analysis and Design*, 40:1619–1640, 2004.

[87] P. A. Raviart and J. M. Thomas. A mixed finite element method for 2-nd order elliptic problems. In A. Dold and B. Eckmann, editors, *Mathematical Aspects of Finite Element Methods*, pages 292–315. Springer:Berlin, 1977.

[88] A. Reuss. Berechnung der Fliessgrenze von Mischkristallen auf Grund der Plastizität Sbedingung fur Einkristalle. *Zeitschrift für angewandte Mathematik und Mechanik*, 9:49–58, 1929.

[89] R. Roscoe. Isotropic composites with elastic or viscoelastic phases: General bounds for the moduli and solutions for special geometries. *Rheologica Acta*, 12:404–411, 1973.

[90] E. Sanchez-Palencia. Non-homogeneous media and vibration theory. In *Lecture Notes in Physics 127*. Springer, 1980.

[91] M. Serafin and W. Cecot. Toward two-scale adaptive FEM modeling of nonlinear heterogeneous materials. *International Journal for Multiscale Computational Engineering*, 8(3):303–317, 2010.

[92] D. Shepard. A two-dimensional interpolation function for irregularly spaced points. In *Proceedings of the ACM Nat. Conf.*, pages 517–524, 1968.

[93] J. C. Simo and T. J. R. Hughes. *Computational Inelasticity*. Springer-Verlag, 1998.

[94] J. C. Simo and R. I. Taylor. Return mapping algorithm for plane stress elastoplasticity. *Int. J. Num. Meth. Engng*, 22:649–670, 1986.

[95] M. Stroeven, H. Askes, and L.J. Sluys. Numerical determination of representative volumes for granular materials. *Comput. Methods Appl. Mech. Engrg.*, 193:3221–3238, 2004.

[96] T. Strouboulis, K. Copps, and I. Babuska. The generalized finite element method. *Comput. Methods Appl. Mech. Eng.*, 190:4081–4193, 2001.

[97] T. Strzelecki. *Mechanika ośrodków niejednorodnych. Teoria homogenizacji*. DWE, 1996.

[98] P. Suquet. *Homogenization Techniques for Composite Media*, chapter Elements of homogenization theory for inelastic solid mechanics. Springer-Verlag, 1987. E. Sanchez-Palencia and A. Zaoui (Eds.), 194-275.

[99] S. Swaminathan, S. Ghosh, and N. J. Pagano. Statistically equivalent representative volume elements for unidirectional composite microstructures: Part I - without damage. *Journal of Composite Materials*, 40(7):583–604, 2006.

[100] B. Szabo and G. Sharmann. Hierarchic plate and shell models based on p-extensions. *International Journal for Numerical Methods in Engineering*, 26:1855–1881, 1988.

[101] I. Temizer and P. Wriggers. An adaptive multiscale resolution strategy for the finite deformation analysis of microheterogeneous structures. *Comput. Methods Appl. Mech. Engrg.*, 200:2639–2661, 2011.

[102] R. Tews and W. Rachowicz. Application of an automatic *hp* adaptive finite element method for thin-walled structures. *Comput. Methods Appl. Mech. Engrg.*, 198:1967–1984, 2009.

[103] J. Thompson. A survey of dynamically-adaptive grids in the numerical solution of partial differential equations. *Applied Numerical Mathematics*, 1:3–27, 1985.

[104] A. Urbański. *The Unified Finite Element Formulation of Homogenization of Structural Members with a Periodic Microstructure*, volume 320 of *Civil Engineering*. Cracow University of Technology Press, 2005.

[105] K. Vemaganti. Modelling error estimation and adaptive modelling of perforated materials. *Int. J. Numer. Meth. Engng*, 59:1587–1604, 2004.

[106] K. S. Vemaganti and J. T. Oden. Estimation of local modeling error and goal-oriented adaptive modeling of heterogeneous materials. Part II. A computational environment for adaptive modeling heterogeneous elastic solids. *Comput. Methods Appl. Mech. Engrg*, 190:6089–6124, 2001.

[107] W. Voigt. Über die Beziehung zwischen den beiden Elastizität Skonst Anten Isotroper Körper. *Wiedemanns Annalen der Physik und Chemie (Leipzig)*, 38:573–587, 1889.

[108] P. Wesseling. *An Introduction to Multigrid Methods*. Wiley, 1992.

[109] W. Wunderlich, H. Cramer, and G. Steinl. An adaptive finite element approach in associated and non-associated plasticity considering localization phenomena. In P. Ladeveze and J. T. Oden, editors, *Adaptive Computational Methods in Mechanics*, pages 293–332. Elsevier, 1998.

[110] Z. Xia, Y. Zhang, and F. Ellyin. A unified periodical boundary conditions for representative volume elements of composites and applications. *International Journal of Solids and Structures*, 40:1907–1921, 2003.

[111] O. C. Zienkiewicz, G. C. Huang, and Y. C. Liu. Adaptive FEM computations of forming processes – application to porus and non-porus materials. *Int. J. Num. Meth. Engng*, 30:1527–1553, 1990.

[112] T. I. Zohdi, J. T. Oden, and G. J. Rodin. Hierarchical modeling of heterogeneous bodies. *Comput. Methods Appl. Mech. Engrg.*, 138:273–298, 1996.

[113] T. I. Zohdi and P. Wriggers. *An Introduction to Computational Micromechanics*, volume 20 of *Lecture Notes in Applied and Computational Mechanics*. Springer, 2008.

STRESZCZENIE

"Zastosowanie *hp*-adaptacyjnej MES do obliczeń dwuskalowych"

ROZDZIAŁ 1: WPROWADZENIE

Innowacyjne materiały są jednym z głównych czynników wpływających na rozwój technologii obserwowany w ostatnich latach. W tej dziedzinie kompozyty metaliczne (składające się przynajmniej z dwóch różnych składników matrycy oraz inkluzji w kształcie np. cząstek, włókien, warstw) stanowią materiał często stosowany przez inżynierów (m.in. w przemyśle samochodowym, lotniczym, kolejowym, militarnym, budownictwie itd.). W celu zmniejszenia zarówno kosztów, jak i czasu eksperymentów niezbędne jest ich uzupełnienie modelowaniem komputerowym, które pozwala przewidzieć nie tylko cechy nowo projektowanego materiału, lecz także zbadać bezpieczeństwo konstrukcji, w których te materiały będą używane.

Modelowanie komputerowe wymaga wprowadzenia pewnych uproszczeń. Jednym z nich jest zastosowanie podejścia wieloskalowego, w którym można przewidzieć ogólne własności materiału przez systematyczne zmniejszanie ogromnej, i zwykle niepotrzebnej, ilości informacji o mikrostrukturze. Taki proces nazywany jest homogenizacją. W szczególności jej obliczeniowa wersja (ang. *computational homogenization*) stanowi efektywne narzędzie do modelowania.

W niniejszej pracy analizowane są elementy konstrukcyjne wykonane z kompozytów metalicznych, modelowane w zakresie sprężystym i poza nim. Do obliczeń wykorzystana jest *hp*-adaptacyjna wersja metody elementów skończonych, która umożliwia efektywne przeprowadzenie obliczeń. Głównym celem pracy jest połączenie homogenizacji obliczeniowej i adaptacyjnej MES, w celu uzyskania skutecznego narzędzia do modelowania wspomnianych kompozytów.

W rozdziale 1 omówiono aktualny stan wiedzy dotyczący metod modelowania wieloskalowego i technik adaptacyjnych w metodzie elementów skończonych. Rozdział 2 zawiera opis modeli matematycznych, sformułowania i ogólne założenia. Rozdział 3 przedstawia wstępne testy homogenizacji obliczeniowej, w tym weryfikację algorytmu i szczegóły dyskretyzacji elementami skończonymi. W kolejnym rozdziale zawarto algorytm modelowania dwuskalowego dla kompozytów w zakresie sprężysto-plastycznym, który został zilustrowany licznymi przykładami. Rozdział 5 dotyczy oszacowania błędu homogenizacji, kluczowego dla uzyskania wiarygodnych wyników. Rozdział 6 przedstawia testy modyfikacji *hp*-adaptacyjnego algorytmu dla zagadnień niesprężystych. W

rozdziale 7 pokazano możliwości zastosowania mieszanego (wielopolowego) sformułowania metody elementów skończonych do modelowania wieloskalowego. Rozdział 8 podsumowuje pracę.

Wszystkie materiały używane w inżynierii mają niejednorodną strukturę, którą można dostrzec w odpowiedniej skali. Różne skale są zdefiniowane przez ich charakterystyczny wymiar, najczęściej jest to wymiar geometrii elementów struktury materiału, np. nominalna średnica kruszywa mieszanki betonowej, ale może to być również długość fali dla problemów akustyki. Dla różnych skal analizy, zarówno w czasie jak i przestrzeni, mogą obowiązywać inne prawa fizyki.

Jedną z możliwych metod analizy ośrodka niejednorodnego jest stworzenie modelu obliczeniowego z uwzględnieniem wszystkich szczegółowych informacji. W tym celu niezbędne jest zastosowanie komputerów dużej mocy oraz efektywnych technik numerycznych, np. adaptacyjne [6, 12, 29, 40] lub wzbogacone [69, 96] metody elementów skończonych, podejścia wielosiatkowe [63, 108], podział na podobszary [1], obliczenia równoległe. Zazwyczaj jednak koszt obliczeniowy takiego podejścia wciąż jest zbyt duży, a szczegółowość uzyskanych wyników nadmierna.

W przypadku kompozytów deformujących się sprężyście najprostszym podejściem jest zastosowanie bezpośredniej albo odwrotnej reguły mieszanin. Kolejną możliwością są metody teoretyczne związane z oszacowaniem górnym i dolnym tensora własności makroskopowych z wykorzystaniem modelu Voigta [107] (jednorodne odkształcenia) i Reussa [88] (jednorodne naprężenia). Są to jednak oszacowania bardzo niedokładne, więcej informacji na ich temat można znaleźć np. w [72]. Dokładniejsze oszacowanie otrzymane z zasady wariacyjnej znane jest jako podejście Hashina-Shtrikmana obliczania efektywnych stałych materiałowych [42, 43]. Wadą metody jest zależność wyniku od wielkości próbki.

Inną możliwością obliczania efektywnych stałych materiałowych jest zastosowanie koncepcji inkluzji typu Eshelbiego dla wzmocnienia elipsoidalnego w nieskończonej matrycy oraz podstawy schematu wewnętrznie zgodnego (ang. *self-consistent*) dla ciał niejednorodnych [21, 32, 47].

Podobną metodę stanowi uśrednianie Mori-Tanaka [71], w którym własności materiału wyznaczane są z rozwiązania analitycznego problemu brzegowego dla pojedynczej inkluzji w nieskończonej matrycy.

Innym podejściem jest metoda tzw. różniczkowego ośrodka efektywnego (ang. *differential effective medium approximation DEM*) [14, 89, 98]. Proces składa się z iteracyjnego zwiększania objętości inkluzji w jednorodnej matrycy przy równoczesnym obliczaniu efektywnych właściwości materiału, aż do uzyskania odpowiedniej założonej zawartości inkluzji.

Dla ośrodków periodycznych i prostych oszacowań możliwe jest zastosowanie homogenizacji asymptotycznej (matematycznej) [13, 60, 86, 90, 97], w której dokonuje się aproksymacji rozwiązania za pomocą rozwinięcia asymptotycznego względem małego parametru $\varepsilon = \frac{l}{L}$, a następnie dokonuje się przejścia granicznego przy ε zmierzającym do 0

$$u(x,y) = u^{(0)}(x,y) + \varepsilon u^{(1)}(x,y) + \varepsilon^2 u^{(2)}(x,y) + \ldots, \qquad y = \frac{x}{\varepsilon}$$

Jednym z nowszych pomysłów jest lokalna homogenizacja obliczeniowa [49, 50] oparta na analizie w dwóch skalach. W skali makro ustala się zgrubną dyskretyza-

cjê elementami skończonymi, a następnie każdy taki element analizuje się niezależnie poprzez zagęszczenie siatki elementów skończonych w celu odzwierciedlenia mikrostruktury i niejednorodności (skala mikro). W tym wypadku homogenizacja polega na obliczeniu efektywnych macierzy sztywności dla każdego elementu w skali makro na podstawie macierzy sztywności z siatki gęstej. Metoda ta jest efektywna przede wszystkim dla zagadnień, gdzie nie zachodzi warunek rozdzielności skal mówiący o tym, że wymiar charakterystyczny inkluzji powinien być przynajmniej dziesięć razy mniejszy od przyjętego obszaru skali mikro.

Jeżeli w skali mikro chcemy uwzględnić dokładnie ziarna powstałe na skutek np. rekrystalizacji, wygodne staje się wykorzystanie podejścia dwuskalowego, w którym w skali mikro materiał będzie modelowany metodą automatów komórkowych (ang. *cellular automata*, CA), natomiast w skali makro jako ośrodek ciągły za pomocą MES, dając w ten sposób metodę CAFE [22, 38, 64].

Najbardziej popularną metodą do modelowania wieloskalowego ostatnich lat jest homogenizacja obliczeniowa [13, 18, 31, 35, 36, 52, 56, 68, 78, 104, 113]. Metoda ta nie potrzebuje żadnych założeń w skali makro o relacji między naprężeniami i odkształceniami. Relacja jest obliczana w każdym punkcie (najczęściej punktach całkowania Gaussa) w skali makro przez dokładną analizę w skali mikro w tzw. reprezentatywnym elemencie objętościowym (z ang. *representative volume element, RVE*) odpowiadającym każdemu punktowi całkowania Gaussa.

W prezentowanej pracy zastosowano podejście oparte na analizie w dwóch skalach - mikro i makro, bazujące na RVE. W makro-skali zakłada się materiał jednorodny, niejednorodność jest brana pod uwagę w skali mikro w RVE, które powinno być na tyle duże, aby statystycznie reprezentować mikrostrukturę ośrodka i na tyle małe, aby spełniony był warunek rozdzielności skal [39, 46, 79]. Należy pamiętać, że rzeczywisty materiał ma mikrostrukturę z inkluzjami rozłożonymi w sposób losowy, dlatego RVE może być wyznaczone tylko w sensie statystycznym (SVE) [79, 86, 99].

Klasyczny algorytm homogenizacji obliczeniowej dla zagadnień nieliniowych rozpoczyna się od dyskretyzacji obszaru w skali makro i ustaleniu punktów (najczęściej punktów całkowania), w których będzie prowadzona dokładna analiza w skali mikro (RVE). W skali makro ustala się wstępne parametry materiału na podstawie np. testu rozciągania przeprowadzonego na RVE lub zgrubnego oszacowania metodą mieszanin w celu określenia aktualnego stanu odkształcenia (lub średnich naprężeń) dla zadanego przyrostu obciążenia. Na tej podstawie przyjmowane są warunki brzegowe dla RVE. Następnie dla każdego kroku czasu rozwiązywany jest problem początkowo-brzegowy w celu wyznaczenia średniego przyrostu odkształceń plastycznych lub naprężeń, zarówno w zakresie sprężystym, jak i poza nim. Poprzez analizę RVE obliczane są również efektywne parametry materiałowe, które są następnie przekazywane do punktów Gaussa w skali makro. W kolejnym etapie dokonywane jest oszacowanie błędu i albo dokonywana jest nowa dyskretyzacja, albo obliczenia są przerywane.

Obliczenia numeryczne wykonywane są za pomocą adaptacyjnej metody elementów skończonych. Adaptacyjny dobór siatki jest niezbędny, aby uzyskać wiarygodne wyniki w stosunkowo krótkim czasie, zwłaszcza dla zagadnień gdzie występują osobliwości i regularne zagęszczanie siatki przestaje być optymalne. Podstawą adaptacyjnego podziału elementów jest oszacowanie błędu a-posteriori. Można wyróżnić dwie główne techniki adaptacji - typu h [6, 40], w której modyfikowany jest rozmiar elementu, a stopień aproksymacji pozostaje bez zmian oraz metodę typu p [9, 10, 12], w której

rozmiar elementu się nie zmienia, natomiast stopień funkcji kształtu jest modyfikowany. Inną grupę stanowią metody typu r [44, 103], polegające na relokacji istniejących węzłów w celu zmniejszenia błędu rozwiązania. Technika ta może być również łączona z innymi typami adaptacji (np. rp [73]). Innym sposobem jest wykorzystanie adaptacji zorientowanej na jakiś cel (ang. *goal-oriented*) [75, 84] np. przemieszczenia w punkcie.

Kolejną możliwość stanowią metody adaptacji hp [29, 40, 41], pozwalające na równoczesne modyfikowanie rozmiaru elementu, jak i stopnia aproksymacji. Główną zaletą tej techniki jest najszybsza ekponencjalna zbieżność ($e^{-\alpha N^{\beta}}$). Warto zwrócić uwagę, że same techniki h lub p-adaptacji pozwalają jedynie na zbieżność algebraiczną (np. $N^{-p/3}$ dla problemów 3D), gdzie N oznacza liczbę stopni swobody, p stopień aproksymacji, $\alpha > 0$ i $\beta > 0$ są pewnymi stałymi.

W pracy zastosowano do obliczeń technikę automatycznej hp-adaptacji, zaproponowaną przez Demkowicza i współpracowników [26, 27, 29], która jest z powodzeniem stosowana w zagadnieniach liniowych. Algorytm jest oparty na oszacowaniu błędu interpolacji. Dla aktualnej dyskretyzaji dokonywany jest podział każdego elementu w każdym kierunku i podnoszony jest stopień aproksymacji, w celu wygenerowania rozwiązania dokładniejszego. Otrzymane rozwiązanie jest interpolowane na wszystkie albo wybrane możliwe nowe siatki. Następnie rozwiązywany jest problem optymalizacji w celu znalezienia siatki, która zapewnia maksymalizację zmniejszenia błędu na każdy dodatkowy stopień swobody. W algorytmie dopuszczone jest istnienie siatek jednonieregularnych z węzłami wiszącymi, co usprawnia działanie adaptacji.

ROZDZIAŁ 2: SFORMUŁOWANIA PROBLEMU

W rozdziale 2 zestawiono sformułowania matematyczne, które były podstawą obliczeń numerycznych. Dla obszaru niejednorodnego w skali makro zadanie sprężystoplastyczne polegałoby na znalezieniu przemieszczeń, odkształceń plastycznych i naprężeń tak, aby w każdej chwili czasu i dla każdego jednorodnego podobszaru spełnione były równania równowagi oraz konstytutywne z uwzględnieniem niesprężystych deformacji ośrodka. Jednak ze względu na złożoność problemu takie obliczenia wymagałyby dużych kosztów. Problem rozwiązuje się stosując podejście dwuskalowe. W skali makro zakłada się, że ośrodek jest jednorodny i poszukiwane są jedynie uśrednione (zhomogenizowane) wartości. Jedynie w skali mikro (RVE) rozwiązywany jest problem niejednorodny. Zakłada się, że naprężenia ograniczone są powierzchnią plastyczności Misesa, postuluje się stowarzyszone prawo płynięcia. Całkowanie w czasie odbywa się za pomocą niejawnej metody Eulera z korektorem typu "rzutowanie po promieniu" (ang. *radial return algorithm*). Poprawność analizy dla obszaru heterogenicznego dodatkowo weryfikuje się za pomocą warunku Hilla - Mandela, który powinien być spełniony dla niejednorodnych materiałów bez uszkodzeń [48].

Na jakość rozwiązania w skali mikro wpływ mają warunki brzegowe (kinematyczne, statyczne, periodyczne). Dla obszarów z inkluzjami rozłożonymi w sposób równomierny najlepsze wyniki daje zastosowanie periodycznych warunków brzegowych do analizy na poziomie RVE [45, 66, 110] ponieważ w najszybszy sposób pozwalają oszacować efektywne parametry materiałowe. Warunki periodyczne mogą zostać uwzględnione na etapie dyskretyzacji (np. za pomocą metody funkcji kształtu lub mnożników Lagrange'a) albo bezpośrednio w sformułowaniu słabym problemu.

ROZDZIAŁ 3: WSTĘPNE WYNIKI HOMOGENIZACJI OBLICZENIOWEJ

Wstępne testy miały za zadanie sprawdzenie poprawności działania algorytmu obliczeń dwuskalowych oraz wpływu dyskretyzacji obszarów niejednorodnych na jakość rozwiązania. Dokonano oszacowania błędu wykorzystując metodę hierarchiczną [26], polegającą na wykonaniu obliczeń na aktualnej siatce i na siatce zagęszczonej równomiernie. Potwierdzono, że istotne znaczenie na dokładność wyników ma dopasowanie siatki elementów skończonych do granic materiałów.

ROZDZIAŁ 4: HOMOGENIZACJA KOMPOZYTÓW W ZAKRESIE SPRĘŻYSTO-PLASTYCZNYM

Do obliczeń wykorzystano wspomnianą wcześniej adaptacyjną metodę elementów skończonych. Dla wybranej struktury periodycznej dobrano RVE i w zakresie sprężystym porównano efektywne parametry materiałowe otrzymane różnymi metodami (metoda mieszanin, odwrotna metoda mieszanin, oszacowania graniczne Hashina-Shtrikmana, podejście Maxwella, homogenizacja numeryczna polegająca na symulacji testu rozciągania). W rozdziale tym przedstawiono wyniki obliczeń efektywnych parametrów materiałowych przy różnych metodach dyskretyzacji i dla różnych kształtów inkluzji. Najlepsze wyniki osiągnięto, gdy siatka elementów skończonych wstępnie uwzględniała rozkład i kształt inkluzji. Taki przypadek dopasowania siatki do kształtu inkluzji jest jednak rzadko możliwy do wykonania. Dobrym rozwiązaniem jest zastosowanie *hp*-adaptacji, która poprzez oszacowanie błędu w jak najlepszy sposób stara się dopasować siatkę do granicy materiałów, poprzez zagęszczenie elementów w okolicach zmiany materiału. Sprawdzono, jaki wpływ na wyniki ma orientacja i rozmiar przyjętego RVE. Dla przypadku inkluzji w kształcie kulek rozłożonych w sposób równomierny w matrycy rozmiar RVE nie ma istotnego wpływu. Pokazano również, że analizowany kompozyt wykazuje własności izotropowe, niezależne od kierunku.

Analiza zagadnień niesprężystych, nawet po zastosowaniu numerycznej homogenizacji, jest bardzo czasochłonna, gdyż obliczenia na poziomie mikro muszą być wykonywane wielokrotnie. W klasycznej homogenizacji każdemu punktowi całkowania Gaussa przyporządkowany jest RVE. Jednak gdy materiał zaczyna wykazywać zachowanie niesprężyste obliczenia stają się dodatkowo czasochłonne. Ponadto pojawia się problem przy stosowaniu adaptacyjnej wersji MES, gdyż po każdym etapie adaptacji dochodzą nowe punkty całkowania, w których historia deformacji w skali makro jest nieznana. Zaproponowano dwie możliwości rozwiązania tego problemu.

Jeżeli deformacje materiału zachodzą w zakresie sprężystym i niejednorodności składników są rozłożone periodycznie wystarczająca jest analiza pojedynczego RVE do oszacowania sprężystych stałych materiałowych, obserwowanych w skali makro. Analogicznie można postąpić w zakresie poza sprężystym i przewidywać globalne sprężysto-plastyczne zachowanie materiału w skali makro. Dla RVE symulowane są testy rozciągania dla różnych ścieżek obciążenia w celu znalezienia relacji między średnimi odkształceniami a naprężeniami. Następnie formułowane jest globalne prawo dla skali makro z efektywnymi parametrami plastycznymi (granica plastyczności, parametr wzmocnienia itp.). Do obliczeń przyjęto kompozyt metaliczny wzmocniony inkluzjami (kulkami)

wykonanymi z innego materiału o wyższej wytrzymałości, rozłożonymi periodycznie. Obydwa materiały wykazywały charakter sprężysto-plastyczny ze wzmocnieniem. Założono, że w skali mikro i makro obowiązuje stowarzyszone prawo płynięcia i hipoteza Misesa. Dla pojedynczego RVE wykonano symulacje testów rozciągania przy różnym obciążeniu. Dla wyznaczonego prawa konstytutywnego przeprowadzono testy w skali makro dla sprawdzenia założonego stowarzyszonego prawa płynięcia. Zweryfikowano, że przyjęty model ze wzmocnieniem kinematycznym jest poprawny.

Jeżeli właściwości materiału po homogenizacji nie są jednakowe w całym obszarze należy zastosować więcej niż jeden RVE. Można jednak przyjąć ich mniej niż punktów całkowania Gaussa [91, 64, 65]. W pracy zaproponowano zastosowanie analizy bazującej na ustalonej liczbie punktów. Na podstawie wstępnej analizy w skali makro podejmowana jest decyzja w jakim obszarze można spodziewać się uplastycznienia i tylko tam rozmieszczane są punkty z przyporządkowanymi im elementami RVE. Jednocześnie należy zapewnić możliwość transferu danych pomiędzy punktami przyjętymi z RVE a punktami Gaussa, i na odwrót. Algorytm został zweryfikowany na przykładzie.

ROZDZIAŁ 5: OSZACOWANIE BŁĘDU HOMOGENIZACJI

Zastąpienie materiału heterogenicznego przez materiał jednorodny z efektywnymi parametrami materiałowymi wprowadza błąd związany z utratą pełnej informacji o mikrostrukturze ośrodka. Jeżeli homogenizacja wprowadza zbyt duży błąd do obliczeń, to nie powinna być stosowana dla całego obszaru albo jego części.

Globalne oszacowanie błędu rozwiązania z wykorzystaniem tensora zhomogenizowanych parametrów materiałowych i dokładnego tensora ze skali mikro zaproponował Zohdi ze współpracownikami. [112]. Z kolei strategia adaptacyjna Temizera i Wriggersa [101] polega na wybraniu podobszarów, odpowiadających strefom z wysokimi gradientami odkształceń, w których wprowadzona zostaje dokładna mikrostruktura.

W tym rozdziale pokazano podejście bazujące na oszacowaniu od góry [77, 105, 106] oraz dwie inne możliwości oszacowania błędu modelowania.

W jednej z nich w skali makro definiuje się obszar, w którym chcemy oszacować jakość rozwiązania. Następnie wyodrębnia się ten obszar i uwzględnia się w nim niejednorodność. Dobierane są warunki brzegowe na podstawie rozwiązania zhomogenizowanego i rozwiązywany jest problem brzegowy. Następnie dokonuje się porównania otrzymanego wyniku z rozwiązaniem zhomogenizowanym. Tam, gdzie błąd jest duży przyjmuje się materiał niejednorodny. Siatka elementów skończonych powinna zatem zapewniać dobre dopasowanie do niejednorodności oraz szybkie rozgęszczanie dla pozostałego obszaru.

Innym pomysłem oszacowania błędu modelowania, przez analogię do oszacowania błędu aproksymacji w MES [7, 8], jest zastosowanie podejścia bazującego na sprawdzeniu residuum spełnienia równania równowagi. Najpierw wyznaczane są efektywne parametry dla obszaru zhomogenizowanego na podstawie analizy RVE. Następnie rozwiązywany jest problem dla jednorodnego obszaru w celu wyznaczenia rozwiązania zhomogenizowanego. W kolejnym etapie obliczane jest residuum równania obszaru niejednorodnego dla rozwiązania zhomogenizowanego w każdym elemencie skończonym w skali makro. W rzeczywistości jest to dystrybucja. Oszacowanie jej normy daje informację o błędzie homogenizacji.

W tym rozdziale, na przykładach numerycznych, przedstawiono procedury doboru

obszarów, w których nie można stosować homogenizacji.

ROZDZIAŁ 6: AUTOMATYCZNA *HP*-ADAPTACJA DLA PROBLEMÓW NIELINIOWYCH

Jak zostało wcześniej wspomniane stosowana adaptacyjna wersja typu *hp* [26, 27, 29, 102] była z powodzeniem wykorzystywana do zagadnień liniowych. Jednak nie ma dowodów, które pokazałyby, że taki sam algorytm zastosowany do zagadnień niesprężystych będzie optymalny.

W tym rozdziale sprawdzono zbieżność *hp*-adaptacji dla zagadnień sprężysto-plastycznych oraz zaproponowano modyfikację algorytmu. Zastosowania adaptacji w plastyczności sięgają lat 80-tych. Cheng [20] oraz Zienkiewicz [111] rozwinęli takie podejście do procesu formowania metali; Peric, Dutko i Owen [81, 82] zastosowali adaptacyjną MES do problemów dużych odkształceń, Cramer i współpracownicy [24] zastosowali podział elementów dla stowarzyszonej i niestowarzyszonej plastyczności. Adaptacja typu *p* została przedstawiona jako efektywna do problemów fizycznie nieliniowych przez Düstera i Ranka [30]. Technika *rp* została użyta przez Nübela i współpracowników [73] w celu dopasowania siatki elementów skończonych do granicy sprężysto-plastycznej i uwzględnienia regularności. Z opisów w literaturze [11, 19, 37, 83] wynika, że niesprężyste deformacje powinny być uwzględnione w specjalny sposób w estymatorze błędu a-posteriori. W rozdziale tym zaproponowano i testowano modyfikację *hp* poprzez wzbogacenie jej o dodatkowe podziały typu *h* w elementach, w których występują zarówno sprężyste jak i poza sprężyste deformacje. Okazuje się, że zastosowanie *hp* bez modyfikacji jest wystarczające do uzyskania szybkiej, ale tylko algebraicznej zbieżności.

ROZDZIAŁ 7: SFORMUŁOWANIE MIESZANE W METODZIE ELEMENTÓW SKOŃCZONYCH

Podstawą MES jest sformułowanie słabe (wariacyjne). W klasycznej wersji przemieszczeniowej sformułowania problemu liniowej teorii sprężystości nieznane są przemieszczenia, natomiast pozostałe pola (odkształceń, naprężeń) obliczane są w wyniku postprocessingu. Wówczas, oprócz błędu aproksymacji przemieszczeń pojawia się błąd związany z pochodnymi rozwiązania, niezbędnymi do wyznaczenia pozostałych pól.

Wygodne wydaje się zastosowanie sformułowania mieszanego (dwupolowego) metody elementów skończonych, w którym w sposób niezależny aproksymowane są pola przemieszczeń i naprężeń. Zastosowania sformułowania mieszanego były rozwijane od lat 70-tych, należy tutaj wymienić przede wszystkim prace takich autorów jak: Brezzi [16], Crouzeix and Raviart [25], Raviart i Thomas [87], Arnold [2, 3, 4]. Trudności związane są z zapewnieniem symetrii tensora naprężenia, przy równoczesnym zapewnieniu ciągłości wektora naprężenia i stabilności aproksymacji.

W pracy zastosowano zmodyfikowaną zasadę Hellingera-Reissnera [4, 85], w której symetria tensora naprężenia jest wymuszana w sposób słaby. Dodatkowo, w celu zagwarantowania stabilności aproksymacji zapewnia się spełnienie warunku $inf - sup$ lub przemienności diagramu Rhama. Przeprowadzone testy potwierdziły poprawność zaproponowanej nowej aproksymacji w zadaniach dwuwymiarowych.

ROZDZIAŁ 8: PODSUMOWANIE

W przedstawionej pracy pokazano w jaki sposób można zastosować *hp*-adaptacyjną metodę elementów skończonych do modelowania kompozytów metalicznych przy wykorzystaniu podejścia dwuskalowego. Przedstawiono sformułowania problemu dla skali mikro i makro, zaproponowano modyfikację klasycznej metody homogenizacji w celu usprawnienia procesu obliczeń, zwłaszcza gdy materiał wykazuje zachowania poza sprężyste. Przedstawiono metody oszacowania błędu modelowania, które jest kluczowe dla uzyskania wiarygodnych wyników. Dokonano próby modyfikacji procesu *hp*-adaptacji dla zagadnień nieliniowych. W pracy zawarto również sformułowanie mieszane elementów skończonych, dzięki któremu można w sposób niezależny bezpośrednio aproksymować naprężenia, ważne z punktu widzenia inżyniera. W obliczeniach wykorzystano adaptacyjne programy MES [26, 27] *hp*1*D*, *hp*2*D* i *hp*3*D* (w języku *Fortran*95), które wzbogacono własnymi procedurami. Dodatkowo część obliczeń wykonano w niezależnie przygotowanych programach w Fortranie oraz w środowisku Matlab. Napisano ponad 20000 linii własnego oprogramowania.

Do oryginalnych elementów pracy można zaliczyć m.in.:

- zastosowanie *hp*-adaptacyjnej MES do modelowania dwuskalowego
- sprężysto-plastyczną analizę kompozytów metalicznych przy wykorzystaniu ograniczonej liczby RVE
- porównanie wpływu kształtu i rozmiaru RVE na wyniki
- oszacowanie błędu modelowania
- modyfikacja i przetestowanie algorytmu automatycznej *hp*-adaptacji dla zagadnień nieliniowych
- zastosowanie sformułowania wielopolowego z nowymi funkcjami kształtu w zadaniach homogenizacji.

Plany dalszych prac obejmują dowody matematyczne stosowanych błędów homogenizacji, adaptacyjne rozmieszczanie ustalonych RVE, zastosowanie innych praw konstytutywnych, uwzględnienie losowości, rozwarstwienia i porównania z eksperymentami.